Karlsruher Institut für Technologie

Dominique T. Thielemann

Novel Functionalized Rare Earth Metal Clusters and Polymers

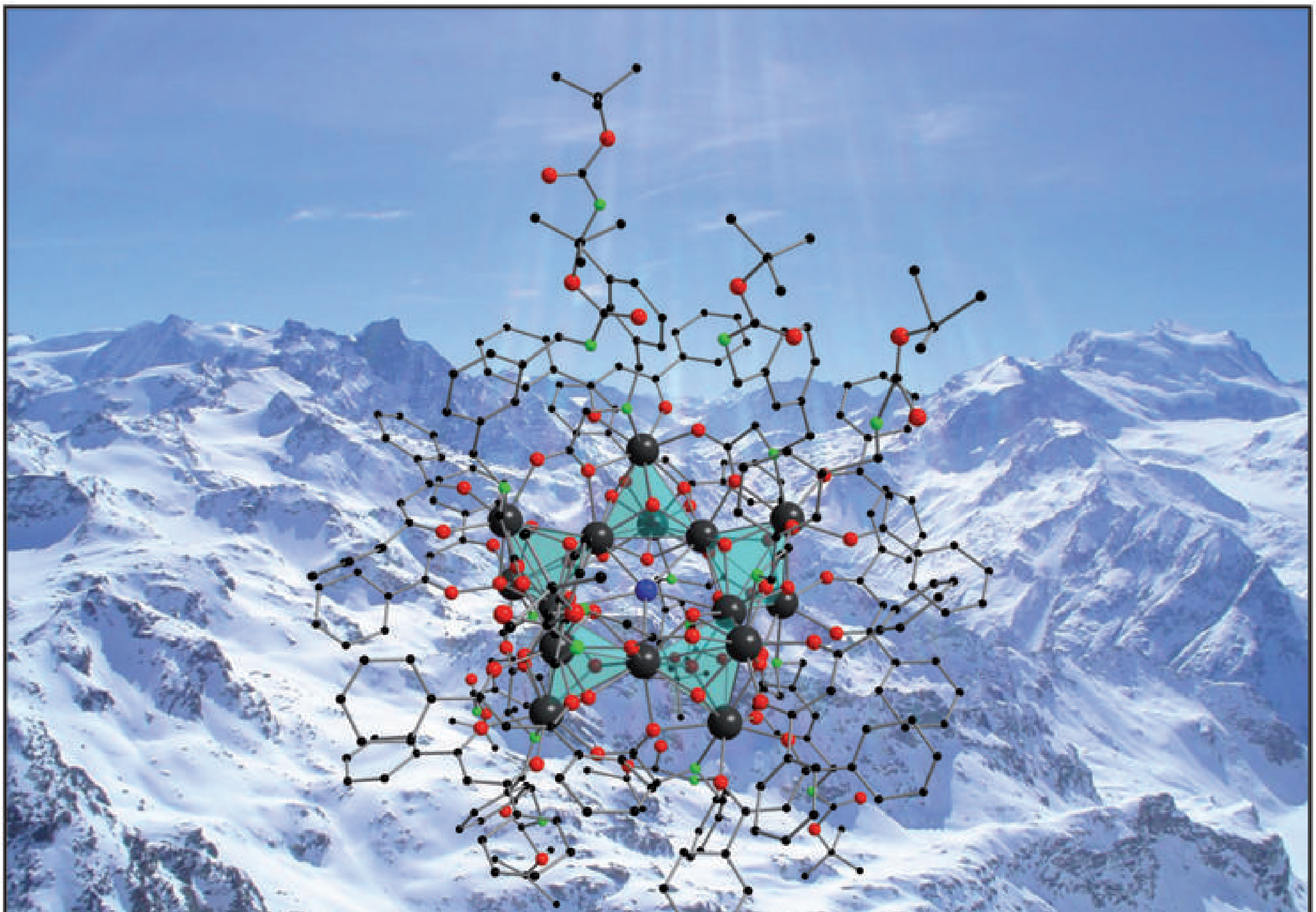

Cuvillier Verlag Göttingen
Internationaler wissenschaftlicher Fachverlag

Novel Functionalized Rare Earth Metal Clusters and Polymers

Neuartige Funktionalisierte Seltenerdmetallcluster und -Polymere

Zur Erlangung des akademischen Grades eines

DOKTORS DER NATURWISSENSCHAFTEN

(Dr. rer. nat.)

an der Fakultät für Chemie und Biowissenschaften

des Karlsruher Instituts für Technologie (KIT) - Universitätsbereich

vorgelegte

DISSERTATION

von

M. Sc. Dominique Tobias Thielemann

aus

Berlin

Dekan: Prof. Dr. S. Bräse
Referent: Prof. Dr. P. W. Roesky
Korreferent: Priv.-Doz. Dr. T. Stumpf
Tag der mündlichen Prüfung: 08.02.2011

Bibliografische Information der Deutschen Nationalbibliothek
Die Deutsche Nationalbibliothek verzeichnet diese Publikation in der
Deutschen Nationalbibliografie; detaillierte bibliografische Daten sind
im Internet über http://dnb.d-nb.de abrufbar.
1. Aufl. - Göttingen : Cuvillier, 2011
Zugl.: Karlsruhe (KIT), Univ., Diss., 2011

978-3-86955-675-8

Die vorliegende Arbeit wurde von 2007 bis 2011 unter Anleitung von Prof. Dr. Peter W. Roesky an der Freien Universität Berlin (FUB) und am Karlsruher Institut für Technologie (KIT, Campus Süd) angefertigt.

Nonnenstieg 8, 37075 Göttingen
Telefon: 0551-54724-0
Telefax: 0551-54724-21
www.cuvillier.de

1. Auflage, 2011
Gedruckt auf säurefreiem Papier

978-3-86955-675-8

„Der Ziellose erleidet sein Schicksal –
der Zielbewusste gestaltet es“

Immanuel Kant (22.04.1724 - 12.02.1804)

und deshalb:

„Der Weg ist das Ziel“

Konfuzius (551 v. Chr. - 479 v. Chr.)

Meiner Familie

(und allen, die sich Ihr zugehörig fühlen)

TABLE OF CONTENTS

1. INTRODUCTION

1.1 The Rare Earth Elements

The rare earth elements comprise 17 metals, starting from scandium (Sc) and yttrium (Y), to be complemented by the 15 lanthanoids ranging from lanthanum (La) to lutetium (Lu). The group three elements scandium, yttrium and lanthanum show a similar chemical behaviour which is derived from the related valence electron configurations [Ar]$3d^1 4s^2$ (Sc), [Kr]$4d^1 5s^2$ (Y) and [Xe]$5d^1 6s^2$ (La).[1] The term "lanthanoid" arises from the chemical similarity compared to lanthanum as its first representative, giving reason for their common occurrence in nature. Generally, the lanthanoids can be classified into two sections: the lighter lanthanoids can be found in the cerite earths and are assigned to the cerite earth elements (*currently abbreviated as* Ct), whereby they include the atomic numbers from 57 to 64 from lanthanum to gadolinium. The heavier lanthanoids exhibiting atomic numbers from 65 to 71 from terbium to lutetium were discovered in the ytter earths and are thus called the ytter earth elements (*currently abbreviated as* Yt). The denotation "rare earths" is assigned to the oxides of the corresponding elements, and the term "rare" is actually not justified as it solely arises from the late discovery compared to most other elements. The term "rare" is misleading, since some of the rare earth metals show a higher occurrence than some transition metals. For example, tin and cobalt are more rare than cerium, lead is more rare than neodymium and also the three precious metals silver, gold and platinum are more rare than europium and thulium.[2]

Pacing from the left to the right in the lanthanoid series, the *4f*-shell is consecutively filled from cerium ([Xe]$4f^1 5d^1 6s^2$) to lutetium ([Xe]$4f^{14} 5d^1 6s^2$). The low spatial extension of the *4f*-electrons and their close proximity to the nucleus obstructs a participation in chemical bond synergism. They can only be removed in rare cases. The more distant $5d^1$- and $6s^2$-electrons exhibit much lower ionization energies than the *4f*-electrons, hence, they can be removed much easier and are mainly responsible for the lanthanoids' similar reactivities. By removing the $5d^1$- and $6s^2$-electrons, the stable octet ($5s^2 5p^6$) is achieved to give the most common oxidation state +3 of the lanthanoids. As the *5s*- and *5p*-electrons additionally shield the *4f*-electrons efficiently, the chemical reactivity of the latter is further minimized. Thus, any chemical bonding involving Ln^{3+} species is based on electrostatic interactions and only an insignificant contribution arises from covalent interactions. This issue discloses a large scope of coordination numbers and the energy barriers between different coordination geometries are comparably low.

Since the occupation of lanthanum's *5d*-orbital with one electron is followed by the filling of the *4f*-orbitals of the remaining 14 lanthanoids prior to continuation of the filling of the *5d*-orbitals in hafnium, the lanthanoid series is quasi embedded into the *5d*-series of the transition metals. In contrast to the conventional periodic table (Fig. 1.1) in which the lanthanoids are positioned below together with the actinoids, the extended periodic table of the elements visualizes this embedding more demonstratively.

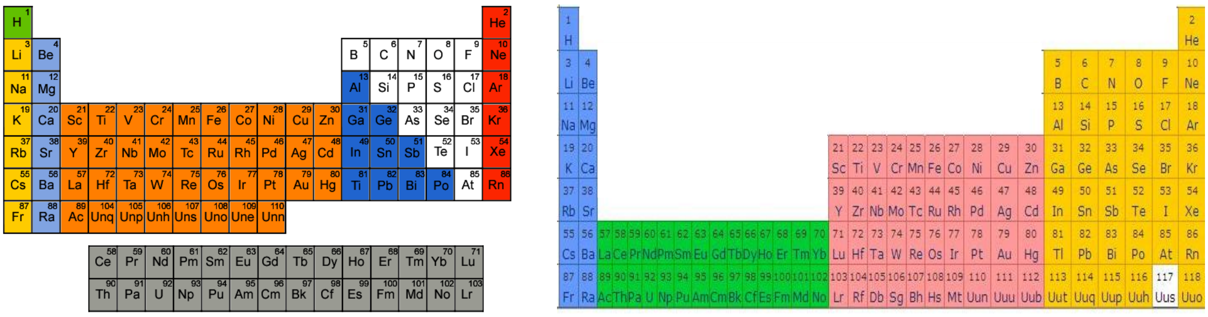

Figure 1.1. Lanthanoid and actinoid series set apart from main periodic table (left) and optional inclusion of lanthanoids and actinoids between the *s*- and *d*-block elements (right).

The lanthanoids' *4f*-orbitals exhibit a shape which is fairly odd compared to its *s*-, *p*- and *d*-analogues, *i.e.* they possess a large surface due to their complex wave functions. In conjunction with the low spatial extension of the *4f*-orbitals, this aspect effectuates a strikingly reduced shielding of the *5s*- and *5p*-electrons, as the *4f*-orbital geometry is not capable of efficiently compensating the nuclear charge. As a result, by increasing the nuclear charge from cerium (58 protons) to lutetium (71 protons), the effective nuclear charge Z_{eff} increases as well, *i.e.* the ionic radii steadily decrease from the early to the late lanthanoid elements (Fig. 1.2).[3] Concomitantly, the effective nuclear charge Z_{eff} of the ion torsi increases. This effect is called the "lanthanide contraction",[4]-[5] making each of the element pairs zirconium and hafnium, niobium and tantalum, as well as molybdenum and tungsten almost chemically indistinguishable. Despite the described electrostatic reasons, additional relativistic effects have been reported in literature as another origin of this contraction.[6]

Ln^{3+}	Ionic radius [Å]	Ln^{3+}	Ionic radius [Å]
La	1.216	Tb	1.095
Ce	1.196	Dy	1.083
Pr	1.179	Y	1.075
Nd	1.163	Ho	1.072
Pm	1.144	Er	1.062
Sm	1.132	Tm	1.052
Eu	1.120	Yb	1.042
Gd	1.107	Lu	1.032

Table 1.1. Ionic radii of trivalent nine-coordinate rare earth metal ions.[3]

1.2 Occurrences and Processing

In nature, there are numerous minerals from which rare earth metals can be gained. The cerite earth elements are mainly present in two minerals: firstly, there is the monazite which is composed of a binary silicate/phosphate host lattice accommodating both cerite earth elements and thorium $(Ct,Th)[(P,Si)O_4]$, whereby those cerite earth elements having even atomic numbers (cerium, neodymium, samarium and gadolinium) make up the major fraction, as required by Harkins' rule. Monazite can primarily be found in Brazil, in South India, in Sri Lanka, in Western Australia, in the USA and in granitic pegmatites in South Norway. The second mineral, bastnaesite, is primarily present in Kongo and New Mexico, but also countries like *e.g.* Hungary, Greece, the Balkan region, Norway, Mongolia, Malawi and Canada have certain occurrences.[7] It displays a carbonate/fluoride containing host lattice which mainly contains cerium, lanthanum and dysprosium, whereby the molar fractions of all the rare earth elements depend on the individual deposits. In contrast, the ytter earth elements are primarily available in minerals like thalenite $Yt_2[Si_2O_7]$, thortveitite $(Yt,Sc)_2[Si_2O_7]$, gadolinite $Be_2Fe(II)Yt_2O_2[SiO_4]_2$ and xenotime $YtPO_4$, whereby their consistencies once more agree well with Harkins' rule. However, about 70 % of the world total rare earth reserves are placed in china, comprising almost all the minerals described.[1]

Purposing to separate the rare earth metals from each other to make them chemically applicable, the purified minerals are dissolved in either very basic or very acidic milieu. Initially, advantage was taken from the different solubilities of the corresponding nitrates or hydroxides applying fractional crystallization.[8] Another possibility is to utilize the different affinities of the individual rare earth elements to form the corresponding tris(*n*-butylphosphate) (TBP) complexes *via* solvent extraction.[9] However, this method is unfeasible since several hundreds of separation steps are necessary. Nowadays, industrial separation of rare earth elements is performed *via* ion exchange.[8-9] Therefore, the corresponding minerals or ores are grinded and dissolved in a hot sodium hydroxide solution. The sparingly soluble hydroxides are separated, dissolved in nitric acid and then charged on an organic ion exchange column. The stationary phase of the column is a resin which is preferably ammonium(polystyrene sulfonate). The adsorbed hydroxides exhibit different binding affinities to this resin, which is based on different hydrodynamic radii originating from individual ionic radii of the Ln^{3+}-ions. The smallest Ln^{3+}-ion Lu^{3+} possesses the highest charge density and the highest degree of hydratisation, hence, it has the largest hydrodynamic radius. Consequently, the hydrated Lu^{3+}-ion provides the loosest bond to the resin of all the Ln^{3+}-ions and is eluted as the first rare earth metal. The principle is *vice versa* valid for the largest Ln^{3+}-ion La^{3+}, hence, it is the last rare earth element to leave the column. The resulting order ranging from lutetium to lanthanum is further enhanced by addition of complexing agents such as *e.g.* EDTA (ethylene diamine tetraacetate) or α-hydroxy acetic acid and a suitable pH-value.[8-10] Once the rare earth elements are entirely separated from each other, they can be easily converted to various starting materials like *e.g.* the corresponding trichloride hydrates $[LnCl_3\cdot(H_2O)_n]$ (n = 6, 7) for continuative reactions.

Regarding potential applications, the main significance of the rare earth elements arises from their unique photophysical[11] and magnetic properties,[4-5] as well as their comparably low toxicity for cellular organisms.[11a, 11d] Based on these characteristics, they have successfully found applications as laser materials (*e.g.* YAG-lasers, yttrium-aluminium-garnet),[12] luminescent devices (erbium doped optical fibres for telecommunication),[13] permanent magnets[4] and MRT contrast agents.[14]

1.3 Rare Earth Metal Luminescence

The described shielding of the *4f*-electrons by the *5s*- and *5p*-electrons permits ligand-induced crystal field splitting only to a low extent. As a result, narrow emission lines are observed for all the rare earth elements, and the wavelengths of emission position are not influenced by individual ligand systems. The only energy split of *4f*-electrons occurs within a range of approximately 100 cm^{-1} as a function of site symmetry, affording the so called “Stark sublevels”.[11e] Nevertheless there is one exception with respect to spectrochemical sensitivity towards changes in the metal-ion environment, as *e.g.* the hypersensitive $^5D_0 \rightarrow {}^7F_2$ transition in europium(III) compounds which varies its wavelength notably upon changes of ligands and site symmetry.[15]

The *4f*-electrons in Ln^{3+}-ions are capable of undergoing *4f*-*4f*-tranisitions which are Laporte forbidden, *i.e.* the sum of the angular momenta of the electrons in the initial and final state do not change by an odd integer.[11e] As a result, Ln^{3+}-ions exhibit low extinction coefficients upon direct excitation. Besides, this is not valid for divalent Ln^{2+}-ions, since they possess Laporte allowed *4f*-*5d*-transitions providing much larger extinction coefficients. Nevertheless, all the rare earth metal atoms provide a certain luminescence, after relevant excited states have once been populated. In this context, the Laporte forbiddance of the *4f*-*4f*-tranisitions even provides one crucial advantage supporting rare earth metal luminescence: the long lifetimes of their excited states which are directly correlated to low probabilities of forbidden transitions. This adds a certain value to the forbiddance of relaxation *via* *4f*-*4f*-tranisitions, since the luminescence of rare earth metal species persists much longer than *e.g.* the autoluminescence of cells. In this context, time resolved luminescence measurements of *e.g.* cellular systems incubated with certain rare earth metal complexes facilitate a reliable localization of the compound *in vivo* and *in vitro*.

The most remarkable representatives are europium and terbium emitting in the visible range of light (360 nm – 760 nm). Neodymium, erbium and ytterbium are capable of emitting luminescence efficiently in the near infrared (NIR) range (760 nm – 2500 nm). The remaining rare earth metal atoms do not provide notable luminescence properties, hence, their applicability as luminescent devices is confined to a minimum.

The discrepancy of the low extinction coefficients can be circumvented by *e.g.* tethering an electronically suitable ligand on a rare earth metal atom to induce a ligand-to-metal energy transfer (LMCT). This process is capable of populating the corresponding excited states of the rare earth metal atoms from which relaxation occurs upon emission of luminescence. Depending on the individual purposes of application, the ligand of choice might be organic like *e.g.* multiply substituted 8-hydroxyquinoline derivatives or inorganic like *e.g.* an oxo ligand. The latter one is currently utilized in europium doped yttrium oxide lattices,[16] which depicts the origin of the phosphors for cathode-ray tubes and fluorescent lamps.[17] For the organic ligands, high energy vibrators like O-H and C-H moieties should be absent to avoid quenching of the luminescence. In this context, usage of perfluorinated ionic liquids instead of standard solvents supports higher quantum yields, as previously shown by several groups.[11d] In addition, three-dimensional molecular networks in terms of *e.g.* metal organic frameworks (MOF) further prevent quenching of luminescence by “swallowing” scaffold vibrations *via* resonance coupling. This effect can also be achieved upon utilization of multidentate ligands which allocate as much donor atoms as possible to facilitate a high degree of chelatization and/or bridging. The latter issues imply the following relation: the lower the vibrational and rotational flexibility of the ligands and of the whole molecular scaffold, the less degrees of freedom are allocated for luminescence quenching.[11d]

1.4 Rare Earth Metal Magnetism

Except Sc^{3+}, Y^{3+}, La^{3+} and Lu^{3+}, all the trivalent rare earth metal ions possess unpaired *4f*-electrons and are thus paramagnetic. The magnetic properties of the rare earth metal ions are given by the ground states,[18] because the rare earth metal ions' excited states are thermally inaccessible. In analogy to the aforementioned lack of spectrochemical sensitivity, the magnetic moments μ_{eff} (given in [μ_{B}], Bohr magneton) of rare earth metal ions are essentially not influenced by their chemical environment. In consequence, the magnetic properties are not modified upon a change of the ligand or the coordination geometries, as observed for transition metal compounds. μ_{eff} is given by the equation:

$$\mu_{\mathrm{eff}} = g_{\mathrm{J}}[(J(J + 1)]^{1/2}$$

J is the quantum number and the Landé factor g_{J} is given by the following relation:

$$g_{\mathrm{J}} = 3/2 + [S(S + 1) - L(L + 1)]/2J(J + 1)$$

S is the spin quantum number and L is the quantum number of angular momentum.

In general, the magnetic moments μ_{eff} is larger for the second half than for the first half of the lanthanoid series, since a more than half-filled *4f*-shell underlies the relation $J = L + S$ and not $J = L - S$, as for the less than half-filled *4f*-shell of the cerite earth elements.[18] Consequently, the heavier homologues such as dysprosium gain more relevance for potential applications.[19] In contrast to the other trivalent rare earth metal ions, Sm^{3+} and Eu^{3+} exhibit spin-orbit coupling to a much lower extent, allowing low-lying paramagnetic excited states to give a contribution to μ_{eff}. This aspect makes the ground state $^7F_2$ in Eu^{3+} thermally accessible and leads to magnetic moments of 3.5 μ_{B} at room temperature, compared to its diamagnetic $^7F_0$ analogue. The same case is valid for Sm^{3+}, in which the thermally populated $^6H_{7/2}$ ground state provides paramagnetic behaviour with a magnetic moment of 1.6 μ_B, in contrast to the corresponding $^6H_{5/2}$ analogue with only 0.85 μ_B.

Dysprosium also exhibits low-lying excited states in terms of Stark sublevels within its $^6H_{15/2}$ ground state,[20] providing a very large magnetic moment of μ_{eff} = 10.60 μ_B. Moreover, the Dy^{3+}-ion is not spherical in shape, as the $4f^9$-configuration offers an ensemble of both paired and unpaired electrons (S = 5/2). This aspect is associated with a distinct anisotropy, which is in addition to the low-lying excited states essential as a requirement for single-molecule-magnet (SMM) behaviour.[20-21] Furthermore, SMMs have a certain blocking temperature being usually in the lower Kelvin scale. Below this temperature, the magnetized SMM compounds show a deceleration of relaxation of magnetization, *i.e.* the magnetization is maintained for up to several years.[22] If an earlier relaxation is purposed, a reversed field is required to bring magnetization back to zero, which makes the magnetism of such compounds switchable and thus flexible on the molecular scale. In this context, the resulting hysteresis below this temperature is of pure molecular origin. Thus, collective long-range magnetic ordering of magnetic moments is not necessary and makes the magnetic spins much more flexible, compared to conventional bulk magnets.

These aspects let SMMs appear as a first approach towards nanomagnets, in which each molecule might serve as the smallest feasible unit for *e.g.* magnetic storage. Optimization of these compounds might further gain applications in fields like quantum computing, high-density information storage and magnetic refrigeration.[23]

1.5 Rare Earth Metal Clusters

Beyond the mononuclear compounds providing the valuable properties above described, the utililization of oligo- to polynuclear rare earth metal compounds promise to enhance all the desired effects. Therefore, rare earth metal based clusters appear as a suitable approach, since they represent molecular intermediates linking molecular and solid state chemistry and they help to understand size-dependent photophysical properties of electronic materials.[24] The chemistry of rare earth metal clusters is by far not as developed as the cluster chemistry of the transition metals (especially of molybdenum,[25] copper,[26] silver[27] and gold[28]), which is surprising since oligomeric lanthanoid structures are proposed to play a key role in some catalytic transformations.[29],[30],[31] Before continuing with this issue, it deserves mentioning that the electronic configurations of the rare earth metals do not allow a cluster formation as defined by Cotton in 1966 within the following quotation:[32]

> *“Metal cluster compounds can be defined as those containing a finite group of metal atoms which are held together entirely, mainly or at least to a significant extent, by bonds directly between the metal atoms.”*

This means, that rare earth metals are not capable of forming interatomic bonds between themselves as they cannot contribute any electrons to a covalent bond. As a result, pseudo-cluster arrangements of the rare earth metal atoms are exclusively facilitated when small Lewis-basic ligands are available to bridge and assemble several (*i.e.* more than one) rare earth metal moieties. Nevertheless, the denotation “cluster” for describing such rare earth metal assemblies has gained international acceptance, although the assignment coordination oligomer might be more accurate.

These Lewis-basic ligands are *e.g.* spherical fluoride anions, which are able to occupy tetrahedral cavities made up by corresponding oligonuclear rare earth metal scaffolds. By this approach, Brennan *et al*. succeeded in preparing a octaeicosanuclear rare earth metal fluoride cluster $[Ln_{28}F_{68}(SePh)_{16}(py)_{24}]$ (Ln = Pr, Nd, py = pyridine) featuring a kind of a heteroscaffold made up by 28 rare earth metal atoms and 68 fluorine atoms, whereby its periphery is saturated by sixteen organic phenyl selenyl ligands (Fig. 1.2).[33] Due to the purely inorganic nature of the cluster core, the quantum efficiency regarding NIR emission is 41 % for Ln = Nd, which is comparable to the quantum efficiencies of neodymium-doped fluoride lattices.[34]

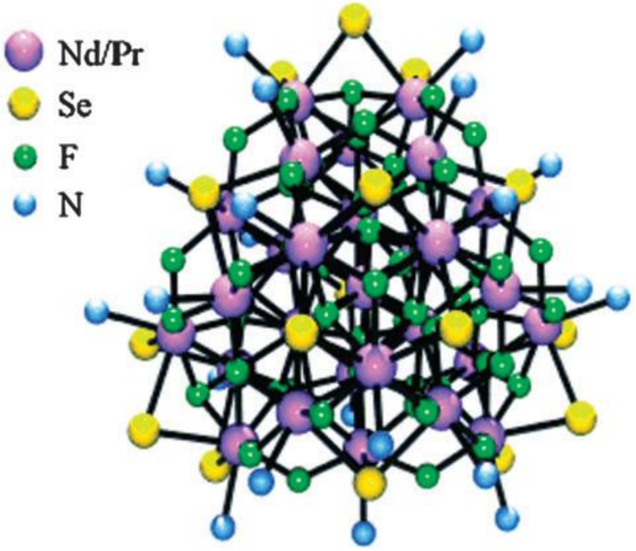

Figure 1.2. Solid state structure of [$Ln_{28}F_{68}(SePh)_{16}(py)_{24}$] (Ln = Pr, Nd) as an example for fluoride-supported rare earth metal clusters.[33]

This conception of construction can be transferred to chalogenide based bridging moieties. Therefore, Brennan *et al.* showed that sulfide and also disulfide bridges in cluster [$Ln_4(\mu_4$-$S)(\mu_2$-$S_2)_4(SC_6F_5)_2(THF)_6$] (Ln = Tm, Yb) facilitate the formation of structurally well defined rare earth metal clusters on the molecular scale,[35] and even the selene based analogues [$Ln_4(\mu_4$-$Se)(\mu_2$-$Se_2)_4(SC_6F_5)_2(THF)_6$] (Ln = Tm, Yb) could be prepared (Fig. 1.3). In these cluster compounds, the μ_4-bridging chalcogenide moiety is surrounded by a square planar coordination polyhedron made up by the rare earth metal atoms, and the four edges of the square are capped by one μ_2-bridging dichalcogenide each.

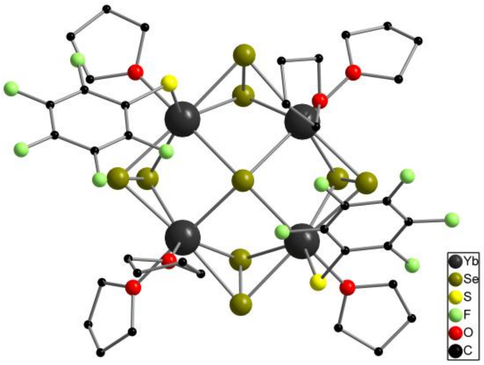

Figure 1.3. Solid state structure of [$Yb_4(\mu_4$-$Se)(\mu_2$-$Se_2)_4(SC_6F_5)_2(THF)_6$] featuring selene based bridging moieties to support the rare earth metal scaffold.

The most frequently reported rare earth metal based cluster scaffolds display hydroxy and oxo ligands as bridging moieties. The design and synthesis of high nuclearity hydroxy/oxo clusters have attracted interest of many research groups within the last two decades.[29, 36] This degree of attention is justified by an outstanding potential for applications as molecular devices, in catalysis[37] and in the development of synthetic nucleases for hydrolysis of phosphate diester bonds, including those present in nucleic acids.[38] Basically, two different approaches towards the preparation of oxo/hydroxy clusters have been established: the hydrolysis of a moisture-sensitive starting material[36f, 36g, 39] and a hydrolytic approach in which the water molecules are deprotonated in a controlled way. The results discussed in this thesis are exclusively based on the latter method. In general, such hybrid-like core-shell compounds consisting of an inorganic lanthanoid hydroxy core surrounded by an organic shell are formed upon a so-called ligand-controlled partial hydrolysis of the metal salts used. The lanthanoid halide hydrates usually tend to undergo an uncontrolled hydrolysis under basic conditions, since the coordinating water molecules are singly or doubly deprotonated in order to induce the formation of structurally undefined oxo/hydroxy polymers. Therefore a suitable ligand preferably possessing a single negative charge and several donor functionalities may be capable of interrupting this undesirable polymerization process by accurately timed saturation of the lanthanoid atoms' coordination sites. For this purpose, ligands like alkoxides,[40] phenoxides,[30] β-diketones[11c, 20, 37, 41] and amino acids[29a, 41h, 42] have been established. As this timing of saturation by an individual ligand is not rationally predictable, the exact formation of the structural motives underlies serendipity in most instances. Despite the very limited checkability of the clusters' final shape, the described methodology has been experienced to afford the target compounds in high yields in most cases. This marks a notable contrast to those rare earth metal hydroxyl clusters which have been synthesized *via* solvothermal methods.[43]

1.5.1 Ph_2acac Ligated Rare Earth Metal Hydroxy Clusters

We and others achieved to establish the dibenzoylmethanide ligand (Ph_2acac) as a suitable supporting ligand stabilizing various rare earth metal hydroxy clusters (*in general*: rare earth metal(s) = Ln). This Ph_2acac ligand belongs to the class of the β-diketonates and, hence, is capable of coordinating in a chelating and/or bridging fashion to metal centres facilitating high nuclearities. Within the last few years large efforts were undertaken to synthesize such compounds, since they often exhibit versatile physical properties increasing their applicability in different fields.

Tetranuclear compounds of formula [$Ln_4(\mu_3\text{-}OH)_2(Ph_2acac)_{10}$] (Ln = Pr,[41c] Nd,[41c] Sm,[41c] Eu[41g]) exhibit the lowest nuclearity amongst this class of cluster compounds (Fig 1.4).

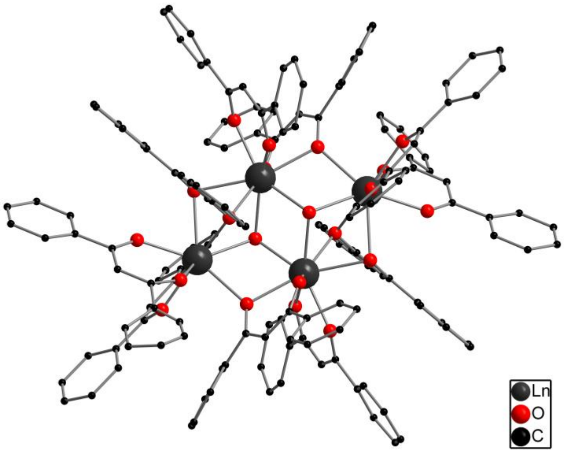

Figure 1.4. Solid state structure [$Ln_4(\mu_3\text{-}OH)_2(Ph_2acac)_{10}$] (Ln = Pr,[41c] Nd,[41c] Sm,[41c] Eu[41g]) as a representative for the tetranuclear rare earth metal hydroxyl clusters.

Their core consists of a parallelogram, in which each corner is occupied by one rare earth metal atom. This parallelogram can be divided into two triangular faces capped by one μ_3-O atom each, giving a $\{Ln_4(\mu_3\text{-}OH)_2\}^{10+}$ scaffold. The ten Ph_2acac ligands feature three different coordination modes (2 x μ:η^2:η^2, 2 x μ:η^2 and 6 x η^2). The Eu-based compound was investigated with respect to its magnetic properties.[41g]

Using rare earth metal atoms possessing smaller ionic radii with regard to same coordination numbers or varying the synthetic route by using the larger ones, pentanuclear rare earth metal hydroxy clusters of formula [$Ln_5(\mu_4\text{-}OH)(\mu_3\text{-}OH)_4(Ph_2acac)_{10}$] (Ln = Y,[37] Nd,[44] Eu,[41b] Gd,[44] Tb,[11c] Dy,[20] Ho,[2] Er,[44] Yb[44]) were obtained (Fig. 1.5).

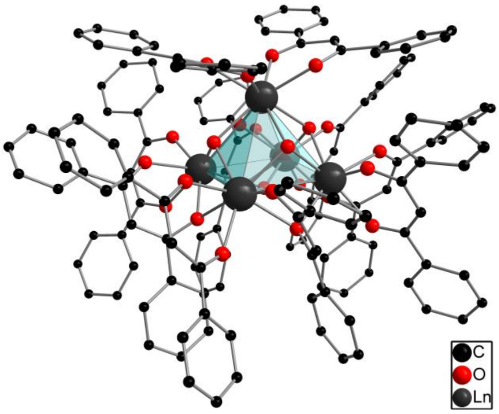

Figure 1.5. Solid state structure of [$Ln_5(\mu_4\text{-}OH)(\mu_3\text{-}OH)_4(Ph_2acac)_{10}$] (Ln = Y,[37] Nd,[44] Eu,[41b] Gd,[44] Tb,[11c] Dy,[20] Ho,[2] Er,[44] Yb[44]) as a representative for pentanuclear rare earth metal hydroxy clusters.

In these cluster compounds the rare earth metal atoms display a square pyramidal coordination polyhedron, and its square face is capped by one μ_4-O atom, whereas its four triangular faces are capped by one μ_3-O atom each. Six out of ten Ph_2acac ligands act as terminal chelates adopting the η^2-modus, *i.e.* the apical rare earth metal atom is coordinated by two η^2-Ph_2acac ligands and the four basal yttrium atoms are chelated by one η^2-Ph_2acac ligand each. The remaining four Ph_2acac ligands simultaneously chelate and bridge basal and adjacent yttrium atoms upon coordination in μ:η^2-modus. In this way, they coordinatively stabilize the $\{Ln_5(\mu_4\text{-}OH)(\mu_3\text{-}OH)_4\}^{10+}$ scaffold from outwards by capping all its basal edges. The yttrium-based analogue showed to be active in oxidizing aliphatic aldehydes to their corresponding carboxylic acids with turnover numbers up to 200 within twelve hours in a homogenous catalytic fashion,[37] whilst the dysprosium based species exhibits certain magnetic properties which are indicative for a typical single-molecule-magnet (SMM).[20] The holmium-based compound showed typical temperature-dependent magnetic moment data.[41g] For those clusters accommodating the NIR-emitting rare earth metal atoms Nd, Er and Yb, according emissive properties could be confirmed.[44] The luminescence properties of the Eu- and Tb-based analogues were investigated as well.[11c]

A more extended lanthanum Ph_2acac cluster was reported by Junk *et al.*, who succeded in preparing a dodecanuclear compound $[La_{12}(\mu_3\text{-}OH)_{12}(H_2O)_4(Ph_2acac)_{18}(Phgly)_2(CO_3)_2]$.[41e] In this cluster compound, a $\{La_{12}(\mu_3\text{-}OH)_{12}\}^{24+}$ core is inwardly stabilized by two μ_6-η^2:η^1:η^1:η^1:η^1:η^1-coordinating carbonate ions, *i.e.* these ions act as template ions, although no carbonate source was added to the reaction mixture. These carbonate ions were assumed to stem from either reacted atmospheric carbon dioxide or from ligand decomposition. The latter possibility appears more plausible in that case, as in addition to 18 Ph_2acac ligands, two further phenylglyoxylato ligands (Phgly) are tethered onto the $\{La_{12}(\mu_3\text{-}OH)_{12}\}^{24+}$ scaffold. This decomposition process has been attributed to an oxidative cleavage of the β-diketonate bridge induced by dioxygen present in the reaction solution.

1.5.2 Amino Acid Ligated Rare Earth Metal Hydroxy Clusters

α-Amino acids represent one of the most significant constituents of the biosphere, since they act as central building blocks of proteins, bioconjugates and other compounds possessing medical and/or biological efficacy.[45] The resulting biocompatibility and accessibility let them appear as attractive supporting ligands for the coordination to rare earth metal centers, targeting a unification of the α-amino acids' recognizability by cellular systems and the rare earth metals' versatile photophysical, optical and magnetic properties for disclosing new fields of application. Within hydrolytic approaches at different pH-values, several groups succeeded in preparing structurally well-defined rare earth metal hydroxy clusters accommodating α-amino acids as either neutral ligands or single deprotonated α-amino carboxylates in their coordination periphery. The associated biological relevance of such compounds for mimicking enzymatic functions of metal-containing nucleases depicts one crucial synthetic goal.[45] Dinuclear species are those with the lowest nuclearity amongst such compounds, and their representatives are $[Tb_2(D/L\text{-Cys})_4(H_2O)_8]Cl_2$ and $[Tb_2(D/L\text{-ValH})_4(H_2O)_8]Cl_6\cdot 2H_2O$ (*D*/*L*-Cys = cysteinate; *D*/*L*-ValH = valine).[46] This subclass of rare earth metal clusters depicts a structural exception since the terbium atoms are not linked by bridging hydroxy groups but exclusively by carboxylate moieties of the amino acid ligands, *i.e.* they can actually not be assigned to the rare earth metal hydroxy clusters. The tetranuclear hydroxy-bridged homologues are $[Eu_4(\mu_3\text{-OH})_4(L\text{-Asp})_2(L\text{-AspH})_3(H_2O)_7]Cl\cdot 11.5H_2O$ (*L*-Asp = *L*-aspartate; *L*-AspH = aspartic acid),[46] $[Sm_4(\mu_3\text{-OH})_4(Gly)_5(H_2O)_{11}(ClO_4)](ClO_4)_7\cdot NaClO_4$ (Gly = glycinate),[47] $[Nd_4(\mu_3\text{-OH})_4(H_2O)_{10}(D/L\text{-Ala})_6](ClO_4)_8\cdot 4NaClO_4\cdot 23H_2O$ (*D*/*L*-Ala = *D*/*L*-alaninate),[47] $[Er_4(\mu_3\text{-OH})_4(H_2O)_{10}(D/L\text{-Val})_5]Cl_8\cdot 15H_2O$ (*D*/*L*-Val = *D*/*L*-valinate)[47] and $[Er_4(\mu_3\text{-OH})_4(L\text{-Glu})_3(H_2O)_8](ClO_4)_5\cdot 6H_2O$ (*L*-Glu = *L*-glutamite).[47] They display a common heterocubane-type $\{Ln_4(\mu_3\text{-OH})_4\}^{8+}$ core, which is coordinatively saturated by the individual α-amino acids used. An octanuclear species $[Eu_8(L\text{-ValH})_{16}(H_2O)_{32}]Cl_{24}\cdot 12.5H_2O$ was postulated by Qu *et al.*,[46] in which the authors claimed to observe an arrangement of four non-equivalent dimeric units.

A more sophisticated structural motif was obtained by Zheng *et al.*, who succeeded in preparing a dodecanuclear iodo-templated rare earth metal hydroxy cluster $[Ln_{12}(\mu_3\text{-OH})_{16}(I)_2(\mu_3\text{-}L\text{-Tyr})_8(H_2O)_{20}](ClO_4)_{10}\cdot 8H_2O$ (Ln = Dy, Er; *L*-Tyr = *L*-tyrosinate). This cluster compound is composed of four such $\{Ln_4(\mu_3\text{-OH})_4\}^{8+}$ heterocubanes which are doubly vertex-sharing to make up a cyclic rare earth metal hydroxy core.[48] In addition to the stabilizing tyrosinate ligands, two μ_4-bridging iodo ligands link four hydroxy protons derived from different heterocubane moieties each, hence, they act as templates. Another example showing the diverse structural motifs of this class of compounds is a tetradecanuclear gadolinium cluster $[Gd_{14}(\mu_4\text{-OH})_2(\mu_3\text{-OH})_{16}(H_2O)_8(L\text{-Ser})_{20}]^{3+}$ (*L*-Ser = *L*-serinate), which is made up by a cascade-like arrangement of four square pyramids to give a $[Gd_{14}(\mu_4\text{-OH})_2(\mu_3\text{-}$

$OH)_{16}]^{24+}$ core.[42b] The two inner pyramids share their four basal gadolinium atoms, whereas the two outer pyramids share their apical gadolinium atoms with one apical gadolinium atom of the inner pyramids each. This structural motif was previously found by Roesky *et al.*, who succeeded in tethering 20 *o*-nitrophenolate ligands onto the $[Ln_{14}(\mu_4\text{-}OH)_2(\mu_3\text{-}OH)_{16}]^{24+}$ (Ln = Dy, Er, Tm, Yb) scaffold instead of *L*-serinate ligands.[36g]

The introduction of halogenide ions for stabilizing cluster compounds of higher nuclearity was continued by preparing pentadecanuclear compounds $[Nd_{15}(\mu_3\text{-}OH)_{20}(\mu_5\text{-}Cl)(\mu_3\text{-}L\text{-}Tyr)_{10}(OH)_3(\mu\text{-}H_2O)(H_2O)_{23}]Cl_3\cdot(ClO_4)_8\cdot 2H_2O$, $[Eu_{15}(\mu_3\text{-}OH)_{20}(\mu_5\text{-}Cl)(\mu_3\text{-}L\text{-}Tyr)_{10}(OH)_2(\mu\text{-}H_2O)_5(H_2O)_{18}](ClO_4)_{12}\cdot 9H_2O$, $[Gd_{15}(\mu_3\text{-}OH)_{20}(\mu_5\text{-}Cl)(\mu_3\text{-}L\text{-}Tyr)_{10}(OH)(\mu\text{-}H_2O)_5(H_2O)_{19}](ClO_4)_{13}\cdot 12H_2O$, $[Pr_{15}(\mu_3\text{-}OH)_{20}(\mu_5\text{-}Br)(\mu_3\text{-}L\text{-}Tyr)_{10}(\mu\text{-}L\text{-}TyrH)_2(\mu\text{-}H_2O)_3(H_2O)_{20}](ClO_4)_{14}\cdot 8H_2O$ and $[Eu_{15}(\mu_3\text{-}OH)_{20}(\mu_5\text{-}Br)(\mu_3\text{-}L\text{-}Tyr)_{10}(\mu\text{-}H_2O)_5(H_2O)_{20}](ClO_4)_{14}\cdot 2H_2O$, in which either a μ_5-chloro or μ_5-bromo template ion supports a ring-shaped $\{Ln_{15}(\mu_3\text{-}OH)_{20}\}^{25+}$ scaffold (*L*-TyrH = *L*-tyrosine).[29a, 48-49] This scaffold is similar to that of the aforementioned dodecanuclear compound, however, the pentadecanuclear one is made up by five instead of four doubly vertex-sharing $\{Ln_4(\mu_3\text{-}OH)_4\}^{8+}$ heterocubane units forming a ring-like structure. The halide ions are positioned in the middle of that ring and bridge the five vertex-sharing rare earth metal atoms centrosymmetrically. The hitherto highest nuclearity is featured by a sodalite-like rare earth metal hydroxy scaffold containing 60 rare earth metal atoms which are coordinated by 34 threoninate ligands (*D*/*L*-Thr), which is so far also the most complex species amongst the series of amino acid ligated rare earth metal hydroxy clusters.[42d] This compound $[Ln_{60}(D/L\text{-}Thr)_{34}(\mu_6\text{-}CO_3)_8(\mu_3\text{-}OH)_{96}(\mu_2\text{-}O)_2(H_2O)_{18}]\ Br_{12}(ClO_4)_{18}\cdot(H_2O)_x$ (Ln = Y, Ho, x = 60; Ln = Er, x = 60, *L*-Thr and *D*-Thr) is made up by 24 $\{Ln_4(\mu_3\text{-}OH)_4\}^{8+}$ heterocubane units being spherically arranged to give a sodalite-related geometry (Fig. 1.6).[42d]

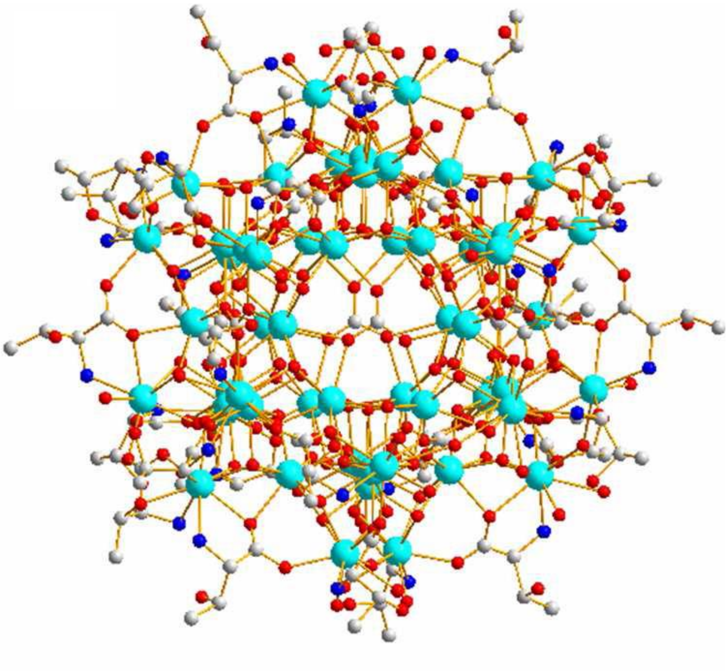

Figure 1.6. Solid state structure of [Er_{60}(*L*-Thr)$_{34}$(μ_6-CO_3)$_8$(μ_3-OH)$_{96}$(μ_2-O)$_2$(H_2O)$_{18}$] Br_{12}(ClO_4)$_{18}$ ·(H_2O)$_{60}$ as the hitherto largest representative amongst rare earth metal hydroxyl clusters.[42d] *Turquoise*: erbium; *red*: oxygen; *blue*: nitrogen; *white*: carbon. Hydrogen atoms are omitted for clarity.

The coordination sphere consists of eight hexagonal heterocubane rings giving octadecanuclear moieties, hence, six doubly vertex-sharing heterocubane units with a total of six vertex-sharing rare earth metal atoms enclose a hexagonal plane. In the middle of this plane a carbonate template ion is positioned centrosymmetrically, which is sixtuply bridging these vertex-sharing rare earth metal atoms in a $\mu_6:\eta_1:\eta_1:\eta_1:\eta_1:\eta_1:\eta_1$ fashion. The origin of this carbonate ion could not be clarified, however, it was supposed to arise from either ligand decomposition or conversion of atmospheric carbon dioxide to carbonate species, as previously reported.[41e, 42c, 42d, 46] Considering the heterocubane subunits, the octadecanuclear moieties are 1,2-linked with adjacent ones and the residual spherical surface is fulfilled by eight square faces. An average distance of 1.2 nm between opposing inner rare earth metal atoms makes space available for six non-coordinating bromide anions.

All the above mentioned rare earth metal clusters accommodating α-amino acids exhibit one common feature: the amino acid ligands never showed to be capable of entirely saturating the cluster cores' coordination environment electrostatically and coordinatively, especially when coordinated in a neutral fashion to the rare earth metal atoms. For the completion of the coordinative saturation neutral ligands like *e.g.* terminally coordinating or bridging water molecules were necessary, whereas the electrostatic saturation (and the coordinative saturation as well) was satisfied by terminally coordinating, bridging halide or hydroxyl ions or even by non-coordinating counteranions. Thus the functionalization of the above mentioned structures was always limited to a certain extent.

1.5.3 Mixed Ligated Rare Earth Metal Hydroxy Clusters

Based on both classes of compounds presented, efforts were made in the Roesky group to prepare mixed ligated rare earth metal cluster compounds bearing two different organic ligands in their coordination environment. Therefore, we applied similar reaction conditions as for the pure Ph_2acac clusters described above, using two organic ligands, namely Ph_2acac and *o*-nitrophenolate (*o*-$O_2NC_6H_4O$) were applied. This strategy gave access to mixed ligated tetra- and pentanuclear rare earth metal hydroxy clusters $[Ln_4(\mu_3\text{-}OH)_2(Ph_2acac)_8(o\text{-}O_2NC_6H_4O)_2]$ (Ln = Yb, Lu) and $HNEt_3^+[Ln_5(\mu_3\text{-}OH)_4(\mu_4\text{-}OH)(Ph_2acac)_7(o\text{-}O_2NC_6H_4O)_3Cl]$ (Ln = Er, Tm),[41f] of which the scaffolds were known from the aforementioned pure Ph_2acac clusters. Considering these compounds, the second supporting ligand or coligand *o*-$O_2NC_6H_4O$ proved to be capable of occupying certain coordination sites of the cluster cores (2 x $\mu{:}\eta^2{:}\eta^2$-mode in tetranuclear species, 2 x $\mu{:}\eta^2$- and 1 x μ-mode in pentanuclear species). As a result, only the tetranuclear compounds appear in a neutral fashion, whereas the molecular scaffold of the pentanuclear compounds possesses a single negative charge, which is due to one chloro ligand remaining in one Ln-atom’s coordination sphere and has to be balanced by one trimethylammonium countercation. To retain the clusters’ coordination geometry, the *o*-$O_2NC_6H_4O$ coordination was accompanied by an instantaneous substitution of the Ph_2acac ligand at these specific binding positions. Up to now, only little work considering these issues has been reported.

2 DEFINITION OF THE PROJECT

The target of this dissertation is centred on a combination of the Ph_2acac ligated (cp. 1.5.1), the amino acid ligated (cp.1.5.2) and the mixed ligated rare earth metal hydroxyl clusters (cp.1.5.3). This ensemble implies the vision of novel structurally well defined mixed ligated rare earth metal hydoxy clusters accommodating both Ph_2acac and amino acid ligands in their coordination environment to provide an additional structure chemical value to this class of compounds. Concomitantly, mechanistic aspects shall be revealed to gain more insight into the systematics of formation for rare earth metal hydroxy clusters in general, focusing a new degree of predictability with regard to structural motives.

In addition, the presence of *e.g.* gene-coded α-amino acids and structurally related ligands exhibiting biological relevance are ought to exhibit accessibility into cellular systems to find new application in possibly medical fields. These biocompatible amino acid-related ligands shall further possess multiple functionalities to allow continuative chemical transformations of the clusters in terms of *e.g.* peptide couplings. Such polar ligands shall further increase the solubility in aqueous media and corresponding tuning of ligand design will be accomplished. In this context, studies in solution shall proof the clusters' stability upon dissolution, paving the way for various *in vitro* investigations.

With regard to the photophysical properties, especially those rare earth elements having usable luminescent transitions shall be assembled in the clusters' scaffolds. Utilization of *e.g.* europium and terbium may afford new luminescent devices, and the resulting clusters shall be internalized into cellular systems whereby the luminescent rare earth metal atoms serve to localize the species *in vitro via* cell imaging experiments. To enhance this effect, the nuclearity of the clusters shall be maximized upon retention of the molecular scale.

By occupying the clusters' metal atom positions with rare earth elements providing distinct magnetic properties, new nanoscopic magnetic materials like *e.g.* single-molecule-magnets (SMM) shall be received.

3. RESULTS AND DISCUSSION

3.1 Tetra- and Pentanuclear Rare Earth Metal Hydroxy Clusters

3.1.1 Rare Earth Metal-Based Cluster-Polymer Hybrid Nanoparticles

IN COOPERATION WITH
PROF. DR. KATHARINA LANDFESTER, DR. CLEMENS K. WEISS AND CHRISTOPH P. HAUSER, MAX-PLANCK-INSTITUTE FOR POLYMER RESEARCH (MAINZ)

Nanocomposite materials from the above mentioned Ph_2acac ligated rare earth metal clusters and polymeric matrices unify useful photophysical properties of the inorganic compounds[11a, 11b, 11d, 24, 50] and the feasible properties of polymeric latexes like *e.g.* the film formation of low glass transition temperature (T_g) polymers as well as the facile processability of aqueous polymer dispersions. Additionally, the encapsulated compound is efficiently protected from the environment by being embedded in a polymeric nanoparticle.[51] A very convenient process for the generation of metal complex/polymer hybrid nanoparticles is the miniemulsion polymerization technique.[52] In theory, all complexes soluble in the desired monomer can be used for this encapsulation process. In contrast to conventional emulsion polymerization techniques governed by diffusion processes, the polymerization reaction in miniemulsion is confined to individual droplets, without net exchange of monomer or of any other compound present in the droplets. Direct miniemulsions are heterophase systems consisting of an organic phase capable of polymerization, which is finely dispersed in an aqueous medium. Monomer droplets with adjustable sizes (Ø = 50 – 300 nm) are created on previously formed macroemulsions by using shear forces derived from *e.g.* ultrasound. Amphiphile additives in terms of surfactants effectively stabilize the droplets against coalescence. Both diffusion processes and related Ostwald ripening are suppressed by addition of a hydrophobic agent to the organic phase. This so-called costabilizer causes an osmotic pressure counteracting the Laplace pressure, which is responsible for Ostwald ripening. Ideally, the droplets can be considered as nanocontainers reacting independently of each other, hence, droplet size and composition remain constant throughout the preparation process and all of the droplets and particles are identical.[53] This uniformity with respect to size and composition cannot be achieved for hybrid particles prepared using other preparation techniques like dispersion polymerization[54] or the so-called “self-organization process”[55] which essentially works *via* a solvent exchange/evaporation-precipitation process.

The encapsulation of monomer-soluble fluorescent dyes or metal organic compounds by the miniemulsion technique is a well-established method for preparing fluorescent or metal complex-containing polymeric nanoparticles.[52b, 56] Moreover, it has been shown that fluorescent dyes[57] and rare earth metal complexes[51] are protected against quenching effects caused by oxygen or water by encapsulation into a polymer matrix. In this context, Ando *et al.* reported the protection of europium-β-diketonato complexes [Eu(NTFA)$_3$] and [Eu(NTFA)$_3$(TOPO)$_2$] (NTFA = tris[(2-naphthoyl)-3,3,3-trifluoroacetonate]; TOPO = bis(trioctylphosphine oxide)) by encapsulation into a polystyrene (PS) matrix.[51] Furthermore, Vancaeyzeele *et al.* described the use of rare earth metal-containing polymer nanoparticles for cell labeling and investigated the rare earth metal content of Ln-polymer hybrid nanoparticles after encapsulation of tris[4,4,4-trifluoro-1-(2-naphthyl-1,3-butanedionate)] rare earth metal complexes (Ln = Pr, Ho, La, Tb, Eu) in polystyrene nanoparticles *via* inductively coupled plasma mass spectrometry (ICP-MS) and optical emission spectrometry (ICP-OES). Upon usage of this technical setup, about 1000 complexes per particle were determined.[52c] Among other complexes, [Eu(tmhd)$_3$]-containing latexes (tmhd = 2,2,6,6,-tetramethylheptanedionate) were used by Vogel *et al.* to determine the metal content of metal complex-containing colloidal dispersions by ICP-OES.[58]

For the generation of new complex/polymer hybrid nanoparticles, tetra- and pentanuclear rare earth metal clusters of formulae [Ln$_4$(OH)$_2$(Ph$_2$acac)$_{10}$] (Ln = Pr, Nd, Sm)[41c] and [Ln$_5$(OH)$_5$(Ph$_2$acac)$_{10}$] (Ln = Y, Eu)[37, 41b] were prepared. These cluster compounds were synthesized according to literature known procedures, however, the Eu-based species was prepared applying a slightly modified procedure (see Experimental Part). Within a common project with Christoph P. Hauser, Dr. Clemens Weiss, Prof. Dr. Katharina Landfester (hybrid nanoparticle syntheses and characterization), Dr. Matthias Adlung and Prof. Dr. Claudia Wickleder (optical investigations), the preparation of the desired hybrid nanoparticles was achieved upon dissolution of the individual clusters in a variety of polymerizable monomers and subsequent induction of polymerization *via* the miniemulsion technique (cp. 3.1.1.2). The resulting aqueous hybrid latexes were applied to prepare luminescent, flexible and thin polymer films (cp.3.1.1.3).[59]

3.1.1.1 Synthesis and Characterization of Cluster-Polymer Hybrid Nanoparticles

Composite nanoparticles were prepared with the above mentioned rare earth metal cluster compounds using several polymers with different T_g's , *i.e.* polystyrene (PS), poly(methyl methacrylate) (PMMA), poly(lauryl methacrylate) (PLMA) and poly(butyl acrylate-*co*-methyl methacrylate) (PBA-*co*-PMMA) as surrounding matrix. While the application of the high T_g polymer PS have lead to brittle films with intact particles after drying, the low T_g polymer PBA-*co*-PMMA have formed continuous films after water evaporation. The individual amounts of inorganic component in the composite particles were determined by ICP-OES. Luminescent films from the low T_g copolymer composite PBA-*co*-PMMA/[$Eu_5(OH)_5(Ph_2acac)_{10}$] were prepared by spin coating or doctor-blading. The morphological characterization of the polymer films was conducted *via* scanning electron microscopy (SEM) and atomic force microscopy (AFM).

In order to evaluate the effect of the rare earth metal clusters' incorporation on the optical properties, emission and excitation spectra of the pure Nd- and Eu-clusters and the hybrid particles were recorded in both aqueous dispersion and dried state. Polymer particles were prepared with different amounts of rare earth metal cluster added to the monomer during the preparation process. Either 2 wt.-% or 10 wt.-% (based on solubility behaviour in monomer) of the respective clusters were dissolved prior to polymerization. While the lower amount of cluster completely dissolved in any monomer to yield a solution by visual inspection, saturated solutions with a low amount of not dissolved cluster could be recognized after mixing 10 wt.-% of rare earth metal compound with the monomer. However, even with 10 wt.-% of cluster, long-term stable dispersions without any coagulation over one year could be obtained for all the complexes applied. With the exception of PMMA-Eu dispersions (entry 4, 10, Table 1), the solids content of the composite dispersion was close to the theoretical value. This indicates that the presence of the complex does not interfere with the polymerization process.

The particle batches and their characterization are presented in Table 3.1. Comparison between pure polymer particles and Ln-polymer hybrid nanoparticles exhibited no significant change in the particle size (measured by photon cross correlation spectroscopy, PCCS), independent of type and amount of the Ln-cluster (Ln = Y, Pr, Nd, Sm, Eu). Moreover, the particle sizes of the PS, PMMA and PBA-*co*-PMMA particles were in the same range and no significant trend was observed. By using PLMA, an increased hydrodynamic diameter was observed with and without the addition of cluster compared to the other monomers/polymers.

This can be attributed to the higher hydrophobicity of PLMA which leads to a higher interfacial tension between the monomer and the water phase and has to be counterweighted by higher coverage of the monomer droplets with surfactant molecules.[56b, 60]

In conclusion, only the type of the monomer/polymer determines the particle size of the rare earth metal polymer hybrid nanoparticles, whereas the type and amount of Ln-cluster do not influence the particle size, which was confirmed by TEM analysis. The TEM images in Figure 3.1 show pure PS nanoparticles and PS nanoparticles with different types and amounts of rare earth metal cluster. In comparison to the pure PS nanoparticles, no difference in size and morphology was observed by embedding different types and amounts of rare earth metal cluster into a polystyrene matrix. The particles are spherical in shape, possess a narrow size distribution, and do not show any sign of inner-layered structure as observed for [Ln(tmhd)$_3$]/polyacrylate nanoparticles, which were also prepared *via* the miniemulsion technique.[52a] This aspect indicates a disperse distribution of rare earth metal cluster throughout the whole polymer matrix.

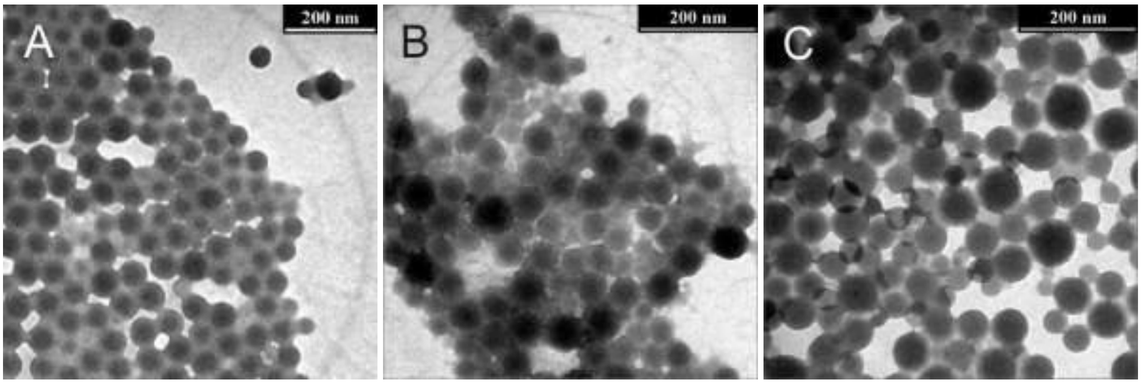

Figure 3.1. TEM images of pure PS nanoparticles (sample PS (A)), PS nanoparticles with 2 wt.-% Eu-cluster (PS-Eu2 (B)) and PS nanoparticles with 10 wt.-% Nd-cluster (PS-Nd10 (C)).

The amount of encapsulated rare earth metal cluster was determined by ICP-OES. For this purpose, Eu- and Nd-cluster containing polymer dispersions as representatives for both structural motives of rare earth metal clusters were thoroughly investigated. The determination of the solids content served to evaluate the encapsulation efficiency. The solids contents of the polymer dispersions and the exact rare earth metal-content of the 1:100 diluted dispersions determined via ICP-OES are presented in Table 3.1.

In general, both complexes could be encapsulated with efficiencies ranging from 70 % to 100 %. Considering the particle size obtained by PCCS and the amount of rare earth metal cluster determined *via* ICP-OES, the numbers of rare earth metal atoms per particle were calculated (Table 3.1). Upon usage of 2 wt.-% of rare earth metal cluster, values ranging from 2000 to 5000 rare earth metal atoms per particle were calculated (entries 2, 4, 6, and 13-15). Due to the significantly larger particle size of PLMA nanoparticles, a lower number of particles (compared to PS or PMMA) was present in the dispersion. As a result, more rare earth metal atoms were dispersed in one PLMA nanoparticle (entries 8 and 16). As expected, the nanocomposites prepared with 10 wt.-% of rare earth metal cluster have incorporated more rare earth metal atoms (entries 9, 11, 12, 17, and 18). Since the particle diameter slightly increases, the value is increased by a factor of more than five. Considering the Eu-cluster to consist of five Eu-atoms and the Nd-cluster to consist of four Nd-atoms, 500 to 1000 rare earth metal clusters per particle were calculated by embedding 2 wt.-% of rare earth metal cluster. These values are comparable to those obtained by Vancaezyeele *et al*.[52c]

Based on the data obtained by ICP-OES, it can be concluded that a successful embedding of both Eu-cluster and Nd-cluster into a matrix of any of the applied polymers was achieved, providing high encapsulation efficiencies. Upon encapsulation into polymeric nanoparticles, more than 1000 $mg \cdot L^{-1}$ of the rare earth metal clusters showed to be dispersible in water.

Entry	Sample	Amount of complex resp. to polymer [%]	Particle size x_{50} [nm]	Solids content experimental [%]	Ln-atoms/ particle
1	PS	0	73	12.4	
2	PS-Eu2	2	69	12.0	2400
3	PMMA	0	77	11.4	
4	PMMA-Eu2	2	67	6.6	4700
5	PBA-*co*-PMMA	0	74	11.1	
6	PBA-*co*-PMMA-Eu2	2	61	10.5	2400
7	PLMA	0	154	12.5	
8	PLMA-Eu2	2	154	11.8	36200
9	PS-Eu10	10	69	11.8	11800
10	PMMA-Eu10	10	62	6.5	n. d.
11	PBA-*co*-PMMA-Eu10	10	107	9.6	84700
12	PLMA-Eu10	10	167	10.1	169000
13	PS-Nd2	2	66	12.3	2000
14	PMMA-Nd2	2	72	11.4	3600
15	PBA-*co*-PMMA-Nd2	2	73	11.6	3900
16	PLMA-Nd2	2	142	11.6	26000
17	PS-Nd10	10	77	12.2	11500
18	PBA-*co*-PMMA-Nd10	10	74	11.0	18600
19	PS-Pr2	2	68	n. d.	n. d.
20	PS-Pr10	10	65	n. d.	n. d.
21	PS-Sm2	2	66	n. d.	n. d.
22	PS-Sm10	10	74	n. d.	n. d.
23	PS-Y2	2	63	n. d.	n. d.
24	PS-Y10	10	90	n. d.	n. d.

Table 3.1. Particle batches and their characterization. Example for terminology: PS-Nd2 means polystyrene polymer doped with 2 wt.-% of Nd cluster; n. d. = not determined.

Lifetime measurements were performed in order to investigate possible changes of the photophysical properties of the cluster upon dispersion in aqueous medium during the miniemulsification step. Generally, rare earth metal luminescence is prone to quenching effects when direct contact between the complex and water allows an energy transfer from the rare earth metal's excited states into high-energy vibronic states of the water molecules. This usually ends up in non-radiative relaxation, which is reflected by shorter lifetimes of the excited states.[61] For the lifetime experiment 2 wt-% Eu-cluster were dissolved in the monomer mixture BA-MMA and the lifetime was measured at an excitation wavelength of λ_{ex} = 355 nm and an emission wavelength of λ_{em} = 625 nm. Subsequently, the Eu-cluster/BA-MMA solution was dispersed in water *via* miniemulsification and the lifetime τ was measured, whereby the lifetime was calculated by fitting the data with a monoexponential function. Both lifetime plots exhibit an identical course (Fig. 3.2). The Eu-cluster in BA-MMA possesses a lifetime $\tau = 111 \pm 2$ µs and the Eu-cluster miniemulsion a lifetime $\tau = 99 \pm 2$ µs. Even though the lifetime of the miniemulsion decreases about 10 % compared to those of the anhydrous sample, it may be concluded that there is only a very small amount of water molecules inside the droplets, else the emission would have been quenched much more efficiently leading to strikingly shorter lifetimes.

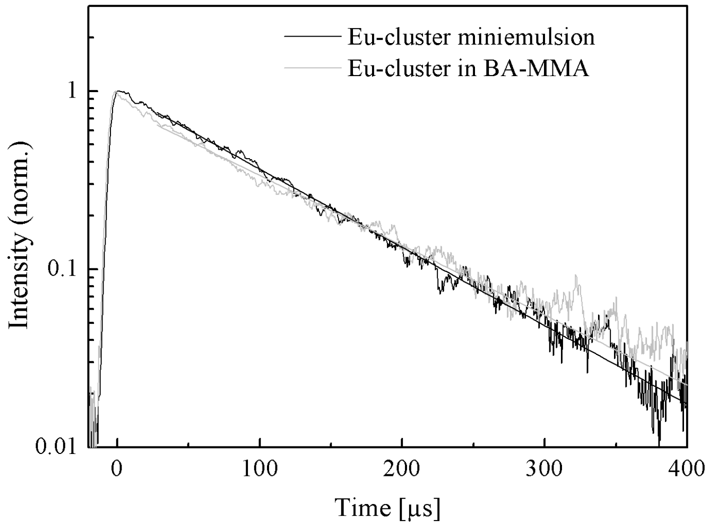

Figure 3.2. Lifetime measurements of Eu-cluster in BA-MMA and of Eu-cluster-miniemulsion.

For film formation experiments, the samples PS-Eu2 and PBA-*co*-PMMA-Eu2 were used based on the different T_g's of the polymer. Thin polymer films were prepared by spin coating at various speeds (1000, 2000 and 4000 rpm) on a pre-treated glass slide. Morphological investigations of the films did not show any influence of the spin coating speed on the film formation. The SEM and AFM images (Fig. 3.3) of the polymer film of PS-Eu2 prepared by spin coating at 4000 rpm showed PS nanoparticles and not an uniform flat polymer film, as expected considering the T_g (78 °C) (a lower T_g compared to pure PS (100 °C) is a result of the presence of hexadecane in the miniemulsion particles). The root-mean-squared (RMS) roughness of the polymer film obtained *via* AFM is 9.9 nm.

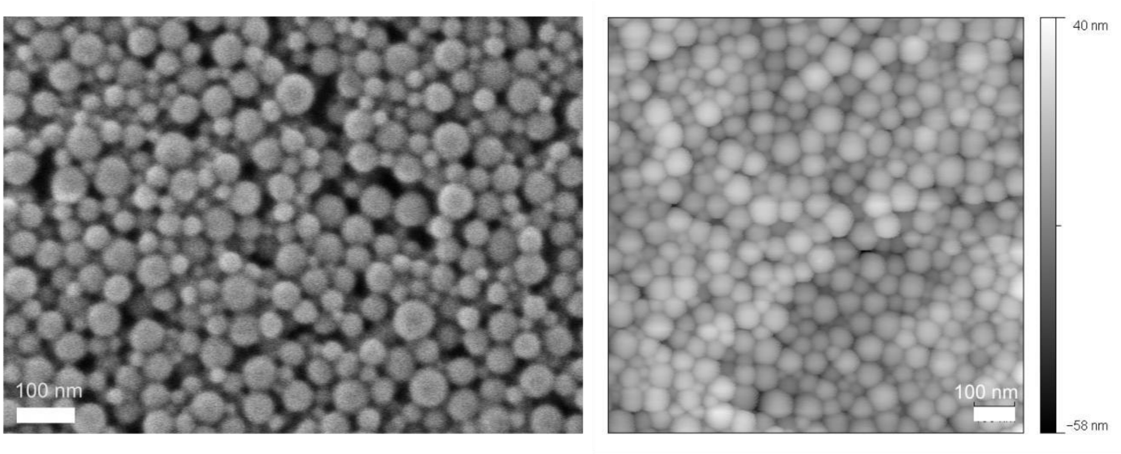

Figure 3.3. SEM image (left) and AFM image (right) of the polymer film of PS-Eu2.

The thickness of the polymer films was determined using a step profiler by grinding a thin groove into the substrate and subsequent scanning of its profile. The film thickness obtained from the scanning profile (Fig. 3.4) of the polymer film is approximately 80 nm. Since this value corresponds well with the particle size obtained by PCCS, SEM, TEM and AFM, it can be concluded that the observed structure is composed of a monolayer made up by PS-Eu2 nanoparticles.

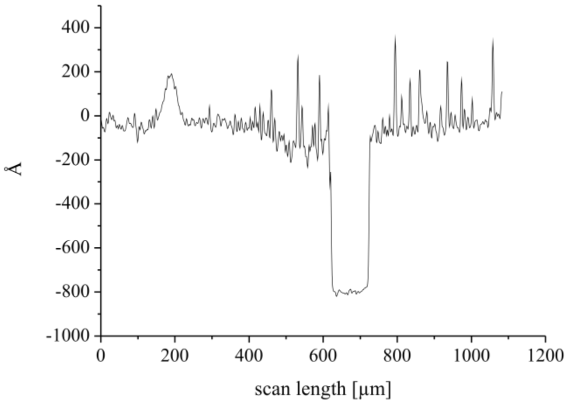

Figure 3.4. Scanning profile of the polymer film of PS-Eu2 recorded with a step profiler.

The SEM and AFM images of the polymer film prepared with PBA-*co*-PMMA-Eu2 are shown in Fig. 3.5. Both the SEM and the AFM image did not reveal particulate structures. In contrast, a uniform polymer film can be seen, hence, film formation successively prevented retention of the particle structure. The RMS roughness of the polymer film obtained via AFM is 2.3 nm.

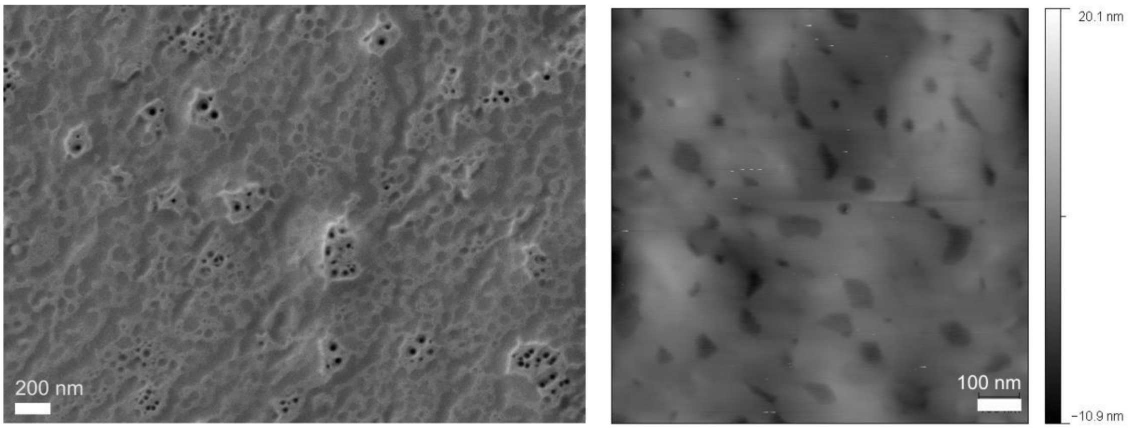

Figure 3.5. SEM image (left) and AFM image (right) of the polymer film of PBA-*co*-PMMA-Eu2.

The thickness of the polymer film was also measured with a step profiler. The scanning profile in Fig. 3.6 revealed a film thickness of about 45 nm.

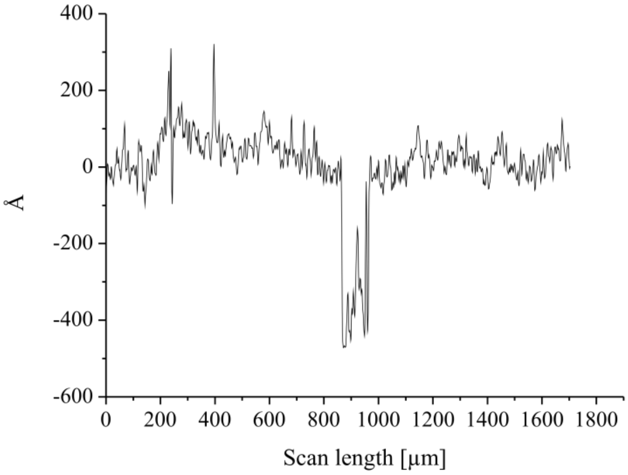

Figure 3.6. Scanning profile of the polymer film of PBA-*co*-PMMA-Eu2 recorded with a step profiler.

The film thickness was lower by 16 nm than the particle size of PS-Eu2 obtained by PCCS. This difference in the film formation behaviour of PBA-*co*-PMMA-Eu2 and PS-Eu2 is a consequence of the different T_g's of the polymers. The PS particles have a T_g of 78 °C, whereas the PBA-*co*-PMMA particles have a T_g of 9 °C, as determined by differential scanning calorimetry (DSC). The T_g of PBA-*co*-PMMA, which is far below room temperature, is responsible for the film formation as well as for the differences in the monolayer morphology. While for PS the particle structure was maintained, the PBA-*co*-PMMA particles flattened during the film formation process, and therefore the difference in the film thickness can be explained. These results obtained from the film formation experiments underline that mainly the polymer matrix is responsible for the thermal behaviour of the composite nanoparticles.

3.1.1.2 Optical Investigations of Cluster-Polymer Hybrid Nanoparticles

IN COOPERATION WITH
PROF. DR. CLAUDIA WICKLEDER AND DR. MATTHIAS ADLUNG, INSTITUTE OF INORGANIC CHEMISTRY, UNIVERSITY OF SIEGEN

The lifetime measurements discussed above show that the photophysical properties of the rare earth metal clusters dissolved in monomer were generally retained after dispersion and polymerization in aqueous media. In addition to these findings, we were interested to study whether the optical properties of the unprocessed cluster are influenced in the presence of large amounts of water after embedding the rare earth metal cluster into a polymer matrix. At first, the optical properties of the pure clusters were investigated and then compared with those after the hybrid nanoparticles' formation in aqueous phase (Fig. 3.7).

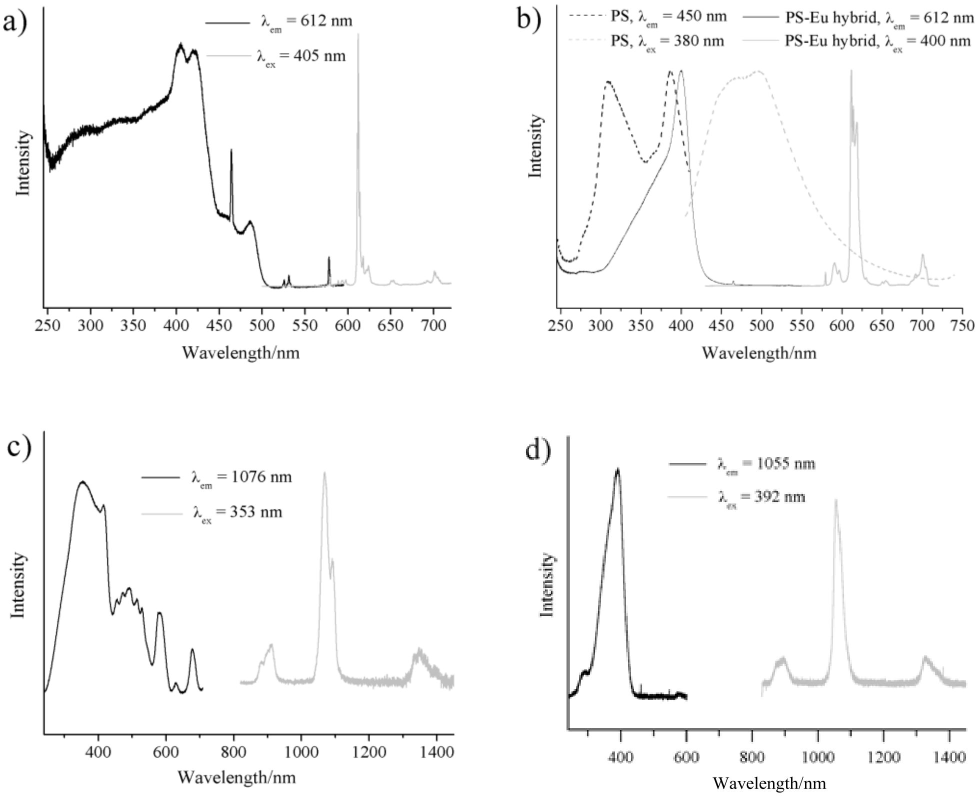

Figure 3.7. a) Luminescence measurement of pure Eu-cluster, b) pure PS and PS-based hybrid nanoparticles with Eu in H_2O, c) pure Nd-cluster, d) PS-based hybrid nanoparticles with Nd in H_2O as continuous phase. λ_{em} denotes the wavelengths at which the excitation spectra were acquired (black curves), λ_{ex}, the wavelengths used for excitation to record the emission spectra (grey curves).

In the luminescence spectra of the pure clusters the Eu-compound exhibited the characteristic luminescence based on a $^5D_0 \rightarrow ^7F_J$ transition,[41b] the large intensity of $^5D_0 \rightarrow ^7F_2$ compared to the hypersensitive transition $^5D_0 \rightarrow ^7F_1$ reveals the low point symmetry of Eu^{3+}-ions in the cluster. The Nd-cluster showed three bands at 880, 1076 (most intense) and 1330 nm as a result of the $^4F_{3/2} \rightarrow ^4I_{9/2}$, $^4I_{11/2}$, and $^4I_{13/2}$ transitions.[62] In the excitation spectra sharp Eu- and Nd-derived *4f-4f* transitions are observed, which are accompanied by broad bands ranging from 250 nm to about 500 nm arising from ligands' $\pi \rightarrow \pi^*$ transitions. The monitored emission of the rare earth metal ions is indicative for an energy transfer process from the ligands to the rare earth metal ions, which is more efficient in the case of the Eu-compound. Due to the different coordination symmetries and bond lengths in the Nd- and Eu-compounds, the excitation bands of both compounds are slightly different leading to different energy transfers.

The luminescence properties of the rare earth metal polymer hybrid nanoparticles in aqueous dispersion were also investigated and compared with those of the pure rare earth metal clusters. Usually, rare earth metal(III)-emission in aqueous media is totally quenched by high energy O-H stretch vibrations arising from interaction between water and the rare earth metal(III) ions.[63] This effect is especially observed for ions like Nd^{3+} emitting in the NIR range. In the present case it is notable that the rare earth metal emission is only quenched to a low extent. The emission of the emulsified and dispersed Eu-clusters can be observed in the visible range and emission of the Nd-clusters could be even detected as NIR radiation. These results indicate that the lanthanide clusters are embedded in the polymer matrix preventing approximation of water molecules to the clusters.

Especially the luminescence properties of the Eu/polymer hybrid nanoparticles are remarkable (Fig. 3.7b). Strong Eu^{3+} $^5D_0 \rightarrow ^7F_2$ transitions which are well resolved even at room temperature could exclusively be observed in the emission spectrum, however, no bands originated from the ligands or polymeric units. In contrast, corresponding measurements of pure PS nanoparticles dispersed in H_2O resulted in unexpected absorption bands ($\lambda = 310$ and 385 nm) and a broad emission band with maxima at about $\lambda = 470$ and 495 nm, respectively. As PS is known to only absorb and emit below $\lambda = 400$ nm,[64] the cause of this behaviour is not understood and requires further investigation. Excitation spectra of the Eu/polymer species show a broad band at $\lambda = 400$ nm with a shoulder at higher energies. This can be ascribed to a mixture of ligand and polymer excitation which is proved by comparison to excitation spectra of the pure Eu-clusters (Fig. 3.7a) and PS without cluster (Fig. 3.7b, blue line). The fact that only Eu^{3+}-emission is observed after ligand/polymer excitation implies a complete energy transfer to the Eu^{3+}-ions, and the brightness of the red emission may be attributed to a low rate of quenching processes. To investigate the long-time stability of this material the samples were re-measured after several months, but no changes of the spectra have been observed.

The emission spectrum of the emulsified Nd-cluster is very similar to the one of the pure cluster, however, crystal field splitting was not resolved giving evidence for the presence of different cluster geometries in the polymer matrix. The absorption spectrum shows that only excitation above 400 nm effects energy transfer to Nd^{3+}-ions.

Based on these observations, we concluded that the rare earth metal clusters are protected by the polymer matrix against quenching effects in water, demonstrating a high potential of these materials for applications as *e.g.* luminescent devices.

In addition to the luminescence in dispersion, the optical properties of the polymer films were investigated. For this purpose, the samples PS-Eu2 and PBA-*co*-PMMA-Eu2 were used to prepare thin polymer films by spin coating at 4000 rpm on a pre-treated glass slide. The luminescent behaviour of the thin polymer films is depicted in Fig. 3.8.

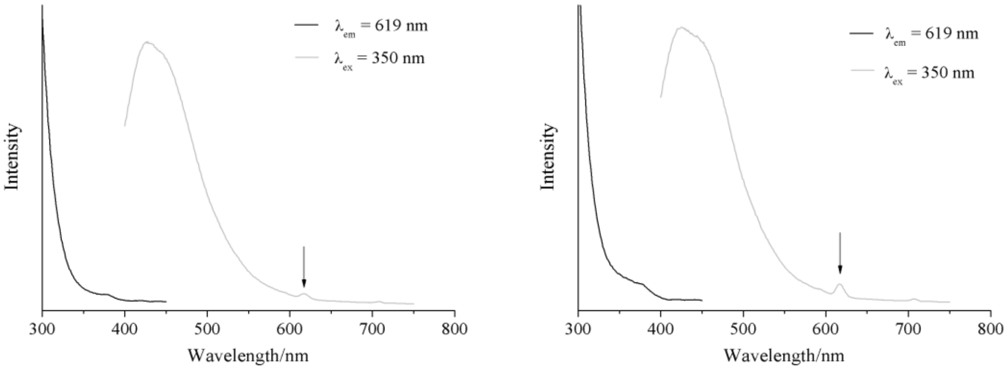

Figure 3.8. Luminescence measurement of thin Eu-containing polymer films of PS-Eu2 (left) and PBA-*co*-PMMA-Eu2 (right). λ_{em} denotes the wavelengths at which the excitation spectra were acquired (black curves), λ_{ex}, the wavelengths used for excitation to record the emission spectra (grey curves).

In both cases a broad band is observed in the emission spectra peaking at $\lambda =$ 420 and 430 nm, which can be assigned to the polymer. Although weak, the emission spectra of PS-Eu2 as well as of PBA-*co*-PMMA-Eu2 exhibit the characteristic $^5D_0 \rightarrow ^7F_2$ Eu^{3+}-emission band around 610 nm, as stated above. Considering the issue that the investigated film exclusively consists of a monolayer of hybrid nanoparticles which is the reason for the presence of only a few thousand Eu-atoms per particle, the visibility of this peak underlines the possible applicability of these Eu-polymer hybrids as luminescent materials.

For visualization purposes, “thick” polymer films of PBA-*co*-PMMA-Eu2 and PBA-*co*-PMMA-Eu10 were prepared by doctor-blading on an untreated glass slide. An intense red emission of the polymer films arisen from UV-light excitation (λ_{ex} = 366 nm) by optical inspection. The respective emission spectra recorded at an excitation wavelength of λ_{ex} = 390 nm are shown in Fig. 3.9. The spectra recorded for the two films exhibit the same characteristics as those recorded with the pure Eu-clusters, but once again without resolution of the crystal field splitting of the Eu^{3+}-ions showing the variability of the complex geometry when embedded in a polymer.

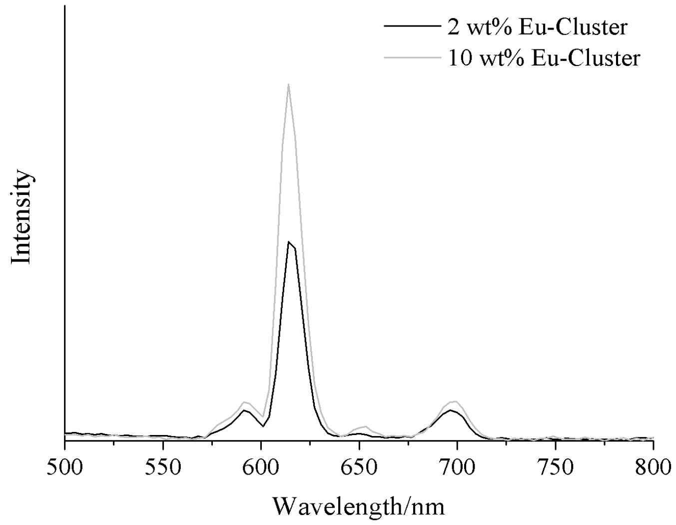

Figure 3.9. Emission spectra of Eu-containing polymer films of PBA-*co*-PMMA-Eu2 and PBA-*co*-PMMA-Eu10 at an excitation wavelength of λ_{ex} = 390 nm.

In summary, two types of rare earth metal clusters were successfully embedded into different polymer matrices *via* the miniemulsion technique and the application of these cluster-polymer hybrid nanoparticles with respect to the formation of luminescent thin polymer films has been presented. It was shown that it is possible to integrate Y, Pr, Nd, Sm and Eu-containing oligomeric clusters into polymeric nanoparticles as long-term stable dispersions. By this nanocomposite formation, more than 1000 mg·L^{-1} of the water insoluble rare earth metal cluster can be dispersed in water. Moreover, different (co-)polymer matrices, PS, PMMA, PLMA, and PBA-*co*-PMMA could be used. Only the polymer matrix has an influence on both particle size and thermal properties of the rare earth metal/polymer composites, regardless of type and amount of rare earth metal cluster. As representatives for the two different structural patterns, the exact amount of Eu- and Nd-atoms in the polymer particles was determined *via* ICP-OES and numbered as several thousands of cluster molecules per particle, with an encapsulation efficiency of 70 % - 100 %. Based on the different glass transition temperatures (T_g) of the various polymers, we investigated their applicability for film formation. The preparation of thin polymer films from low T_g PBA-*co*-PMMA particle monolayers was confirmed by scanning the profile and determining the film thickness.

The optical properties of the compounds in pure and encapsulated state have shown the clusters to retain their luminescence after embedding, which is especially remarkable in the case of the NIR-emitting Nd-cluster. Furthermore, the respective results for the Eu-containing hybrid material have shown a complete energy transfer which is very promising for various applications in the field of *e.g.* luminescent devices. The luminescence measurement of the thin polymer films prepared by spin coating facilitated the observation of characteristic Eu^{3+}-luminescence.

To put it in a nutshell, it was shown that the miniemulsion technique allows the integration of luminescent rare earth metal compounds into polymeric nanoparticles for protection and processability. As a function of the polymers' thermal properties, the nanocomposites can be obtained either as particles or as hybrid films. The protection of the complex from aqueous environment and the retention of luminescence is crucial for water-based (*e.g.* biomedical) applications, whilst luminescent thin films could be applied in optical devices.

3.1.2 Amino Acid and Ph_2acac Ligated Rare Earth Metal Hydroxy Clusters

Due to these findings, we were encouraged to analogously functionalize the clusters' ligand shell by utilizing chiral coligands in terms of both gene-coded and artificial α-amino acids. The postulated target compounds promised to exhibit properties like optical rotation as well as an increase of solubility in water compared to its pure Ph_2acac analogues, since the amino acid moieties ought to increase the polar character of the clusters' periphery, which is decisively responsible for the clusters' solubility. Bearing the mixed ligated *o*-$O_2NC_6H_4O$-containing clusters[41f] in mind as model compounds, this approach might confirm the tolerance of the coordination chemistry of such clusters with regard to ligand modification.

Furthermore, by using α-amino acids we aimed at a systematic pathway towards new mixed ligated yttrium hydroxy clusters being accessible for the biosphere.

3.1.2.1 Synthetic aspects of $[Y_5(\mu_4\text{-OH})(\mu_3\text{-OH})_4(\alpha\text{-AA})_4(Ph_2acac)_6]$ **(1-5)**

To realize this idea, dibenzoylmethane (Ph_2acacH) and one α-amino acid (α-AAH), *i.e.* either *D*-phenyl glycine (*D*-PhGlyH), *L*-proline (*L*-ProH), *L*-valine (*L*-ValH), *L*-tryptophan (*L*-TrpH) or 2,2-diphenyl glycine (Ph_2GlyH) were reacted with $[YCl_3{\cdot}(H_2O)_6]$ (α-AAH = *D*-PhGlyH, *L*-ProH, *L*-ValH, *L*-TrpH) in methanol under basic conditions to give the neutral mixed ligated rare earth metal clusters $[Y_5(\mu_4\text{-OH})(\mu_3\text{-OH})_4(\alpha\text{-AA})_4(Ph_2acac)_6]$ (α-AA = *D*-PhGly (**1**), *L*-Pro (**2**), *L*-Val (**3**), *L*-Trp (**4**), Ph_2Gly (**5**) (Scheme 3.1).[41h]

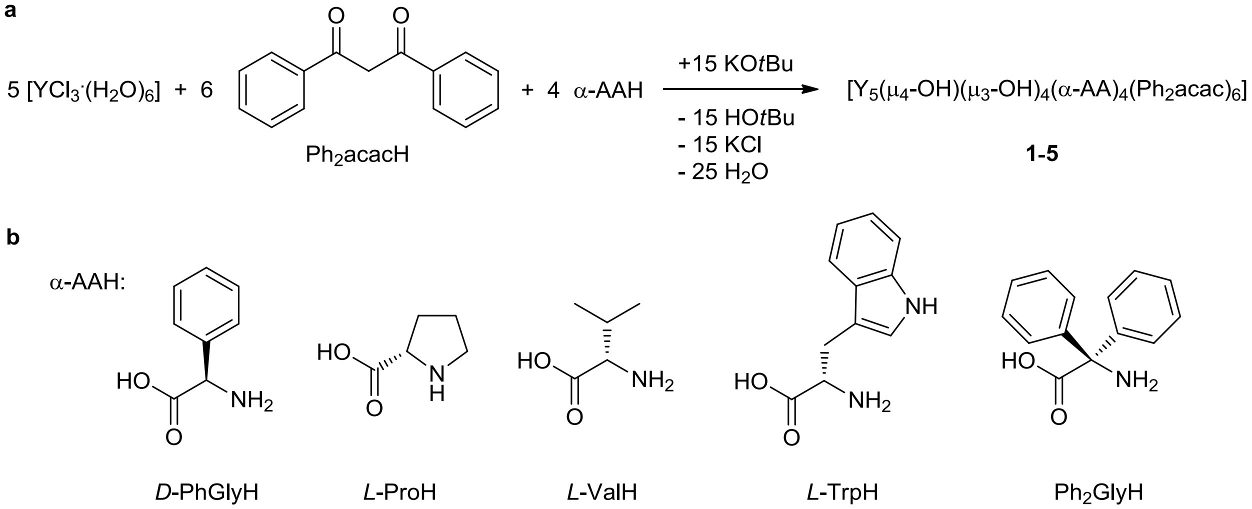

Scheme 3.1. a) Preparation of $[Ln_5(\mu_4\text{-OH})(\mu_3\text{-OH})_4(\alpha\text{-AA})_4(Ph_2acac)_6]$ (**1**-**5**), b) structural formulae of neutral α-amino acids. Keto-enol tautomery of Ph_2acacH and zwitterionic character of α-amino acids are neglected.

As base we used potassium *tert*-butoxide (KO*t*Bu), in order to circumvent the formation of undesired byproducts being hard to remove like *e.g.* triethylammonium chloride when using triethylamine (NEt_3).[11c, 37, 41c-g] Since the products formed prior to crystallization are separated from the reaction mixture *via* precipitation and subsequent filtration, the byproducts *tert*-butanol (HO*t*Bu) and potassium chloride (KCl) stay almost quantitatively in solution and can thus be easily removed. Moreover, the very high pK_a-value of KO*t*Bu facilitates a stoichiometric employment with respect to all starting materials needed, making the whole procedure more economical compared to the much less basic NEt_3 which requires in most cases excess amounts.

The clusters have been characterized by standard analytical and spectroscopic techniques, and the solid state structures of all compounds were established by single crystal X-ray diffraction (Fig. 3.10-3.14). The specific optical rotations of the chiral compounds **1-4** were determined polarimetrically (cp. 3.1.4.6). Additionally, PGSE NMR diffusion experiments (cp. 3.1.4.7) and various multidimensional NMR experiments were performed with **3** to investigate their behaviour in solution (cp. 3.1.4.8).

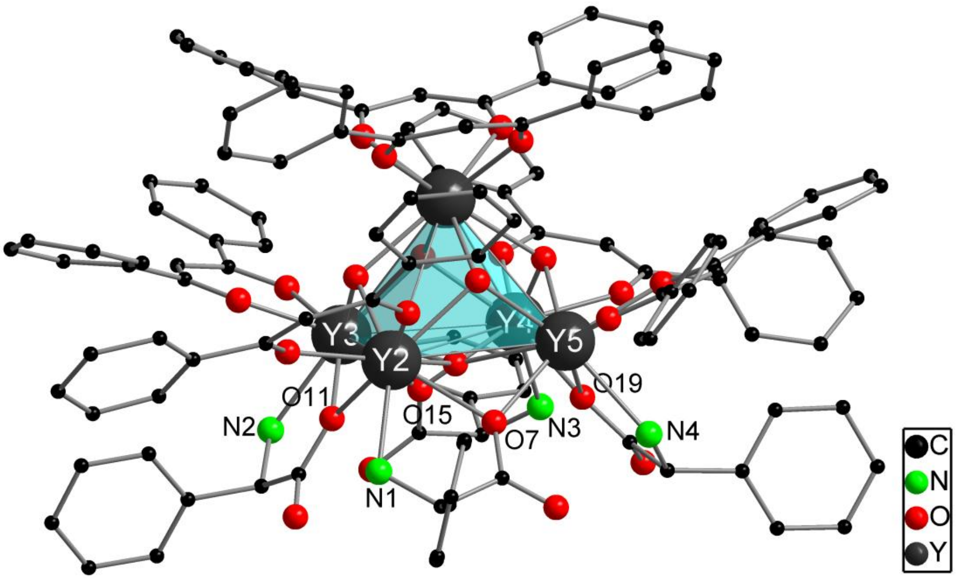

Figure 3.10. Perspective view of the molecular structure of **1**. Hydrogen atoms are omitted for clarity. Selected distances [Å] and angles [°]: N1–Y2 2.503(5), N2–Y3 2.484(6), N3–Y4 2.469(6), N4–Y5 2.502(6); O7–Y2 2.394(5), O7–Y5 2.413(5), O11–Y2 2.431(5), O11–Y3 2.337(4), O15–Y3 2.416(5), O15–Y4 2.392(5), O19–Y4 2.428(5), O19–Y5 2.330(5); Y2–O7–Y5 96.6(2), Y2–O11–Y3 97.6(2), Y3–O15–Y4 96.4(2), Y4–O19–Y5 96.8(2).

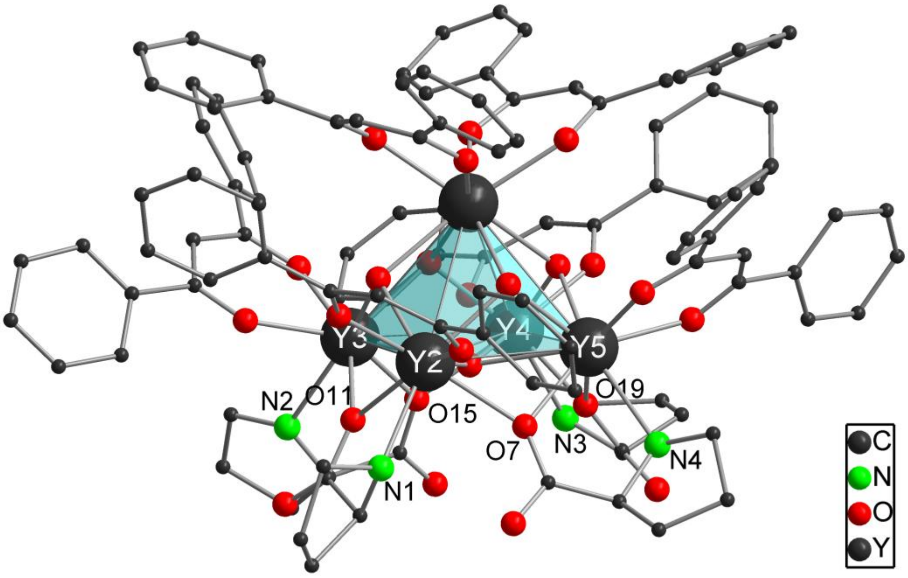

Figure 3.11. Perspective view of the molecular structure of **2**. Hydrogen atoms are omitted for clarity. Selected distances [Å] and angles [°]: N1–Y2 2.510(9), N2–Y3 2.529(10), N3–Y4 2.535(11), N4–Y5 2.525(10), O7–Y2 2.385(8), O7–Y5 2.375(7), O11–Y2 2.380(8), O11–Y3 2.391(8), O15–Y3 2.395(9), O15–Y4 2.408(7), O19–Y4 2.390(7), O19–Y5 2.378(8); Y2–O7–Y7 97.3(2), Y2–O11–Y3 97.0(3), Y3–O15–Y4 97.1(3), Y4–O19–Y5 97.6(3).

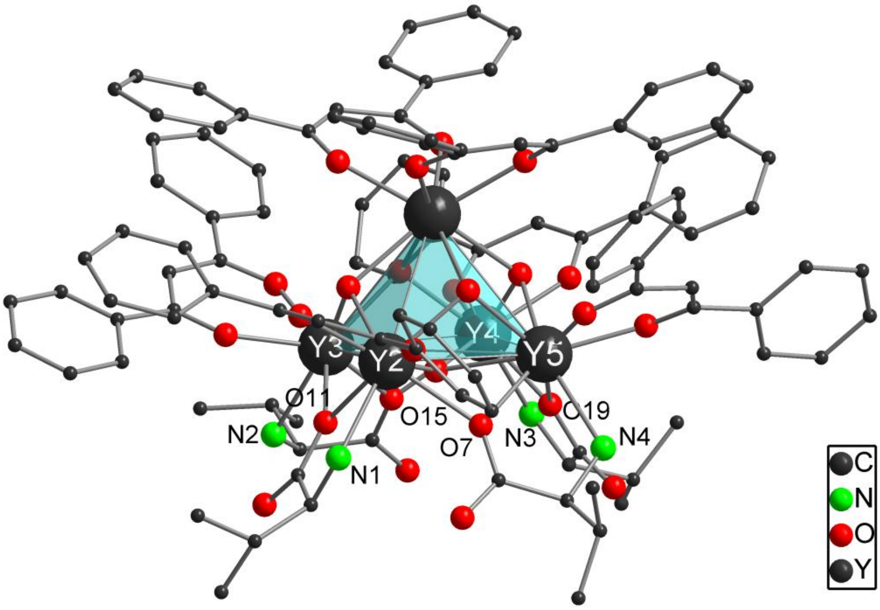

Figure 3.12. Perspective view of the molecular structure of **3**. Hydrogen atoms are omitted for clarity. Selected distances [Å] and angles [°]: N1–Y2 2.483(6), N2–Y3 2.453(5), N3–Y4 2.455(6), N4–Y5 2.452(6), O7–Y2 2.370(4), O7–Y5 2.335(4), O11–Y2 2.324(4), O11–Y3 2.401(4), O15–Y4 2.357(4), O15–Y3 2.364(4), O19–Y4 2.334(4), O19–Y5 2.377(4); Y2–O7–Y5 97.38(15), Y2–O11–Y3 96.51(15), Y3–O15–Y4 96.90(14), Y4–O19–Y5 97.2(2).

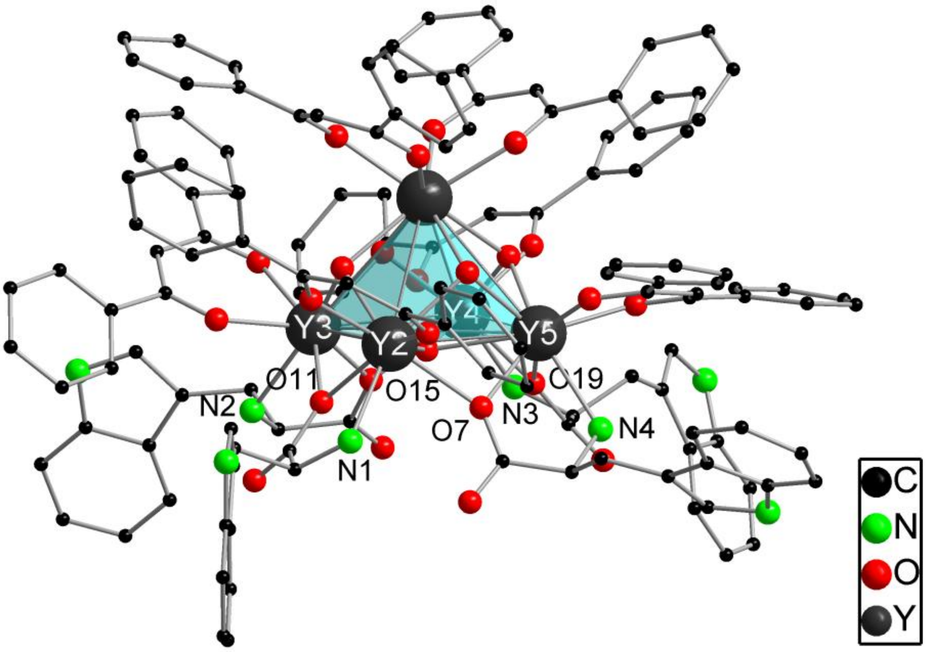

Figure 3.13. Perspective view of the molecular structure of **4**. Hydrogen atoms are omitted for clarity. Selected distances [Å] and angles [°]: N1–Y2 2.477(8), N2–Y3 2.522(7), N3–Y4 2.510(8), N4–Y5 2.500(8), O7–Y2 2.395(6), O7–Y5 2.385(6), O11–Y2 2.347(5), O11–Y3 2.391(6), O15–Y3 2.371(6), O15–Y4 2.415(6), O19–Y4 2.379(7), O19–Y5 2.381(6); Y2–O7–Y5 96.4(2), Y2–O11–Y3 97.1(2), Y3–O15–Y4 97.0(2), Y4–O19–Y5 98.1(2).

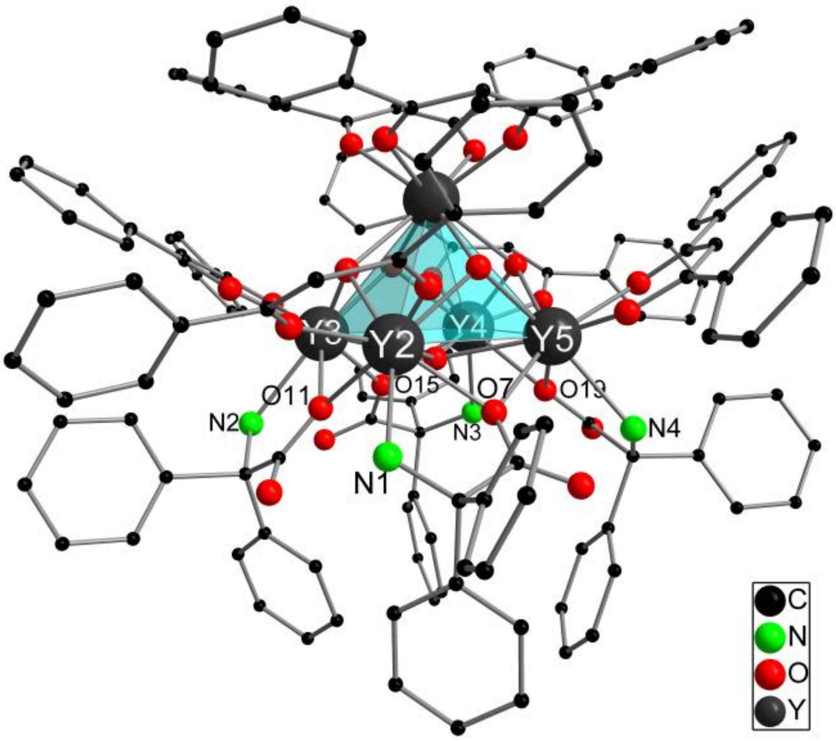

Figure 3.14. Perspective view of the molecular structure of **5**. Hydrogen atoms are omitted for clarity. Selected distances [Å] and angles [°]: N1–Y2 2.498(9), N2–Y3 2.504(9), N3–Y4 2.498(9), N4–Y5 2.485(9), O7–Y2 2.389(7), O7–Y5 2.417(6), O11–Y2 2.443(7), O11–Y3 2.348(7), O15–Y3 2.449(7), O15–Y4 2.355(7), O19–Y4 2.426(7), O19–Y5 2.355(7); Y2–O7–Y5 96.3(3), Y2–O11–Y3 96.4(2), Y3–O15–Y4 95.6(3), Y4–O19–Y5 97.1(3).

3.1.2.2 Structure discussion on $[Y_5(\mu_4\text{-OH})(\mu_3\text{-OH})_4(\alpha\text{-AA})_4(Ph_2acac)_6]$ (**1-5**)

Besides the achiral cluster compound **5**, the cluster compounds **1**–**4** having chiral amino acids in their coordination spheres could be received as enantiopure compounds. The chiral compounds **1-4** all crystallize in the orthorhombic space group $P2_12_12_1$ with four molecules in the unit cell, whereas compound **5** crystallizes in the monoclinic space group $P1$ with two molecules per unit cell. In all compounds, the yttrium atoms display a square pyramidal coordination polyhedron by occupying its vertices. The pyramid’s four triangular faces are capped by one μ_3-O atom each, whereas the pyramid’s square face is capped by one μ_4-O atom (Scheme 3.2a). All these capping oxygen atoms depict fragments of hydroxo bridges stabilizing the pyramidal shape from inwards. This assumption is centered on characteristic O-H-stretch vibrations observed in infrared spectra, and it is consistent with other works. Thus, the rare earth metal hydroxy cores of compounds **1-5** adopt a common structural motif which has already been reported [11c, 20, 37, 41b, 41d, 41f, 41g, 44] and which was briefly described above. Each basal yttrium atom is chelated by one Ph_2acac ligand and the apical one is chelated by two of these ligands (Scheme 3.2b). All six Ph_2acac ligands act as terminal chelates coordinating in η^2-modus, *i.e.* they remain in the same positions as compared to the pure Ph_2acac clusters $[Ln_5(\mu_4\text{-OH})(\mu_3\text{-OH})_4(Ph_2acac)_{10}]$ (see above). Considering the latter cluster type, the four bridging and chelating $\mu{:}\eta^2$-coordinating Ph_2acac ligands are now formally substituted by the amino acids. The deprotonation of the amino acids occurred at the acid function or, with regard to their zwitterionic nature, at the ammonium function. The amino acids chelate one basal yttrium atom each in η^2-fashion *via* the nitrogen atom of the amino group and one oxygen atom of the carboxyl group. This oxygen atom simultaneously bridges the chelated yttrium atom with an adjacent basal yttrium atom. Thus, the amino acid ligands adopt the $\mu{:}\eta^2$-coordination modus to cap all four basal edges of the pyramid (Scheme 3.2c-g). In summary, in **1-5** each basal yttrium atom is coordinated to seven oxygen atoms and one nitrogen atom, whereas the apical yttrium atom is coordinated to eight oxygen atoms. Despite the differing substitution patterns, each yttrium atom of the pyramid is surrounded by a more or less distorted square antiprismatic coordination polyhedron made up by the individual donor atoms.

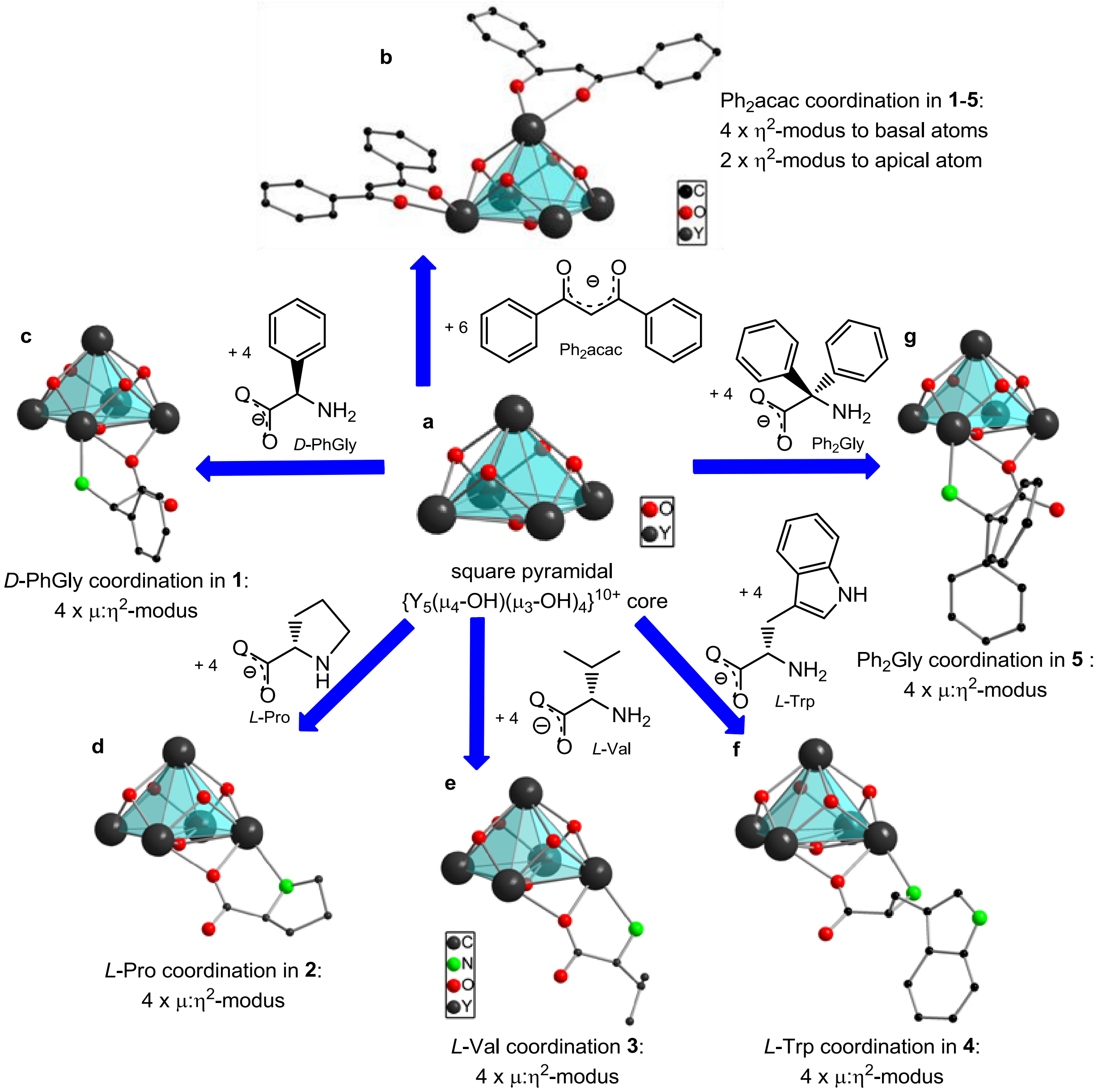

Scheme 3.2. Genesis of amino acid ligated yttrium hydroxy clusters. Hydrogen atoms are omitted for clarity. a) The square pyramidal $\{Y_5(\mu_4\text{-OH})(\mu_3\text{-OH})_4\}^{10+}$ scaffold is surrounded b) by six Ph$_2$acac ligands and four amino acid ligands each (c-g).

3.1.2.3 Steric aspects of $[Y_5(\mu_4\text{-OH})(\mu_3\text{-OH})_4(\alpha\text{-AA})_4(Ph_2acac)_6]$ (**1-5**)

Even though the amino acids have significantly different steric demands (tertiary (**1-4**) and quarternary (**5**) glycinic carbon atom) and different Lewis basicities (primary (**1**, **3**, **4**) and secondary amino nitrogen atoms (**2**)) (Scheme 3.3), there are no significant differences in bond lengths and angles of compounds **1–5** and the coordination chemistry is retained. As an example, the bond distances between the yttrium atoms and the amino acid ligands vary only very slightly (av. Y–N: 2.490 Å (**1**), 2.525 Å (**2**), 2.461 Å (**3**), 2.502 Å (**4**), 2.496 (**5**) and av. Y–(μ-O) 2.393 Å (**1**), 2.388 Å (**2**), 2.358 Å (**3**), 2.375 (**4**), 2.398 Å (**5**)). This issue can be attributed to a high tolerance of the coordination chemistry of these cluster compounds towards the bulkiness and the electronic nature of the amino acid ligands.

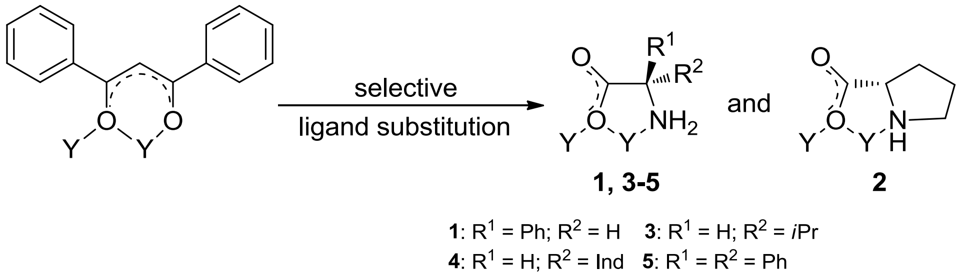

Scheme 3.3. Selective substitution of Ph_2acac ligands with amino acid ligands in (μ-O)-η^2 modus.

The different steric demand of the amino acid ligands is also not reflected by the dihedral angles φ_{av} between the Y_{bas}-(μ-O)-Y_{bas} planes A and the corresponding Y_{bas}-Y_{ap}- Y_{bas} planes B (Fig. 3.15). This could have been attributed to possible repulsive interactions between the α-amino acids' bulky residues and the basally coordinated Ph_2acac ligands. Thus, there is no steric repulsion between these two supporting ligands giving reason for average values of the dihedral angle φ_{av}(A;B) which vary only within a range of a little more than 1° (φ_{av}(A;B) = 2.284° (**1**), 2.934° (**2**), 1.708° (**3**), 2.203° (**4**), 1.975° (**5**)).

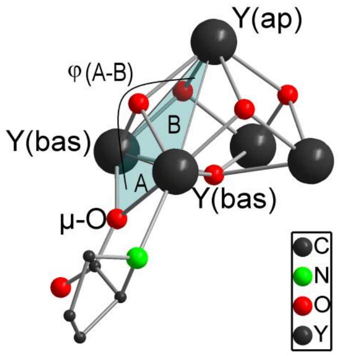

Figure 3.15. Dihedral angle φ(A;B) betweenY_{bas}-(μ-O)-Y_{bas} plane A and Y_{bas}-Y_{ap}-Y_{bas} plane B, shown exemplarily for proline cluster **2**.

None of the clusters have a crystallographic symmetry element, but both the apical yttrium atom and the μ_4-oxygen atom lie on a twofold symmetry axis that can be drawn through the cluster's interior. Owing to these results, we are now able to predict the position in which the amino acids coordinate to the pentanuclear yttrium core, and neither steric nor electronic modifications with respect to the chosen amino acid ligands have shown to influence the coordination chemistry of such mixed ligated cluster compounds.

3.1.2.4 Synthesis of [$Dy_5(\mu_4$-OH)(μ_3-OH)$_4$(*D*-PhGly)$_4$(Ph_2acac)$_6$] (**6**)

Besides the sterically related investigations with respect to the amino acid coligand, it appeared appropriate to check whether the yttrium atoms in such mixed ligated pentanuclear clusters can be exchanged by other rare earth metal atoms of similar ionic radius. This motivation has arisen from the aspect that structurally comparable compounds, such as the above mentioned tetra- and pentanuclear cluster species [$Ln_4(\mu_3$-OH)$_2$(Ph_2acac)$_{10}$],[41c, 41g] [$Ln_5(\mu_4$-OH)(μ_3-OH)$_4$(Ph_2acac)$_{10}$], [11c, 20, 37, 41b, 41d, 41f, 41g, 44] **[**$Ln_4(\mu_3$-OH)$_2$(Ph_2acac)$_8$(*o*-$O_2NC_6H_4O)_2$][41f] and $HNEt_3^+$[$Ln_5(\mu_3$-OH)$_4$(μ_4-OH)(Ph_2acac)$_7$(*o*-$O_2NC_6H_4O)_3$Cl]$^-$,[41f] had shown to accept the occupation of the metal atom positions by other rare earth metal atoms with different ionic radii. In the second case, it was even possible to occupy the metal atom positions with almost every rare earth metal atom, irrespective of their individual ionic radii. As we strived to show this structural and electronic tolerance to be also valid for the new amino acid ligated clusters, we decided to attempt a synthesis of the Dy-based *D*-PhGly analogue [$Dy_5(\mu_4$-OH)(μ_3-OH)$_4$(*D*-PhGly)$_4$(Ph_2acac)$_6$] by applying the same reaction conditions as for compounds **1**-**5** and using [$DyCl_3\cdot(H_2O)_6$] instead of [$YCl_3\cdot(H_2O)_6$]. Since Dy^{3+} possesses an ionic radius of 1.048 Å (CN = 6), which is very similar to that of Y^{3+} being 1.032 Å (CN = 6),[65] it ought to fit into the square antiprismatic cavities once accommodated by Y^{3+}.

Indeed this approach afforded the isostructural Dy-based compound **6**, which could be confirmed by single crystal X-ray diffraction giving the corresponding solid state structure (Fig. 3.16). Compared to the Y-based compound **1**, the average bond distances between the *D*-PhGly ligands' nitrogen and bridging oxygen atom vary only within 3 pm for the Dy-N-bond and 2 pm for the Dy-(μ-O)-bond, respectively, *i.e.* they are almost neglectable (av. Dy-N: 2.523 Å and av. Dy-(μ-O): 2.412 Å). The average dihedral angle φ_{av}(A;B) between the triangular planes A and B (explained above) has a value of 2.168°, which is 0.116° lower than for the Y-analogue.

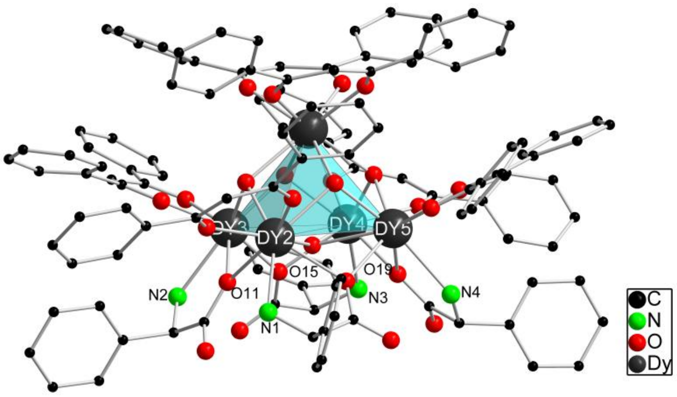

Figure 3.16. Perspective view of the molecular structure of **6**. Hydrogen atoms are omitted for clarity. Selected distances [Å] and angles [°]: N1–Dy2 2.533(8), N2–Dy3 2.518(8), N3–Dy4 2.517(8), N4–Dy5 2.523(8), O7–Dy2 2.400(6), O7–Dy5 2.429(6), O11–Dy2 2.458(6), O11–Dy3 2.349(6), O15–Dy3 2.437(6), O15–Dy4 2.412(6), O19–Dy4 2.456(6), O19–Dy5 2.358(6); Dy2–O7–Dy5 97.1(2), Dy2–O11–Dy3 97.5(2), Dy3–O15–Dy4 96.3(2), Dy4–O19–Dy5 96.3(2).

Since the dataset of the crystal measurement of **6** was quite poor, we decided to recrystallize the compound from hot toluene. Solution and refinement of the new dataset revealed an unprecedented rearrangement of compound **6** to its pure Ph_2acac analogue $[Dy_5(\mu_4\text{-OH})(\mu_3\text{-OH})_4(Ph_2acac)_{10}]$, which has once been synthesized in our group by Michael T. Gamer.[20] No further investigations with regard to this undesirable rearrangement have been carried out so far.

3.1.2.5 Spectral properties of compounds **1-4**

Since compounds **1-4** possess four stereo centres per molecule due to the accommodation of four amino acid ligands each, we were interested in the specific optical rotations of these enantiopure compounds. The corresponding measurements were determined in CH_2Cl_2. As expected, they always show negative values for the clusters containing the *L*-configured amino acids ($[a]^{20}$ = -782.01° (**2**, *c* = 0.63 M); -818.76° (**3**, *c* = 0.71 M); -702.69° (**4**, *c* = 0.47 M) and a positive value for the cluster with the *D*-configured one ($[a]^{20}$ = 754.92° (**1**, *c* = 0.60 M)). The ^{1}H NMR spectra exhibit few unambiguous signals for the Ph_2acac ligand in the aromatic region, and two sets of singlets in a 1:2 ratio are observed for the methyne bridges of the Ph_2acac ligands. This is attributed to two different coordination environments for this ligand, as stated above. The major signal can be ascribed to those methyne bridges of the Ph_2acac ligands coordinating to the basal metal atoms (four ligands), whereas the minor one can be assigned to those coordinating to the apical metal atom (two ligands). All signals of the amino acids were observed in the expected region. The OH and NH_2 protons do not give unambiguous signals in all compounds. In the IR spectra the hydroxy groups of the cluster core show broad peaks between 3350 and 3650 cm^{-1}.

3.1.2.6 PGSE diffusion experiments with $[Y_5(\mu_4\text{-OH})(\mu_3\text{-OH})_4(L\text{-Val})_4(Ph_2acac)_6]$ (**3**)

IN COOPERATION WITH
DR. IGNACIO FERNÁNDEZ, INSTITUTE OF ORGANIC CHEMISTRY, UNIVERSITY OF ALMERIA (SPAIN)

The nuclearity of these pentanuclear yttrium clusters in solution has hitherto not been evaluated. A first answer to this question has been derived from the so-called pulsed field gradient spin-echo diffusion (PGSE) experiments, which have been performed in cooperation with Ignacio Fernández. This NMR-based diffusion methodology allows one to estimate molecular volumes and ion pairing in solution.[66] Therefore, valine cluster **3** served as a model compound and the PGSE method was accomplished with a deuterated chloroform solution of **3** for the determination of its diffusion coefficient as a function of concentration. Subsequent appliance of the received individual diffusion coefficients D into the Stokes-Einstein equation gave the desired hydrodynamic radius (r_H) of **3**, which may be compared to that one determined from X-ray data. The PGSE diffusion data for model cluster **3** are listed in Table 3.2, where the experimentally determined r_H value of 8.6 Å (c = 6 mM) agree very well with the one deduced from X-ray data. An increase of the concentration up to 44 mM provides a significant decrease of D (3.701 $m^2 \cdot s^{-1}$) and consequently leads to a marked increase of r_H to 10.0 Å. Despite of a change of viscosity at higher concentrations, the notable difference in radii (Δr_H = 1.4 Å, 16 %) seems likely to be due to aggregation of **3**. As a possible result, formation of intermolecular hydrogen bonds might decrease the size-related diffusion coefficient of a certain molecule from that expected in a given medium at a certain temperature. Considering a rapid exchange between sites on the NMR timescale, we suggest a hydrogen bond aggregation in rather concentrated solutions as the large amount of XH_n (X = O (n = 1), N (n = 2)) moieties in cluster **3** ought to be able to provide intermolecular hydrogen bonding, resulting in an averaged diffusion coefficient.

This NMR-based subproject served give evidence for this kind of amino acid ligated rare earth metal clusters to be stable and to retain their shape in chloroform solution, whereby **3** has acted as a representative for the remaining cluster species. However, this method allows to confirm this issue only up to a certain concentration threshold, since **3** has clearly shown to be prone to aggregation when concentration rises of 44 mM.

Concentration [mM]	$D\,[10^{10}\ \mathrm{m}^2\ \mathrm{s}^{-1}]^a$	r_H [Å]^b	$r_{\text{X-ray}}$ [Å]^c
6	4.314	8.6	8.6
12	4.262	8.7	
22	4.183	8.9	
44	3.701	10.0	

Table 3.2. PGSE diffusion data of **3**. ^{a} The experimental error in the D values is ±2 %. ^{b} The viscosity η used in the Stokes–Einstein equation was taken from Perry's Chemical Engineers' Handbook 8th Edition (www.knovel.com) and is $0.5737 \cdot 10^{-3}\ \mathrm{kg \cdot m^{-1} \cdot s^{-1}}$. ^{c} Deduced from the X-ray structure by considering the volume of the crystallographic cell divided by the number of contained asymmetric units, the latter one is regarded to be spherical in shape.

3.1.2.7 HMQC and TOCSY experiments with $[Y_5(\mu_4\text{-OH})(\mu_3\text{-OH})_4(L\text{-Val})_4(Ph_2acac)_6]$ **3**

IN COOPERATION WITH
DR. IGNACIO FERNÁNDEZ, INSTITUTE OF ORGANIC CHEMISTRY, UNIVERSITY OF ALMERIA (SPAIN)

Owing to these findings showing the stability of such cluster compounds in solution, we urged to conduct continuative multidimensional NMR experiments with **3** to observe ^{1}H-^{89}Y scalar interactions, proving *e.g.* the existence of two chemically different yttrium atoms. This kind of experiments is possible due to the diamagnetic nature of Y^{3+} species,[67] and all pieces of information arising from these compounds can be used to model structures and estimate reactivities of related rare earth metal complexes due to their similar ionic radii.[65] Furthermore, the ^{89}Y nucleus as a monoisotopic species of spin $I = ½$ makes it attractive for NMR studies and its chemical shift range spanning ca. 1300 ppm implies a high sensitivity towards small changes in its coordination sphere.[68] On the other hand, ^{89}Y possesses a rather low receptivity ($D^C = 0.7$) and long T_1 relaxation times what make conventional pulse-acquisition ^{89}Y NMR spectroscopy quite time-consuming.[68-69] Helpful coupling information has emerged from their respective monodimensional spectra of nuclei to which ^{89}Y is scalarly coupled, like $^{1}H,^{89}Y$-,[70] $^{13}C,^{89}Y$-,[70b, 70f] $^{15}N,^{89}Y$-,[71] $^{29}Si,^{89}Y$-,[72] $^{31}P,^{89}Y$-[72-73] and $^{77}Se,^{89}Y$-coupling.[74]

Bearing these aspects in mind, we continued the cooperation with Ignacio Fernández who carried out different 1D and 2D NMR experiments with a 60 mM chloroform solution of cluster **3** at room temperature. The ^{1}H NMR spectrum of **3** showed its usual set of signals as stated in chapter 3.1.4.6. This clearly evidence two different coordination environments, as deduced from the X-ray structure.[21] Surprisingly, the OH protons were not detected in the spectrum, whereas the NH_2 were clearly assigned with the help of two different experiments. On the one hand, 1D gTOCSY (total correlation spectroscopy) NMR experiments revealed an ABCX spin system for the *L*-valine moiety, in which each of the amino protons show significantly different chemical shifts (Fig. 3.17).

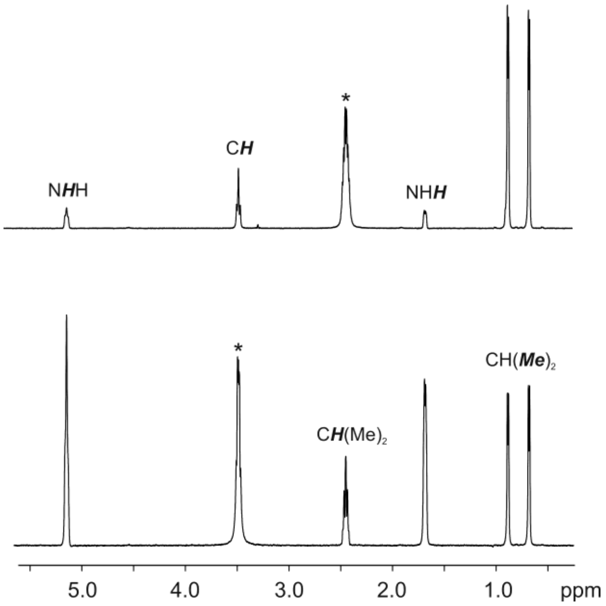

Figure 3.17. 1D gTOCSY NMR (500.13 MHz) expansion of valine cluster **3** in $CDCl_3$ at room temperature (τ_{SL} = 120 ms). The asterisks indicate the irradiated signal.

On the other hand, the 2D $^{1}H,^{13}C$ gHMQC (heteronuclear multiple quantum coherence) spectrum does not show any scalar interaction to those signals located at $\delta_H = 1.68$ and $\delta_H = 5.15$ ppm, supporting the assignment. The two NH_2 resonances were unambiguously correlated to the ^{89}Y NMR resonance at $\delta_Y = 59.2$ ppm by $^{1}H,^{89}Y$ gHMQC NMR experiments (Fig. 3.18). Unfortunately, no coupling was observed to any of the above mentioned Ph_2acac methyne signals, preventing the chemical shift identification of the apical yttrium atom.

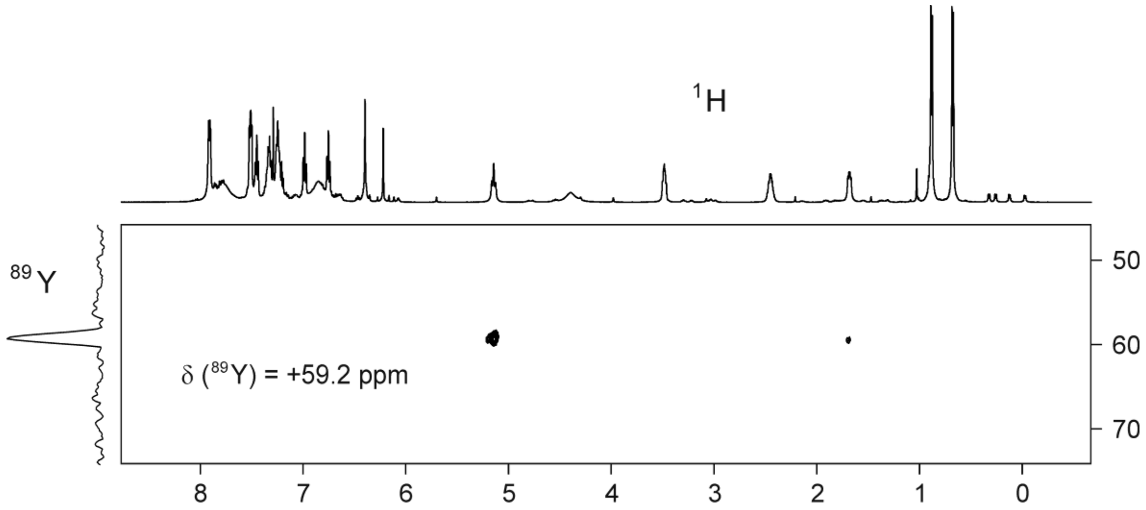

Figure 3.18. ^{1}H,^{89}Y gHMQC spectrum (500.13 MHz) for a 60 mM sample of cluster **3** in $CDCl_3$ at 292 K. Complete data set was acquired in 2h 40 min with a preparation delay optimized for a 12 Hz coupling constant. The internal projection on the left edge and the 1D ^{1}H NMR spectrum on top are both shown. The spectral references used were TMS and $Y(NO_3)_3$ for ^{1}H and ^{89}Y, respectively. The gradient ratio was calculated according to the γ values and set to 60:20:43.9.

In summary, the first yttrium- and dysprosium-based amino acid clusters with accessory organic coligands were synthesized and structurally characterized, including the determination of the individual specific optical rotations. Preliminary PGSE NMR diffusion experiments have been performed with such species for the first time proving the clusters' stability in solution. Moreover the tendency of such species to aggregate in chloroform solution above a certain concentration could be shown. Continuative 2D ^{1}H,^{89}Y-NMR spectra unambiguously exhibited cross peaks between the yttrium metal and hydroxy protons, where the presence of two chemically different yttrium atoms in the cluster could be underlined spectroscopically. It could also be shown that the amino acids coordinate *via* the nitrogen atom of the amino group and one oxygen atom of the carboxyl group in a chelating fashion. Concomitantly, the carboxyl groups are also bridging two adjacent basal metal atoms *via* the same oxygen atom. Furthermore, modifications with respect to electronic properties and steric demand of the amino acid ligands used were tolerated by the coordination chemistry of this cluster scaffold.

Based on these results, we are now able to predict the position in which the amino acids will coordinate within a pentanuclear structural motive.

3.2 Pentadecanuclear Rare Earth Metal Hydroxy Clusters

These structurally well defined nanoscaled metal hydroxy clusters bearing bioactive ligands[41h] provided a significant contribution towards new bioaccessible compounds on the molecular level. By replacing yttrium with metals of the chemically similar rare earth metal series, distinct photophysical properties like *e.g.* luminescence[11a-d, 44] as well as certain magnetic properties[20] might be easily inserted into this class of compounds to broaden their scope of potential applications. Considering the aspects of bioaccessibility and biocompatibility as well as the fact that the clusters' periphery is decisively responsible for their solubility properties, a tailored ligand system had to be designed to agree with cellular requirements, *i.e.* to maximize their water solubility in particular.

As we yearned to unify this ensemble of valuable characteristics in one compound, a comprehensive cooperation with Dr. Esther Birtalan, Dominik Kölmel, Dr. Birgit Rudat, Prof. Dr. Stefan Bräse (peptoid ligand synthesis, optical investigations), Dr. Ute Schepers (*in vitro* experiments), Dr. Marco Neumaier (ESI-MS studies), Dr. Yanhua Lan, Prof. Dr. Annie K. Powell (magnetic measurements) and Dr. Ignacio Fernández (multidimensional NMR studies) was initiated.

Therefore, we conceived a bifunctionalized ligand possessing an α-amino carboxyl moiety as one of its termini targeting to offer the metal-binding site, in analogy to those examples mentioned in chapter 3.4.1. In order to explore the tolerance of the clusters' coordination chemistry in terms of their steric demand, we chose an *N*-substituted α-amino carboxylate instead of an α-amino acid. The attachment of the residue to the nitrogen atom instead of the glycinic carbon atom makes this moiety comparable to the *L*-proline ligand in cluster **2** (cp. 3.4.1). However, in contrast to *L*-proline a stereogenic centre is absent. The second terminus consists of a *tert*-butyloxycarbonyl (Boc) protected amine group, namely a *tert*-butyl carbamate. Protecting the ligand's second functionality was considered confidently, since in our case, using other entirely unprotected bifunctionalized amino acids like *e.g.* *L*-tyrosine have shown to prevent the formation of the desired mixed ligated cluster compounds. We assume that in this case the numerous different functional groups competed too much in coordination to the metal atoms, hence, a selective formation of a certain structural motif could not be facilitated.

The two termini are linked by a *meta*-xylylene fragment with each other. To sum up, the ligand depicts a *single site*-protected peptoid compound ($PepCO_2H \cdot HCl$) (Fig. 3.19) which is usually used as a precursor for the preparation of *e.g.* FRET-capable oligopeptoids possessing additional functionalities like disulfide bridges undergoing enzymatic cleavages in cellular media.[75]

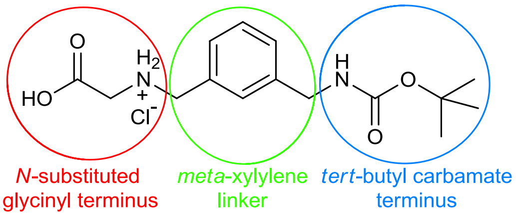

$PepCO_2H·HCl$

Figure 3.19. Bifunctionalized ligand $PepCO_2H·HCl$ can be divided into three sections: An unprotected *N*-substituted glycinyl terminus (red) and a *tert*-butyloxycarbonyl-protected amine function (blue) are separated by a *meta*-xylylene linker (green).

As in the past the Ph_2acac ligand often proved to be a reliable supporting ligand stabilizing various rare earth metal hydroxy structural motives,[11c, 20, 37, 41c, 41e-h, 44] we decided to continue its employment within the following synthetic approaches to achieve the coordinative goal of a mixed ligation in an even more challenging fashion than presented in chapter 3.4.1.

3.2.1. Synthetic Aspects of $[Ln_{15}(\mu_3\text{-}OH)_{20}(PepCO_2)_{10}(Ph_2acac)_{10}Cl]Cl_4$ (7-9)

IN COOPERATION WITH
PROF. DR. STEFAN BRÄSE, DR. ESTHER BIRTALAN AND DOMINIK KÖLMEL, INSTITUTE OF ORGANIC CHEMISTRY, KARLSRUHE INSTITUTE OF TECHNOLOGY

This goal was achieved upon reaction of the rare earth metal trichloride hexahydrates $[LnCl_3·(H_2O)_6]$ (Ln = Y, Tb, Dy) with $PepCO_2H·HCl$, Ph_2acacH and potassium *tert*-butoxide (KO*t*Bu) as Brønsted base in methanol. To our surprise, this approach did not afford the expected aforementioned pentanuclear pyramidal structural motif, but an even more sophisticated pentadecanuclear mixed ligated lanthanoid hydroxy cluster $[Ln_{15}(\mu_3\text{-}OH)_{20}(PepCO_2)_{10}(Ph_2acac)_{10}Cl]Cl_4$ (Ln = Y (**7**), Tb (**8**), Dy (**9**)) (Fig. 3.20a). The inorganic core of this compound is made up by a ring-shaped rare earth metal hydroxy scaffold[29a, 48] which is coordinatively and sterically saturated by both the peptoid ($PepCO_2$) and the Ph_2acac ligands in a stoichiometric 1:1 ratio, *i.e.* a quantity of ten ligands each stabilizes the inorganic core outwardly. A central chloro ion stabilizes the ring structure inwardly. The resulting quadruply positive charge is balanced by four non-coordinating chloride anions. Single crystal

X-ray analysis revealed the solid state structures of compounds **7-9** to be isostrucural (Fig. 3.20b-d).

Clusters **7-9** have been characterized by standard analytical and spectroscopic techniques, and the solid state structures of all compounds were established by single crystal X-ray diffraction. Within corporate projects with the previously mentioned scientists, clusters **7-9** underwent the following additional experiments: kinetic investigations of **9** were carried out *via* electrospray ionization mass spectrometry (ESI-MS) (cp. 3.2.3), PGSE NMR diffusion experiments and continuative 2D NMR experiments were performed with compound **7** for understanding the behaviour of such compounds in solution (cp. 3.2.4 and 3.2.5). Magnetic properties of compound **9** were studied (cp. 3.2.6), and luminescent characteristics were elucidated for compound **8** (cp. 3.2.7). To allow statements in terms of biocompatibility and bioaccessibility of the clusters, *Cervex* tumor cells were incubated with **7-9** to subsequently accomplish corresponding *in vitro* localization and toxicity studies (cp.3.2.8). Finally, first attempts to deprotect the peptoids' amine functionality are briefly discussed (cp. 3.2.9).

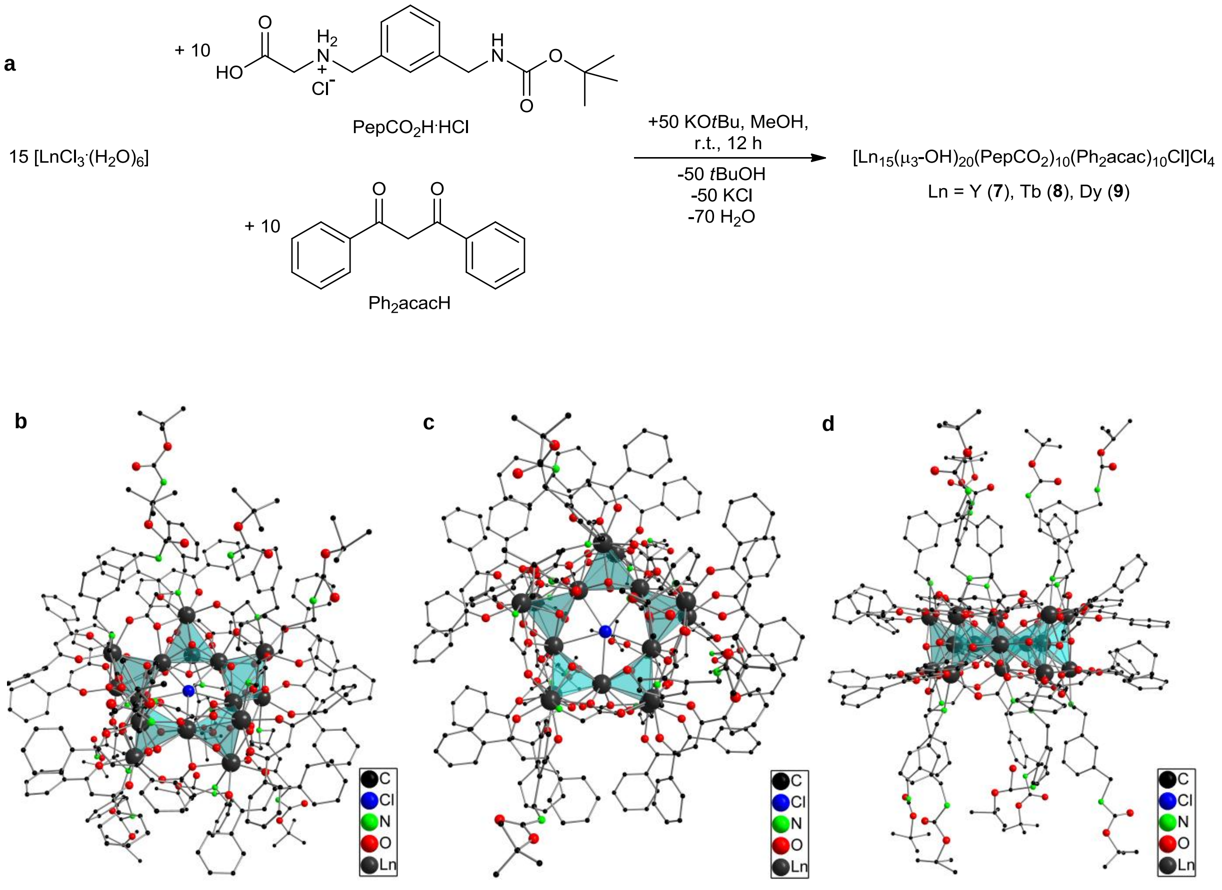

front view top view side view

Figure 3.20. a) Synthesis and b)-d) different perspectives of the solid state structure of $[Ln_{15}(\mu_3\text{-}OH)_{20}(PepCO_2)_{10}(Ph_2acac)_{10}Cl]Cl_4$ with Ln = Y (**7**), Tb (**8**) and Dy (**9**).

3.2.2 Structural Discussion on $[Ln_{15}(\mu_3\text{-}OH)_{20}(PepCO_2)_{10}(Ph_2acac)_{10}Cl]Cl_4$ (7-9)

The central structural motif, a $\{Ln_{15}(OH)_{20}Cl\}^{24+}$ moiety, has been previously observed.[29a, 48-49] The structure consists of five doubly vertex-sharing $\{Ln_4(\mu_3\text{-}OH)_4\}^{8+}$-heterocubanes (Fig. 3.21a) displaying a cyclic arrangement. The rare earth metal atoms themselves display three parallel pentagonal planes, whereby the two outer planes are larger than the inner plane. The rare earth metal atoms of the inner plane solely serve to interconnect the heterocubane segments. The cyclic shape of this rare earth metal hydroxy scaffold is additionally stabilized by a centered μ_5-bridging chloride ligand which exclusively coordinates to the inner rare earth metal atoms (Fig. 3.21b). That is why it can be evaluated as a structure-determining module being mainly responsible for the design of this scaffold and may, hence, be described as a template ion. The Ln_{15}-core structure has a non-crystallographic C_5-axis through the chloro ligand, which is perpendicularly aligned to the pentagonal planes. An additional C_2-axis goes through the chloride template ion and one of the inner rare earth metal atoms. As there are five inner rare earth metal atoms, a total of five of these C_2-axes are present, hence, the $\{Ln_{15}(OH)_{20}Cl\}^{24+}$ scaffold provides D_{5h} symmetry.

Each of the ten monoanionic Ph_2acac ligands uniformly chelate an outer rare earth metal atoms each with both oxygen atoms in a η^2-coordination modus. The resulting face enclosed by an almost planar six-membered metallacycle is made up by the β-diketonate fragment and the individual rare earth metal atom is coplanarily arranged to the metal-based pentagonal faces. Unlike the Ph_2acac ligands, the ten single-deprotonated $PepCO_2$ ligands are perpendicularly aligned to the pentagonal faces. Five $PepCO_2$ ligands are attached to one side of the cyclic rare earth metal hydroxy scaffold each in a mirror-inverted fashion. For this purpose, both the carboxylate oxygen atoms and the glycinic nitrogen atom are used as donor functionalities for coordination to the rare earth metal atoms. They chelate one of the outer rare earth metal atoms each by employing one of the carboxylate oxygen atoms and the glycinic nitrogen atom. This carboxylate oxygen atom simultaneously bridges the chelated rare earth metal atom with an inner rare earth metal atom which is next to it. The second carboxylate oxygen atom serves as a η^1-coordinating donor atom, *i.e.* it binds to a neighbouring outer lanthanoid atom which belongs to the same pentagonal plane as the aforementioned one (Fig. 3.21c). Thus, the $PepCO_2$ ligands act as tridentate supporting ligands coordinating in $\mu_3{:}\eta^2{:}\eta^1{:}\eta^1$-modus. Those rare earth metal atoms occupying the vertices of the inner pentagonal planes adopt a coordination number of nine, whereas those of the outer planes adopt a coordination number of eight (Fig. 3.21d).

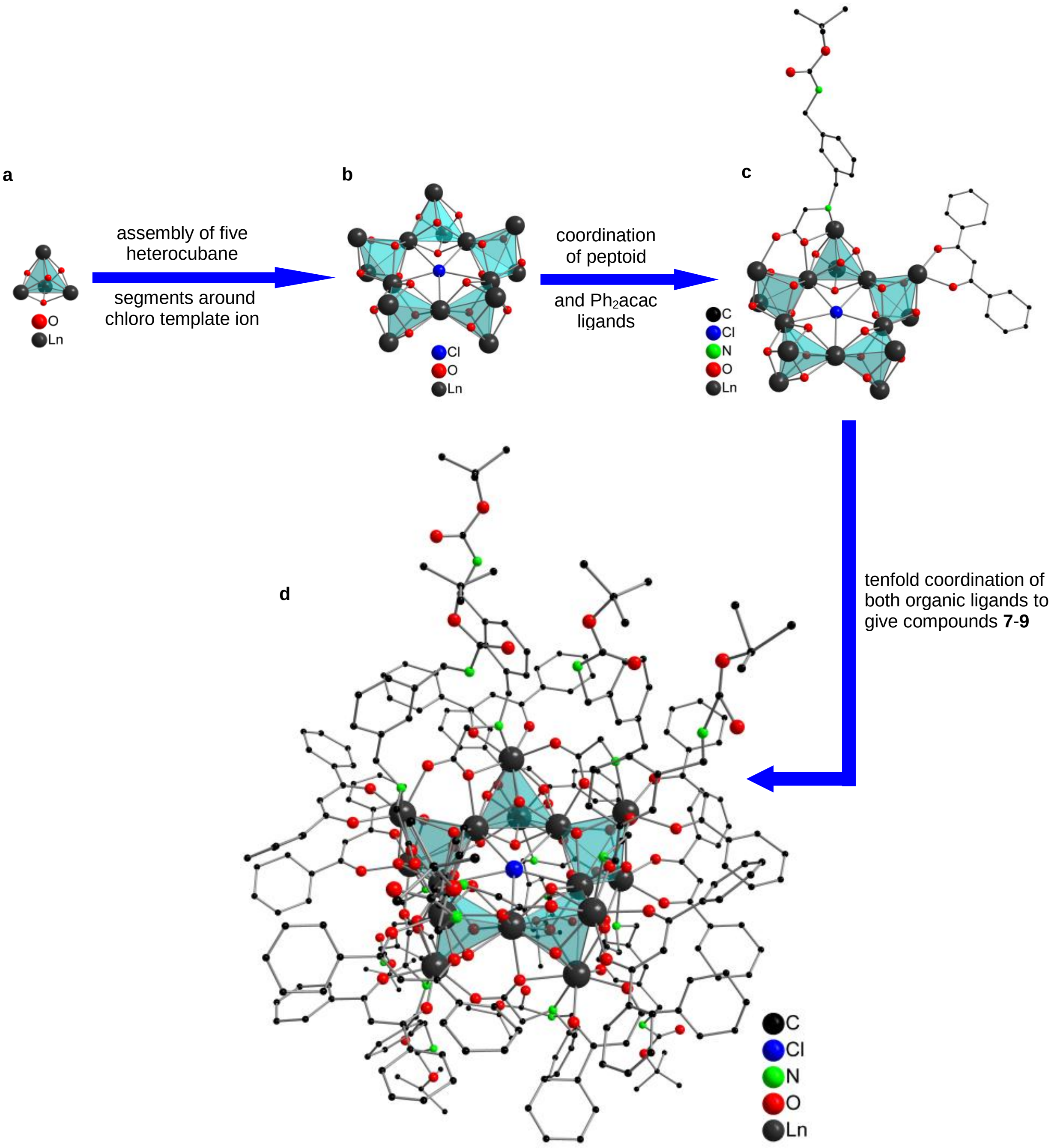

Figure 3.21. Structural genesis of $[Ln_{15}(OH)_{20}(PepCO_2)_{10}(Ph_2acac)_{10}Cl]Cl_4$. a) The heterocubanes are made up by two interlaced tetrahedrons of rare earth metal atoms and hydroxy oxygen atoms. b) Five doubly vertex-sharing heterocubanes and the chloro template ion display the cluster's inorganic core, c) whereas the Ph_2acac ligands and the $PepCO_2$ ligands display the organic shell to end up with compounds **7**-**9** (d).

The average interatomic distances between inner rare earth metal atoms are slightly shorter (av. Ln2-Ln6: 3.760 Å (**7**), 3.786 Å (**8**), 3.775 Å (**9**)) than in Zheng's Eu-based pentadecanuclear tyrosine cluster $[Eu_{15}(\mu_3\text{-}OH)_{20}(\mu_5\text{-}Cl)(\mu_3\text{-}L\text{-}Tyr)_{10}(OH)_2(\mu\text{-}H_2O)_5(H_2O)_{18}](ClO_4)_{12}\cdot 9H_2O$ (av. Eu_{inner}-Eu_{inner}: 3.896 Å),[48] which agrees well with the larger ionic radius of Eu^{3+} (1.21 Å) compared to Y^{3+} (1.155 Å), Tb^{3+} (1.18 Å) or Dy^{3+} (1.17 Å) when assuming coordination numbers of eight.[65] Accordingly, the average interatomic distances between the outer rare earth metal atoms (*e.g.* Ln1-Ln3 or Ln4-Ln5, Fig 3.22) of compounds **7-9** are 6.046 Å (**7**), 6.089 Å (**8**) and 6.071 Å (**9**), which are also a little shorter than in Zheng's Eu-analogue (Eu_{outer}-Eu_{outer}: 6.331 Å). As expected, the shortening of the interatomic Ln-distances in **7-9** compared to the Eu-cluster results in a shorter mean interatomic distance between the inner rare earth metal atoms and the chloro template ion, *i.e.* the corresponding Ln_{inner}-Cl-values (*i.e.* Ln2/4/5-Cl1, Fig. 3.22) of 3.194 Å (**7**), 3.216 Å (**8**) and 3.205 Å (**9**) are shorter by approximately 0.11 Å compared to the Eu-cluster.[48] The average bond distances between N1 and Ln1 are 2.550 Å for **7**, 2.557 Å for **8** and 2.555 Å for **9**, and they are ca. 0.1 Å shorter than in the europium compound. The values for the bond distances between O1 and Ln1 behave similarly, *i.e.* the values of 2.435 Å (**7**), 2.456 Å (**8**) and 2.448 Å (**9**) are smaller by about 0.1 Å. The mean bond distances between the bridging O1 and the inner Ln2 are 2.474 Å (**7**), 2.483 Å (**8**) and 2.480 Å (**9**), and the average bond distances between the bridging O2 to the adjacent outer rare earth metal atom Ln3 are 2.355 Å (**7**), 2.373 Å (**8**) and 2.366 Å (**9**), respectively. The average bond distances between the oxygen atoms O3 and O4 of the Ph_2acac ligands adopt values of 2.282 Å (**7**), 2.306 Å (**8**) and 2.297 Å (**9**), which are comparable to those derived from related structures containing this ligand.[20, 37, 41b, 41c, 41e, 41f]

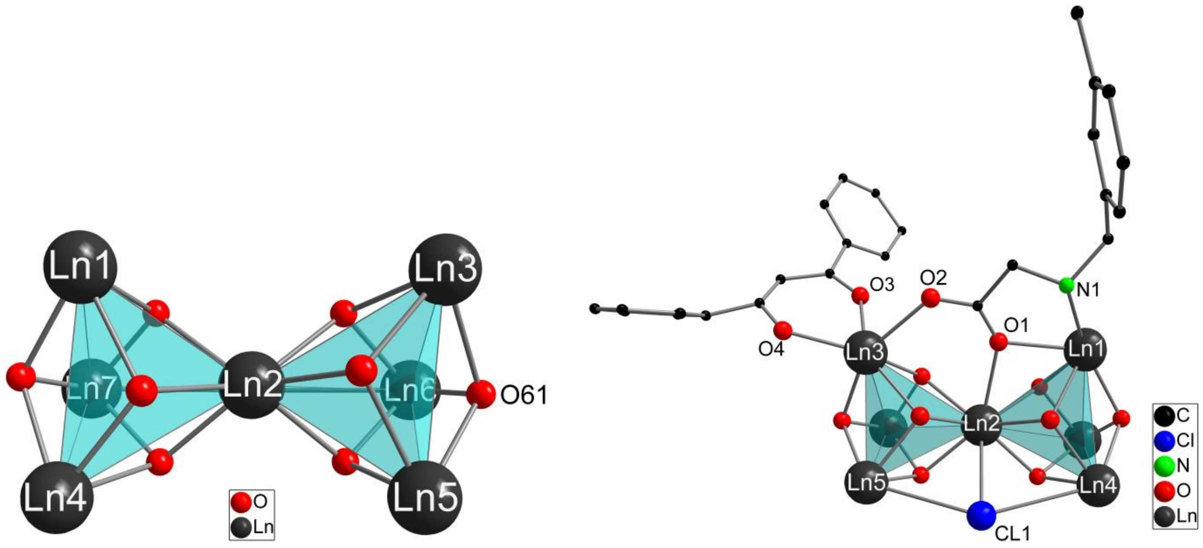

Figure 3.22. Moieties of solid state structures of **7-9**. Hydrogen atoms and *tert*-butyl carbamate functionality are omitted for clarity. Selected average distances [Å] and angles [°]: Ln2-Ln1,5 3.591, Ln2-Ln3/4 3.833, Ln2-Ln6 3.774, Ln1-Ln3 or Ln4-Ln5 6.069; Ln1/4-Ln2-Ln3/5 109.7, Ln6-Ln2-Ln7 108.0, φ(Ln2-Ln3-Ln5; Ln2-O61-Ln6) 81.3; Ln2/4/5-Cl1 3.205, N1-Ln1 2.554, O1-Ln1 2.446, O1-Ln2 2.479, O2-Ln3 2.484, O3-Ln3 2.295; Ln2-Cl1-Ln4/5 72.0, N1-Ln1-O1 64.6, Ln1-O1-Ln2 93.4, O3-Ln3-O4 72.8.

3.2.3 ESI-MS Investigations of $[Ln_{15}(\mu_3\text{-}OH)_{20}(PepCO_2)_{10}(Ph_2acac)_{10}Cl]Cl_4$ (7-9)

IN COOPERATION WITH
DR. MARCO NEUMAIER, INSTITUTE OF INORGANIC CHEMISTRY, KARLSRUHE INSTITUTE OF TECHNOLOGY

Since the single crystal analyses of cluster compounds **7-9** have elucidated their corresponding shape in the solid state, we were now further interested in the disclosure of their behaviour in solution. For this purpose, ESI-MS appeared as an attractive method, as it allows a detection of singly and/or multiply charged compounds up to mass/charge ratios *m*/*z* of several tens to even hundreds of thousands. The restriction of this method to charged compounds might be eligible for clusters **7-9**, because they are uniformly composed of a complex core possessing a quadruple positive charge which is compensated by four non-coordinating chloride anions, as stated above. The latter ones may be assumed to dissociate upon dissolution due to their loose bonding to the complex core. This process could possibly leave a complex bearing one or more positive charges. Furthermore, the necessity of a carrier solvent for facilitating the dissolved compound to be sprayed into the acceleration channel implies a possible identification of the compounds when being in the liquid phase, even with regard to possible equilibria. Thus, the only requirements for such an investigation are a good solubility of the targeted compound in the carrier solvent chosen, since the sensitivity of detection is limited to a certain lowest concentration threshold. The detection of the *m*/*z* ratio itself shall be accomplished by a Fourier transform ion cyclotron resonance (FTICR) device, which allows a satisfactory resolution upon Fourier transformation ion-induced cyclotron resonance, extending the whole apparatus to a FTICR-ESI-MS spectrometer.

Dissolution of 5 mg of clusters **7-9** in approx. 5 mL of MeOH gave a sufficiently concentrated solution to detect individual *m*/*z* ratios *via* FTICR-ESI-MS. The resulting spectra have shown that clusters **7-9** get dissolved upon dissociation of two non-coordinating chloride anions each to give the corresponding dicationic species $[\{Ln_{15}(\mu_3\text{-}OH)_{20}(PepCO_2)_{10}(Ph_2acac)_{10}Cl\}Cl_2]^{2+}$ **7a**-**9a**, as unambiguously indicated by the individual isotopic patterns (Fig. 3.23-3.25). The calculated and experimentally determined *m*/*z* values agree very well in all three cases. These spectra have given a first evidence for this kind of rare earth metal complex scaffold to be maintained during the dissolution process in methanol.

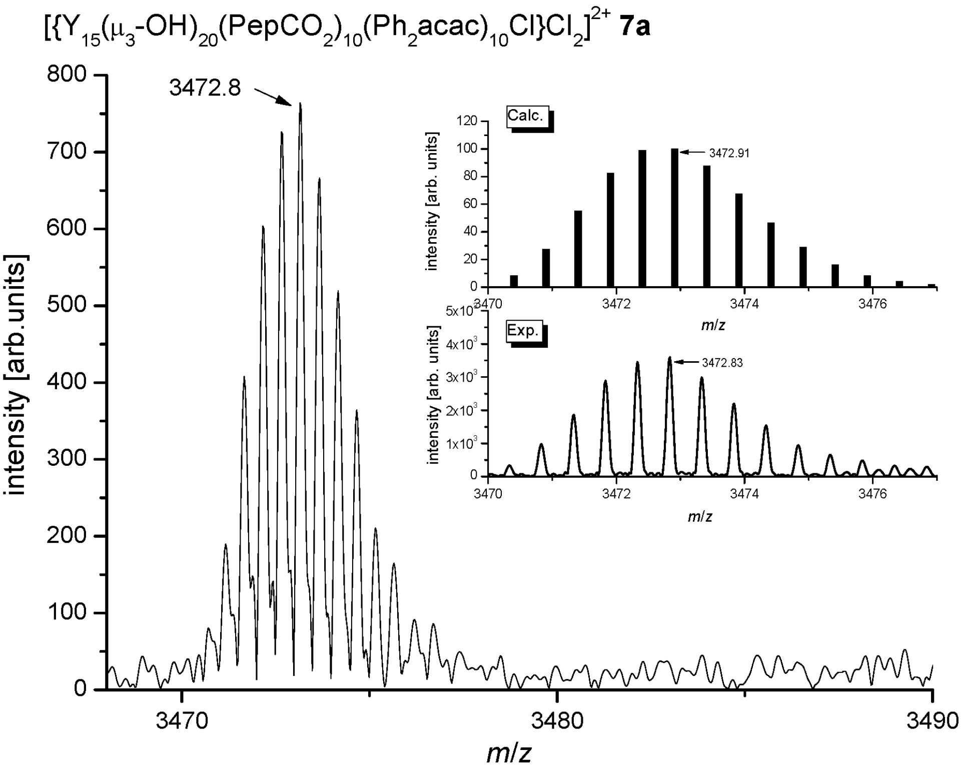

Figure 3.23. FTICR-ESI-MS spectrum of dicationic species [{Y$_{15}$(μ$_3$-OH)$_{20}$(PepCO$_2$)$_{10}$ (Ph$_2$acac)$_{10}$Cl}Cl$_2$]$^{2+}$ **7a** from a methanol solution including comparison between calculated and experimentally determined spectra.

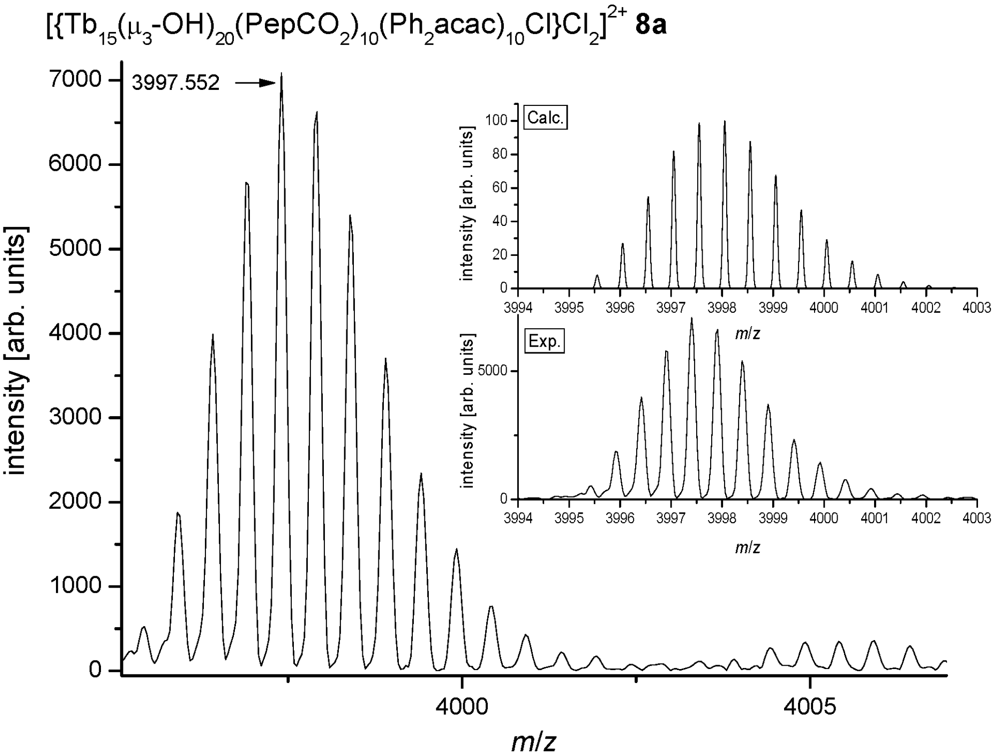

Figure 3.24. FTICR-ESI-MS spectrum of dicationic species [{Tb$_{15}$(μ$_3$-OH)$_{20}$(PepCO$_2$)$_{10}$ (Ph$_2$acac)$_{10}$Cl}Cl$_2$]$^{2+}$ **8a** from a methanol solution showing comparison between calculated and experimentally determined spectra.

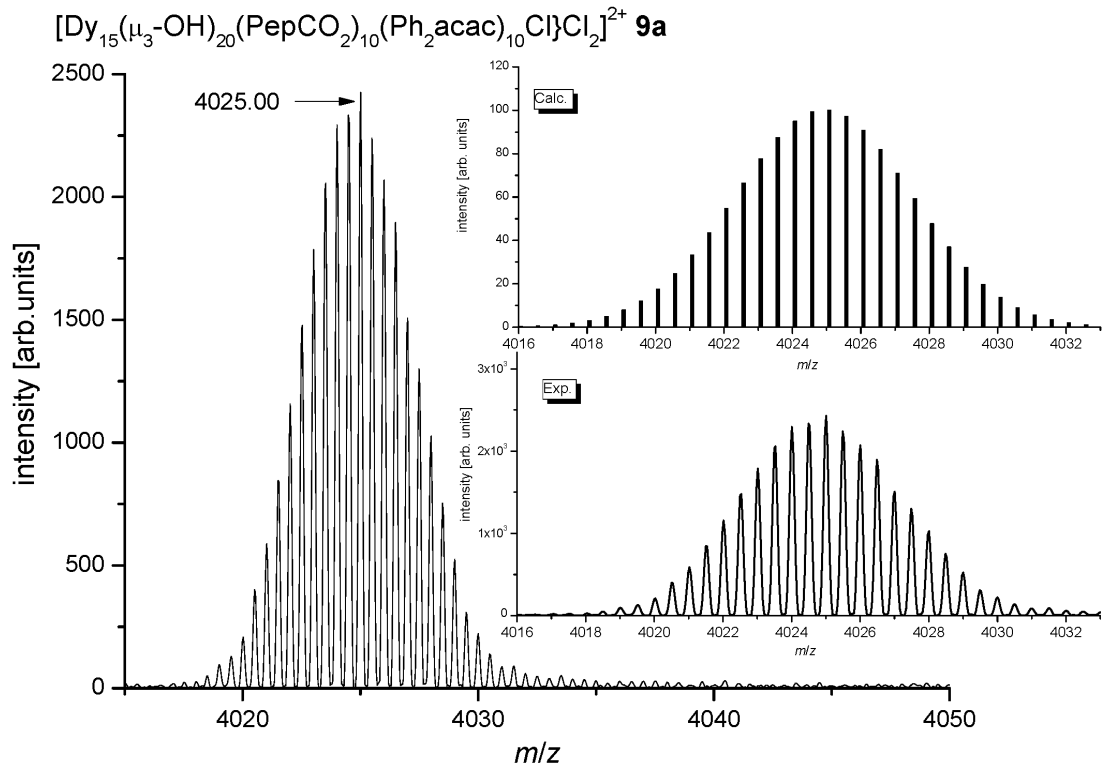

Figure 3.25. FTICR-ESI-MS spectrum of dicationic species $[\{Dy_{15}(\mu_3\text{-}OH)_{20}(PepCO_2)_{10}(Ph_2acac)_{10}Cl\}Cl_2]^{2+}$ **9a** from a methanol solution including comparison between calculated and experimentally determined spectra.

When leaving the methanol samples of **7a**-**9a** at room temperature for several hours and measuring them once again, we surprisingly observed additional signal sets showing the same isotopic ratios, but being shifted towards higher *m*/*z* ratios with regard to the original molar peaks. A more comprehensive investigation for the disclosure of this phenomenon was exemplarily performed with species **7a** and **9a**.

When considering the *m*/*z* difference of approximately 7 *m*/*z* (with $z = 2$) between these two signal sets, it may unambiguously concluded that a solvent-induced hydroxy-methoxy exchange is responsible for these adjacent signal sets (Fig. 3.26). This exchange process could primarily be observed 50 minutes after preparation of the sample solutions. Formally, the high Brønsted acidity of the methanol's hydroxy proton seems to cause a methanolysis reaction to give the single-alkoxylated species $[\{Dy_{15}(OCH_3)(\mu_3\text{-}OH)_{19}(PepCO_2)_{10}(Ph_2acac)_{10}Cl\}Cl_2]^{2+}$ **9b**.

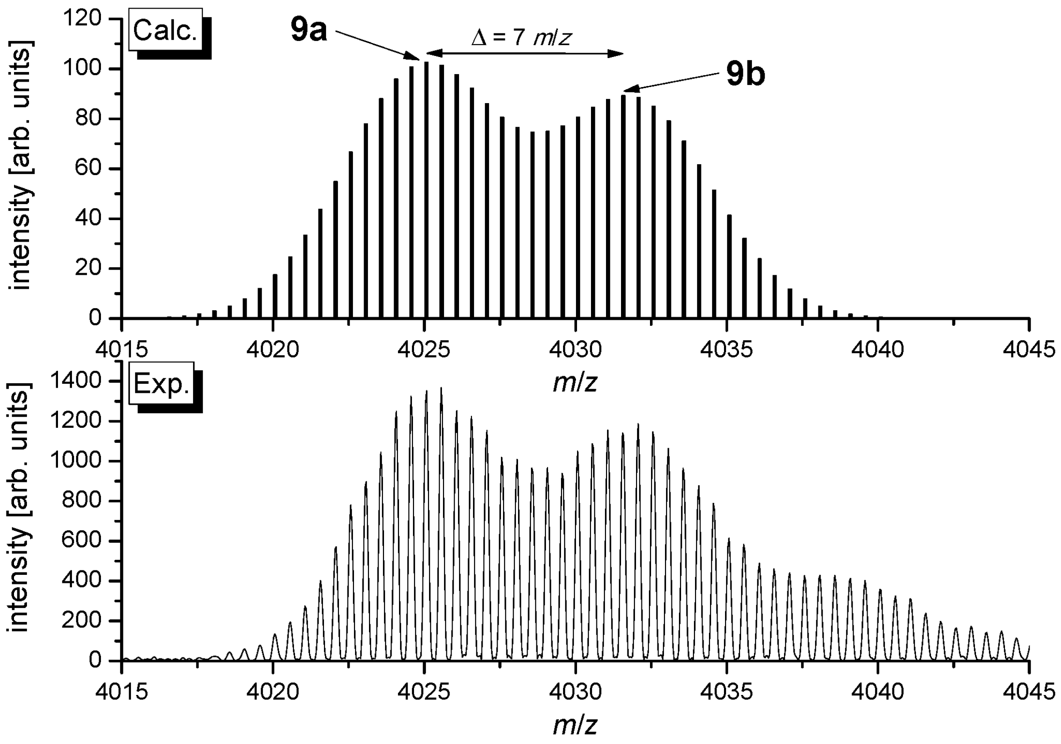

Fig. 3.26. Single hydroxy-methoxy exchange in methanol from **9a** to **9b**, $z = 2$.

Furthermore, having a closer look onto weaker signals at a little higher *m*/*z* values reveals not only a single but even multiple methanolysis reactions (Fig. 3.27a), which were assumed to be formed as a function of time, *i.e.* obeying a reaction rate of a certain order. Therefore, we prepared a fresh methanol solution of **7a** and repeated the measurements after different exposition times. Indeed the course of concentration of compound **7a** exhibited an exponential decrease following a reaction rate of first order, whereas the course of concentration of up to fourfold methoxylated cluster species steadily increased (Fig. 3.27b). The generation of the multiply methoxylated species $[\{Y_{15}(OCH_3)_n(\mu_3\text{-}OH)_{20-n}(PepCO_2)_{10}(Ph_2acac)_{10}Cl\}Cl_2]^{2+}$ (n = 1 (**7b**); 2 (**7c**); 3 (**7d**), 4 (**7e**)) has shown to occur consecutively, since their initial appearance was detected within the second and third measurement. These observations underline the above described suspicion, that the exchange process mechanistically occurs *via* a stepwise methanolysis reaction (Fig. 3.27c), whereby the cluster scaffold is retained.

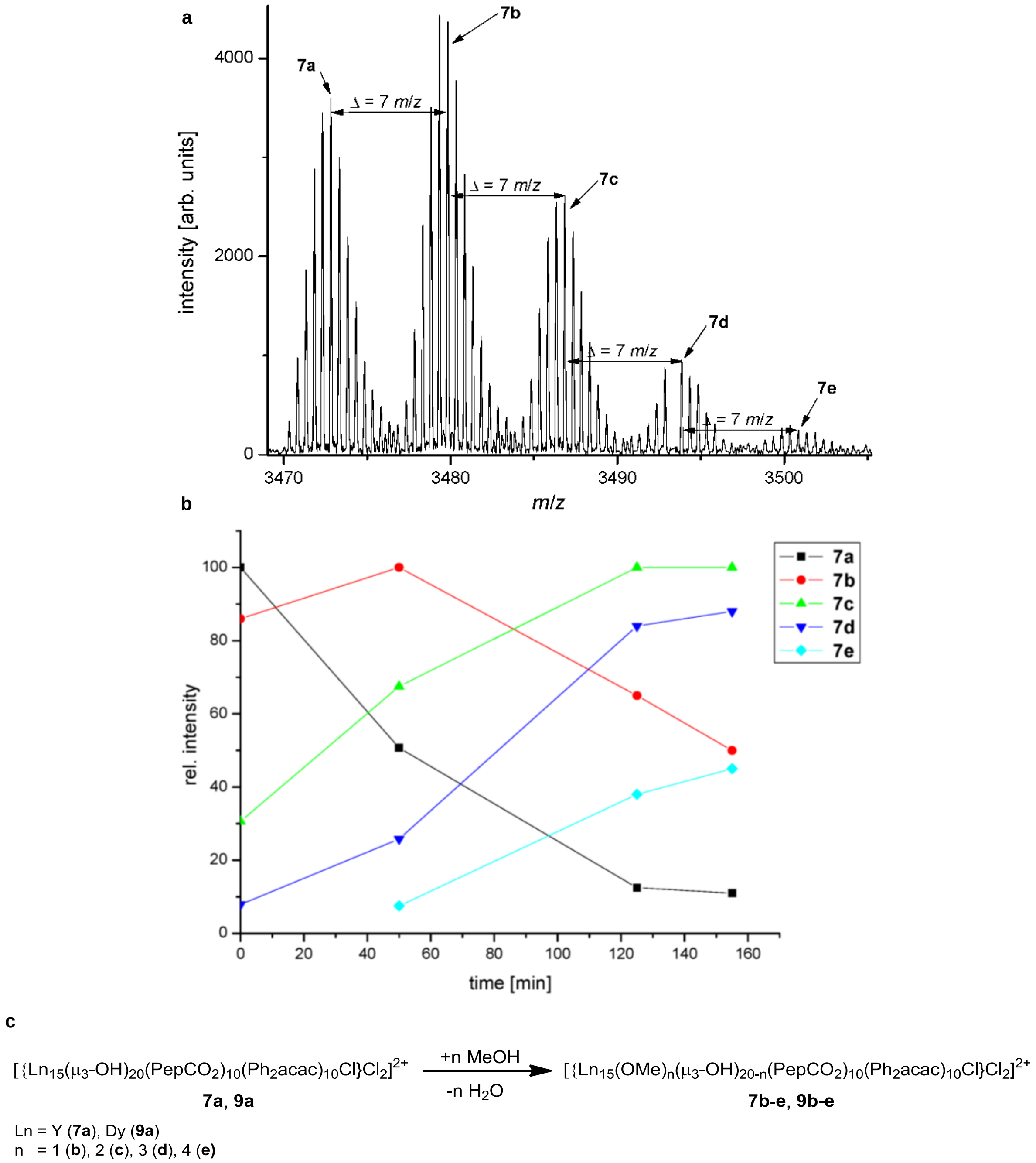

Figure 3.27. a) Exemplified signal sets of **7** undergoing multiple methanolysis and b) corresponding course of intensity or concentration as a function of time; c) Generalized schematic description of exchange process in methanol.

As there were no differences noted between the various yttrium and dysprosium based derivatives of **7** and **9** with respect to the individual exchange velocities, we assumed the terbium-based analogues to behave in the very same way, hence, analogous studies on compound **8** were not of interest.

Owing to its highly protic character, methanol has induced the spontaneous multiple methanolysis in solution. Now we were interested in how far the pK$_a$-value and the steric demand of the solvent used might influence the rate of this hydroxy-methoxy exchange. For this purpose, we firstly used ethanol which is not as Brønsted-acidic but more sterically demanding than methanol, hence, usage of ethanol ought to slow down this exchange process strikingly. An ethanol solution of **9** with the same concentration showed the same set of signals of **9** as observed for the methanol solution. A hydroxy-ethoxy exchange has also been observed, *i.e.* an analogous ethanolysis reaction has occurred, however, only a single one which started to be detectable after three days. Thus, the ethanolysis of **7** and **9** operates in a very different timescale than the previously described methanolysis. To finally confirm the effect of pK_a-value and steric demand on the exchange processes, another equi-concentrated *n*-propanol solution was prepared. Beyond the expected dissociation of **9**, even after a week no exchange was observed, which gives evidence for the hydroxy-alkoxy exchange rate to be a function of solvent's pK_a-value.

In conclusion, dissociation processes of compounds **7** and **9** were conducted *via* FTICR-ESI-MS. Furthermore, an unprecedented multiple hydroxy-methoxy exchange concerning the μ_3-hydroxy bridges of these rare earth metal hydroxy clusters was observed when using methanol as carrier solvent. An interrelation between the Brønsted acidity of the alcohol's hydroxy proton and the exchange rate could be drawn: methanol mediates the fastest hydroxy-methoxy exchange due to its lowest pK_a-value, whereas the less acidic ethanol lets the exchange strikingly slow down and the least acidic *n*-propanol has shown to stabilize the dicationic species **7a** and **9a** permanently. As a consequence, alcoholysis reactions of **7a** and **9a** have shown to be promoted by a preferably low solvent-derived pK_a-value, which has revealed to be the decisive driving force for this exchange process.

3.2.4 PGSE Diffusion Experiments with $[Y_{15}(\mu_3\text{-OH})_{20}(PepCO_2)_{10}(Ph_2acac)_{10}Cl]Cl_4$ (7)

IN COOPERATION WITH
DR. IGNACIO FERNÁNDEZ, INSTITUTE OF ORGANIC CHEMISTRY, UNIVERSITY OF ALMERIA (SPAIN)

As the ESI-MS results confirm that compounds **7-9** are stable in solution, we sought for underlining the clusters' stability in solution, by applying a second method. In analogy to valine cluster **3** (cp. 3.1.4.6), another cooperation with Ignacio Fernández facilitated NMR-based PGSE diffusion measurements for the determination of the hydrodynamic radius of the diamagnetic cluster compound **7**.

For this purpose, single crystals of **7** were dissolved in THF-d_8 to give a 10 mM solution. However, four instead of two compounds (cluster **7** and non-deuterated THF) were detected *via* the PGSE method, providing four different *D*-values (Table 3.3). At first, the compound giving the lowest *D*-value ($2.848 \cdot 10^{-10}$ $m^2 \cdot s^{-1}$) and therefore the largest r_H (15.9 Å) can be clearly assigned to a doubly positive charged species $[\{Y_{15}(\mu_3\text{-}OH)_{20}(PepCO_2)_{10}(Ph_2acac)_{10}Cl\}Cl_2]^{2+}$ **7a**, as derived from the ESI-MS data. This clarity is due to a very similar r_H-value of 16.2 Å deduced from the solid state structure of **7**, since an absolute difference of 0.3 Å to the experimentally determined value lies within the acceptable error range. Nevertheless, besides the cluster, the non-deuterated THF and the DMF signal which depicts lattice solvent enclosed upon crystallization, an additional unknown species with a *D*-value of $6.591 \cdot 10^{-10}$ $m^2 \cdot s^{-1}$ and a r_H-value of 6.6 Å was observed. Although we did hitherto not put any further efforts into the characterization of this undesired compound, we assume the latter to arise from a degradation process initiated by dissolution in THF-d_8, as the compound dissolved was of single crystalline quality.

Compound	D [10^{-10} $m^2 \cdot s^{-1}$][a]	r_H [Å][b]	$r_{X\text{-}Ray}$ [Å][b]
Cluster	2.848	15.9	16.2
Unknown	6.591	6.6	
DMF	22.834	2.0	
THF	25.538	1.8	

Table 3.3. Diffusion coefficient (*D*) and hydrodynamic radius (r_H) values for cluster **7** at 294 K in THF-d_8 [a] Experimental error in *D* values is ±2 %.[b] The viscosity η used in the Stokes-Einstein equation is 0.4763×10^{-3} $kg \cdot m^{-1} \cdot s^{-1}$. Viscosity was taken from www.knovel.com.[c] Deduced from the X-ray structure by simply dividing the volume of the crystallographic cell by the number of contained asymmetric units. This "unknown" species has signals at $\delta = 8.14$ and 7.43 ppm (cp. 3.2.5).

Figure 3.28 depicts a logarithmic plot of the ratio of signal intensity versus gradient square amplitude, which clearly indicates the presence of an unknown compound diffusing strikingly slower than both solvents, but faster than **7**.

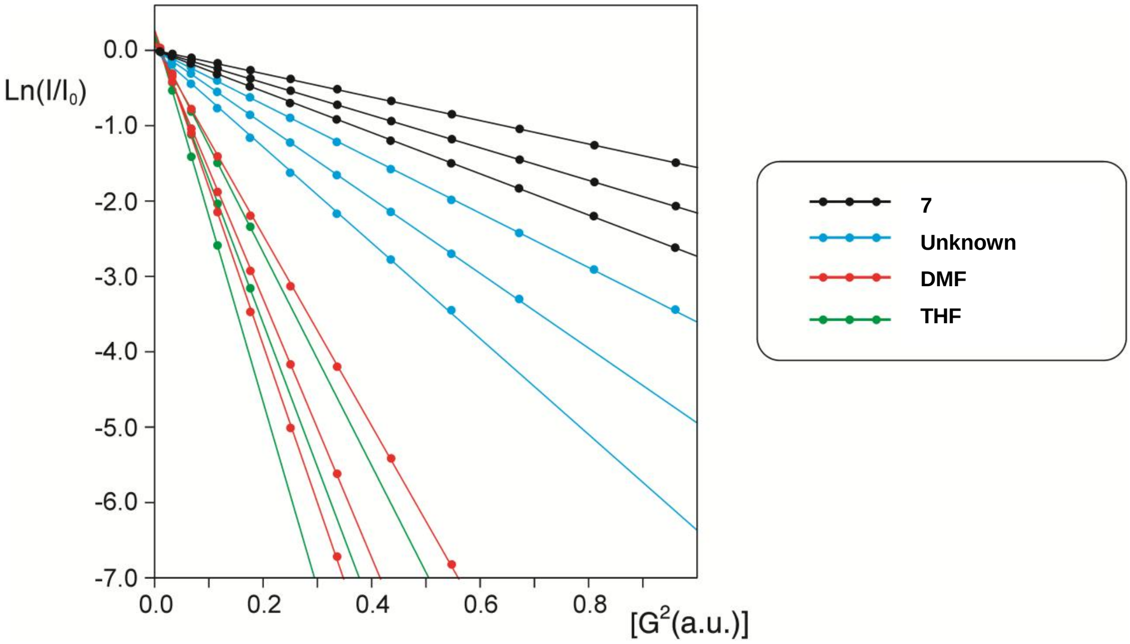

Figure 3.28. Plot of ln (I/I_0) vs. arbitrary units proportional to the square of the gradient amplitude for ^{1}H PGSE diffusion measurements of a 10 mM sample of cluster **7** in THF-d_8 at 294 K. Intensity attenuations of DMF, THF and an unknown species are also shown.

To sum up, cluster **7** has shown to undergo partial decomposition when dissolved in THF-d_8. The fact that within the aforementioned ESI-MS experiments dissolution of cluster **7** in ethanol did not show any decomposition within the exposition time applied, we assume a solvent-induced decomposition caused by THF-d_8. This conclusion gives rise for a set of comparative measurements in *e.g.* ethanol-d_6 instead of THF-d_8, targeting a PGSE diffusion experiment which is not disturbed by any unfavourable decomposition processes.

3.2.5 2D NMR Experiment with [Y$_{15}$(μ$_3$-OH)$_{20}$(PepCO$_2$)$_{10}$(Ph$_2$acac)$_{10}$Cl]Cl$_4$ (7)

IN COOPERATION WITH

DR. IGNACIO FERNÁNDEZ, INSTITUTE OF ORGANIC CHEMISTRY, UNIVERSITY OF ALMERIA (SPAIN)

Based on the findings regarding the behaviour of **7** in solution, we urged to check whether heteronuclear correlations between ^{1}H and ^{89}Y nuclei are observable, in analogy to valine cluster **3** (cp. 3.1.4.8).

Therefore, a ^{1}H,^{89}Y gHMQC measurement was performed using a 10 mM solution by dissolving single crystals of **7** in THF-d_8. The resulting spectrum is presented in Figure 3.29, which clearly shows a heteronuclear interaction between ^{1}H- and ^{89}Y-nuclei, whereby the coupling protons are derived from μ$_3$-hydroxy bridges. The appearance of two well resolved signals at different ^{89}Y chemical shifts $\delta = 106.2$ ppm and 107.3 ppm, respectively, gives evidence for the presence of two chemically distinguishable yttrium atoms, which agrees well with the findings deduced from the corresponding solid state structure (cp.3.2.2). However, besides the expected signals of **7**, crystallization-derived DMF and residual non-deuterated THF, the ^{1}H-NMR spectrum has disclosed the presence of an unknown species, which has obviously once again arisen from solvent-induced decomposition caused by THF-d_8 (cp. 3.2.4). This finding enhances our idea of using non-destructive deuterated solvents like *e.g.* ethanol-d_6 within continuative multidimensional NMR studies on this kind of cluster compounds.

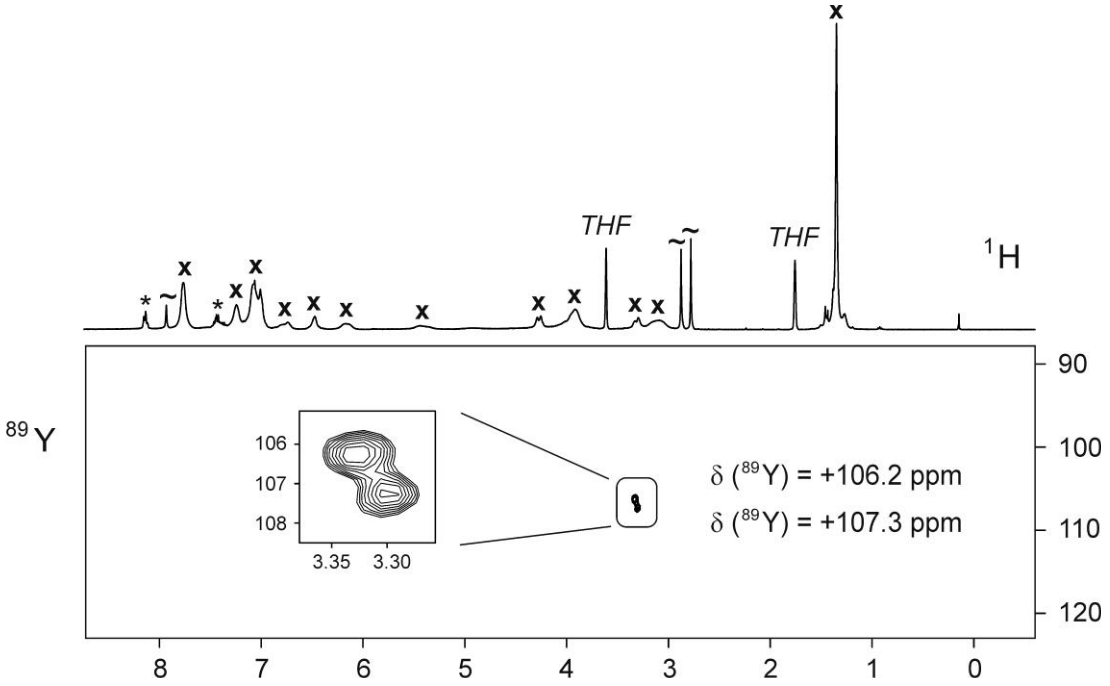

Figure 3.29. Natural abundance ^{1}H,^{89}Y gHMQC spectrum (500.13 MHz) for a 10 mM sample of **7** in THF-d_8 at 294 K. Complete data set was acquired in 4 h 20 min with a preparation delay optimized for a 7 Hz coupling constant. The spectral references used were TMS and $Y(NO_3)_3$ for ^{1}H and ^{89}Y, respectively. The gradient ratio was calculated according to the g values and set to 60:20:43.9 (x = signals of the cluster; * = signals of unknown compound; ~ = signals of DMF).

3.2.6 Magnetism of $[Dy_{15}(\mu_3\text{-}OH)_{20}(PepCO_2)_{10}(Ph_2acac)_{10}Cl]Cl_4$ (9)

IN COOPERATION WITH
PROF. DR. ANNIE K. POWELL AND DR. YANHUA LAN, INSTITUTE OF INORGANIC CHEMISTRY, KARLSRUHE INSTITUTE OF TECHNOLOGY

One crucial point of this rare earth metal coordination chemistry is to afford multinuclear compounds exhibiting distinct magnetic properties for application in according fields. Even though the study of paramagnetic metal-ion aggregates has been of increasing interest in attempts to assemble single-molecule-magnets (SMMs), little articles reporting on rare earth metal based systems have been published. In general, SMM behaviour typically requires paramagnetic metal atoms having high-energy ground states, and a large magnetic moment μ_{eff} is advantageous. Oligo- to polynuclear dysprosium(III) species provide these prerequisites, since the $4f^9$-configuration implies four paired and five unpaired $4f$-electrons which cause an extended anisotropic character and a high magnetic moment ($\mu_{\text{eff}} = 10.63\ \mu_B$; μ_B = Bohr magneton).[18] Furthermore, higher nuclearities might enhance the desirable magnetic properties due to intramolecular communication between different spin carriers. In this context, the Powell group recently prepared hydroxy-bridged dysprosium triangles showing SMM behaviour of thermally excited spin states,[21a, 76] noting that dysprosium(III) shows versatile magnetic behaviour and was the first known example demonstrating the so-called “spin ice” effect.[19]

Therefore a cooperation with Dr. Yanhua Lan and Prof. Dr. Annie K. Powell was aspired to investigate the magnetic properties of the pentadecanuclear dysprosium based cluster **9**. In Figure 3.31, the interrelation between susceptibility χ and magnetization M as a function of either temperature T or magnetic field strength H is presented. The RT susceptibility product χT of **9** is 196.15 $cm^3{\cdot}K{\cdot}mol^{-1}$, which is low in comparison to the expected value of 212.55 $cm^3{\cdot}K{\cdot}mol^{-1}$ for 15 non-interacting Dy^{3+}-ions ($S = 5/2$, $L = 5$, $g = 4/3$, $^6H_{15/2}$, $C = 14.17$ $cm^3{\cdot}K{\cdot}mol^{-1}$; S = spin, L = orbital angular momentum quantum number, g = gyromagnetic ratio, C = Curie constant). Nevertheless, others have shown that this issue is quite common for Dy^{3+}-based compounds.[21, 76-77] Upon cooling, χT steadily decreases to reach a minimum of 170.89 $cm^3{\cdot}K{\cdot}mol^{-1}$ at 11 K when applying a magnetic field of 1000 Oe and then rapidly increases to reach 181.61 $cm^3{\cdot}K{\cdot}mol^{-1}$ at 1.8 K (Fig. 3.30a). This course of χT unambiguously indicates that compound **9** is a ferrimagnetic cluster. The M versus H plots shows the presence of anisotropy (Fig. 3.30b), and the magnetization M at 2 K and 7 T is 75.0 μ_B.

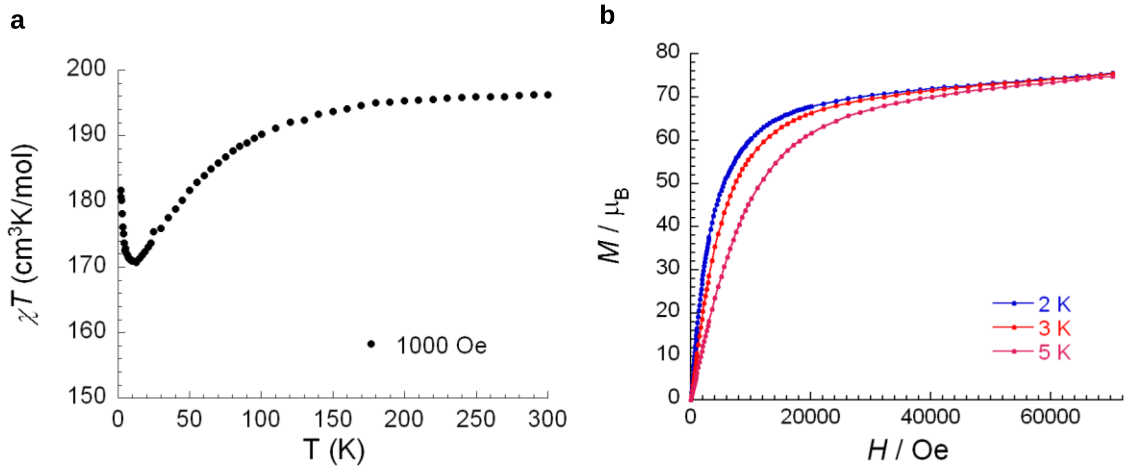

Figure 3.30. a) The plot of χT product versus T reveals **9** to be a ferrimagnetic compound, and b) its magnetization exhibits a temperature dependence of magnetization M when decreasing magnetic field strength H.

The lack of a clear saturation on the M versus H data confirms the effects arising from low-lying excited states and/or anisotropy. It is also worth noting that no hysteresis on the M versus H data has been observed above 2.0 K.

Susceptibility measurements applying alternate current (ac) have shown that this compound exhibits slow relaxation of magnetization below 8 K. Both the frequency-dependent in-phase and out-of-phase signals do not pass through maxima, suggesting that this compound is a SMM (Fig. 3.31). However, for compound **9** this behaviour is associated with a blocking temperature below 1.8 K, even at a frequency of 1500 Hz.

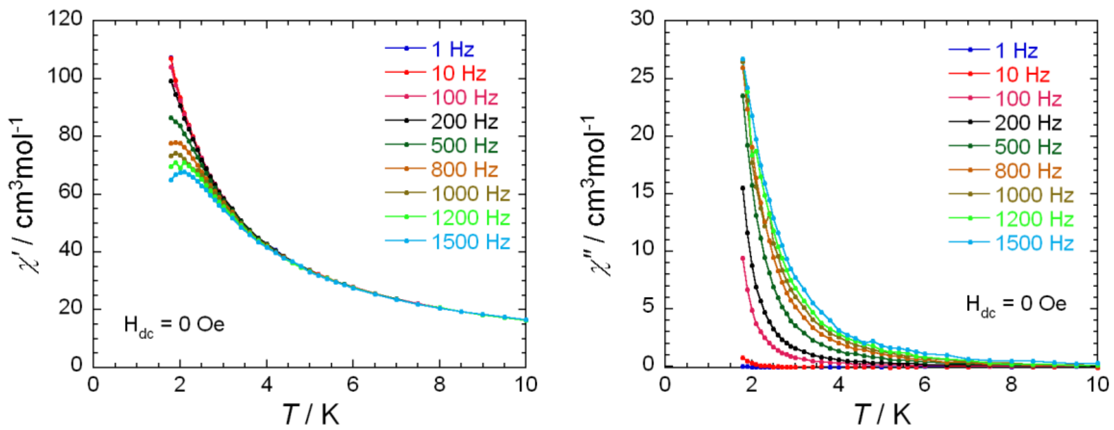

Figure 3.31. Susceptibility measurements of **9** as a function of temperature when applying alternate current.

When applying an external static field, the magnetic relaxation slows down. This may be ascribed to quantum tunneling effects influencing this compound, which are often observed in SMMs. The optimum field was observed at a magnetic field strength of 2000 Oe (Fig. 3.32).

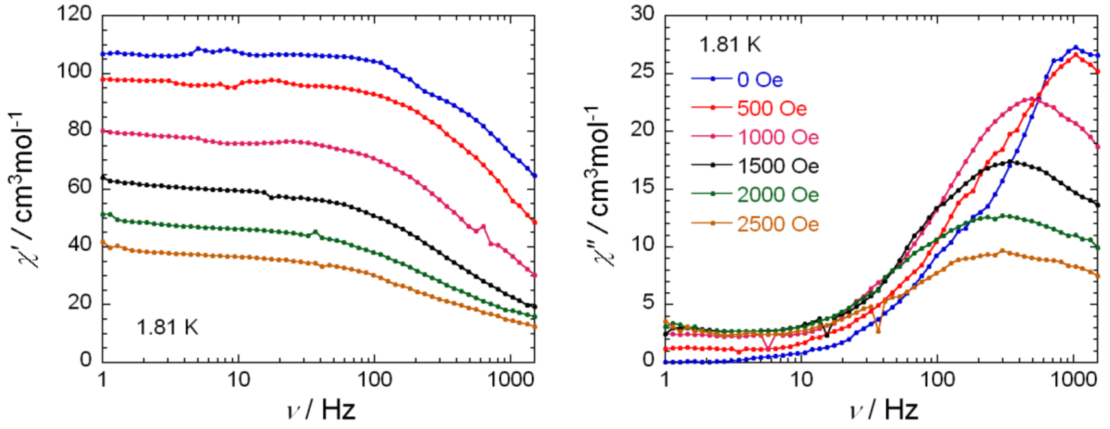

Figure 3.32. Susceptibility measurements of **9** as a function of frequency when applying 1.81 K.

Therefore the ac susceptibility measurements were once more performed in this field (Fig. 3.33). The relaxation time deduced from the frequency sweeping ac data follows an activated Arrhenius law behaviour, providing an energy gap Δ of 9.2 K and a pre-exponential factor τ_0 of $3.5 \cdot 10^{-6}$ s (Fig. 3.34).

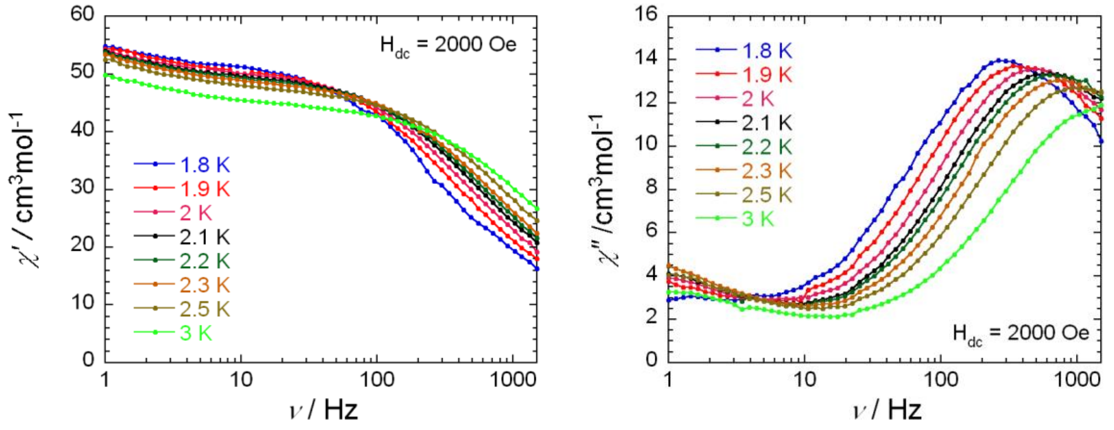

Figure 3.33. Measurements of ac susceptibility as a function of frequency when applying 2000 Oe and temperatures ranging from 1.8 to 3.0 K.

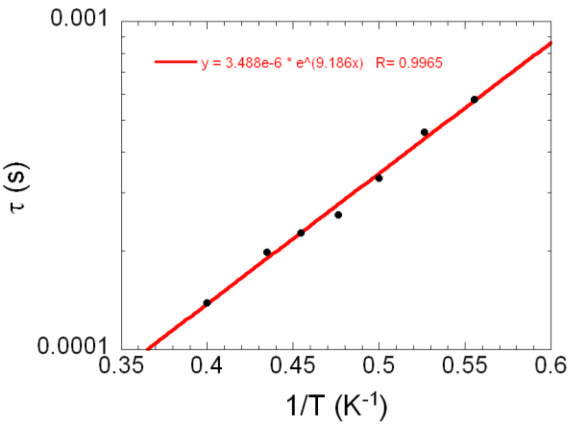

Figure 3.34. Plot of relaxation time τ versus reciprocal temperature T^{-1}: a linear dependency is observed which is quantified by the pre-exponential factor τ_0 providing the slope.

In summary, both static and dynamic magnetic properties of **9** have been studied, whereby the course of the χT product as a function of temperature features **9** to be a ferromagnetic cluster compound. The appearance of slow relaxation of the magnetization below a temperature of 8 K may be attributed to **9** being a SMM.

3.2.7 Luminescence of $[Tb_{15}(\mu_3\text{-}OH)_{20}(PepCO_2)_{10}(Ph_2acac)_{10}Cl]Cl_4$ (8)

IN COOPERATION WITH

PROF. DR. STEFAN BRÄSE AND DR. BIRGIT RUDAT, LIGHT TECHNOLOGY INSTITUTE, KARLSRUHE INSTITUTE OF TECHNOLOGY

Since Tb^{3+} amongst the chosen rare earth metal series exhibits characteristic electronic transitions mediating luminescent emission in the visible range of the electromagnetic spectrum, we sought to investigate the photophysical properties of compound **8**. For this purpose, absorption spectroscopy of compound **8** in dry THF revealed an absorption band at λ = 354 nm indicating a $\pi \rightarrow \pi^*$-transition of the ligands' aromatic moieties. Excitation of this transition with a wavelength of 350 nm effectuated Tb^{3+}-specific fluorescence emissions at λ = 490 nm ($^5D_4 \rightarrow {}^7F_6$), 546 nm ($^5D_4 \rightarrow {}^7F_5$), 585 nm ($^5D_4 \rightarrow {}^7F_4$) and 613 nm ($^5D_4 \rightarrow {}^7F_3$) *via* ligand-to-metal charge transfer (LMCT) (Fig. 4a).[11b, 11d] LMCT, which is colloquially also described as "*antenna effect*", depicts a well-established energy transfer mechanism for circumventing the Laporte-forbidden *f*-*f*-transitions by excitation of the organic ligands instead of the rare earth metal atoms, since the latter approach would end up in comparably low quantum yields.[11a-d], [78] Unlike direct excitation of lanthanide ions, LMCT implies an excitation of the organic ligands (in our case $\pi \rightarrow \pi^*$-transitions) with an appropriate excitation wavelength to promote the ligand from its ground state S_0 into vibronic levels of its first excited state S_1, which is in most cases a singulet state. After reaching the ground state of the S_1 state *via* non-radiative internal conversion, the excited electron accomplishes a transition into an energetically more favourable triplet state *via* inter system crossing (ISC). To be efficient, this transition requires an energy difference of approximately 5000 cm^{-1} between the singlet and the triplet state. The triplet state serves as donor level for the energy-migration path from the ligand to the rare earth metal atom's first excited state. Thus, an energy transfer from this triplet state to a suitable acceptor level of the metal atom's excited state has to be the predominant transition for mediating efficient LMCT. As energy back-transfer and other non-radiative relaxation paths depict competing excited state-deactivation mechanisms, this last transition represents the rate-determining step of this process. Finally, a rare earth metal-mediated emission may then induce the desired luminescence.[11d]

Although the 546 nm band was the most intense one (Fig. 3.35a), we could not observe any green colour *via* visual inspection, as reported for similar compounds in recent articles.[11b] However, when switching to time-resolved luminescence spectroscopy, a striking predominance of the 613 nm emission band was observed, whereas the other emissions bands mentioned almost disappeared in the noise signal (Fig. 3.35b). As this wavelength can be associated with an orange colour, this appearance is consistent with the observed colour of a solid sample of **8** when irradiated with the long-wave range (365 nm) of a commercial UV lamp. As a consequence, we exclusively focused on time-resolved luminescence experiments for all following measurements, and a screening of the luminescence intensity of different concentrations of compound **8** clearly gave evidence for a linear dependency of intensity and concentration, as expected (Fig. 3.35c,d).

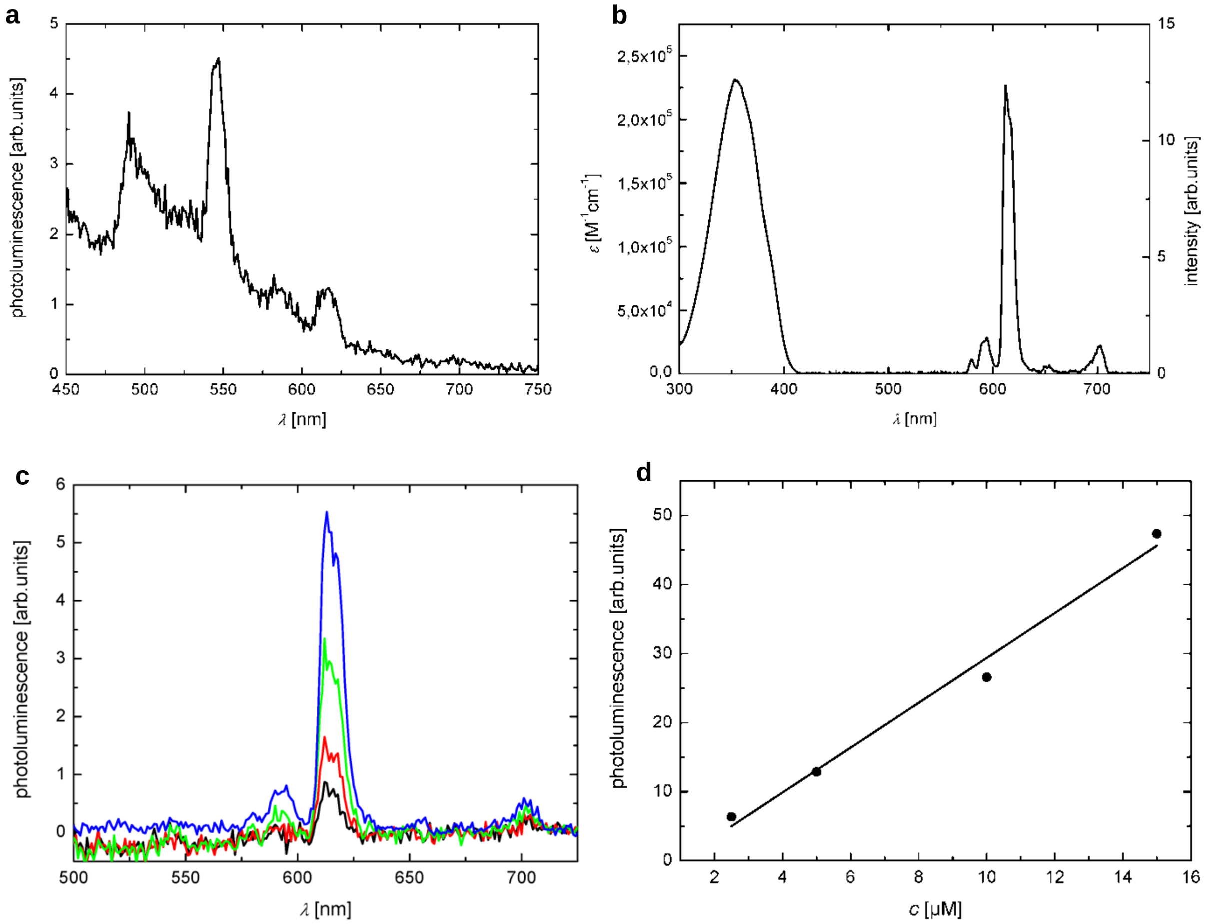

Figure 3.35. a) Luminescence intensity of **8** as a function of detection modus and concentration. Noisy fluorescence spectrum of 50 μM THF solution of **8** and b) corresponding time-resolved emission spectrum including absorption band. c) Comparative time-resolved emission spectra of **8** in THF with concentrations 2.5 μM, 5.0 μM, 10 μM and 15 μM; d) corresponding plot of photoluminescence versus concentration.

It is well-known that high energy stretch vibrations of *e.g.* O-H and C-H groups generally decrease luminescence intensity due to quenching effects.[11b, 11d, 41b] To avoid this effect at least within the solvent used, a 50 μM solution of compound **8** in THF-d_8 was exposed to the same spectroscopic conditions. The extinction coefficients ε of the solution with equi-concentrated non-deuterated THF solutions were higher ($\varepsilon_{\mathrm{THF}}$ = 230000 ± 8000 $\mathrm{M^{-1}cm^{-1}}$) compared to the deuterated ones ($\varepsilon_{\mathrm{THF}\text{-}d8}$ = 54000 ± 2000 $\mathrm{M^{-1}cm^{-1}}$), however, in concomitance with a much stronger emission intensity of the orange 613 nm band when irradiated with λ = 350 nm. Irradiation with λ = 400 nm caused an inverse relation, *i.e.* the emission of the terbium cluster solution with non-deuterated THF gave a slightly more intense emission than the one with the deuterated THF (Fig. 3.36).

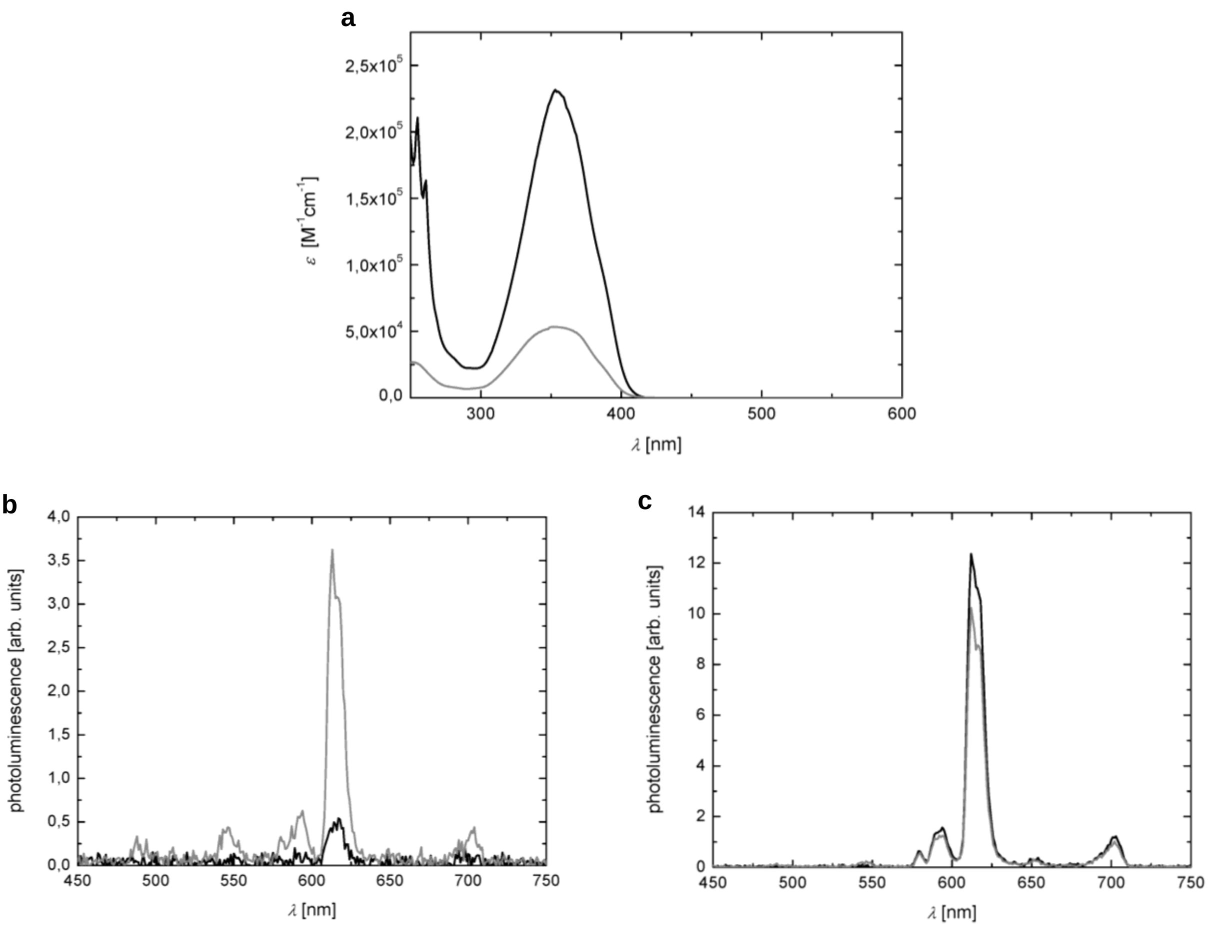

Figure 3.36. a) Time-resolved absorption and emission spectra of compound **8** in THF (black) and in THF-*d*$_8$ (grey). Comparative absorption spectrum of solutions of **8** (50 µM) with THF-*d*$_8$ and non-deuterated THF. Corresponding emission spectra with excitation wavelengths b) λ = 350 nm and c) λ = 400 nm.

Owing to the rare case of the targeted stimulation of this emission in the orange range of Tb^{3+} complexes, further investigations on the relaxation behaviour from the excited $^5D_4$ state into the $^7F_3$ ground state appeared promising. This aspect increases the photophysical impact of compound **8**, because usually the LMCT-stimulated transition from the excited $^5D_4$ state into the $^7F_5$ ground state giving green luminescence (λ = 545 nm) is in most cases favoured and thus much more common. The predominant emission band at λ = 613 nm detected in the time-resolved experiments gave thus rise for lifetime measurements with both the cluster solutions with deuterated and non-deuterated THF solutions (excitation wavelength λ = 400 nm). The sample in THF-*d*$_8$ showed a lifetime of τ = 0.356 ± 0.004 ms, which is roughly 10 % longer than in the non-deuterated THF solution being τ = 0.335 ± 0.003 ms (Fig. 3.37). This experimental observation is in good agreement with the proportionality between luminescence intensity and quantum yield, since a longer lifetime is generally indicative for a stronger luminescence intensity and, hence, quantum yield as well. As the latter dimension could not be determined in an absolute fashion, the presented data merely depict a relative comparison with respect to luminescence intensities and thus the quantum yield itself. That is why these results allow a comparatively qualitative evaluation of the terbium cluster's luminescence intensity as a function of both THF deuteration and concentration.

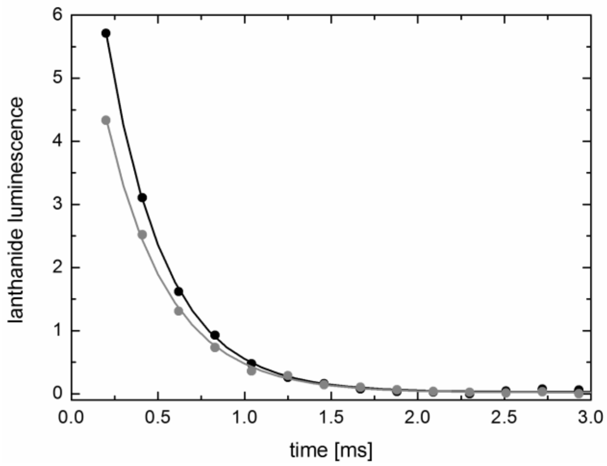

Figure 3.37. Comparative lifetime measurements for emission band at 613 nm of compound **8** in THF (black) and THF-d_8 (grey).

In summary, luminescence investigations with Tb-cluster **8** have revealed its propensity to provide LMCT-induced photoluminescence. The combination of the three ligands (μ_3-OH, Ph_2acac and $PepCO_2$) and the coordination geometry of Tb^{3+}-ions as a result of the structural motif obtained in **8** have facilitated a favoured feeding of Tb^{3+}'s excited state $^5D_4$ to preferably relaxate into its $^7F_3$ ground state. This has shown to provide the rare case of orange photoluminescence at 613 nm, as proven *via* time-resolved emission spectra. Moreover the absence of solvent-based high-energy C-H-stretch vibrations in THF-d_8 has confirmed to avoid quenching of the photoluminescence observed. Higher luminescence intensities and longer lifetimes of excited states compared to usage of non-deuterated THF have reflected this issue.

3.2.8 *In Vitro* Investigations of $[Ln_{15}(\mu_3\text{-}OH)_{20}(PepCO_2)_{10}(Ph_2acac)_{10}Cl]Cl_4$ (7-9)

IN COOPERATION WITH

DR. UTE SCHEPERS, INSTITUTE FOR TOXICOLOGY AND GENETICS, KARLSRUHE INSTITUTE OF TECHNOLOGY

Obviously there is a large gap in size between well defined mononuclear metal complexes and polynuclear nanoparticles. The size of the latter can only be controlled within a certain limit leading to particle size distribution and not less defined structures. Between these two extremes oligonuclear clusters are positioned, which are much larger than mononuclear compounds and have a well defined size and composition.[29a, 79] Unlike nanoparticles, these particular characteristics simplify the study of function and properties of these cluster compounds. To the best of our knowledge oligonuclear clusters of the rare earth metals have hitherto not been used for any biological application. Based on this consideration we were interested in synthesizing rare earth metal based clusters having suitable luminescent properties for various *in vitro* experiments. To reach this goal, the anchoring of a cell penetrating agent onto a structurally well defined rare earth metal cluster is necessary. As previously mentioned chapter 3.2, the peptoid ligand $PepCO_2$ was originally developed and designed for accessing cellular systems. Thus, within this project cluster compounds **7-9** ought to represent a species which unifies rare earth metals' valuable photophysical properties and peptoid ligand's biorelevant chemical properties to provide novel bioaccessible and – compatible structures on the molecular scale.

For all the *in vitro* experiments described in this chapter, the procedures necessary for enquiries and colocalization studies were conducted following a certain scheme applying a 5 % CO_2 atmosphere and a temperature of 37 °C: these humane Cervix carcinoma cells are cultivated to adherend confluence in DMEM (Dulbecco's Modified Eagle Serum) upon treatment with individual amounts of foetal calf serum (FCS; 10 %), penicillin (100 units/mL) and streptomycin (100 μg/mL). Then the cells are washed with PBS (phosphate buffered saline) and coated with a trypsin/EDTA solution (trypsin: 0.025 %; EDTA: 0.01 %). For the live imaging experiments, 10,000 of the pretreated cells are sown in 200 μL DMEM/FCS in a wall of a suitable chamber slide and then incubated with certain amounts of clusters **7**, **8** or **9** to afford the individual concentrations. The incubated cells are washed with DMEM for several times to subject them to confocal fluorescence microscopy experiments. Therefore, photophysical excitation of the incubated cells occurred by irradiation with both a UV argon laser and a white laser with $\lambda = 368$ and/or 405 nm, whereupon emission was enquired within various wavelength ranges, with or without delay.

Upon treatment of HeLa cells with clusters **7-9**, confocal live imaging experiments have revealed an internalization process of the clusters into the cells, although only little amounts could enter the cells due to their low solubility in aqueous media (exemplified for yttrium cluster **7** in Fig. 3.38). The HeLa cell is a cell type in an immortal cell line amongst which it depicts one of the oldest and most commonly used human cell lines.[80]

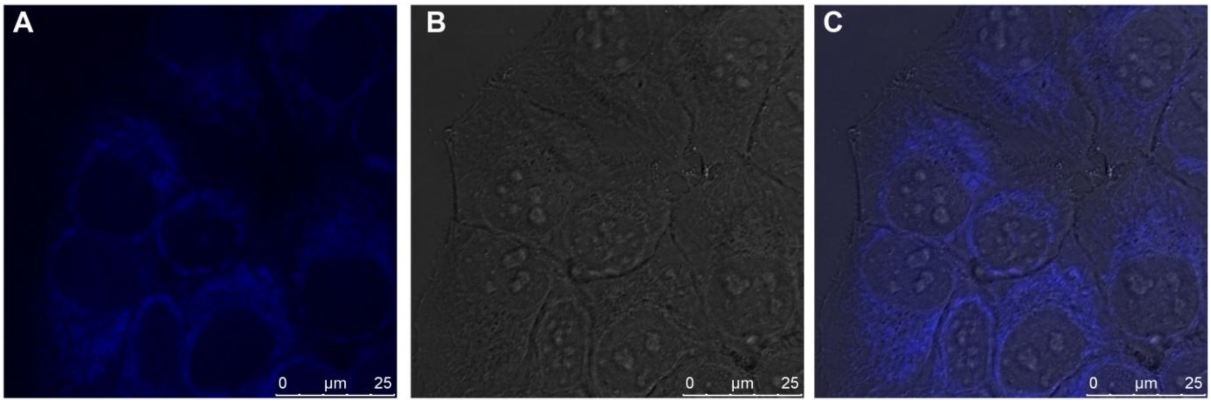

Figure 3.38. Images of HeLa cells incubated with Y-cluster **7**. Incubation of cells occurred with 1 µM of **7** for 24 hours. Excitation was carried out with different lasers (λ = 368 and 405 nm), emission bandwidth ranged from λ = 384 to 476 nm. The left image (box A) shows the UV fluorescence, the middle one (box B) the phase contrast and the right one (box C) the overlap of both.

However, when increasing the cluster concentration above 10 µM, the limited solubility in water results in formation of undesirable plates and crystals (exemplified for cluster **9** in Fig. 3.39). The cell-derived fluorescence shows to exhibit rather low intensity compared to that of the crystals formed. Additionally, Figure 3.39 obviously reveals a favoured enrichment of cluster 9 in the endoplasmatic reticulum. Within comparative experiments, this has also been shown to be valid for yttrium cluster 7.

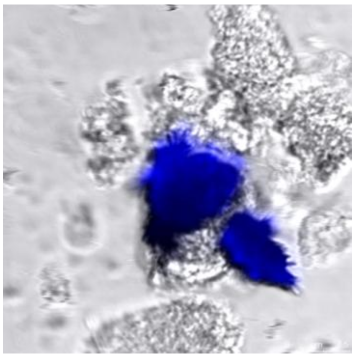

Figure 3.39. Images of HeLa cells incubated with Dy-cluster **9**, showing formation of plates and crystals (deep blue spot). Incubation of cells occurred with 10 µM of **9** for 24 hours. Excitation was carried out with different lasers (λ = 368 and 405 nm), emission bandwidth ranged from λ = 384 to 476 nm.

As expected, excitation of **7** with a UV laser (λ = 368 nm) effectuates a bathochromic shift of emission, *i.e.* to higher wavelengths (λ = 482-571 nm; this range was also observed for **9**) (Fig. 3.40).[81] The luminescence of the yttrium based cluster **7** is much more intense compared to the terbium and dysprosium analogues **8** and **9**; and it already glares dark blue when irradiated with a fluorescent lamp. Thus, the light yield of **7** is strikingly higher than for **8** and **9**, however, the clusters' general low solubility in aqueous media induces precipitation inside the cells which is associated with an enhanced toxicity, in particular when exceeding concentrations of 10 μM.

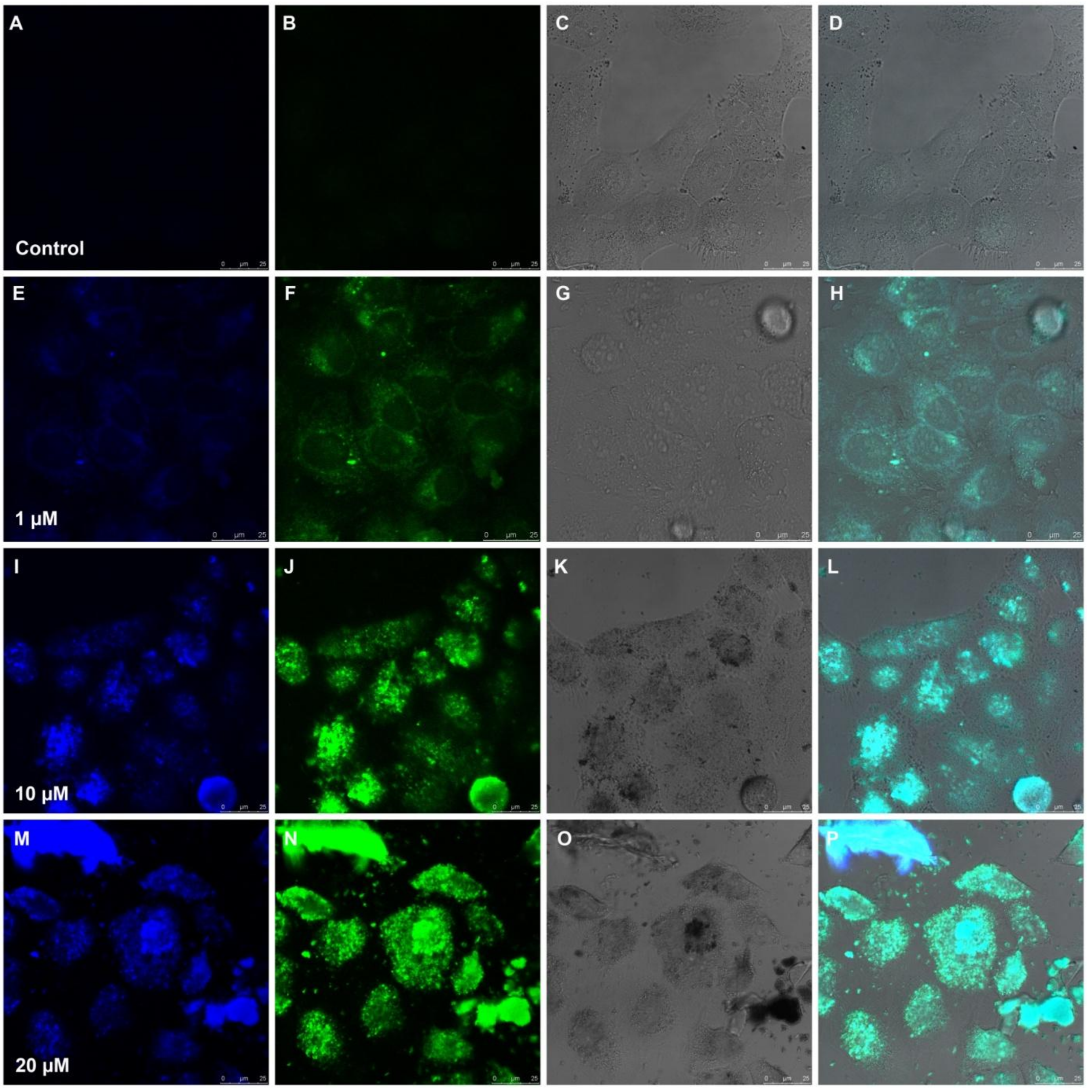

Figure 3.40. Images of HeLa cells incubated with different concentrations of cluster **7**. Laser excitation occurred with λ = 368 nm; treatment with 0 μM (boxes A-D; control, *i.e.* blank test), 1 (boxes E-H), 10 (boxes I-L) and 20 μM (boxes M-P) of **7**. The left column (boxes A, E, I and M) presents the emission enquiry ranging from λ = 380-474 nm, the second column (boxes B, F, J and N) presents the emission enquiry ranging from λ = 482-571 nm, the third column (boxes C, G, K and O) presents the phase contrast and the right column (boxes D, H, L and P) the overlap of the former two emission ranges.

The luminescence of terbium cluster **8** comprises a wider range of wavelengths (λ = 482-696 nm), and in contrast to **7** and **9**, it is enriched in both the cytosol and cell nucleus (Fig. 3.41).

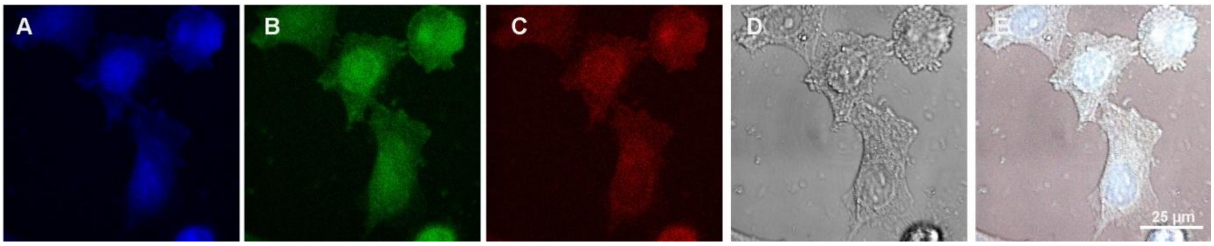

Figure 3.41. Images of HeLa cells incubated with cluster **8**. Laser excitation occurred with λ = 368 nm. The left box A presents the emission enquiry ranging from λ = 380-474 nm, the second box B presents the emission enquiry ranging from λ = 499-552 nm, the third box C presents the emission enquiry ranging from λ = 581-696 nm, whereby the fourth box D shows the phase contrast and the right box E shows the overlap of the former three emission ranges.

Since the terbium cluster **8** has shown to provide orange luminescence with a stimulated emission band at λ = 613 nm when irradiated with λ = 350 or 400 nm (cp. 3.1.2.7), we sought to underline this issue within these *in vitro* investigations by time-resolved luminescence measurements. Therefore, the detection of incubated cells' luminescence emission was accomplished with a delay of three minutes after laser excitation with λ = 368 nm. Figure 3.42 clearly underlines this assumption when comparing **8** (bottom row) with **7** and **9** (second and third row). The deep red colour in the emission range λ = 581-696 nm depicted in Box M again gives evidence for a long-living excited $^5D_4$ state of the Tb^{3+} atoms in **8** before favourably relaxing into their $^7F_3$ ground state upon emission of orange luminescence (λ = 613 nm).

Thus, such terbium cluster species seem to be appropriate compounds for giving accurate and locally well resolved localization images of cluster-incubated cellular systems *via* confocal fluorescence microscopy in this section of the electromagnetic spectrum.

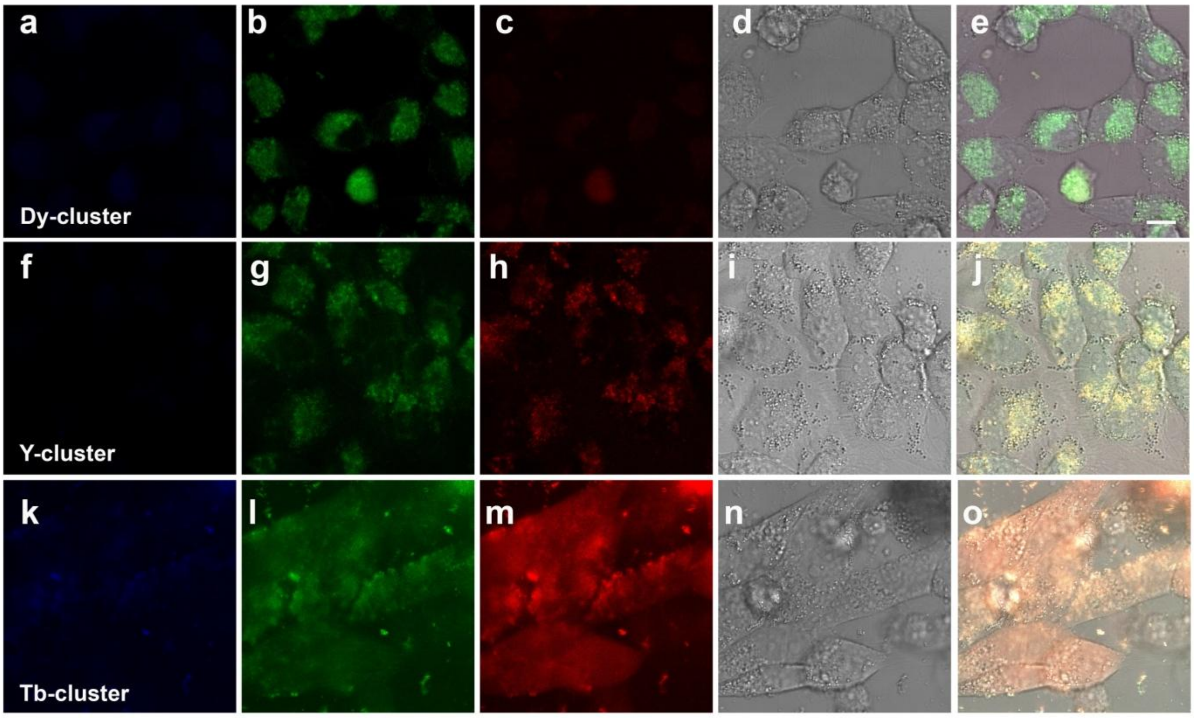

Figure 3.42. Comparative images of HeLa cells incubated with clusters **7**-**9**. Laser excitation occurred exclusively with $\lambda = 368$ nm, and the individual emissions were enquired with a delay of three minutes. The left column (boxes A, F and K) presents the emission enquiry ranging from $\lambda = 380$-474 nm, the second column (boxes B, G and L) presents the emission enquiry ranging from $\lambda = 499$-552 nm and the third column (boxes C, H and M) presents the emission enquiry ranging from $\lambda = 581$-696 nm; the fourth column (boxes D, I and N) shows the phase contrast of each row and the right column (boxes E, J and O) shows the overlap of the former three emission ranges for one cluster each.

As a logic continuative experiment, we strived for proving the retention of the clusters' shape in aqueous cellular media, *i.e.* to show that the luminescence detected within the previous live imaging experiments *de facto* arises from the dissolved cluster species. For this purpose, the cell walls of the incubated cells were destroyed by ultrasonication, and the residual lysis was used to perform ESI-MS measurements, in analogy to chapter 3.2.3.

Unfortunately, the presence of intact clusters in cellular media could hitherto not be evidenced, *i.e.* the expected signals of the above discussed dianionic species **7a**-**9a** were not observed in the corresponding ESI-MS spectra. On the one hand, this aspect may be attributed to very low cluster concentrations in the lysis isolated, which might be underneath the lower detection limit of the apparatus. That means the sensitivity of the ESI-MS device is not high enough leading to a signal-noise ratio which makes the identification of potential cluster compounds impossible. Targeting to explore the technical limitations of the ESI-MS apparatus with respect to its sensitivity, a dilution series of yttrium cluster **7** in ethanol was prepared. This series of measurement has revealed that the threshold of sensitivity is reached when going below a concentration of 20 μM, which clearly exceeds the maximum cluster concentration of 10 μM acceptable for live imaging experiments (see above).

Thus, four instances may be summed up as follows: firstly, only a certain molar fraction of the clusters is dissolved to be activated for internalization; secondly, only another molar fraction of cluster is accessed by the cell for internalization; thirdly, the precipitation of cluster after internalization reduces the effective dissolved compound to another extent and fourthly, the sensitivity of the ESI-MS apparatus used is not sufficient for detecting cluster concentrations below 20 μM. As a result of the former three instances, the effective cluster concentration in the final lysis might be in the lower nanoscale or even below. Within further experiments, the summation of these effects might be investigated and quantified by time-resolved luminescence measurements by using the corresponding luminescence benchmarks defined in chapter 3.2.7.

On the other hand, the case of cluster decomposition upon dissolution in cellular media might appear as a realistic scenario, since no evidence can be given for the presence of any intact clusters inside the cells. In this case, a partial or even complete degradation in the cell serum may be assumed, perhaps with differing rate constants when comparing cluster **7** and **9** with cluster **8**. The latter suggestion is based on the different compartments in which the clusters have shown to enrich. This aspect might be indicative for higher or lower rate constants of degradation, when comparing the spots of enrichment of cluster **8** to those of **7** and **9**. After all, a certain cluster fragment bearing more or less organic ligands ought to be accepted by different cellular compartments.

Based on these results, the necessity of cluster compounds exhibiting a better solubility in aqueous media has arisen. Furthermore, the dissociation process would have to demonstrably occur in a non-destructive fashion. An increase of the water solubility is inevitably associated with a higher polarity of the clusters' periphery, *i.e.* having polar functional groups like *e.g.* alkoxy-, nitro or ester functionalities at their peripheral parts might present an attractive alternative. With regard to the peptoid ligand used in particular, a controlled cleavage of the *tert*-butyloxycarbonyl moieties would release ten unprotected amine functionalities. This would effectuate a strong increase of the cluster's overall polarity due to the absence of ten peripherally positioned unpolar *tert*-butyl groups. In addition, the modified cluster periphery would generally gain a higher degree of bioacceptance, as previously shown for related oligopeptoids bearing unprotected primary amine functions.

3.2.9 First Attempts to Deprotect the Amine Functionalities of 7

Beyond the previously discussed aim to maximize the bioaccessibilty and –compatibility, the controlled and quantitative deprotection of the peripheral primary amine functionalities also ought to depict strategic points of continuative experiments and chemical transformations. The possible scope of continuative chemical transformations is almost infinite, it ranges from the generation of new peptide bonds, the preparation of cluster based Schiff bases *via* condensation reaction with aldehydes or ketones to *e.g.* utilization as donor synthons for manifold nucleophilic conversions with various suitable acceptor synthons. The alignment of the amine functionalities reminds of an amphora offering a well defined cavity which even might facilitate fixation of *e.g.* certain transition metal atoms for the generation of novel heterobimetallic cluster compounds.

In a first attempt to deprotect the aforementioned amine functionalities, a standard protocol using TFA (TFA = trifluouroactetic acid) was applied.[82] This Brønsted-acidic cleavage of the *tert*-butyloxy moieties is accompanied by an intense gas formation, as this moiety is cleaved upon release of *iso*-butylene and carbon dioxide. When performing this reaction in either TFA, a 1:1 vol.-ratio of TFA and dichloromethane (CH_2Cl_2) or a 1:1 vol.-ratio of TFA and methanol, this gas evolution could be clearly observed. However, after working up the reaction mixture, needle-shaped single crystals of neutral dibenzoylmethane (Ph_2acacH) were reisolated (Scheme. 3.5). This issue signifies TFA to be too Brønsted-acidic for selectively and exclusively deprotecting the amine functions, resulting in an undesired protolytic cleavage of one of the supporting ligands.

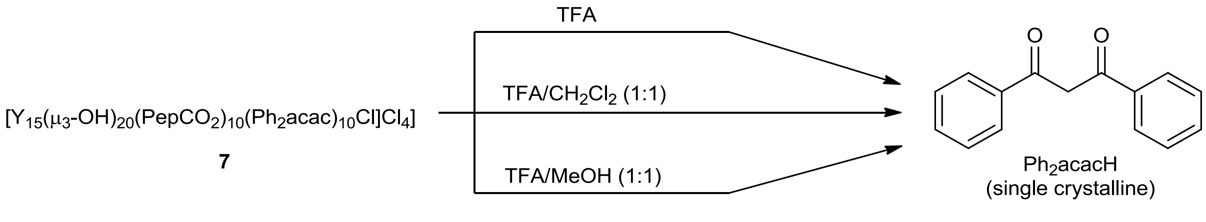

Scheme 3.5. Attempted deprotection of yttrium cluster **7** with TFA in different media.

We also attempted to induce the amine functionalities' deprotection in a kind of inverse fashion, *i.e.* by using a Brønsted-basic instead of a Brønsted-acidic deprotection agent. Therefore TBAF (tetrabutylammonium fluoride) appeared as another option for reaching this synthetic target. Although this agent is rather Brønsted-basic, the cleavage mechanism has been reported to be very similar to that of TFA, but arising from a different initial step. As described in the according literature procedure, the reaction was carried out in THF with a tenfold excess of TBAF (Scheme 3.6).[83] Again, the expected gas evolution could be unambiguously observed. Different work-up procedures could not afford the desired single crystals of the unprotected compound, however, ^1H NMR experiments of the “crude product” clearly revealed the absence of the *tert*-butyl group. This has given evidence for a reaction course which seems to proceed in the favourable way at least in part.

$$[\mathrm{Y_{15}(\mu_3\text{-}OH)_{20}(PepCO_2)_{10}(Ph_2acac)_{10}Cl]Cl_4} \xrightarrow{\text{TBAF/THF}} ? + \text{gas evolution}$$

7

Scheme 3.6. Attempted deprotection of yttrium cluster **7** with TBAF in THF.

Despite the limited success with regard to these first deprotection experiments, there are still much further different methods known in literature for deprotecting *tert*-butyl carbamates remaining to be attempted later on. These methods include utilization of deprotection reagents ranging from sodium carbonate (Na_2CO_3),[84] ceric ammonium nitrate (CAN),[85] a ceric trichloride heptahydrate-sodium iodide coupled system ($CeCl_3(H_2O)_7 \cdot NaI$),[86] sodium *tert*-butoxide (NaO*t*Bu),[87] formic acid[88] and tin(II)triflate ($Sn(OTf)_2$)[89] to anhydrous TBAF.[90] Future experiments will hopefully reveal one of these methods to be suitable for a quantitative and selective deprotection of clusters’ carbamate functionalities in a non-destructive fashion.

3.3 Nonanuclear Rare Earth Metal Hydroxy Clusters

3.3.1 Cluster nuclearity as a function of ligand's steric demand

In chapter 3.1 it was shown that the nuclearity of a rare earth metal hydroxy cluster is decisively influenced by the ionic radius of the rare earth metal atom.[37, 41c, 41f] However, in some cases the individual work-up procedures revealed an intriguing variability with respect to reaction of a certain rare earth metal atom with a certain supporting ligand. For example, reaction of europium trichloride hexahydrate [$EuCl_3 \cdot (H_2O)_6$] with PhacacH and NEt_3 in methanol gave a pentanuclear species when working up the reaction's precipitate,[41b] or a tetranuclear species when working up the reaction's filtrate.[41g] This issue is certainly due to low energy differences between different coordination numbers and geometries of the rare earth metals in general.[1] Furthermore, the steric demand of ligands (*here*: only β-diketonates and β-ketoesterates are compared with each other) has also an influence on the clusters' nuclearities, since the ligands' side groups provide a different degree of steric crowding. This aspect is associated with a different coordinative saturation of the rare earth metal atoms, allowing a different number of ligands to coordinate to each rare earth metal atom.

For example, when substituting the Ph_2acac ligand bearing two bulky phenyl residues by a sterically less demanding β-ketoesterate ligand allyl acetylactetate (aacac) or ethyl acetoacetate (acacOEt), the corresponding nuclearity is increased from five to nine upon linking of two vertex-sharing square pyramidal moieties (Fig. 3.43).[11c, 41a] The same structural motif could also be obtained by using the β-diketonate benzoylacetonate[91] (BA) or acetylacetatonate (acac).[92] However, when using β-diketonate acac and modifying the reaction conditions, a tetradecanuclear cluster exhibiting four square pyramids is generated, whereby these pyramids are attached to each other by either sharing their basal faces or their vertices (as described above with *o*-nitrophenolato ligand).[42a]

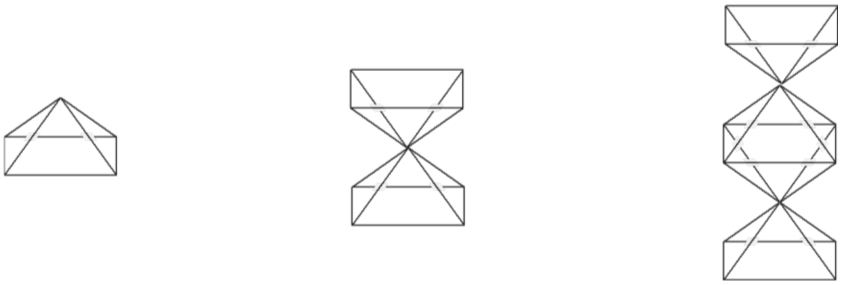

$[Ln_5(\mu_4\text{-}OH)(\mu_3\text{-}OH)_4(Ph_2acac)_{10}]$ $[Ln_9(\mu_4\text{-}O)_2(\mu_3\text{-}OH)_8(aacac)_{16}]^-$ $[Ln_{14}(\mu_4\text{-}OH)_2(\mu_3\text{-}OH)_{16}(acac)_{24}]$

Figure 3.43. Fusion of square pyramidal units. Decrease of ligands' steric demand generates clusters of higher nuclearity, *i.e.* the Ph_2acac ligands induces formation of a pentanuclear cluster (left), the aacac ligands induces formation of a nonanuclear cluster (middle) and the acac ligand induces formation of a tetradecanuclear cluster (right).

3.3.2 Synthesis of $[Ln_9(\mu_4\text{-}O)(\mu_4\text{-}OH)(\mu_3\text{-}OH)_8(acacOEt)_{16}]$ (10-12)

Keeping these nonanuclear structures and the desire to generate new SMMs and NIR-emissive materials in mind, we urged to prepare corresponding cluster compounds in which the positions of the metal atoms are occupied by rare earth metal atoms exhibiting certain magnetic and photoelectronic properties.

Targeting to broaden the scope of application of these nonanuclear compounds, we reacted the trichloride hexahydrates of yttrium, neodymium and dysprosium with ethyl acetylacetate (acacOEtH) and sodium hydroxide to give the nonanuclear cluster compounds $[Ln_9(\mu_4\text{-}O)(\mu_4\text{-}OH)(\mu_3\text{-}OH)_8(acacOEt)_{16}]$ (Ln = Y (**10**),[41a] Nd (**11**), Dy (**12**)) (scheme 3.7).

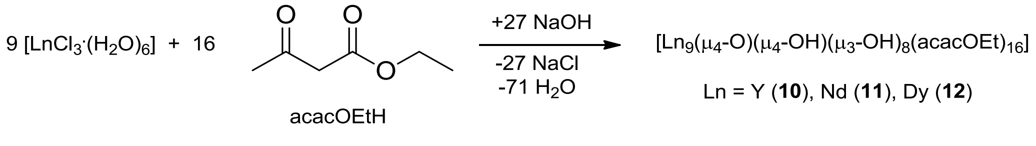

Scheme 3.7. Synthesis of nonanuclear clusters $[Ln_9(\mu_4\text{-}O)(\mu_4\text{-}OH)(\mu_3\text{-}OH)_8(acacOEt)_{16}]$ with Ln = Y (**10**), Nd (**11**), Dy (**12**).

The clusters have been characterized by standard analytical and spectroscopic techniques, and the solid state structures of all compounds were established by single crystal X-ray diffraction (Fig. 3.44).

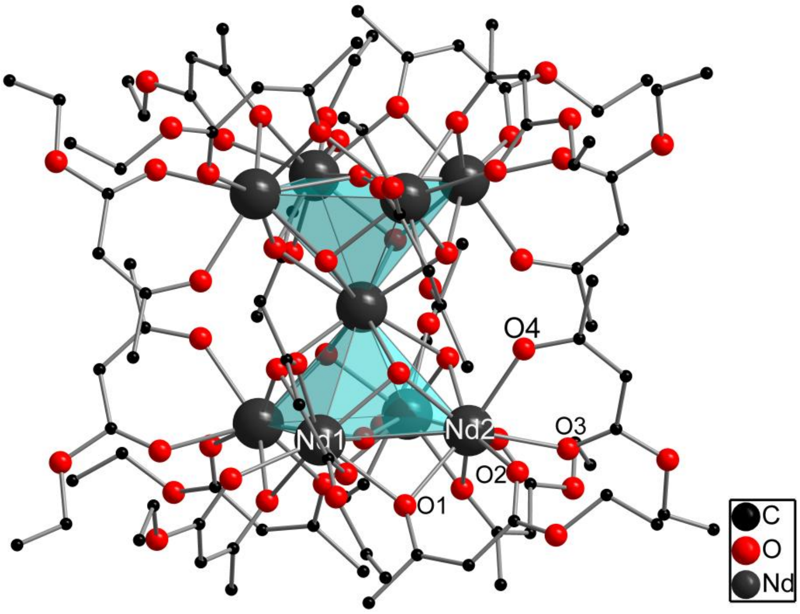

Figure 3.44. Perspective view of the molecular structure of [$Ln_9(\mu_4\text{-}O)(\mu_4\text{-}OH)(\mu_3\text{-}OH)_8(acacOEt)_{16}$] exemplified for **11**. Clusters **10** and **12** are isostructural to **11**. Hydrogen atoms are omitted for clarity. Selected distances [Å] and angles [°]for **10**-**12**: **10** (Ln = Y): Y1-O1 2.342(14), Y2-O1 2.355(14), Y2-O2 2.305(13), Y2-O3 2.339(13), Y2-O4 2.238(13); Y1-O1-Y2 98.3(4), O1-Y2-O2 71.1(4), O3-Y2-O4 76.3(4); **11** (Ln = Nd): Nd1-O1 2.483(9), Nd2-O1 2.485(8), Nd2-O2 2.443(9), Nd2-O3 2.389(9), Nd2-O4 2.359(8); Nd1-O1-Nd2 97.2(3), O1-Nd2-O2 68.9(3), O3-Nd2-O4 72.1(3); **12** (Ln = Dy): Dy1-O1 2.410(4), Dy2-O1 2.408(5), Dy2-O2 2.373(5), Dy2-O3 2.327(5), Dy2-O4 2.302(4); Dy1-O1-Dy2 96.00(2), O1-Dy2-O2 70.4(2), O3-Dy2-O4 73.6(2).

3.3.3 Structure discussion on [$Ln_9(\mu_4\text{-}O)(\mu_4\text{-}OH)(\mu_3\text{-}OH)_8(acacOEt)_{16}$] (10-12)

The scaffold of the nonanuclear cluster compounds is made up by two square pyramidally shaped {$Ln_5(\mu_4\text{-}O/OH)\ (\mu_3\text{-}OH)_4$}$^{9+/10+}$ moieties (cp. 3.1.4.2) (Fig. 3.45a), which are fused with each other by sharing their apical rare earth metal atoms (Fig. 3.45b). In the resulting double pyramid the two square faces are parallel to each other, and they adopt a staggered conformation providing D_{4d} symmetry. Thus the centrally arranged apical rare earth metal atom is surrounded by the residual eight basal rare metal atoms and occupies the cavity of a square antiprism. Owing to the μ_3-hydroxy groups being positioned very centred above the corresponding triangular faces, they also display a square antiprismatic polyhedron around the apical rare earth metal atom. Thus the apical rare earth metal atom has a coordination number of eight. Eight out of the sixteen acacOEt ligands chelate one basal rare earth metal atom in η^2-modus each. The residual eight acacOEt ligands also chelate one basal rare earth metal atom each, whereby one ketonate oxygen atom is simultaneously bridging the chelated metal atom with an adjacent basal atom resulting in $\mu\text{-}\eta^2$-mode (Fig. 3.45c). Thus, the basal rare earth metal atoms also exhibit a coordination number of eight, and again the eight donating oxygen atoms are square antiprismatically arranged around each of these rare earth metal atoms.

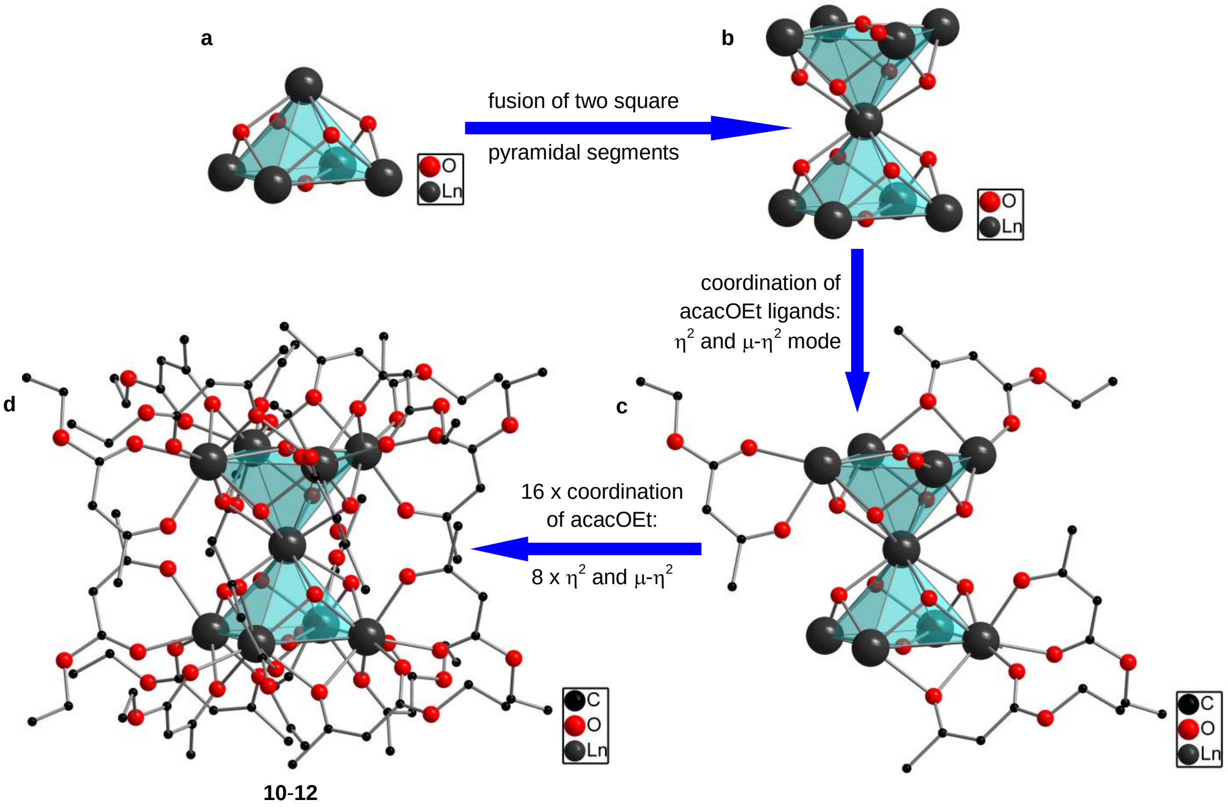

Figure 3.45. Genesis of nonanuclear clusters [$Ln_9(\mu_4\text{-}O)(\mu_4\text{-}OH)(\mu_3\text{-}OH)_8(acacOEt)_{16}$] **10-12** and trilogy of square antiprisms. a) Two square pyramidal units are fused to give the b) nonanuclear double pyramid. c) Ligands are η^2- and μ-η^2-coordinated to d) give **10-12** with eight of each.

At first, the final sum formula could not be confirmed confidently, since the required electroneutrality can initially not be fully guaranteed. This is due to the fact that one μ_4-oxygen atom would have to be an oxo ligand and the other one would have to be a hydroxy ligand to neutralize the whole cluster. However, since the two μ_4-oxygen atoms are not crystallographically distinguishable as there is only one μ_4-oxygen atom in the asymmetric unit, the second one is generated by translational symmetry operations given by the crystal system (cubic) and the space group ($Pn\bar{3}n$). Thus, the chemical nature of both μ_4-oxygen atoms is identical, and, hence, a distinction derived by different distances with respect to the capped square faces becomes irrelevant. In the literature, there are three nonanuclear clusters [$Ln_9(\mu_4\text{-}O)_2(\mu_3\text{-}OH)_8(Phacac)_{16}$]$^-$ (Ln = Sm, Eu, Gd, Dy, Er; Phacac = benzoylacetonate),[91] [$Y_9(\mu_4\text{-}O)_2(\mu_3\text{-}OH)_8(aacac)_{16}$]$^-$ (aacac = allyl acetylacetate)[41a] and [$Y_9(\mu_4\text{-}O)_2(\mu_3$-

$OH)_8(acacOEt)_{16}]^{-[41a]}$ reported, which were found to be monoanionic, assuming the presence of two μ_4-oxo ligands. This statement was more or less unambiguously underlined by the presence of countercations $[HNEt_3]^{+[91]}$ or $[Na(EtOH)_6]^{+[41a]}$ in the unit cells. On the other hand, one nonanuclear cluster $[Ln_9(\mu_3\text{-}OH)_{10}(acac)_{16}]^-$ has been reported which was found to be monocationic, since a suitable counteranion $[HCr_2(CO)_{10}]^-$ could be assigned in the unit cell.[92] The monocationic nature of this cluster scaffold unambiguously implies the presence of two μ_4-hydroxy ligands. In the present structures, however, there was not sufficient residual electron density in the unit cell left to be assigned to any kind of either a countercation or a counteranion. When Petit *et al.* were once confronted with the same structural problem, they attributed the absence of any counterions to the presence of one disordered hydroxy proton, which is formally bound to both μ_4-oxygen atoms with a site occupancy factor (s.o.f.) of 0.5 each.[11c] This approach allows these nonanuclear compounds to be described as neutral species, giving rise for the justifiable assumption to consider clusters **10-12** as neutral compounds. Thus, we adopted this viewpoint and accepted the sum formula $[Ln_9(\mu_4\text{-}O)(\mu_4\text{-}OH)(\mu_3\text{-}OH)_8(acacOEt)_{16}]$.

In addition, this assignment could be underlined *via* exemplified ESI-MS spectra of dysprosium compound **12** from methanol in the positive mode. In this spectrum, a predominant signal of a monocationic species providing the expected isotope pattern at *m*/*z* = 3698.6 was observed. Since the previously postulated sum formula $[Dy_9(\mu_4\text{-}O)(\mu_4\text{-}OH)(\mu_3\text{-}OH)_8(acacOEt)_{16}]$ is ascribed to a molar mass of 3697.91 g/mol, the detected signal of this monocationic species might be attributed to a single protonation of **12** upon dissolution to give $[H\{Dy_9(\mu_4\text{-}O)(\mu_4\text{-}OH)(\mu_3\text{-}OH)_8(acacOEt)_{16}\}]^+$ **12a**, whereby the necessitated proton might originate from methanol (Fig. 3.46). However, this assignment remains a vague assumption, as the data do not give the final evidence.

Furthermore, two further signal sets are observed in vicinity to the aforementioned one, which are shifted by approximately *m*/*z* = 14 each towards lower *m*/*z* ratios. Since these signal sets also exhibit the dysprosium specific isotope pattern, they might be derived from CH_2-extrusions in the ethyl residue of the acacOEt ligands. This would mean that one or two acacOEt ligands are transformed upon rearrangement to give the corresponding methyl analogues acacOMe. Beyond the extrusion, the assumption that a transesterification might have been induced by methanol appears more likely, since ESI-MS is a comparatively mild method which is not supposed to induce CH_2-extrusions. However, no further efforts have been put into the disclosure of this transformation.

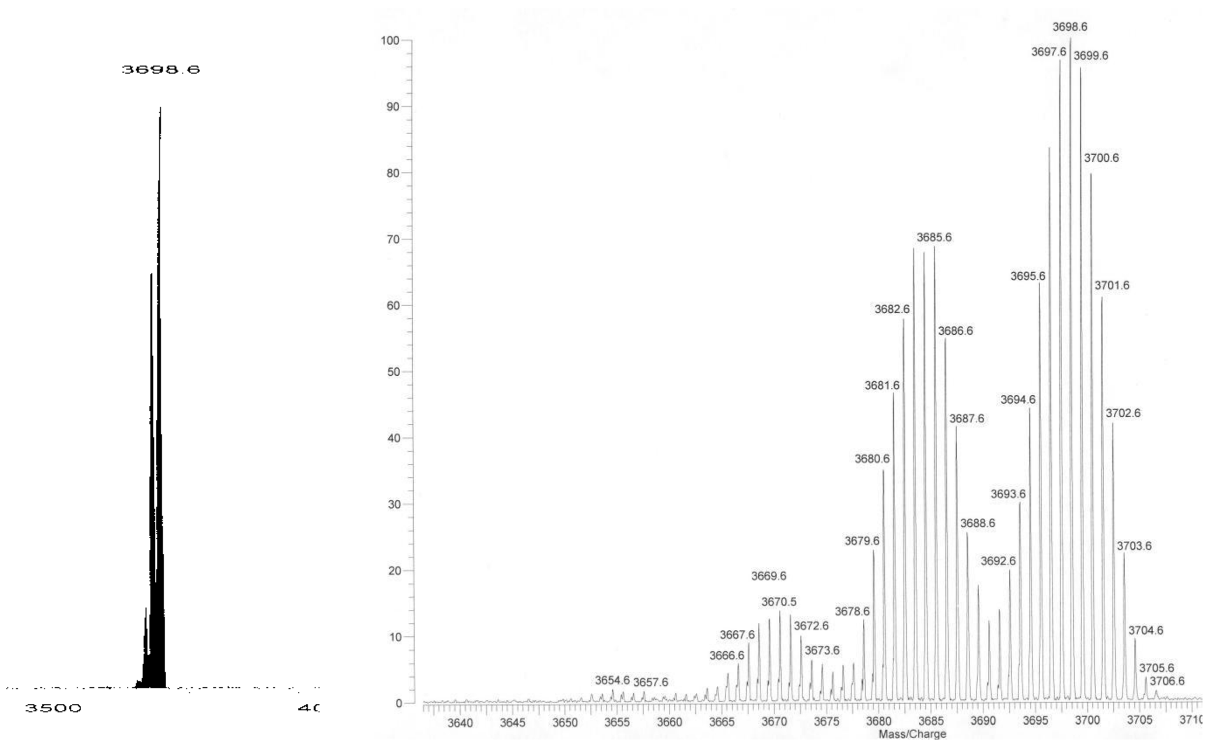

Figure 3.46. ESI-MS spectrum of $[H\{Dy_9(\mu_4\text{-}O)(\mu_4\text{-}OH)(\mu_3\text{-}OH)_8(acacOEt)_{16}\}]^+$ **12a**. Main signal of **12a** (left) and expanded spectrum (right) showing adjacent signal sets shifted to lower *m*/*z* ratios.

Thus, in analogy to compounds **7-9**, the exemplified ESI-MS measurement of **12a** has shown that this nonanuclear cluster scaffold also retains its shape when being dissolved in protic polar solvents. In contrast to **7-9**, no methanolysis was observed, giving rise for the assumption that the μ_3-hydroxy bridges are better shielded by the acacOEt ligands than by the Ph_2acac and $PepCO_2$ ligands in **7-9**.

The desired photophysical properties of **11** and the magnetic properties of **12** could not give satisfactory results, *i.e.* **11** did not provide any NIR-emissive properties which would have been worth mentioning and **12** did not show SMM-typical behaviour as previously shown for the related pentanuclear compound $[Dy_5(\mu_4\text{-}OH)(\mu_3\text{-}OH)_4(Ph_2acac)_{10}]$. No further modifications of the nonanuclear compounds have been intended to improve these properties.

3.4 1D-Polymers of Ph_2acac Ligated Rare Earth Metal Compounds

IN COOPERATION WITH
PROF. DR. PETER C. JUNK, PROF. DR. GLEN B. DEACON AND PROF. DR. PHIL ANDREWS, SCHOOL OF CHEMISTRY, MONASH UNIVERSITY (MELBOURNE, AUSTRALIA)

3.4.1 Attempts to Prepare Rare Earth Metal Clusters with Alendronic Acid

As we strive to synthesize biorelevant rare earth metal based cluster compounds possessing potential biomedical efficacies, we were seeking for further ligands to be combined with Ph_2acac, facilitating the generation of new mixed-ligated rare earth metal clusters which are accepted by cellular systems to gain applicability. For this purpose, we decided to introduce alendronic acid into our procedures for cluster synthesis. Alendronic acid, (4-amino-1-hydroxybutylidene)biphosphonic acid,[93] is an aminobiphosphonate derivative exhibiting efficacy in postmenopausal osteoporosis,[94] Paget’s disease[95] and malignant hypercalcemia.[95] It is taken up rapidly by the skeleton and is capable of inhibiting osteoclast-mediated bone resorption.[96] Thus it acts as a reconstructing agent for stabilizing the apatite structure of human bones by donating phosphonate moieties which are *in vivo* converted to phosphate functions.

Besides all these useful aspects mentioned, alendronic acid possesses several different heteroatoms necessitated for coordination to rare earth metal atoms (Scheme3.9). Furthermore it may be described as a bifunctionalized ligand which might facilitate versatile continuative chemical transformation, since it must not be assumed that all functional groups are blocked by metal coordination.

We therefore launched a corporate project with Prof. Dr. Peter C. Junk, Prof. Dr. Glen B. Deacon and Prof. Dr. Phil Andrews. Bearing all these intentions in mind, we applied a similar procedure as previously described for the pentadecanuclear clusters **7-9**, in which neodymium trichloride hexahydrate $[NdCl_3{\cdot}(H_2O)_6]$ was reacted with Ph_2acacH and alendronic acid monohydrate in methanol with KO*t*Bu as base. However, working up this reaction mixture did not yield the desired mixed ligated rare earth metal hydroxy cluster with alendronic acid as one supporting ligand, but an unprecedented onedimensional polymeric chain $[K\{Nd(Ph_2acac)_4\}(CH_2Cl_2)_2]_n$ **13** which exhibits an inorganic backbone composed of alternating neodymium and potassium atoms (Scheme 3.9). The monomeric unit of **13** can be described as an *ate*-complex, as the monoanionic $[Nd(Ph_2acac)_4]^-$-moiety is electrostatically balanced by the potassium cation. Since in the solid state the potassium cation is directly coordinated by the $[Nd(Ph_2acac)_4]^-$-moiety, **13** may also be considered as a polymeric arrangement of contact ion pairs. The coordination periphery of both metal atoms is made up by four Ph_2acac ligands.

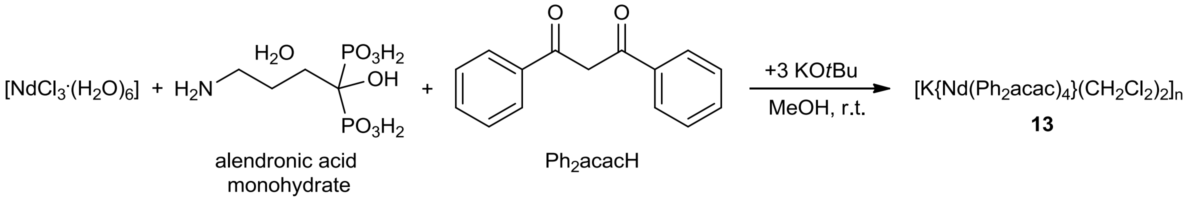

Scheme 3.9. Fortuitous synthesis of 1D coordination polymer $[K\{Nd(Ph_2acac)_4\}(CH_2Cl_2)]_n$ **13**. Zwitterionic nature of alendronic acid and keto-enol tautomery of Ph_2acacH are neglected.

3.4.2 Directed Synthesis of $[K\{Nd(Ph_2acac)_4\}(CH_2Cl_2)_2]_n$ (13)

As the stoichiometry in scheme 3.9 reveals, the preparation of **13** was not intended which, however, disclosed an unprecedented polymeric rare earth metal based coordination compound. Targeting to prove that the formation of **13** was expectedly neither catalyzed nor initiated by alendronic acid, the synthesis of **13** had to be reproduced in a directed fashion, *i.e.* excluding the utilization of alendronic acid and adapting the stoichiometry. Therefore $[NdCl_3{\cdot}(H_2O)_6]$ was reacted with Ph_2acacH in methanol, using KO*t*Bu as base once again. Working up this reaction mixture gave single crystals from a 1:4 CH_2Cl_2/*n*-hexane mixture, which showed to be the desired coordination polymer **13** as proven *via* single crystal X-ray analysis. To show the general validity of this type of reaction for similarly sized rare earth metal atoms, the very same reaction was carried out using $[SmCl_3{\cdot}(H_2O)_6]$ and $[PrCl_3{\cdot}(H_2O)_7]$ instead of $[NdCl_3{\cdot}(H_2O)_6]$. Surprisingly, the expected polymeric chains were not afforded, but the literature known tetranuclear rare earth metal hydroxy clusters $[Ln_4(\mu_3\text{-}OH)_2(Ph_2acac)_{10}]$, which have once been reported by Roesky *et al.* (Fig. 3.49).[41c] This result was confirmed by both single crystal X-ray analysis and microanalysis.

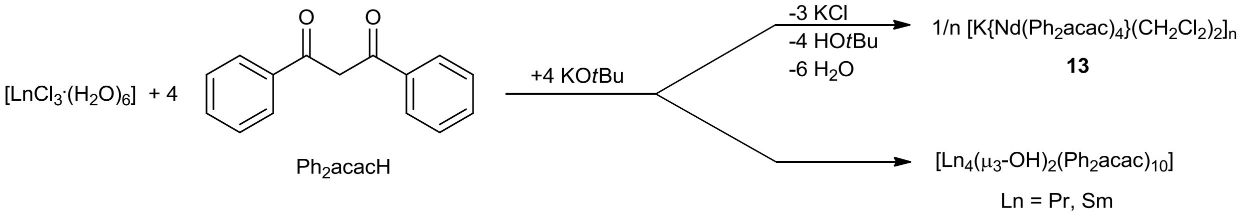

Scheme 3.10. Directed synthesis of $[K\{Nd(Ph_2acac)_4\}(CH_2Cl_2)_2]_n$ **13** and fortuitous syntheses of $[Ln_4(\mu_3\text{-}OH)_2(Ph_2acac)_{10}]$ with Ln = Pr, Sm.

Coordination polymer **13** has been characterized by standard analytical and spectroscopic techniques, and the solid state structure of **13** was established by single crystal X-ray diffraction (Fig. 3.46). The polymer's behaviour in solution was investigated *via* ESI-MS (cp. 3.4.6). A corporate project with Priv.-Doz. Dr. Andreas-Neil Unterreiner and Dr. Melanie Klinger facilitated the performance of femtosecond laser spectroscopy experiments with **13**, targeting to gain insight into the spectrochemical characteristics of rare earth metal-based coordination polymers (cp. 3.4.7).

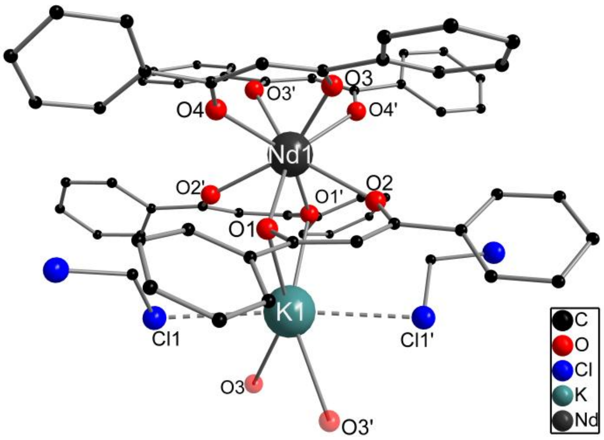

Figure 3.46. Perspective view of monomeric unit of the molecular structure of $[K\{Nd(Ph_2acac)_4\}(CH_2Cl_2)_2]_n$ **13**. Hydrogen atoms are omitted for clarity. Semitransparent atoms belong to adjacent monomeric unit. Selected distances [Å] and angles [°]: Nd1-K1 3.956(2), Nd1-O1 2.451(4), Nd1-O2 2.410(4), Nd1-O3 2.464(5), Nd1-O4 2.428(4), K1-O1 2.891(5), K1-O3 2.913(5), K1-Cl1 3.394(2); O1-Nd1-O2 76.8(2), O3-Nd1-O4 76.5(2), Nd1-O1-K1 95.69(15) Nd1-O3-K1 95.54(15), Nd1-K1-Nd1 180.00(5), O1-K1-O1' 75.4(2), O3-K1-O3' 74.7(2), Cl1-K1-Cl1' 174.42(9); φ = (O1-K1-O1';O3-K1-O3') = 50.068(6)°.

3.4.3 Structure Discussion on [K{Nd(Ph_2acac)$_4$}(CH_2Cl_2)$_2$]$_n$ (13)

Polymer **13** crystallizes in a monoclinic crystal system in the space group *C*2/*c*, having four molecules in the unit cell. The interatomic distance between the potassium atoms and the neodymium atoms in the backbone of the onedimensional polymer **13** is 3.956(2) Å and the angle Nd1-K1-Nd1 is 180.00(5)°, giving reason for its almost ideal linear shape. Since the polymeric chain has grown along the *b*-axis of the unit cell and as exactly one monomeric unit [K{Nd(Ph_2acac)$_4$}(CH_2Cl_2)$_2$] per unit cell is aligned along the *b*-axis, the length of this axis is exactly the doubled value of the neodymium-potassium distance (b = 7.911(2) Å, see crystallographic section). Considering several polymeric chains in several adjacent unit cells, an inverse arrangement of vicinal chains with respect to their backbone atoms is observed. Additionally, the interatomic distances between certain backbone atoms adopt identical values in all three spatial dimensions. This results in two face centred cubic arrangements of caesium and neodymium atoms each, which are interlaced in each other.

The neodymium atoms are chelated by all the four Ph_2acac ligands, hence, they have a coordination number of eight. Usually, a square antiprismatic arrangement of the donating oxygen atoms around the neodymium atom would have been expected. However, this is not the case since each Ph_2acac ligand contributes one oxygen atom serving to bridge the neodymium atom with the above lying potassium atom, providing μ:η^2-mode. Thus, the bond distance between the bridging oxygen atom and the neodymium atom (2.451(4) Å and 2.464(5) Å) is elongated by up to 5 pm compared to the bond distance between the non-bridging oxygen atom and the neodymium atom (2.410(4) Å and 2.428(4) Å). In consequence, the β-diketonate planes of the Ph_2acac ligands which would have been coplanarily arranged in the case of an ideal square antiprismatic geometry, are inclined sidewards to distort the square anitprismatic coordination geometry (Fig. 3.47). As a result, the coordination polyhedron displayed by the oxygen atoms surrounding the neodymium atom can be rather described as a dodecahedron.

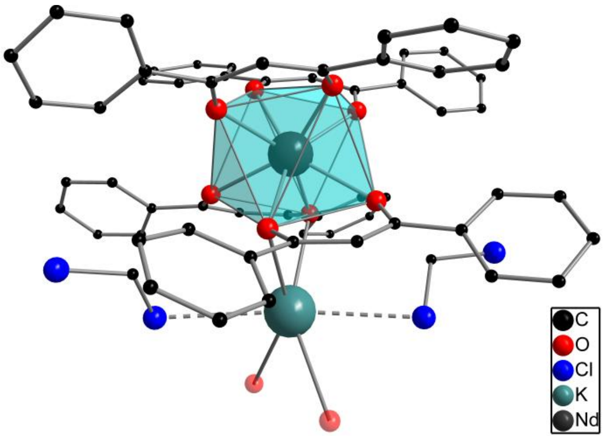

Figure 3.47. Dodecahedral coordination polyhedron made up by oxygen atoms of Ph_2acac ligands surrounding the neodymium atom.

Since the potassium atom is also surrounded by four Ph_2acac ligands but only singly coordinated by each ligand, it provides four bonds to Ph_2acac oxygen atoms. Finally, the coordination environment of the potassium atom might be thought to be saturated by two chlorine atoms of two *end on*-coordinating (η^1) dichloromethane molecules which are almost linearly arranged by enclosing a Cl1-K1-Cl1’ angle of 174.42(9)°. However, the exact nature of the potassium-chlorine interaction cannot be unambiguously clarified, since a comparably long bond distance of K1-Cl1 = 3.394(2) Å might also imply a mere packing effect. On the other hand, there is *e.g.* one example in literature, which reports on a coordination of dichloromethane molecules to silver atoms in $[Ag_2(CH_2Cl_2)_2Pd(OTeF_5)_4]$.[97] In this work, a η^2-coordination of both chlorine atoms has been observed in the corresponding solid state structures, providing mean bond distances of Ag-Cl of approximately 2.85 Å. The shortening of this bond distances compared to those in **13** ought to be indicative for the bidentate coordination in the silver compound, whereupon the dichloromethane coordination in **13** is assumed to be monodentate. In addition, the ionic radius of silver(I) is slightly smaller than the ionic radius of potassium(I) when regarding same coordination numbers.[3, 65] However, the exact coordination behaviour of dichloromethane to the silver atoms in $[Ag_2(CH_2Cl_2)_2Pd(OTeF_5)_4]$ had further been underlined *via* infrared spectroscopy, which is not the case for **13**. Thus, the dichloromethane molecules in **13** are assigned to be non-coordinating to avoid speculations which might appear as too vague, and the overall coordination number of the potassium atom is assigned to be four.

The coordination polyhedron displayed by the oxygen atoms can best be described as an extremely distorted tetrahedron (Fig. 3.48b). The vague inclusion of the chlorine atoms into the potassium atom’s coordination geometry would, hence, not allow the assignment to an even octahedron, but roughly to a distorted one (Fig. 3.48a).

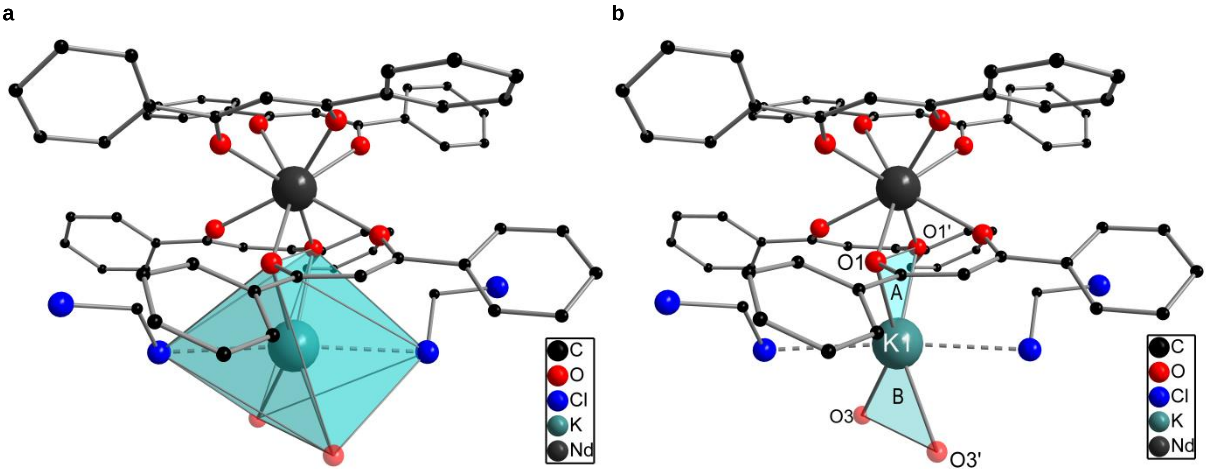

Figure 3.48. a) Distorted octahedral coordination geometry of oxygen and chlorine atoms surrounding the potassium atom and b) visualization of the dihedral angle φ made up by triangular faces A and B (50.068(6)°), whereby A is enclosed by O1, O1’ and K1, and B is enclosed by O3, O3’ and K1.

There are no hydroxy and/or oxo ligands accommodated in the coordination sphere of the neodymium atom. This appears surprising since numerous groups have shown that experiments applying very similar reaction conditions with differing stoichiometries give multinuclear cluster compounds possessing a certain content of hydroxy and or oxo ligands.[20, 29a, 36g, 37, 41, 47-49, 70d]

The [K{Nd(Ph_2acac)$_4$}(CH_2Cl_2)$_2$] moieties assemble linearly and are infinitely continued along the *b*-axis to finally give the chainlike 1D-coordination polymer **13** (Fig. 3.49).

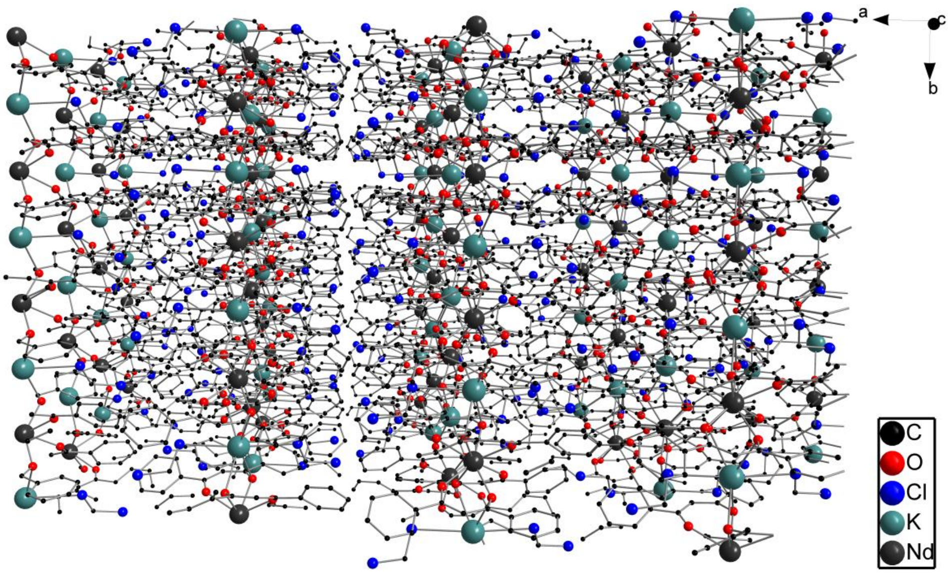

Figure 3.49. Solid state structure of polymer **13** showing several polymeric domains in several unit cells.

3.4.4 ESI-MS Investigations on $[K\{Nd(Ph_2acac)_4\}(CH_2Cl_2)_2]_n$ (13)

Subsequent ESI-MS investigations were carried out with **13**. Therefore the polymer was dissolved in *N*,*N*-dimethylformamide (DMF) and then sprayed into the ESI-MS apparatus as usual. The resulting mass spectrum revealed the polymeric structure to be broken up upon dissolution in DMF, giving the monoanionic $[Nd(Ph_2acac)_4]^-$-fragment peaking at *m*/*z* = 1037.2203 as the predominant species in solution (Fig. 3.50). This finding gives evidence at least for the instability of such rare earth metal based polymeric *ate*-complexes as **13** in solution.

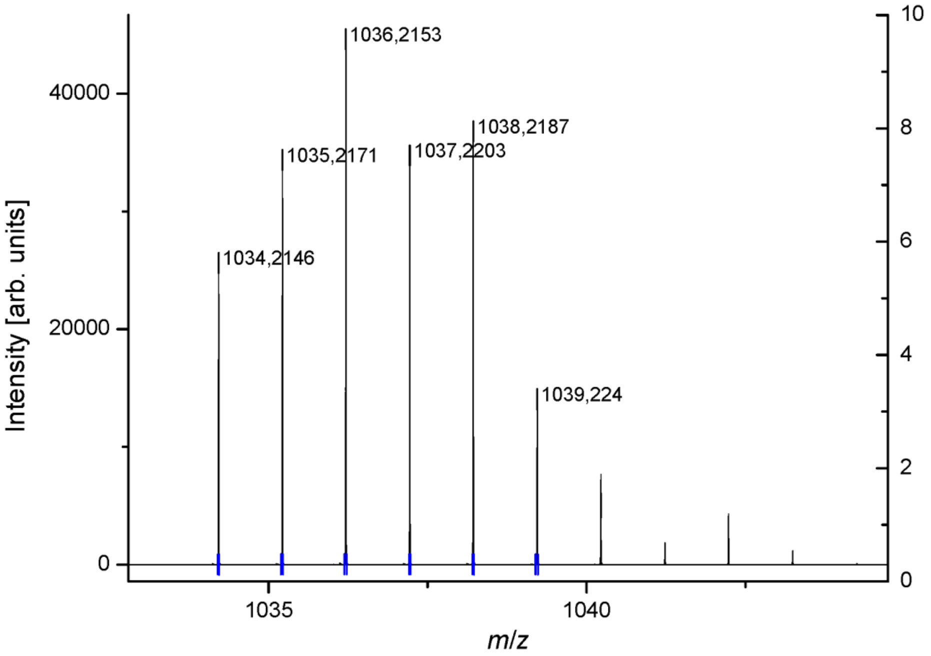

Figure 3.50. ESI-MS spectrum of dissolved polymer **13** showing $[Nd(Ph_2acac)_4]^-$-moiety at *m*/*z* = 1037.2203 exclusively.

3.4.5 Synthesis of $[Cs\{Ln(Ph_2acac)_4\}(C_3H_7NO)_2]_n$ (14-17)

As the higher homologues of the alkaline metal series ought to exhibit higher coordination numbers than potassium, analogous reactions as discussed in the latter chapters might afford novel heterobimetallic coordination polymers with even more sophisticated structural patterns. This assumption is centred on the different ionic radii of potassium(I) and *e.g.* caesium(I) cations with respect to a coordination number of *e.g.* six, which is 1.52 Å for potassium(I) and 1.84 Å for caesium(I).[65]

Keeping this vision in mind, we used caesium containing bases instead of the potassium-containing ones as described for polymer **13**. Therefore, $[LnCl_3(H_2O)_n]$ (Ln = Pr (n = 7), Nd, Sm, Dy (n = 6)) was reacted with Ph_2acacH and caesium carbonate (Cs_2CO_3) in methanol. Working up the corresponding reaction mixtures afforded onedimensional coordination polymers $[Cs\{Ln(Ph_2acac)_4\}(C_3H_7NO)_2]_n$ (Ln = Pr (**14**), Nd (**15**), Sm (**16**) and Dy (**17**)), which are isostructural to each other (Scheme 3.11). These polymeric compounds also display a purely inorganic backbone which is made up by caesium and the individual rare earth metal atom in an alternating fashion. In analogy to compound **13**, it may be assigned to the class of polymeric *ate*-complexes.

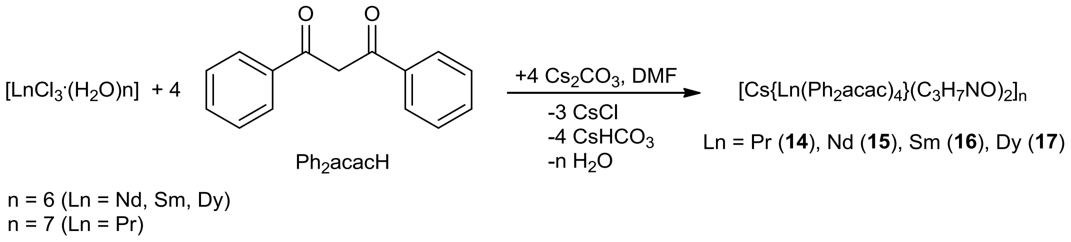

Scheme 3.11. Synthesis of $[Cs\{Ln(Ph_2acac)_4\}(C_3H_7NO)_2]_n$ with Ln = Pr (**14**), Nd (**15**), Sm (**16**) and Dy (**17**).

Coordination polymers **14-17** have been characterized by standard analytical and spectroscopic techniques, and the corresponding solid state structures were established by single crystal X-ray diffraction (Fig. 3.51). The polymers' behaviour in solution was investigated *via* ESI-MS (cp. 3.4.6). Continuing the above mentioned corporate project with Dr. Andreas-Neil Unterreiner and Dr. Melanie Klinger facilitated the performance of femtosecond laser spectroscopy experiments with **14-17** as well, targeting to gain insight into the spectrochemical characteristics of these caesium-containing rare earth metal-based coordination polymers (cp. 3.4.7).

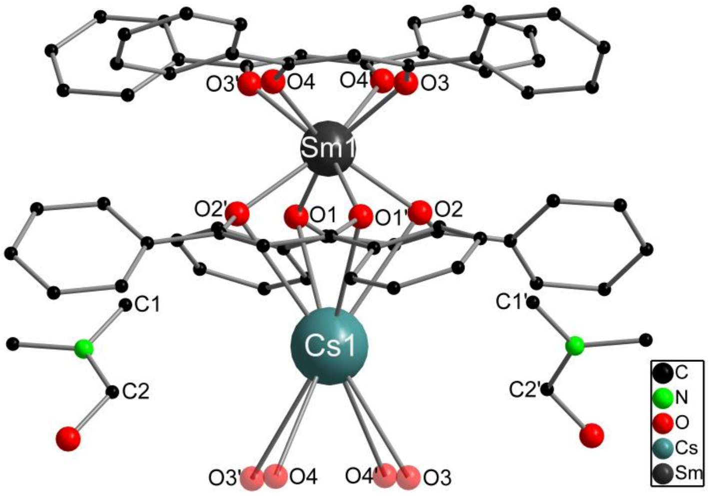

Figure 3.51. Perspective view of one monomeric unit of the molecular structure of $[Cs\{Sm(Ph_2acac)_4\}(C_3H_7NO)_2]_n$ exemplified for **16**. Clusters **14-15** and **17** are isostructural to **16**. Hydrogen atoms are omitted for clarity. Semitransparent atoms belong to adjacent monomeric unit. Selected distances [Å] and angles [°] for **14-17**: **14** (Ln = Pr): Pr1-Cs1 3.9589(15), Pr1-O1 2.428(8), Pr1-O2 2.457(8), Pr1-O3 2.429(7), Pr1-O4 2.439(7), Cs1-O1 3.265(9), Cs1-O2 3.267(9), Cs1-O3 3.302(8), Cs1-O4 3.267(8); Pr1-Cs1-Pr1 180.0(5), O1-Pr1-O2 68.3(2), O3-Pr1-O4 69.0(2), Pr1-O1-Cs1 86.8(2), Pr1-O2-Cs1 86.3(2), O1-Cs1-O2 53.6(2), O3-Cs1-O4 53.0(2), Cs1-O3-Pr1 86.2(2), Cs1-O4-Pr1 86.8(2); **15** (Ln = Nd): Nd1-Cs1 3.9652(10), Nd1-O1 2.432(3), Nd1-O2 2.416(3), Nd1-O3 2.414(3), Nd1-O4 2.445(3), Cs1-O1 3.258(3), Cs1-O2 3.301(3), Cs1-O3 3.251(3), Cs1-O4 3.272(3); Nd1-Cs1-Nd1 180.0(5), O1-Nd1-O2 73.76(9), O3-Nd1-O4 73.74(9), Nd1-O1-Cs1 87.08(8), Nd1-O2-Cs1 86.35(9), O1-Cs1-O2 49.58(7), O3-Cs1-O4 49.86(7), Cs1-O3-Nd1 87.03(9), Cs1-O4-Nd1 86.05(8); **16** (Ln = Sm): Sm1-Cs1 4.0039(12), Sm1-O1 2.405(6), Sm1-O2 2.396(6), Sm1-O3 2.387(6), Sm1-O4 2.415(6), Cs1-O1 3.282(7), Cs1-O2 3.358(7), Cs1-O3 3.330(7), Cs1-O4 3.300(7); Sm1-Cs1-Sm1 180.0(5), O1-Sm1-O2 69.7(2), O3-Sm1-O4 69.5(2), Sm1-O1-Cs1 88.2(2), Sm1-O2-Cs1 87.4(2), O1-Cs1-O2 51.41(14), O3-Cs1-O4 51.62(14), Cs1-O1-Sm1 88.2(2), Cs1-O2-Sm1 86.5(2); **17** (Ln = Dy): Dy1-Cs1 3.9519(12), Dy1-O1 2.340(6), Dy1-O2 2.345(6), Dy1-O3 2.350(6), Dy1-O4 2.348(6), Cs1-O1 3.297(7), Cs1-O2 3.276(7), Cs1-O3 3.261(7), Cs1-O4 3.339(7); Dy1-Cs1-Dy1 180.0(5), O1-Dy1-O2 73.3(2), O3-Dy1-O4 73.2(2), Dy1-O1-Cs1 87.4(2), Dy1-O2-Cs1 87.8(2), O1-Cs1-O2 50.36(15), O3-Cs1-O4 50.19(15), Cs1-O3-Dy1 88.3(2), Cs1-O4-Dy1 86.5(2).

3.4.6 Structure Discussion on $[Cs\{Ln(Ph_2acac)_4\}(C_3H_7NO)_2]_n$ (14-17)

The average interatomic distance between the caesium atoms and the rare earth metal atoms in the backbone of the polymers **14-17** is 3.9700 Å (3.9589(15) Å (**14**), 3.9652(10) Å (**15**), 4.0039(12) Å (**16**) and 3.9519(12) Å (**17**)), which is only 0.014 Å more than for the potassium based polymer **13** (3.956(2) Å). As this elongation lies almost in the error range of given distance values, it appears neglectible and cannot not be ascribed to the much larger ionic radius of caesium(I) compared to potassium(I) when assuming equal coordination numbers.[65] The Ln1-Cs1-Ln1 angle of 180.00(5)° in all four compounds **14-17** is evident for the linear shape of the backbone. In analogy to **13**, the polymeric chains of **14-17** are aligned along the *b*-axis of the unit cell and one monomeric unit $[Cs\{Ln(Ph_2acac)_4\}(C_3H_7NO)_2]$ per unit cell is aligned along the *b*-axis, leading again to a doubled length of this axis compared to the caesium-rare earth metal distance (*b* = 7.927(2) Å (**14**), 7.913(2) Å (**15**), 8.002(2) Å (**16**), 7.913(2) Å (**17**), see crystallographic section). The crystallographic analogy to potassium polymer **13** is also reflected in the relative arrangement of adjacent polymer chains in the unit cell, *i.e.* the caesium and rare earth metal atoms are aligned as two interlaced face centred cubic lattices providing the sodium chloride structure (Fig. 3.57). In conclusion, compounds **14-17** may also be described as onedimensional heterobimetallic polymers which are made up by infinitely repetitive *ate*-complex moieties $[Cs\{Ln(Ph_2acac)_4\}(C_3H_7NO)_2]$.

The rare earth metal atom is chelated by all the four Ph_2acac ligands, hence, it has a coordination number of eight (Fig. 3.52). In contrast to **13**, an even square antiprismatic arrangement of the donating oxygen atoms around the rare earth metal atom is observed. This is due to the fact that the larger caesium atom in **14-17** allows both oxygen atoms of each Ph_2acac ligand to bridge the caesium atom with a rare earth metal atom in next proximity. Thus, in **14-17** the Ph_2acac ligands adopt the bridging and doubly chelating $\mu:\eta^2:\eta^2$ coordination mode. Concomitantly, the β-diketonate planes are not inclined sidewards providing a more accurate non-crystallographic D_{4d} symmetry around the rare earth metal atom than in **13**. This aspect of less distortion of symmetry elements is reflected in very similar rare earth metal-oxygen bond distances, *i.e.* they deviate by only one to three Ångstroms instead of five Ångstroms as in **13** due to identical connectivity (range of Ln-O = 2.428(8)-2.457(8) Å (**14**), 2.414(3)-2.445(3) Å (**15**), 2.387(6)-2.415(6) Å (**16**) and 2.340(6)-2.350(6) Å (**17**)).

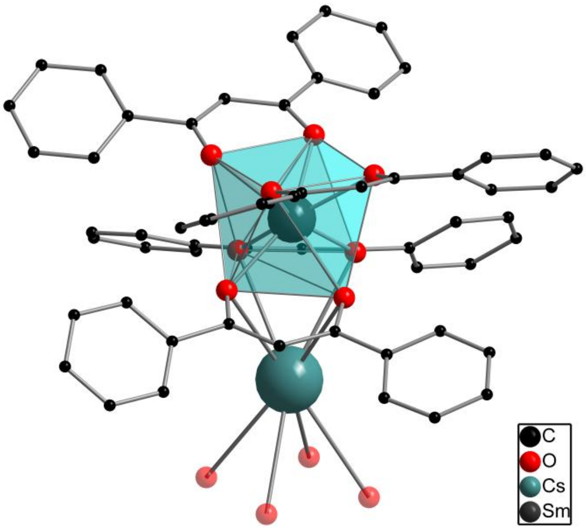

Figure 3.52. Square antiprismatic coordination polyhedron made up by oxygen atoms of Ph_2acac ligands surrounding the rare earth metal atom.

The $\mu:\eta^2:\eta^2$ coordination mode of the Ph$_2$acac ligands and the resulting elevated symmetry surrounding the rare earth metal atom has also an impact on the coordination geometry of the caesium atom. At first, it is also chelated by each Ph$_2$acac ligand leading to a coordination number of eight. Secondly, the donating oxygen atoms display a quite clear square antiprismatic coordination polyhedron around the caesium atom, since the Ph$_2$acac ligands are not inclined, as previously discussed (Fig. 3.53). The latter aspect is once more reflected within very similar bond distances between the caesium atom and the oxygen atoms (range of Cs-O = 3.265(9)-3.302(8) Å (**14**), 3.301(3)-3.251(3) Å (**15**), 3.282(7)-3.358(7) Å (**16**) and 3.261(7)-3.339(7) Å (**17**)). In compounds **14-17**, the coordination environment of the caesium atom is not saturated by additionally coordinating solvent molecules, but the large cavity left between the Ph$_2$acac layers surrounding the caesium atom allow an incorporation of two non-coordinating DMF molecules.

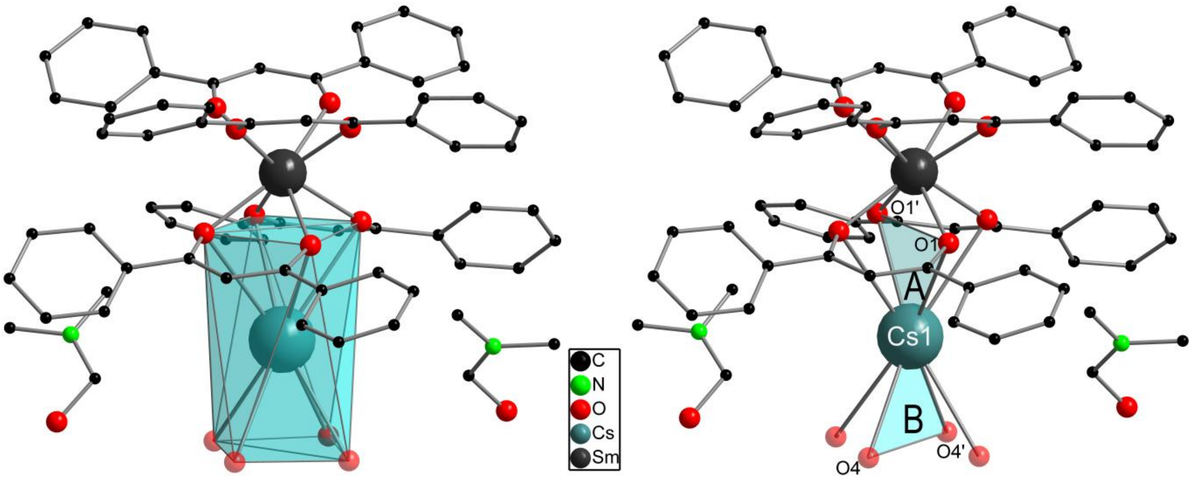

Figure 3.53. Square antiprismatic coordination environment of caesium atom (left), dihedral angle φ(A;B) for quantifying the accuracy of the antiprismatic shape (right).

In analogy to potassium based polymer **13**, there are no hydroxy and/or oxo ligands present in the coordination sphere of the rare earth metal atom, which is surprising due to the same reasons as given above for **13**.

The [Cs{Ln(Ph$_2$acac)$_4$}(C$_3$H$_7$NO)$_2$] moieties described assemble linearly and are infinitely continued along the *b*-axis to finally give the chainlike 1D-coordination polymers **14-17** (Fig. 3.54).

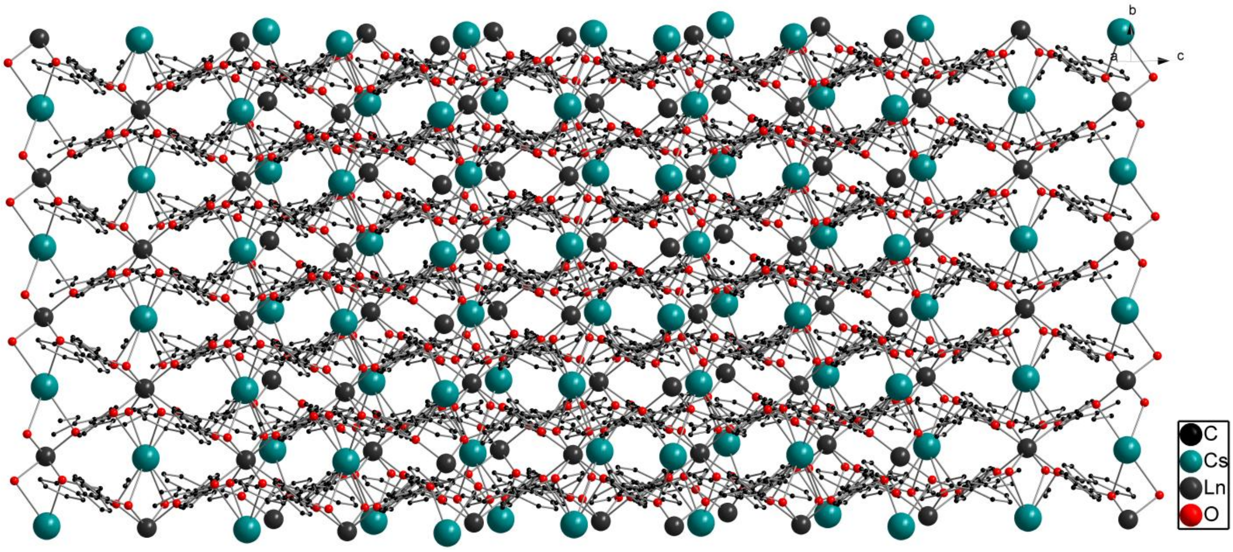

Figure 3.54. Solid state structure of polymers **14-17** showing several polymeric domains in several unit cells.

3.4.7 ESI-MS Investigations on [Cs{Ln(Ph_2acac)$_4$}(C_3H_7NO)$_2$]$_n$ (14-17)

Subsequent ESI-MS investigations were also performed with **14-17**, applying the same procedure as for **13**. Therefore the polymers were dissolved in DMF to be sprayed into the ESI-MS apparatus afterwards. The resulting mass spectrum revealed the polymeric structure to be broken up upon dissolution in DMF, giving the monoanionic [Ln(Ph_2acac)$_4$]$^-$-fragments peaking at *m*/*z* = 1033.208 (**14**), 1036.204 (**15**), 1046.234 (**16**) and 1056.227 (**17**) as the predominant species in solution (Fig. 3.55-3.58). These findings underline the fact of such polymeric *ate*-complexes to be instable in solution, as derived from their structural relative **13**.

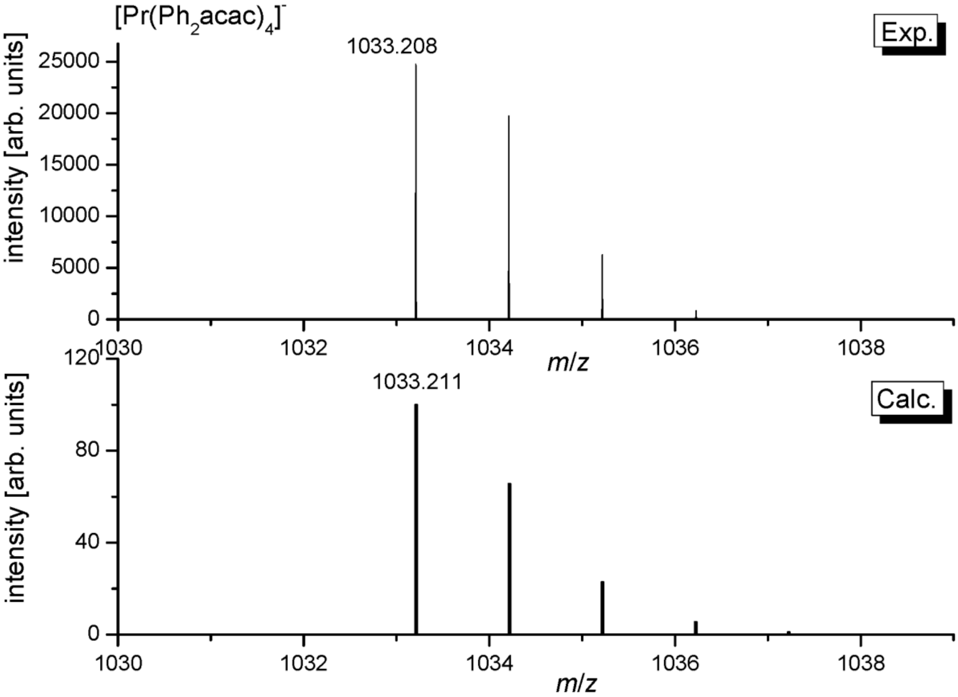

Figure 3.55. ESI-MS spectra of dissolved polymer **14** showing [Pr(Ph$_2$acac)$_4$]$^-$-moiety experimentally and calculated.

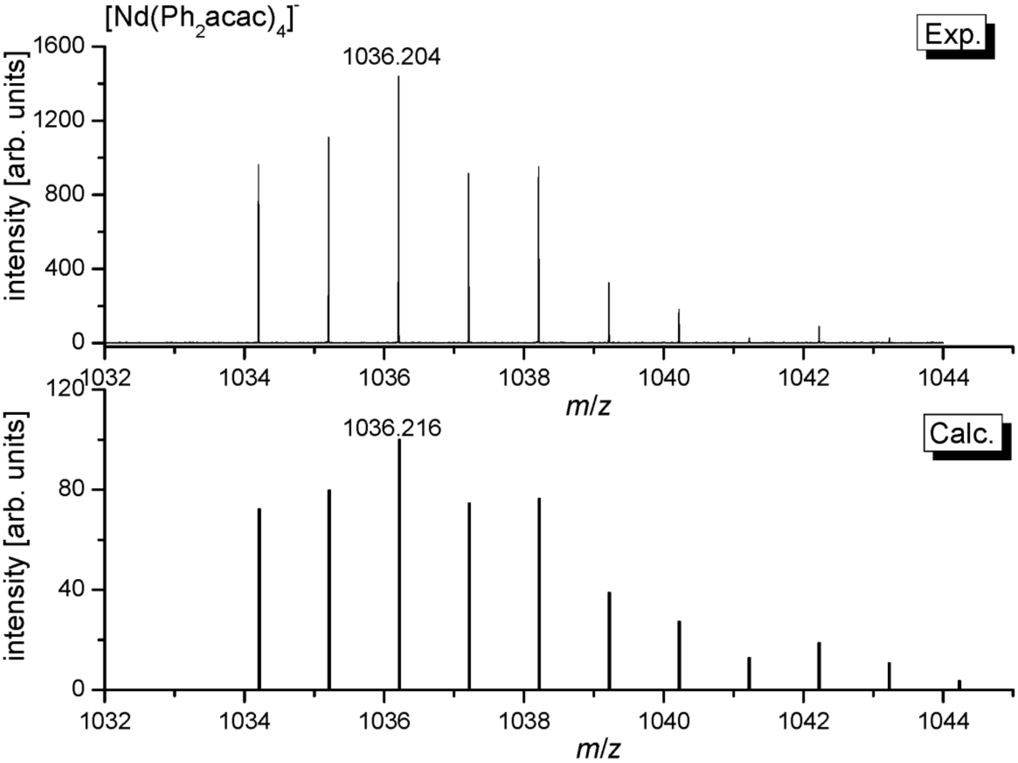

Figure 3.56. ESI-MS spectra of dissolved polymer **15** showing [Nd(Ph$_2$acac)$_4$]$^-$-moiety experimentally and calculated.

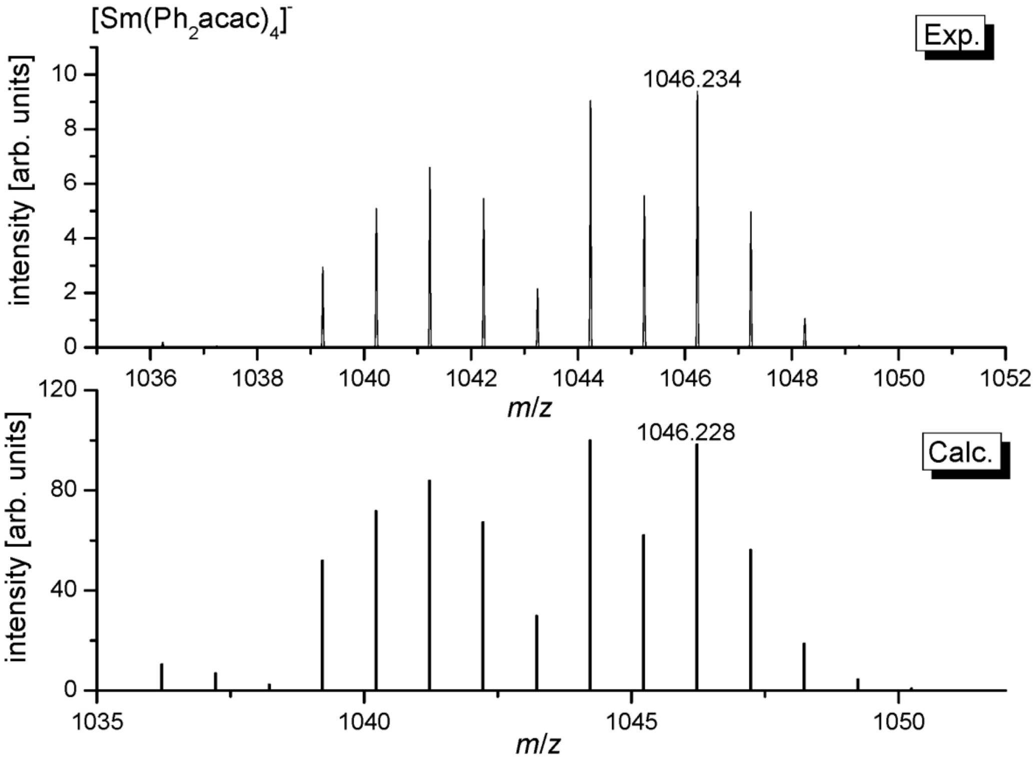

Figure 3.57. ESI-MS spectra of dissolved polymer **16** showing [Sm(Ph_2acac)$_4$]$^-$-moiety experimentally and calculated.

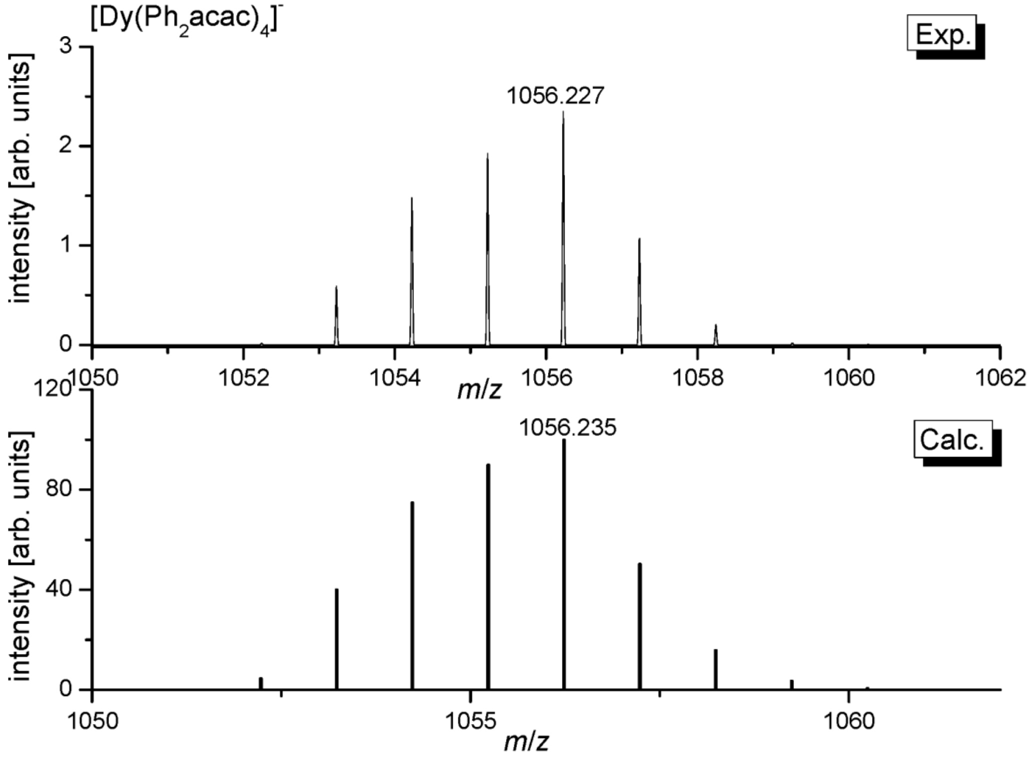

Figure 3.58. ESI-MS spectra of dissolved polymer **17** showing [Dy(Ph_2acac)$_4$]$^-$-moiety experimentally and calculated.

Beyond these signals originating from $[Ln(Ph_2acac)_4]^-$ moieties, the ESI-MS spectra of **14-17** also revealed other ionic species having larger molar masses. Since these species show to have *e.g.* several rare earth metal atoms but no caesium atoms or *vice versa*, they must are supposed to derive from certain rearrangement mechanisms occurring in solution. The simultaneous presence of the different species possessing both positive and negative charges is indicative for a complex equilibrium in solution. This aspect will be discussed regarding neodymium compounds **15** as a representative for **14**, **16** and **17** which have shown to make up the same species in solution.

Figure 3.59 visualizes this issue, showing signal sets of more sophisticated anionic species of **15** in the negative mode which may unambiguously be assigned to $[Nd_2(Ph_2acac)_7]^-$, $[Cs\{Nd(Ph_2acac)_4\}_2]^-$ and $[Nd_3(Ph_2acac)_9OH]^-$, beside the previously discussed $[Nd(Ph_2acac)_4]^-$ species.

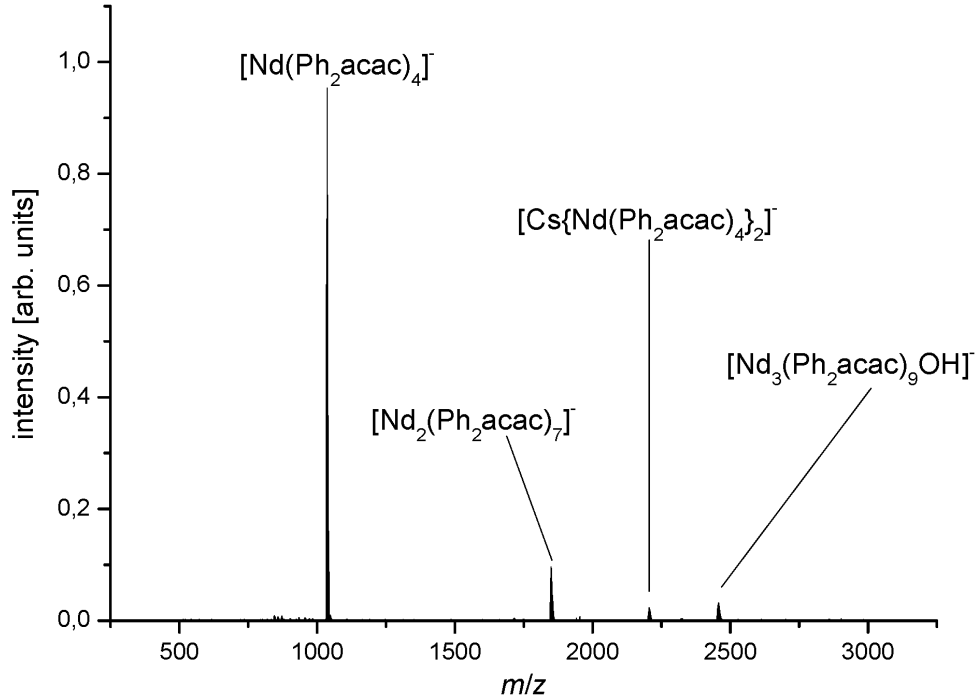

Figure 3.59. ESI-MS spectrum of **15** dissolved in DMF applying negative mode, showing monoanionic species of higher nuclearity.

When switching the ESI-MS apparatus to the positive modus and measuring the same DMF solution of **15** as before gives evidence for the simultaneous presence of structurally related monocationic species. Figure 3.60 reveals the oligonuclear cations $[Cs_2\{Nd(Ph_2acac)_4\}]^+$, $[Cs_2\{Nd_2(Ph_2acac)_7\}]^+$ and $[Cs_3\{Nd_2(Ph_2acac)_8]^+$. The detection of the corresponding signals stemming from the same solution as the signals detected in negative mode underline the suggestion of complex equilibria of **14-17** when dissolved in DMF. Although the structures of these postulated species could not yet be clarified, one might have a certain idea of possible structural arrangements of some of the species when keeping the corresponding solid state structures of **14-17** in mind. However, more precise statements concerning the structural nature of the detected ionic species cannot be made, since further mechanistic and structural investigations have not been performed yet.

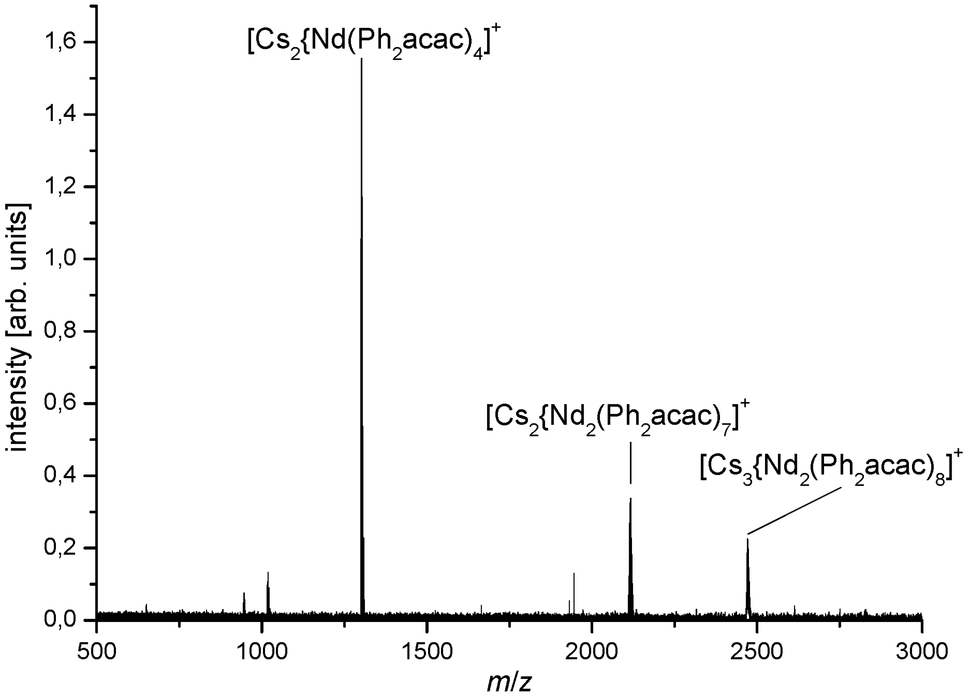

Figure 3.60. ESI-MS spectrum of **15** dissolved in DMF applying positive mode, showing monocationic species of higher nuclearity.

3.4.8 Femtosecond Laser Spectroscopy with 13, 14 and 15

IN COOPERATION WITH
PRIV.-DOZ. DR. ANDREAS-NEIL UNTERREINER AND DR. MELANIE KLINGER, INSTIUTE OF PHYSICAL CHEMISTRY, KARLSRUHE INSTITUTE OF TECHNOLOGY

Next, we performed time-resolved femtosecond laser spectroscopic experiments with dissolved samples of **13**, **14** and **15** in DMF. This project was targeting on gaining first insights into ultra-short-time-dynamics of such species, as certain photoinduced processes are exclusively observable in the femtosecond scale.

UV-Vis absorption spectra of DMF solutions of **13**, **14** and **15** were recorded. The samples uniformly gave an absorption maximum at a wavelength of approximately 350 nm (in analogy to Ph_2acac containing clusters in chapter 3.2.7), suggesting a common π → π* transition derived from delocalized π-electrons of the Ph_2acac ligands (Fig. 3.61). Beyond the almost indistinguishable absorption behaviour of **13**-**15**, a photophysical degradation has revealed to occur within approximately one week.

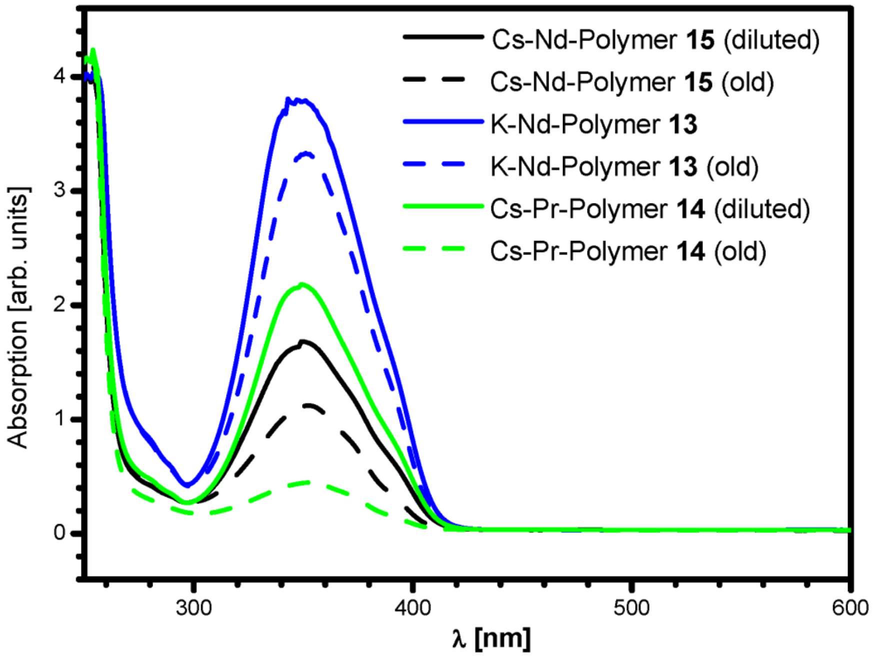

Figure 3.61. Absorption spectra of DMF solutions of **13**-**15** with absorption intensities as a function of exposition period.

Based on this absorption behaviour, subsequent laser excitation of DMF solutions of **13**, **14** and **15** occurred with an excitation wavelength of 388 nm. Temporal profiles were recorded *via* pump-probe experiments with probe wavelengths of 550, 630, 720 and 900 nm, giving a plot of the change of the optical density (ΔOD) as a function of time which is resolved up to the femtosecond scale.

The transient absorption dynamics of the ΔOD-values of **13**-**15** unambiguously show that the relaxation behaviour after the excitation exclusively depends on the individual rare earth metal atom used. When comparing the relaxation behaviour of the potassium and caesium containing neodymium compounds **13** and **15**, the same time constants are observed. These are given by the relaxation time constant of six ps in both cases, which is apparently not influenced by the alkaline metal atom. However, when probing with the same wavelengths, **13** and **15** revealed different transient absorption dynamics (Fig. 3.62 and 3.63). The aspect of the rare earth metal specific relaxation rate is further underlined when exciting the caesium containing praseodymium compound **14** with the same wavelength (Fig. 3.64). It exhibits a time constant of 26 ps, *i.e.* the transient absorption dynamic is much slower than for **13** and **15**. This issue implies a strikingly longer lifetime of the responsible excited states of praseodymium compared to those of neodymium.

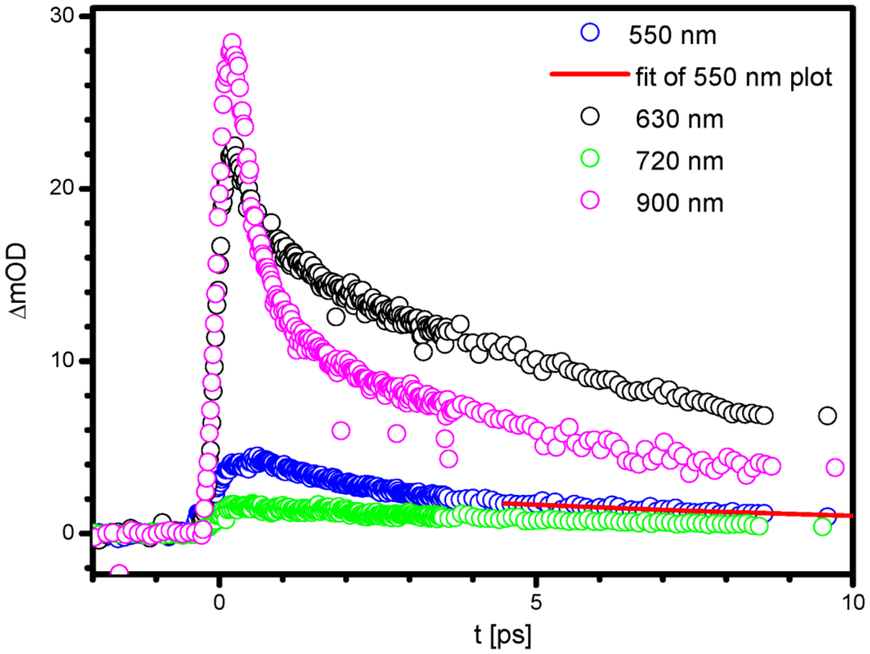

Figure 3.62. Time-resolved transient absorption profile of ΔOD of **13** in DMF after excitation with λ_{ex} = 388 nm. Probing wavelengths were λ = 550, 630, 720 and 900 nm.

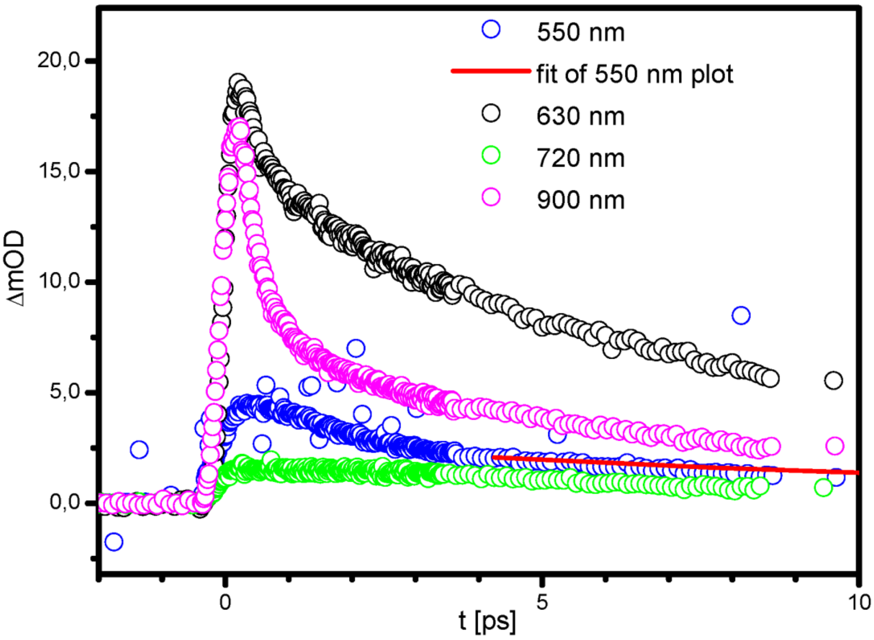

Figure 3.63. Time-resolved transient absorption profile of ΔOD of **15** in DMF after excitation with λ_{ex} = 388 nm. Probing wavelengths were λ = 550, 630, 720 and 900 nm.

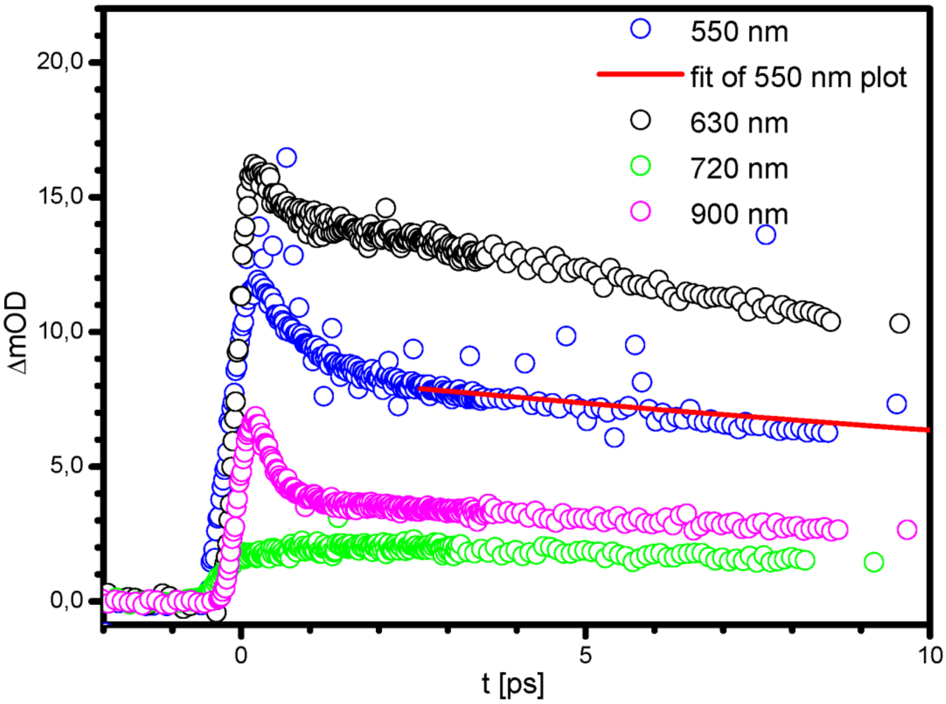

Figure 3.64. Time-resolved transient absorption profile of ΔOD of **13** in DMF after excitation with λ_{ex} = 388 nm. Probing wavelengths were λ = 550, 630, 720 and 900 nm.

The mechanism of excitation and emission described above (Scheme 3.12) utilizes the "antenna effect" discussed in chapter 3.2.7. With this technical setup, a proposed interpretation of this mechanism is allowed in a time-resolved fashion: an initial ultrashort excitation of the individual solution promotes the Ph_2acac ligands into their first excited singlet state S_1 (Fig. 3.65). Within one to two picoseconds (ps), the excited electron undergoes an ultrafast intersystem crossing into a triplet state of the ligand, from which the desirable ligand-to-metal energy transfer occurs partially, *i.e.* this path competes with other manifold relaxation mechanisms. After the energy transfer to the excited state of the rare earth metal atom has taken place, the following secondary relaxation process roughly after the first two picoseconds was measured observing the same rare earth metal specific time constants for all probe wavelengths used.

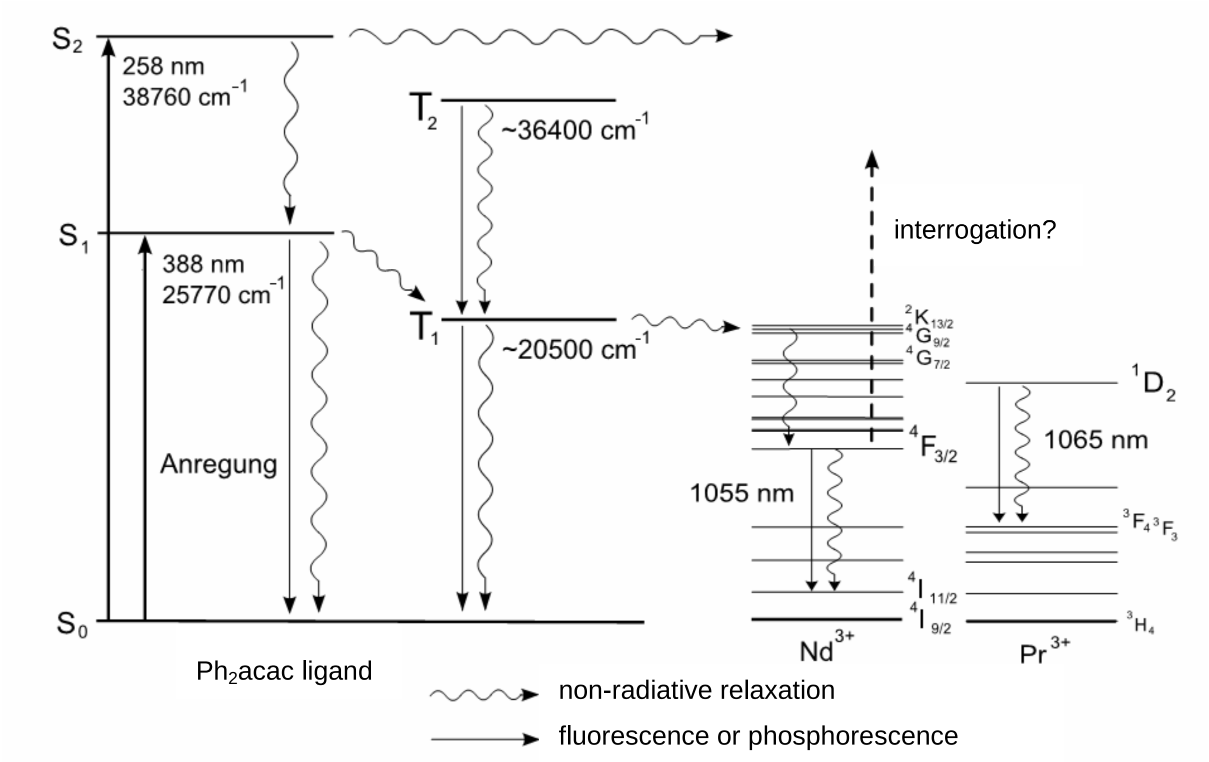

Figure 3.65. Extended Jablonski diagram showing possible relaxation pathways in **13-15**.

As stated above, the time constants do not depend on the ligand and are solely determined by the individual rare earth metal atom (in this case: neodymium or praseodymium). In case of the praseodymium compound, the corresponding time constant may presumably be assigned to the lifetime of the $^1D_2$ state. For the neodymium compound, the time constant may be attributed to the lifetime of the excited $^4F_{3/2}$ state before relaxation occurs in the $^4I_{9/2}$, the $^4I_{11/2}$ or the $^4I_{13/2}$ state.

Within the presented femtosecond laser experiments, this aspect would actually imply a stimulated emission at 1055 nm arising from a laser-induced transition from the $^4F_{3/2}$ into the $^4I_{11/2}$ state, which would have resulted in negative ΔOD values. However, such a stimulated emission was not observed irrespective of individual conditions chosen, and even a spectral confinement could not induce negative ΔOD values. Based on these observations, we conclude that the fluorescent quantum yield of **13**, **14** and **15** must be very low (less than 1/1000). To increase the quantum yield, usage of ionic solvents instead of standard solvents might be appropriate. Another option might be that the absorption of electronically excited states of higher energy is predominant. This criterion might depict a general problem for accessing electronic properties in rare earth metal based compounds using this method, as these elements exhibit a large number of electronically excited states which are very close to each other.

The appearance of the described femtosecond dynamic signifies that the energy transfer process is not exclusively restricted to the pathway from the ligand to the rare earth metal atom. One competing path might be a charge transfer onto the solvent molecules possibly leading to the generation of a solvated electron. Regarding this possibility, the different time constants taken from the relaxation of the ΔOD values might originate from rare earth metal atom-specific affinities to recapture the solvated electron. The subsequent relaxation associated with this mechanism ought to induce analogous changes of optical density. However, the dynamic which might be ascribed to a solvated electron solely appears after ten ps. This aspect rather underlines the assignment to an energy transfer dynamic between ligand and metal atom.

In general, the praseodymium based compound **14** has shown to be less photo- and thermoresistant than its neodymium analogues **13** and **15**, as indicated by its striking degradation after one week. However, this issue must not only be attributed to the laser irradiation, as the degradation seemed to be mainly thermally activated and supported by reaction with oxygen from air.

Targeting to confirm the proposed rare earth metal atom specific time constants once more, we performed a comparative experiment by using the literature known cluster compounds $[Ln_4(\mu_3\text{-}OH)_2(Ph_2acac)_{10}]$ (Ln = Pr, Nd).[41c] Therefore, initial UV/Vis spectra were recorded showing the same absorption behaviour as **13-15** (Fig. 3.66), underlining the assumption that the $\pi \rightarrow \pi^*$-transitions originate from the Ph_2acac ligands.

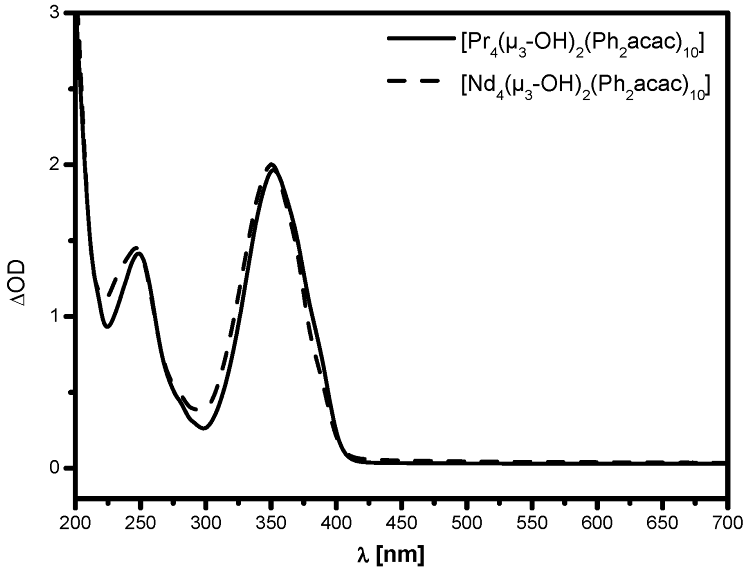

Figure 3.66. UV/Vis spectra of $[Ln_4(\mu_3\text{-}OH)_2(Ph_2acac)_{10}]$ (Ln = Pr, Nd) showing maxima at λ = 250 nm and 350 nm.

Applying a pump/probe combination of 388/1065 nm exhibited the same rare earth metal atom specific relaxation behaviour as for **13-15** (Fig. 3.67). This issue has been underlined by identical time constants (Pr = 26 ps; Nd = 6 ps) as for the dissolved polymer compounds **13-15**, *i.e.* the process which are responsible for this kind of dynamic are the same.

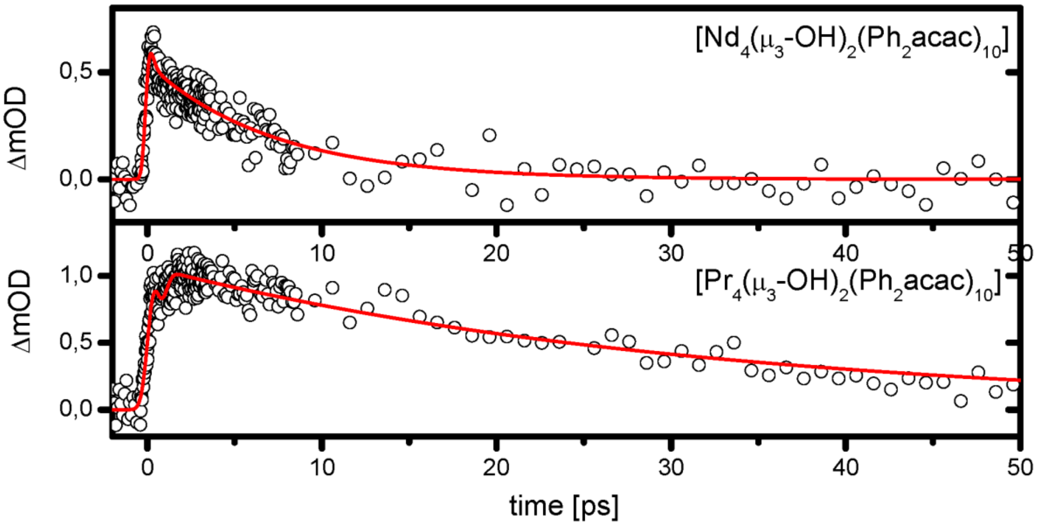

Figure 3.67. Temporal profiles of [Ln$_4$(μ$_3$-OH)$_2$(Ph$_2$acac)$_{10}$] (Ln = Pr, Nd) in MeOH at a pump/probe combination of 388/1065 nm.

4. EXPERIMENTAL SECTION

4.1 General Considerations

4.1.1 Working Technique

The rare earth metal salts were synthesized from their corresponding oxides by neutralizing with concentrated hydrochloric acid, followed by evaporation to dryness. Dibenzoylmethane, potassium *tert*-butoxide, methyl acetylacetate, ethyl acetylacetate, *D*-phenyl glycine, *L*-proline, *L*-valine, *L*-tryptophan, 2,2-diphenyl glycine, trifluoroactetic acid, tetrabutylammonium fluoride, sodium hydroxide and the solvents (methanol, ethanol: *p.a.* grade) were used as purchased from commercial sources without further purification.
Deuterated chloroform ($CDCl_3$) was obtained from Chemotrade Chemiehandelsgesellschaft mbH (≥ 99 atom % D).

4.1.2 Spectroscopy and Spectrometry

NMR spectra were recorded on a Bruker Avance 400, on a Bruker Avance II 300, on a Bruker AM 400 or on a Bruker DRX 500 spectrometer. Chemical shifts δ are referenced relative to internal solvent resonances in ppm ($CDCl_3$: 7.26 ppm (^1H) 77.0 ppm ($^{13}C\{^1H\}$) and are reported relatively to tetramethylsilane. Elemental analyses given in % were carried out using an Elementar Vario EL or an Elementar Vario Microcube and are given in %. Infrared (IR) spectra obtained from a Bruker IFS 113 v spectrometer via the Attenuated Total Reflection method (ATR). Raman spectra were measured on a Jobin Yvon Labram spectrometer. The spectroscopic positions of the absorption bands (IR) and intensity sets (Raman) are both given in cm^{-1}. Optical rotations were determined with a Jasco P-2000 spectrometer (Na, 589 nm). Electron Spray Ionization Mass Spectrometry (ESI-MS) was conducted with a Varian IonSpec Ultima FTICR (Fourier Transformed Ion Cyclotron Resonance) spectrometer equipped with a 7 T magnet. All signal sets of MS experiments are given in *m*/*z*.

4.2 Preparation of the Novel Compounds

4.2.1 Preparation of the Clusters 1-12

4.2.1.1 Procedures for $[Ln_4(\mu_3\text{-OH})_2(Ph_2acac)_{10}]$ and $[Ln_5(\mu_4\text{-OH})(\mu_3\text{-OH})_4(Ph_2acac)_{10}]$

$[Ln_4(\mu_3\text{-OH})_2(Ph_2acac)_{10}]$ (Ln = Pr, Nd, Sm) and $[Y_5(\mu_4\text{-OH})(\mu_3\text{-OH})_4(Ph_2acac)_{10}]$ were prepared as previously reported.[37, 41c] $[Eu_5(\mu_4\text{-OH})(\mu_3\text{-OH})_4(Ph_2acac)_{10}]$ was prepared *via* a slightly modified procedure compared to the literature known one:[41b]
To a stirred solution of KO*t*Bu (1.144 g, 9.89 mmol, 3 eq.) in 20 mL of methanol, HPh_2acac (1.48 g, 6.59 mmol, 2 eq.) was added. Subsequently, dropwise addition of $[EuCl_3\cdot(6\ H_2O)]$ (1.21 g, 3.30 mmol, 1 eq.) in 20 mL of methanol induced precipitation of a yellowish solid. After stirring the reaction mixture overnight, the precipitate was filtered off and washed with 3 × 10 mL of methanol and dried in *vacuo*. The residue was taken up with 20 mL of dichloromethane and filtered. The filtrate was then cooled to -80 °C and layered with 80 mL of *n*-hexane to afford 1.12 g of $[Eu_5(\mu_4\text{-OH})(\mu_3\text{-OH})_4(Ph_2acac)_{10}]$ as yellow block-shaped crystals after 12 h. Yield: 55% (single crystals). The corresponding solid state structure was confirmed *via* single crystal X-ray diffraction analysis.[59]

4.2.1.2 General Procedure for $[Ln_5(\mu_4\text{-OH})(\mu_3\text{-OH})_4(\alpha\text{-AA})_4(Ph_2acac)_6]$ (**1**-**6**)[41h]

To a stirred solution of KO*t*Bu (1.168 g, 9.89 mmol, 3 eq.) in 20 mL of methanol, the α-amino acids (2.64 mmol, 0.8 eq.) *D*-PhGlyH (**1**, **6**) (399 mg), *L*-ProH (**2**) (304 mg), *L*-ValH (**3**) (309 mg), *L*-TrpH (**4**) (539 mg) or Ph_2GlyH (**5**) (612 mg) were given. Subsequently, Ph_2acacH (905 mg, 3.96 mmol, 1.2 eq.) was added to this mixture to turn its colour from colourless to pale yellow. After stirring for 15 minutes, a solution of either $[YCl_3\cdot(H_2O)_6]$ (1.00 g, 3.30 mmol, 1 eq.) (**1**-**5**) or $[DyCl_3\cdot(H_2O)_6]$ (1.243 g, 3.30 mmol, 1 eq.) (**6**) in 20 mL of methanol was added dropwise and a flaky white precipitate was formed. The reaction was stirred overnight at room temperatur. Then the precipitate was filtered off to be washed with methanol (3 x 20 mL) and air-dried afterwards. The resulting yellow solids of compounds **1**-**4** were extracted with 20 mL of dichloromethane. The solutions were filtered off and cooled to -80 °C. Layering these solutions with 80 mL of *n*-hexane (not precooled) yielded yellowish rhombic crystals suitable for single crystal X-ray analysis after one day.

$[Y_5(\mu_4\text{-}OH)(\mu_3\text{-}OH)_4(D\text{-}PhGly)_4(Ph_2acac)_6]$ (**1**)

Yield (single crystals): 22 %; $[\alpha]^{20}$ = 754.92 (CH_2Cl_2, *c* = 0.60); ^1H NMR ($CDCl_3$, 400 MHz): *δ* 5.29 (2H, s, CH_2Cl_2), 6.15 (4H, t, *J*=10.3 Hz, C*H* (PhGly)), 6.23 (4H, s, C*H* (Ph_2acac_{bas})), 6.42 (2H, s, C*H* (Ph_2acac_{ap})), 6.71 (10H, m, CH_{ar}), 6.84 (8H, m, CH_{ar}), 7.04 (10H, m, CH_{ar}), 7.11 (10H, m, CH_{ar}), 7.16 (10H, m, CH_{ar}), 7.36 (12H, m, CH_{ar}), 7.62 (20H, m, CH_{ar}), 7.82 (8H, br s, NH_2); $^{13}C\{^1H\}$ NMR ($CDCl_3$, 400 MHz): *δ* 60.7 (*α*-*C*H), 95.3 (*C*H (Ph_2acac)), 127.2 (CH_{ar}), 127.4 (CH_{ar}), 127.7 (CH_{ar}), 128.2 (CH_{ar}), 129.0 (CH_{ar}), 130.7 (*p*-CH_{ar}), 131.1 (*p*-CH_{ar}), 140.0 (*i*-CH_{ar}), 141.6 (*i*-CH_{ar}), 180.7 (CO_2), 182.4, 183.5, 185.7 (CO ($Ph_2acac_{ap/bas}$)); IR [cm^{-1}]: 3348, 3285, 3060, 1593, 1552, 1517, 1478, 1453, 1395, 1311, 1024, 1009, 943, 597; Raman [cm^{-1}]: 3055, 1594 (*ν*CO), 1487, 1439, 1288, 1283, 1175, 1059, 1004, 998, 939, 780, 669, 604, 396; $C_{122}H_{103}N_4O_{25}Y_5{\cdot}CH_2Cl_2$ (2554.60): calcd. C, 57.83, H, 4.14, N, 2.19; found C, 57.76, H, 4.25, N, 1.87.

$[Y_5(\mu_4\text{-}OH)(\mu_3\text{-}OH)_4(L\text{-}Pro)_4(Ph_2acac)_6]$ (**2**)

Yield (single crystals): 31 %; $[\alpha]^{20}$ = -782.01 (CH_2Cl_2, *c* = 0.63); ^1H NMR ($CDCl_3$, 400 MHz): *δ* 1.48, 1.60 (8H, 2 m, γ-CH_2), 1.80 (4H, br s, N*H*), 2.06, 2.21 (8H, 2 m, β-CH_2), 2.62, 2.81 (8H, 2 m, δ-CH_2), 4.09 (4H, q, *J*=8.3 Hz, α-C*H*), 5.87 (2H, s, C*H* (Ph_2acac_{ap})), 6.22 (4H, s, C*H* (Ph_2acac_{bas})), 6.65 (4H, m, CH_{ar}), 6.73 (8H, m, CH_{ar}), 7.01 (4H, m, CH_{ar}), 7.13 (3H, m, CH_{ar}), 7.20 (4H, m, CH_{ar}), 7.30 (10H, m, CH_{ar}), 7.37 (6H, m, CH_{ar}), 7.41 (5H, m, CH_{ar}), 7.49 (8H, d, CH_{ar}), 7.92 (8H, m, CH_{ar}); $^{13}C\{^1H\}$ NMR ($CDCl_3$, 400 MHz): *δ* 26.2 (γ-CH_2), 30.4 (β-CH_2), 46.6 (δ-CH_2), 62.9 (α-*C*H), 94.3 (*C*H (Ph_2acac)), 126.8 (CH_{ar}), 127.5 (CH_{ar}), 127.8 (CH_{ar}), 128.1 (CH_{ar}), 130.6 (*p*- CH_{ar}), 131.0 (*p*- CH_{ar}), 138.3 (*i*- CH_{ar}), 139.5 (*i*- CH_{ar}), 181.5 (CO_2), 182.7, 183.6 (*C*O ($Ph_2acac_{ap/bas}$)); IR [cm^{-1}]: 3614 (*ν*OH), 1702, 1597 (*ν*CO), 1553, 1521, 1479, 1456, 1391, 1108, 1025, 751, 721, 689, 642; Raman [cm^{-1}]: 3055, 1594 (*ν*CO), 1486, 1439, 1288, 1283, 1174, 1057, 998, 988, 916, 781, 779, 665, 363; $C_{110}H_{103}N_4O_{25}Y_5$ (2325.54): calcd. C, 56.81, H, 4.46, N, 2.41; found C, 56.68, H, 4.54, N, 2.06.

$[Y_5(\mu_4\text{-}OH)(\mu_3\text{-}OH)_4(L\text{-}Val)_4(Ph_2acac)_6]$ (**3**)

Yield (single crystals): 28 %; $[\alpha]^{20}$ = -818.76 (CH_2Cl_2, *c* = 0.71); ^1H NMR ($CDCl_3$, 400 MHz): *δ* 0.64, 0.85 (24H, 2 d, *J*=6.9 Hz, CH_3), 2.31 (4H, m, C*H*-$(CH_3)_2$), 3.45 (4H, m, *α*-C*H*), 4.36, 5.10 (8H, 2 br s, NH_2), 6.18 (2H, s, C*H* (Ph_2acac_{ap})), 6.37 (4H, s, C*H*

(Ph$_2$acac$_{\text{bas}}$)), 6.72 (5H, m, C*H*$_{\text{ar}}$), 6.82 (5H, br s, O*H*), 6.95 (4H, m, C*H*$_{\text{ar}}$), 7.21 (12H, m, C*H*$_{\text{ar}}$), 7.29 (8H, m, C*H*$_{\text{ar}}$), 7.41 (5H, m, C*H*$_{\text{ar}}$), 7.48 (10H, m, C*H*$_{\text{ar}}$), 7.74 (8H, m, C*H*$_{\text{ar}}$), 7.88 (8H, m, C*H*$_{\text{ar}}$); ^{13}C{^{1}H} NMR (CDCl$_3$, 400 MHz): δ 16.4 (*C*H$_3$), 20.1 (*C*H$_3$), 30.4 (*i*Pr-*C*H), 61.2 (α-*C*H), 93.2 (*C*H (Ph$_2$acac$_{\text{ap}}$)), 94.5 (*C*H (Ph$_2$acac$_{\text{bas}}$)), 126.8, 127.4, 127.6 (*m*-*C*H$_{\text{ar}}$), 127.7, 127.9, 128.0 (*o*-*C*H$_{\text{ar}}$), 130.8 (*p*-*C*H$_{\text{ar}}$), 139.0, 139.9, 140.2 (*i*-*C*H$_{\text{ar}}$), 180.9 (*C*O$_2$), 182.4, 183.2, 183.7, 184.7 (*C*O (Ph$_2$acac$_{\text{ap/bas}}$)); ^{1}H,^{89}Y gHMQC (CDCl$_3$, 500.13 MHz): δ 59.2; IR [cm^{-1}]: 3615 (νOH), 1680, 1597 (νCO), 1554, 1521, 1479, 1456, 1391, 1102, 1032, 751, 721, 689, 642; Raman [cm^{-1}]: 3055 (νOH), 1595 (νCO), 1488, 1440, 1290, 1283, 1176, 1061, 1002, 998, 939, 789, 782, 671, 604, 372; $C_{110}H_{111}N_4O_{25}Y_5$ (2333.60): calcd. C, 56.62, H, 4.79, N, 2.40; found C, 56.35, H, 4.81, N, 2.13.

[Y$_5$(μ_4-OH)(μ_3-OH)$_4$(L-Trp)$_4$(Ph$_2$acac)$_6$] **(*4*)**

Yield (single crystals): 13 %; $[\alpha]^{20}$ = -702.69 (CH$_2$Cl$_2$, *c* = 0.47); ^{1}H NMR (CDCl$_3$, 400 MHz): δ 3.03 (4H, dd, *J*=9.4 Hz, 14.6 Hz, C*H*$_2$), 3.34 (4H, m, C*H*$_2$), 4.02 (br s, N*H*$_2$), 4.37 (4H, br s, N*H*), 5.18 (4H, t, *J*=9.3 Hz, α-C*H*), 6.24 (6H, s, C*H* (Ph$_2$acac)), 6.66 (4H, m, C*H*$_{\text{ar}}$), 6.77 (10H, m, C*H*$_{\text{ar}}$), 6.93 (4H, m, C*H*$_{\text{ar}}$), 7.02 (4H, m, C*H*$_{\text{ar}}$), 7.07 (6H, m, C*H*$_{\text{ar}}$), 7.17 (8H, m, C*H*$_{\text{ar}}$), 7.22 (4H, m, C*H*$_{\text{ar}}$), 7.35 (14H, m, C*H*$_{\text{ar}}$), 7.49 (10H, m, C*H*$_{\text{ar}}$), 7.80 (14H, m, C*H*$_{\text{ar}}$); ^{13}C{^{1}H} NMR (CDCl$_3$, 400 MHz): δ 26.9 (*C*H$_2$), 40.7 (α-*C*H), 94.5 (*C*H (Ph$_2$acac)), 110.7 (γ-*C$_q$*), 118.6 (*C*H$_{\text{ar}}$), 126.9 (*C*H$_{\text{ar}}$), 127.1 (*C*H$_{\text{ar}}$), 127.3 (*C*H$_{\text{ar}}$), 127.7 (*C*H$_{\text{ar}}$), 127.9 (*C*H$_{\text{ar}}$), 128.1 (*C*H$_{\text{ar}}$), 128.3 (*C*H$_{\text{ar}}$), 128.7 (*C*H$_{\text{ar}}$), 136.1 (*i*- *C*H$_{\text{ar}}$), 140.2 (*i*-*C*H$_{\text{ar}}$), 181.4 (*C*O$_2$), 181.9 (*C*O$_2$), 184.5, 185.2 (*C*O(Ph$_2$acac$_{\text{ap/bas}}$)); IR [cm^{-1}]: 3628 (νOH), 3449, 3056, 1653, 1596, 1551, 1517 (νCO), 1478, 1453, 1417, 1392, 1311, 1223, 1180, 1069, 1024, 1000, 942, 784, 720, 687, 656, 609, 524; Raman [cm^{-1}]: 3056, 1594 (νCO), 1487, 1439, 1290, 1285, 1175, 1058, 998, 937, 669; $C_{134}H_{115}N_8O_{25}Y_5$ (2681.91): calcd. C, 60.01, H, 4.32, N, 4.18; found C, 59.76, H, 4.47, N, 3.93.

[Y$_5$(μ_4-OH)(μ_3-OH)$_4$(Ph$_2$Gly)$_4$(Ph$_2$acac)$_6$] **(*5*)**

Yield (single crystals): 40 %; ^{1}H NMR (CDCl$_3$, 400 MHz): δ 6.20 (4H, s, C*H* (Ph$_2$acac$_{\text{bas}}$), 6.27 (2H, s, C*H* (Ph$_2$acac$_{\text{ap}}$)), 6.43 (4H, m, C*H*$_{\text{ar}}$), 6.75 (8H, m, C*H*$_{\text{ar}}$), 6.87 (4H, m, C*H*$_{\text{ar}}$), 6.97 (10H, m, C*H*$_{\text{ar}}$), 7.03 (10H, m, C*H*$_{\text{ar}}$), 7.20 (16H, m, C*H*$_{\text{ar}}$), 7.24 (6H, m, C*H*$_{\text{ar}}$), 7.29 (6H, m, C*H*$_{\text{ar}}$), 7.37 (10H, m, C*H*$_{\text{ar}}$), 7.54 (20H, m, C*H*$_{\text{ar}}$), 8.00 (6H, m, C*H*$_{\text{ar}}$); ^{13}C{^{1}H} NMR (CDCl$_3$, 400 MHz): δ 70.9 (α-C), 95.1 (CH (Ph$_2$acac)), 125.3 (*C*H$_{\text{ar}}$), 127.2 (*C*H$_{\text{ar}}$), 127.4 (*C*H$_{\text{ar}}$), 127.6 (*C*H$_{\text{ar}}$), 127.9 (*C*H$_{\text{ar}}$), 128.2 (*C*H$_{\text{ar}}$), 128.7 (*C*H$_{\text{ar}}$), 129.0 (*C*H$_{\text{ar}}$), 137.9 (*C*H$_{\text{ar}}$), 140.1 (*C*H$_{\text{ar}}$), 143.0 (*C*H$_{\text{ar}}$), 146.3 (*C*H$_{\text{ar}}$), 179.2 (*C*O$_2$)), 183.1 (*C*O$_2$)), 185.9

(CO($Ph_2acac_{ap/bas}$)); IR [cm^{-1}]: 3619 (νOH), 1665 (νCO), 1596, 1551, 1520, 1479, 1452, 1442, 1387, 1313, 1225, 1200, 1069, 1023, 943, 804, 751, 721, 689, 619, 526; Raman [cm^{-1}]: 3120, 1593 (νCO), 1291, 1285, 1175, 1061, 998, 912; $C_{146}H_{118}N_4O_{25}Y_5$ (2773.04): calcd. C, 63.24, H, 4.29, N, 2.02; found C, 62.64, H, 4.35, N, 1.75.

*[$Dy_5(\mu_4$-OH)(μ_3-OH)$_4$(D-PhGly)$_4$($Ph_2acac)_6$] (**6**)*

Yield (single crystals): 35 %; IR [cm^{-1}]: 3352, 3285, 1596, 1553, 1521, 1480, 1459, 1396, 1311, 1027, 1012, 948, 600; Raman [cm^{-1}]: 3045, 1592 (νCO), 1487, 1443, 1290, 1283, 1178, 1064, 1005, 998, 941, 784, 670, 608, 398; $C_{122}H_{103}N_4O_{25}Dy_5 \cdot CH_2Cl_2$ (2922.57): calcd. C, 50.55, H, 3.62, N, 1.92; found C, 50.19, H, 3.58, N, 1.70.

4.2.1.3 General Procedure for [$Ln_{15}(\mu_3$-OH)$_{20}$($PepCO_2)_{10}$($Ph_2acac)_{10}$Cl]Cl_4 (**7**-**9**)

$PepCO_2H \cdot HCl$ (647 mg, 1.96 mmol, 0.59 eq.) was suspended in a stirred solution of KO*t*Bu (1.017 g, 8.79 mmol, 2.67 eq.) in 20 mL of methanol. The resulting colourless suspension was stirred for 30 min at ambient temperature. Subsequently, a solution of [$LnCl_3 \cdot (H_2O)_6$] (Ln = Y: 1.00 g; Tb: 1.23 g; Dy: 1.24 g, 3.30 mmol, 1.00 eq.) in 20 mL of methanol was added dropwise. After stirring for further 45 min, Ph_2acacH (503 mg, 2.20 mmol, 0.67 eq.) in 20 mL of methanol was slowly added using a dropping funnel. The turbid, viscous reaction mixture (**7**: colourless; **8**, **9**: yellow) was allowed to stir overnight at r.t.. The solid phase was removed via filtration leaving a clear colourless (**7**) or yellow (**8**, **9**) filtrate which was evaporated to dryness *in vacuo* afterwards. The crude yellow residues were dissolved in 3 mL of DMF, whereas a colourless salt-like fraction remained undissolved and, hence, had to be filtered off. Slow diffusion of water into the mother liquor under reduced pressure induced formation of large crystals of **7** (540 mg, colourless), **8** (585 mg, orange) and **9** (964 mg, yellow) suitable for single crystal X-ray analysis after two weeks (all yields refer to the amounts of [$LnCl_3 \cdot (H_2O)_6$] applied).

*[$Y_{15}(\mu_3$-OH)$_{20}$($PepCO_2)_{10}$($Ph_2acac)_{10}$Cl]Cl_4 (**7**)*

Yield (single crystals): 35 %; ^{1}H NMR (500 MHz, $CDCl_3$): δ 1.31 (s, 90H, 10 x C(CH_3)$_3$), 3.01 (br s, 20H, 10 x α-CH_2), 3.25 (br s, 20H, 20 x OH), 3.71, 4.30 (2 br s, 20H, 10 x CH_2-NH_{Boc}), 3.85 (br s, 20 H, 10 x C_6H_4-CH_2-NH_{Gly}), 4.23 (s, 10H, 10 x O_2C-CH_2-NH), 4.72 (s, 10 H, 10 x NH_{Boc}), 6.30 (s, 10H, CO-CH-CO) 6.82 (m, 20H, CH_{ar}), 6.94 (m, 40H, CH_{ar}), 7.07

(m, 20H, CH_{ar}), 7.30 (m, 20H, CH_{ar}), 7.57 (m, 20H, CH_{ar}), 7.66 (m, 20H, CH_{ar}); $^{13}C\{^1H\}$ NMR (500 MHz, $CDCl_3$): δ = 28.3 (C(CH_3)$_3$), 31.3 (CH_2-NH_{Boc}), 44.0 (α-CH_2), 52.8 (C_6H_4-CH_2-NH_{Gly}), 78.7 (C-(CH_3)$_3$), 94.0 (CO-CH-CO), 126.8 (CH_{ar}), 127.2 (CH_{ar}), 127.9 (CH_{ar}), 128.5 (CH_{ar}), 128.6 (CH_{ar}), 130.4 (CH_{ar}), 132.4 (CH_{ar}), 137.6 (CH_{ar}), 139.5 (CH_{ar}), 139.9 (CH_{ar}), 156.1 ($CO_2C(CH_3)_3$), 181.0 (CH_2COO), 184.7 ppm (CO-CH-CO); ^1H,^{89}Y gHMQC ($CDCl_3$, 500.13 MHz): δ 106.2, 107.3; IR [cm^{-1}]: 3240, 1701, 1592, 1555, 1521, 1507, 1455, 1391, 1374, 1315, 1226, 1168, 1070, 1025, 944, 785, 751, 722, 688, 659, 610, 604, 523, 420 cm^{-1}; Raman [cm^{-1}]: 3057, 1597, 1489, 1442, 1316, 1287, 1178, 1063, 1001, 940, 793, 763, 647, 593, 380, 214; ESI-MS (MeOH): $[M\text{-}2Cl^-]^{2+}$, 3472.9 *m/z* (100 %); $C_{300}H_{340}Cl_5N_{20}O_{80}Y_{15}\cdot(H_2O)_3\cdot(C_3H_7NO)_3$ (7290.18): calcd. C, 50.91, H, 5.07, N, 4.42; found C, 51.28, H, 5.36, N, 4.11.

*$[Tb_{15}(\mu_3\text{-}OH)_{20}(PepCO_2)_{10}(Ph_2acac)_{10}Cl]Cl_4$ (**8**)*

Yield (single crystals): 33 %; IR [cm^{-1}]: 3063, 2976, 2928, 1706, 1663, 1588, 1551, 1515, 1478, 1442, 1382, 1301, 1285, 1249, 1222, 1162, 1092, 1066, 1023, 1000, 942, 924, 859, 784, 747, 721, 689, 618, 608, 517 cm^{-1}; Raman [cm^{-1}]: 3080, 1597, 1491, 1444, 1291, 1285, 1178, 1063, 999, 757, 675, 375; ESI-MS (EtOH): $[M\text{-}2Cl^-]^{2+}$, 3997.9 *m/z* (100 %); $C_{300}H_{340}Cl_5N_{20}O_{80}Tb_{15}\cdot(H_2O)_4\cdot(C_3H_7NO)_3$ (8358.48): calcd. C, 44.40, H, 4.45, N, 3.85; found C, 44.03, H, 4.80, N, 3.74.

*$[Dy_{15}(\mu_3\text{-}OH)_{20}(PepCO_2)_{10}(Ph_2acac)_{10}Cl]Cl_4$ (**9**)*

Yield (single crystals): 54 %; IR [cm^{-1}]: 1705, 1590, 1552, 1519, 1504, 1476, 1386, 1374, 1315, 1225, 1160, 1066, 1025, 1019, 943, 926, 860, 785, 749, 720, 686, 651, 609, 600, 521, 403 cm^{-1}; Raman [cm^{-1}]: 3054, 1597, 1489, 1442, 1290, 1285, 1178, 1062, 1000, 939, 783, 671, 587, 374, 212 cm^{-1}; ESI-MS (EtOH): $[M\text{-}2Cl^-]^{2+}$, 4025.0 *m/z* (100 %); $C_{300}H_{340}Cl_5N_{20}O_{80}Dy_{15}\cdot$(8120.76): calcd. C, 44.37, H, 4.22, N, 3.45; found C, 44.19, H, 4.48, N, 3.20.

4.2.1.4 General Procedure for $[Ln_9(\mu_4\text{-}O)(\mu_4\text{-}OH)(\mu_3\text{-}OH)_8(acacOEt)_{16}]$ (**10-12**)

NaOH (396 mg, 9.89 mmol, 3 eq.) was dissolved in 20 mL of ethanol and acacOEtH (1.25 mL, 9.89 mmol, 3 eq.) was added. After 40 minutes, a solution of $[LnCl_3\cdot(H_2O)_6]$ (Ln = Y: 1.00 g; Ln = Nd: 1.18 g; Ln = Dy: 1.24 g, 3.30 mmol, 1.00 eq.) in 20 mL of ethanol was added dropewise to give a homogeneous suspension (**10** and **12**: colourless, **11**: blueish). The reaction mixture was stirred overnight at room temperature and filtered, whereupon the filtrate was evaporated to dryness. Subsequently, block-shaped single crystals of compounds **10-12** were received upon slowly cooling a down a hot saturated ethanol solution after twelve hours.

*$[Y_9(\mu_4\text{-}O)(\mu_4\text{-}OH)(\mu_3\text{-}OH)_8(acacOEt)_{16}]$ (**10**)*

Yield (single crystals): 34 %; IR [cm^{-1}]: 1643, 1641, 1549, 1516, 1416, 1394, 1305, 1254, 1170, 1098, 1060, 1021, 970, 787, 635, 584; Raman [cm^{-1}]: 2963, 2919, 1544, 1507, 1362, 1239, 1165, 1093, 1012, 971, 862, 724; $C_{96}H_{153}O_{58}Y_9\cdot(H_2O)_3\cdot$(3089.41): calcd. C, 37.32, H, 5.19; found C, 36.94, H, 4.90.

*$[Nd_9(\mu_4\text{-}O)(\mu_4\text{-}OH)(\mu_3\text{-}OH)_8(acacOEt)_{16}]$ (**11**)*

Yield (single crystals): 31 %; IR [cm^{-1}]: 1644, 1640, 1550, 1514, 1412, 1393, 1305, 1251, 1168, 1097, 1062, 1016, 971, 787, 635; Raman [cm^{-1}]: 2966, 2924, 1541, 1504, 1365, 1243, 1165, 968, 725, 577, 343; $C_{96}H_{153}Nd_9O_{58}\cdot(H_2O)_3\cdot$(3587.43): calcd. C, 32.14, H, 4.47; found C, 31.77, H, 4.34.

*$[Dy_9(\mu_4\text{-}O)(\mu_4\text{-}OH)(\mu_3\text{-}OH)_8(acacOEt)_{16}]$ (**12**)*

Yield (single crystals): 42 %; IR [cm^{-1}]: 1644, 1641, 1550, 1516, 1416, 1393, 1305, 1254, 1168, 1098, 1062, 1018, 971, 787, 635, 582; Raman [cm^{-1}]: 2957, 2913, 1549, 1509, 1431, 1357, 1243, 1166, 1098, 1017, 972, 862, 726; ESI-MS (MeOH): $[M+H^+]^-$, 3698.6 *m/z* (100 %); $C_{96}H_{153}Dy_9O_{58}\cdot$(3697.71): calcd. C, 31.18, H, 4.17; found C, 30.94, H, 4.25.

4.2.2 Preparation of the Polymers 13-17

4.2.2.1 Preparation of $[K\{Nd(Ph_2acac)_4\}(CH_2Cl_2)_2]$ (**13**)

To a stirred solution of KO*t*Bu (1.526 g, 13.2 mmol, 4 eq.) in 40 mL of methanol, Ph_2acacH (2.96 g, 1.65 mmol, 4 eq.) was added. Subsequently, dropwise addition of $[NdCl_3\cdot(H_2O)_6]$ (1.18 g, 3.30 mmol, 1 eq.) in 20 mL of methanol induced precipitation of a green solid. After stirring the reaction mixture overnight, the precipitate was separated via filtration and washed with 3 x 10 mL of methanol to be dried *in vacuo* afterwards. The residue was taken up with 10 mL of dichloromethane and filtered. Layering of the resulting filtrate with 25 mL of *n*-

hexane afforded 0.02 g of $[K\{Nd(Ph_2acac)_4\}(CH_2Cl_2)_2]_n$ as green rectangularly shaped crystals after 4 d.

*$[K(CH_2Cl_2)_2\{Nd(Ph_2acac)_4\}]$ (**13**)*

Yield (single crystals): 4 %; IR [cm^{-1}]: 3649, 3060, 2324, 1756, 1593, 1539, 1510, 1476, 1453, 1377, 1309, 1221, 1058, 1022, 938, 783, 783, 743, 713, 681, 617; Raman [cm^{-1}]: 3065, 1596, 1567, 1514, 1492, 1444, 1359, 1319, 1286, 1223, 1183, 1163, 1062, 1028, 1002, 942, 619; ESI-MS (DMF): $[M\text{-}K^+\text{-}2CH_2Cl_2]^-$, 1037.220 *m/z* (100 %); $C_{60}H_{44}NdO_8$·(1037.23): calcd. C, 66.95, H, 4.12; found C, 66.99, H, 4.14.

4.2.1.2 General Procedure for $[Cs\{Ln(Ph_2acac)_4(C_3H_7NO)_2]_n$ (**14-17**)

To a stirred solution of cesium carbonate (Cs_2CO_3) (2.63 g, 8.00 mmol, 4 eq.) in 20 mL of methanol, dibenzoylmethane (Ph_2acacH) (1.83 g, 8.00 mmol, 4 eq.) was added. Subsequently, dropwise addition of $[LnCl_3\cdot(H_2O)_n]$ (Ln = Pr: 746 mg (n = 7); Nd: 717 mg (n = 6), Sm: 730 mg (n = 6); Dy: 754 mg (n = 6), 2.00 mmol, 1 eq.) in 20 mL of methanol induced precipitation of a blueish solid. After stirring the reaction mixture overnight, the precipitate was separated via filtration and washed with 3 x 10 mL of methanol to be dried *in vacuo* afterwards. The desired polymeric *ate*-compounds were obtained via crystallization from a either a hot concentrated THF/DMF solution (volume ratio: 1/5) or from slow diffusion of diethylether into a concentrated DMF solution to give colourless needle-shaped crystals of $[Cs\{Ln(Ph_2acac)_4\}\cdot(C_3H_7NO)_2]_n$ **14-17** after two days.

*$[Cs\{Pr(Ph_2acac)_4\}(C_3H_7NO)_2]$ (**14**)*

Yield (single crystals): 55 %; IR [cm^{-1}]: 1677, 1593, 1543, 1509, 1476, 1455, 1384, 1301, 1279, 1219, 1180, 1154, 1083, 1066, 1058, 1022, 1000, 990, 939, 926, 847, 811, 782, 749, 715, 683, 617, 606; Raman [cm^{-1}]: 3064, 1597, 1566, 1514, 1491, 1444, 1318, 1284, 1222, 1184, 1157, 1062, 1026, 1003, 942, 794, 619; ESI-MS (DMF): $[M\text{-}Cs^+\text{-}2C_3H_7NO]^-$, 1033.228 *m/z* (100 %); $C_{60}H_{44}CsO_8Pr\ (C_3H_7NO)_2$·(1312.99): calcd. C, 60.37, H, 4.45, N, 2.13; found C, 60.01, H, 4.24, N, 1.75.

[Cs{Nd(Ph$_2$acac)$_4$}(C$_3$H$_7$NO)$_2$] ***(15)***

Yield (single crystals): 34 %; IR [cm^{-1}]: 1667, 1594, 1547, 1513, 1477, 1460, 1416, 1305, 1280, 1220, 1179, 1155, 1067, 1058, 1023, 1000, 940, 925, 847, 811, 782, 740, 721, 689, 618, 607; Raman [cm^{-1}]: 3065, 1597, 1569, 1514, 1492, 1445, 1378, 1318, 1282, 1223, 1184, 1159, 1062, 1003, 942, 794, 619; ESI-MS (DMF): [M-Cs$^+$-2C$_3$H$_7$NO]$^-$, 1036.204 *m*/*z* (100 %); $C_{60}H_{44}CsNdO_8$ $(C_3H_7NO)_2$·(1316.32): calcd. C, 60.22, H, 4.44, N, 2.13; found C, 60.23, H, 4.18, N, 1.65.

[Cs{Sm(Ph$_2$acac)$_4$}(C$_3$H$_7$NO)$_2$] ***(16)***

Yield (single crystals): 84 %; IR [cm^{-1}]: 1677, 1594, 1546, 1512, 1477, 1309, 1281, 1220, 1179, 1155, 1089, 1067, 1060, 1022, 1000, 940, 928, 847, 811, 783, 748, 740, 719, 689, 660, 618, 608; Raman [cm^{-1}]: 3064, 1597, 1568, 1514, 1491, 1445, 1318, 1284, 1222, 1184, 1157, 1125, 1062, 1027, 1003, 942, 869, 794, 687, 619; ESI-MS (DMF): [M-Cs$^+$-2C$_3$H$_7$NO]$^-$, 1046.234 *m*/*z* (100 %); $C_{60}H_{44}CsO_8Sm$ (C_3H_7NO)·(1249.35): calcd. C, 60.57, H, 4.11, N, 1.12; found C, 60.41, H, 3.95, N, 0.92.

[Cs{Dy(Ph$_2$acac)$_4$}(C$_3$H$_7$NO)$_2$] ***(17)***

Yield (single crystals): 58 %; IR [cm^{-1}]: 1678, 1595, 1548, 1510, 1478, 1456, 1419, 1397, 1311, 1301, 1281, 1220, 1180, 1155, 1061, 1023, 1000, 986, 976, 940, 925, 848, 811, 791, 783, 749, 739, 716, 689, 683, 617, 608; Raman [cm^{-1}]: 3065, 1596, 1514, 1492, 1445, 1318, 1283, 1222, 1184, 1160, 1063, 1028, 1002, 943, 793, 688, 620; ESI-MS (DMF): [M-Cs$^+$-2C$_3$H$_7$NO]$^-$, 1056.227 *m*/*z* (100 %); $C_{60}H_{44}CsDyO_8$ $(C_3H_7NO)_{0.5}$·(1224.94): calcd. C, 60.30, H, 3.91, N, 0.57; found C, 60.11, H, 3.64, N, 0.05.

4.3 Single Crystal X-Ray Analysis

4.3.1 General Considerations

A suitable crystal of compounds **1-17** was covered in mineral oil (Aldrich) and mounted onto a glass fiber. The crystal was transferred directly to the -67 °C, -73 °C or -123 °C cold N$_2$ stream of a Stoe IPDS 2 or a Bruker Smart 1000 CCD diffractometer. Subsequent computations were carried out on an Intel Pentium Core2Duo PC.

All structures were solved by the Patterson method (SHELXS-97).[98] The remaining nonhydrogen atoms were located from successive difference Fourier map calculations. The refinements were carried out by using full-matrix least-squares techniques on F^2, minimizing the function $(F_o\text{-}F_c)^2$, where the weight is defined as $4F_0{}^2/2(F_o{}^2)$ and F_o and F_c are the observed and calculated structure factor amplitudes using the program SHELXL-97.[98] Carbon-bound hydrogen atom positions were calculated and allowed to ride on the carbon atoms to which they are bonded. The hydrogen atom contributions of compounds **1**-**17** were calculated, but not refined. The locations of the largest peaks in the final difference Fourier map calculation as well as the magnitude of the residual electron densities in each case were of no chemical significance.

4.3.2 Crystallographic data

4.3.2.1 $[\mathrm{Y_5(\mu_4\text{-}OH)(\mu_3\text{-}OH)_4}(\textit{D}\text{-}\mathrm{PhGly})_4\mathrm{(Ph_2acac)_6}]\cdot 3(\mathrm{CH_2Cl_2})$ (**1**)

Chemical formula	$C_{125}H_{109}Cl_6N_4O_{25}Y_5$
Crystal system	orthorhombic
Space group	$P2_12_12_1$
a [Å]	18.175(5)
b [Å]	19.080(5)
c [Å]	33.846(5)
Volume of unit cell [Å^3]	11737(5)
Temperature [K]	200(2)
Z (no. of formula units per unit cell)	4
Type of absorption correction	integration
μ [mm^{-1}] (absorption coefficient)	2.657
Flack parameter	-0.026(5)
No. of reflections measured	82578
No. of independent reflections	16835
R_{int}	0.0733
R_1 ($I > 2\sigma(I)$)	0.0449
wR_2 (all data)	0.1314
Goof (Goodness of fit)	1.054

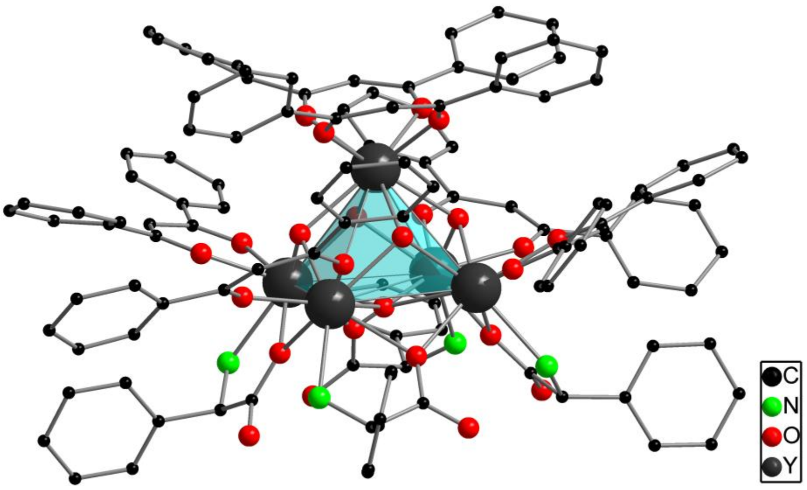

4.3.2.2 $[Y_5(\mu_4\text{-OH})(\mu_3\text{-OH})_4(\mathit{L}\text{-Pro})_4(Ph_2acac)_6]$ (**2**)

Chemical formula	$C_{110}H_{103}N_4O_{25}Y_5$
Crystal system	orthorhombic
Space group	$P2_12_12_1$
a [Å]	16.587(3)
b [Å]	20.348(4)
c [Å]	31.568(6)
Volume of unit cell [$Å^3$]	10655(4)
Temperature [K]	203(2)
Z (no. of formula units per unit cell)	4
Type of absorption correction	integration
μ [mm^{-1}] (absorption coefficient)	2.768
Flack parameter	-0.014(9)
No. of reflections measured	37524
No. of independent reflections	18159
R_{int}	0.1522
R_1 ($I > 2\sigma(I)$)	0.0839
wR_2 (all data)	0.1662
Goof (Goodness of fit)	1.037

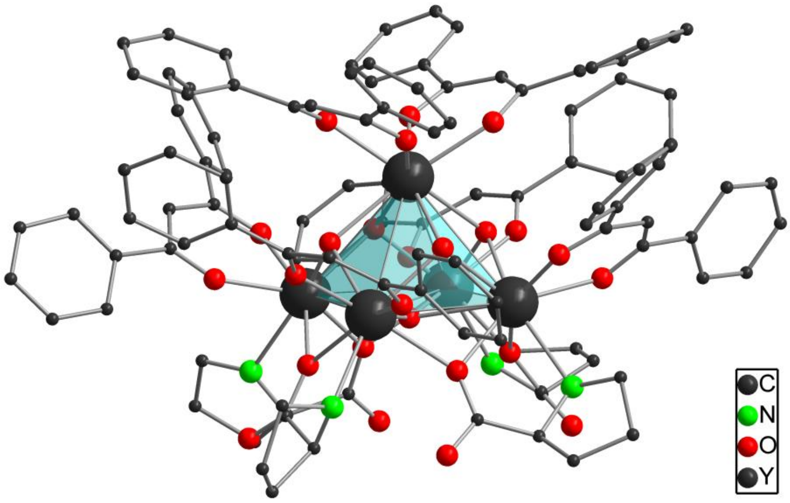

4.3.2.3 $[Y_5(\mu_4\text{-OH})(\mu_3\text{-OH})_4(L\text{-Val})_4(Ph_2acac)_6]$ (**3**)

Chemical formula	$C_{110}H_{111}N_4O_{25}Y_5$
Crystal system	orthorhombic
Space group	$P2_12_12_1$
a [Å]	16.792(3)
b [Å]	20.108(4)
c [Å]	31.514(6)
Volume of unit cell [Å^3]	10650(4)
Temperature [K]	203(2)
Z (no. of formula units per unit cell)	4
Type of absorption correction	integration
μ [mm^{-1}] (absorption coefficient)	2.769
Flack parameter	-0.018(5)
No. of reflections measured	74142
No. of independent reflections	20101
R_{int}	0.1599
R_1 ($I > 2\sigma(I)$)	0.0564
wR_2 (all data)	0.1256
Goof (Goodness of fit)	1.073

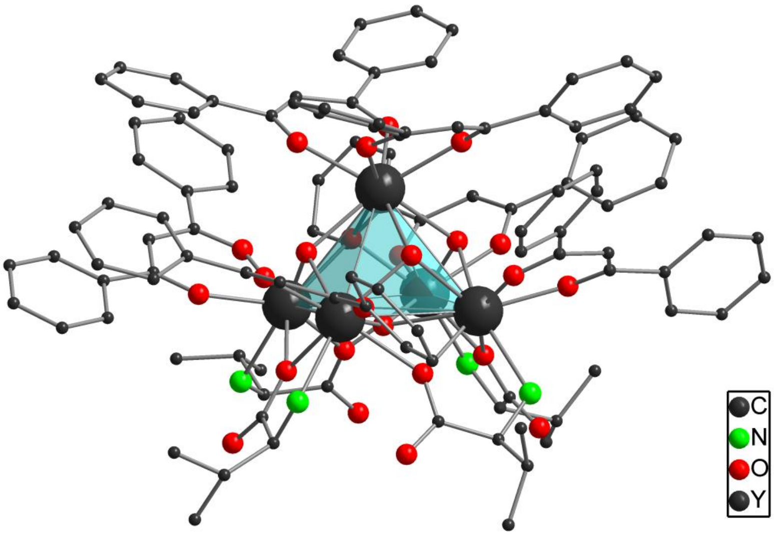

4.3.2.4 $Y_5(\mu_4\text{-OH})(\mu_3\text{-OH})_4(L\text{-Trp})_4(Ph_2acac)_6]\cdot3(CH_2Cl_2)\cdot CH_4O\cdot H_2O$ (**4**)

Chemical formula	$C_{138}H_{127}Cl_6N_4O_{27}Y_5$
Crystal system	orthorhombic
Space group	$P2_12_12_1$
a [Å]	19.306(4)
b [Å]	23.271(5)
c [Å]	30.474(6)
Volume of unit cell [Å^3]	13691(5)
Temperature [K]	150(2)
Z (no. of formula units per unit cell)	4
Type of absorption correction	integration
μ [mm^{-1}] (absorption coefficient)	2.287
Flack parameter	0.027(7)
No. of reflections measured	86650
No. of independent reflections	24156
R_{int}	0.1278
R_1 ($I > 2\sigma(I)$)	0.0784
wR_2 (all data)	0.1992
Goof (Goodness of fit)	1.071

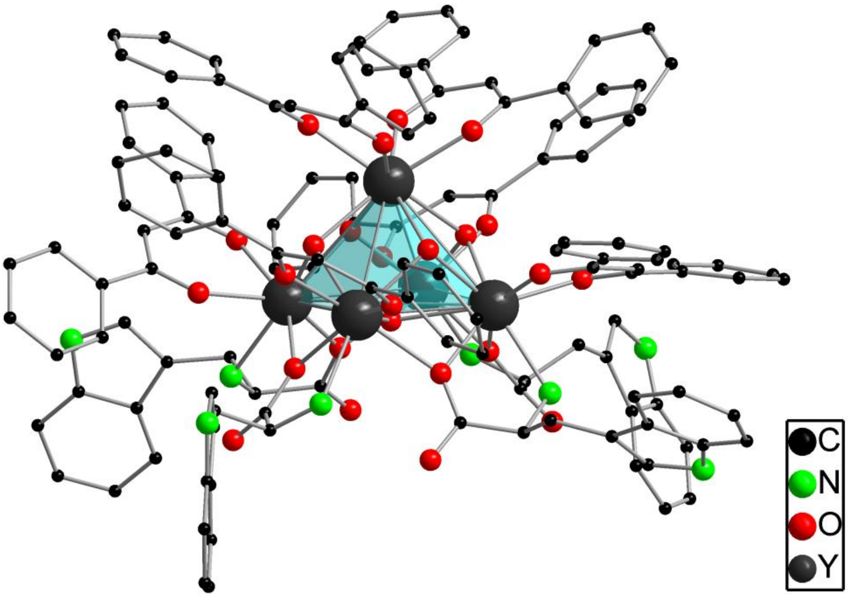

4.3.2.5 $Y_5(\mu_4\text{-}OH)(\mu_3\text{-}OH)_4(Ph_2Gly)_4(Ph_2acac)_6]\cdot 1.5C_7H_8\cdot CH_4O$ (**5**)

Chemical formula	$C_{157.5}H_{135}N_4O_{26}Y_5$
Crystal system	triclinic
Space group	$P\bar{1}$
a [Å]	16.750(3)
b [Å]	18.614(4)
c [Å]	25.866(5)
α [°]	83.65(3)
β [°]	74.96(3)
γ [°]	75.81(3)
Volume of unit cell [Å^3]	7541(3)
Temperature [K]	200(2)
Z (no. of formula units per unit cell)	2
Type of absorption correction	integration
μ [mm^{-1}] (absorption coefficient)	1.971
No. of reflections measured	26614
No. of independent reflections	9432
R_{int}	0.1505
R_1 ($I > 2\sigma(I)$)	0.0861
wR_2 (all data)	0.2096
Goof (Goodness of fit)	0.850

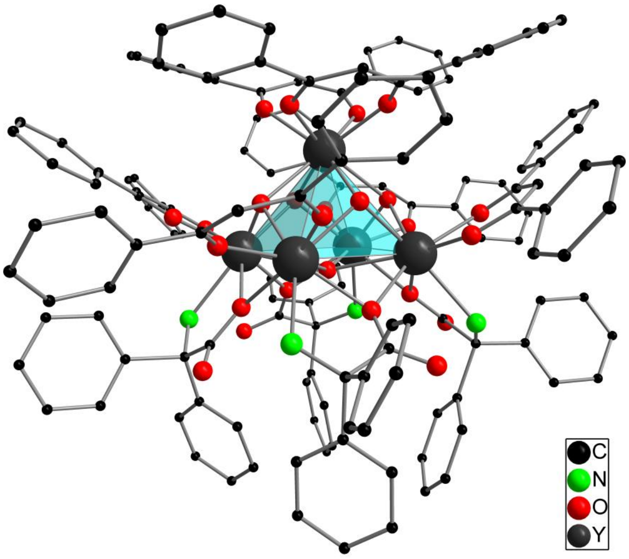

4.3.2.6 $Dy_5(\mu_4\text{-}OH)(\mu_3\text{-}OH)_4(\textit{D}\text{-}PhGly)_4(Ph_2acac)_6]$ (**6**)

Chemical formula	$C_{125}H_{109}Cl_6Dy_5N_4O_{25}$
Crystal system	orthorhombic
Space group	$P2_12_12_1$
a [Å]	18.213(4)
b [Å]	19.227(4)
c [Å]	33.930(7)
Volume of unit cell [Å^3]	11882(4)
Temperature [K]	150(2)
Z (no. of formula units per unit cell)	4
Type of absorption correction	none
μ [mm^{-1}] (absorption coefficient)	3.315
Flack parameter	not determined
No. of reflections measured	26172
No. of independent reflections	14108
R_{int}	0.1956
R_1 ($I > 2\sigma(I)$)	0.0530
wR_2 (all data)	0.1367
Goof (Goodness of fit)	1.017

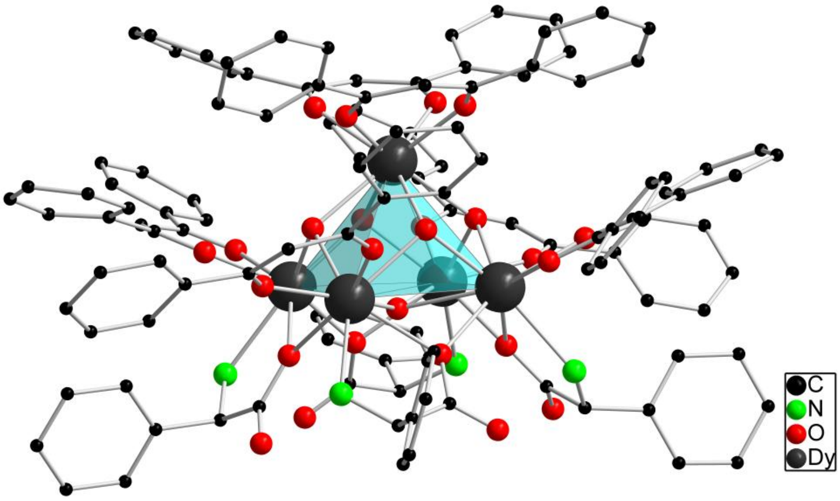

4.3.2.7 $[Y_{15}(\mu_3\text{-}OH)_{20}(PepCO_2)_{10}(Ph_2acac)_{10}Cl]Cl_4\cdot 4(C_3H_7NO)\cdot 7(H_2O)$ (**7**)

Chemical formula	$C_{312}H_{382}Cl_5N_{24}O_{91}Y_{15}$
Crystal system	monoclinic
Space group	$P2_1/n$
a [Å]	25.244(5)
b [Å]	47.870(10)
c [Å]	31.503(6)
β [°]	102.29(3)
Volume of unit cell [Å^3]	37.197(13)
Temperature [K]	200(2)
Z (no. of formula units per unit cell)	4
Type of absorption correction	integration
μ [mm^{-1}] (absorption coefficient)	2.421
No. of reflections measured	62003
No. of independent reflections	34764
R_{int}	0.1517
R_1 ($I > 2\sigma(I)$)	0.1156
wR_2 (all data)	0.3397
Goof (Goodness of fit)	1.027

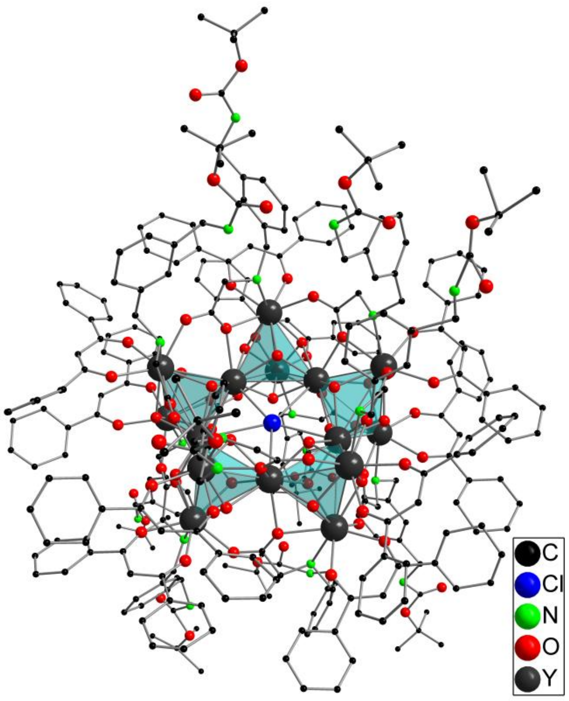

4.3.2.8 $[Tb_{15}(\mu_3\text{-}OH)_{20}(PepCO_2)_{10}(Ph_2acac)_{10}Cl]Cl_4\cdot 3(C_3H_7NO)\cdot 3(H_2O)$ (**8**)

Chemical formula	$C_{309}H_{367}Cl_5N_{23}O_{86}Tb_{15}$
Crystal system	monoclinic
Space group	$P2_1/n$
a [Å]	25.264(5)
b [Å]	47.896(10)
c [Å]	31.413(6)
β [°]	102.01(3)
Volume of unit cell [Å^3]	37179(13)
Temperature [K]	200(2)
Z (no. of formula units per unit cell)	4
Type of absorption correction	integration
μ [mm^{-1}] (absorption coefficient)	2.920
No. of reflections measured	62084
No. of independent reflections	24102
R_{int}	0.1610
R_1 ($I > 2\sigma(I)$)	0.0787
wR_2 (all data)	0.2214
Goof (Goodness of fit)	0.847

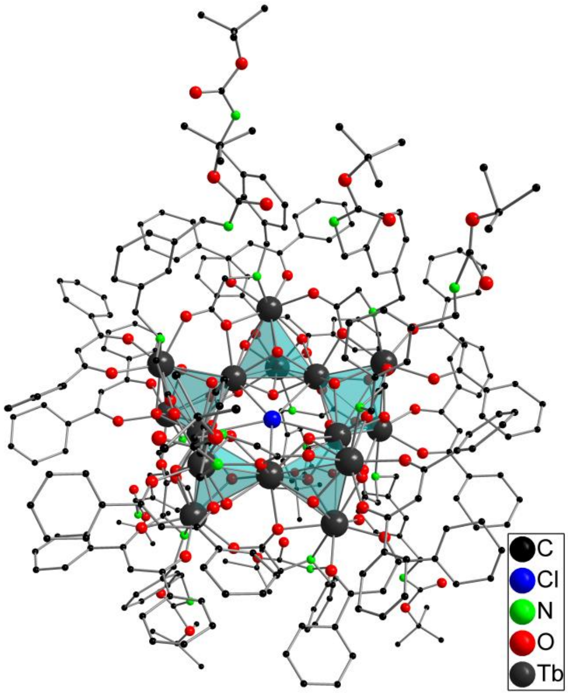

4.3.2.9 $[Dy_{15}(\mu_3\text{-}OH)_{20}(PepCO_2)_{10}(Ph_2acac)_{10}Cl]Cl_4\cdot 3(C_3H_7NO)\cdot 3(H_2O)$ (**9**)

Chemical formula	$C_{309}H_{367}Cl_5Dy_{15}N_{23}O_{86}$
Crystal system	monoclinic
Space group	$P2_1/n$
a [Å]	25.328(5)
b [Å]	47.966(10)
c [Å]	31.389(6)
β [°]	102.10(3)
Volume of unit cell [Å^3]	37.286(13)
Temperature [K]	200(2)
Z (no. of formula units per unit cell)	4
Type of absorption correction	integration
μ [mm^{-1}] (absorption coefficient)	3.073
No. of reflections measured	65449
No. of independent reflections	42040
R_{int}	0.0849
R_1 ($I > 2\sigma(I)$)	0.0634
wR_2 (all data)	0.2061
Goof (Goodness of fit)	0.971

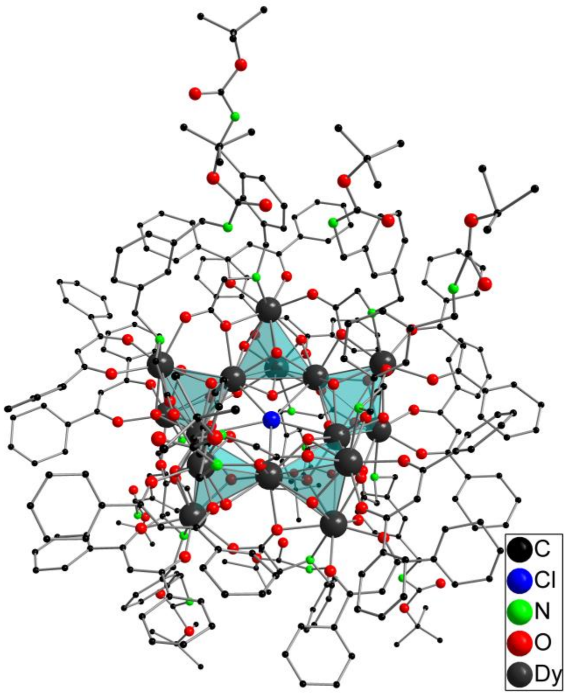

4.3.2.10 $[Y_9(\mu_4\text{-O})(\mu_4\text{-OH})(\mu_3\text{-OH})_8(\text{acacOEt})_{16}]\ 8(C_2H_6O)$ (**10**)

Chemical formula	$C_{112}H_{201}O_{66}Y_9$
Crystal system	cubic
Space group	$Pn\bar{3}n$
a [Å]	29.994(4)
Volume of unit cell [$Å^3$]	26984(5)
Temperature [K]	150(2)
Z (no. of formula units per unit cell)	6
Type of absorption correction	none
μ [mm^{-1}] (absorption coefficient)	2.932
No. of reflections measured	3838
No. of independent reflections	313
R_{int}	0.1680
R_1 ($I > 2\sigma(I)$)	0.0704
wR_2 (all data)	0.1936
Goof (Goodness of fit)	0.376

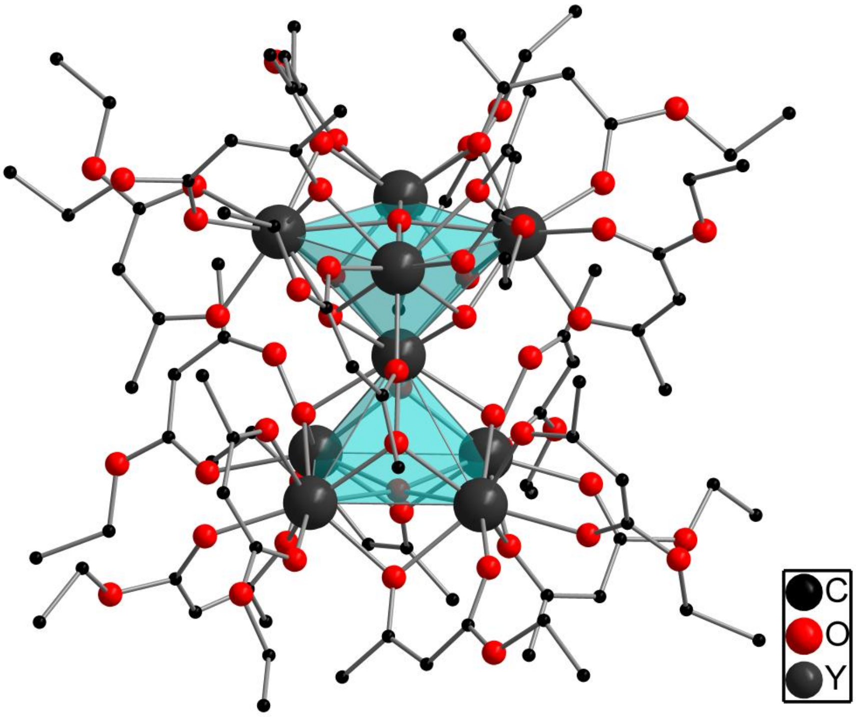

4.3.2.11 $[Nd_9(\mu_4\text{-}O)(\mu_4\text{-}OH)(\mu_3\text{-}OH)_8(acacOEt)_{16}]\ 8(C_2H_6O)$ (**11**)

Chemical formula	$C_{112}H_{201}Nd_9O_{66}$
Crystal system	cubic
Space group	$Pn\bar{3}n$
a [Å]	30.502(4)
Volume of unit cell [Å^3]	28378(6)
Temperature [K]	150(2)
Z (no. of formula units per unit cell)	6
Type of absorption correction	integration
μ [mm^{-1}] (absorption coefficient)	2.492
No. of reflections measured	4491
No. of independent reflections	3353
R_{int}	0.1773
R_1 ($I > 2\sigma(I)$)	0.0872
wR_2 (all data)	0.2107
Goof (Goodness of fit)	1.136

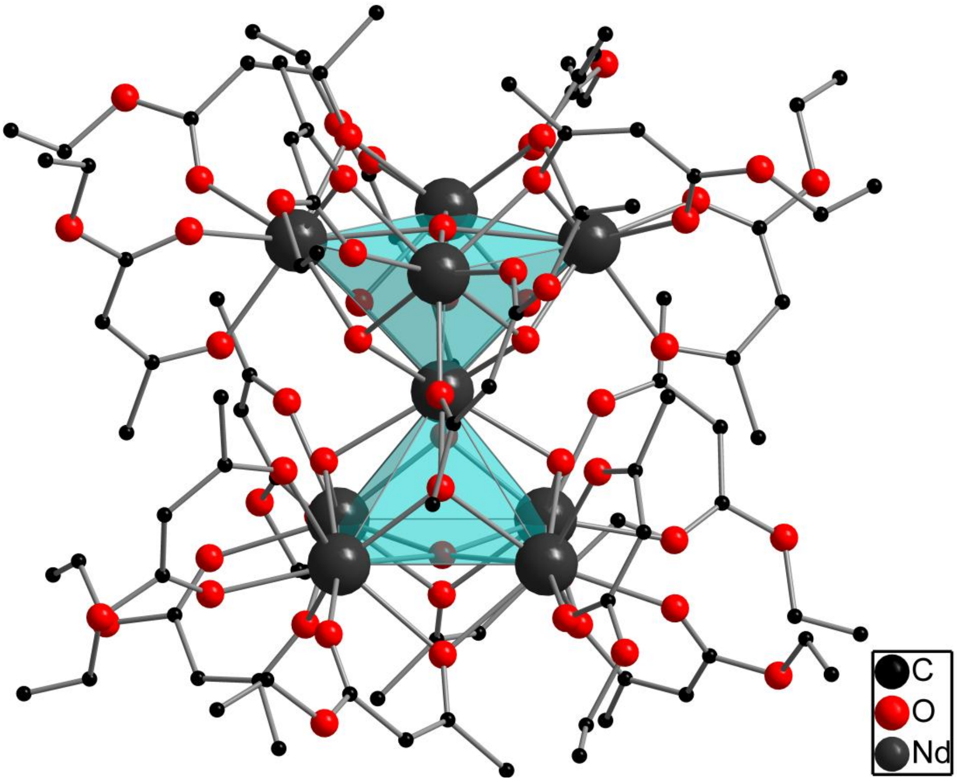

4.3.2.12 $[Dy_9(\mu_4\text{-}O)(\mu_4\text{-}OH)(\mu_3\text{-}OH)_8(acacOEt)_{16}]\ 6(C_2H_6O)$ (**12**)

Chemical formula	$C_{112}H_{189}O_{64}Y_9$
Crystal system	cubic
Space group	$Pn\bar{3}n$
a [Å]	30.076(4)
Volume of unit cell [Å^3]	27207(5)
Temperature [K]	150(2)
Z (no. of formula units per unit cell)	6
Type of absorption correction	none
μ [mm^{-1}] (absorption coefficient)	3.731
No. of reflections measured	4026
No. of independent reflections	3192
R_{int}	0.1754
R_1 ($I > 2\sigma(I)$)	0.0396
wR_2 (all data)	0.1116
Goof (Goodness of fit)	1.092

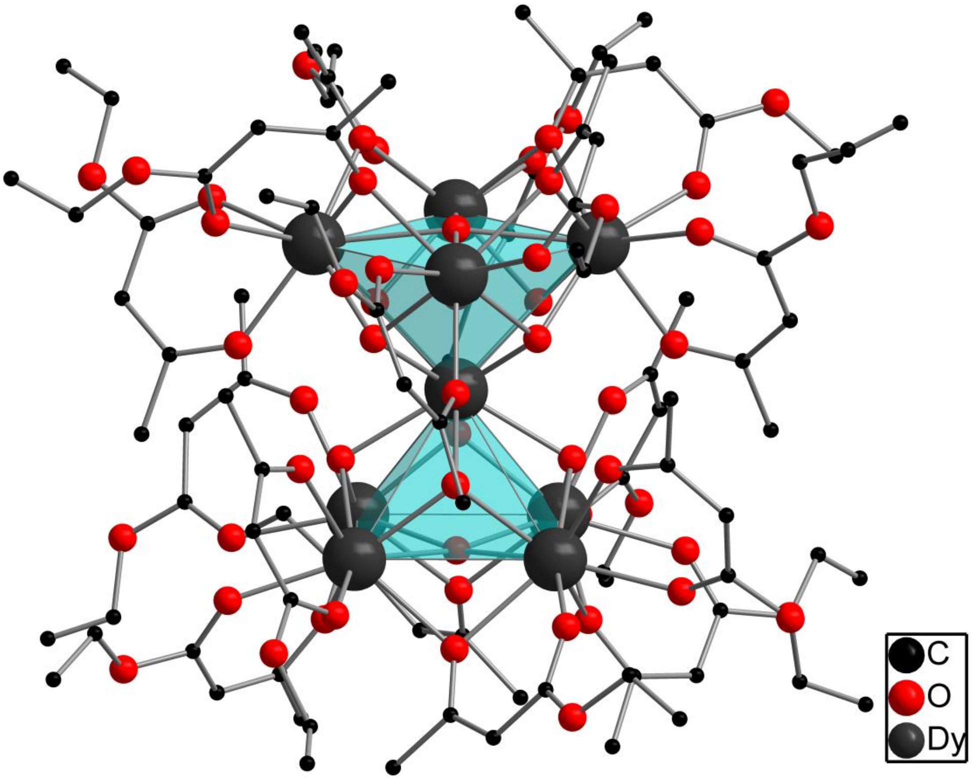

4.3.2.13 $[K\{Nd(Ph_2acac)_4\}(CH_2Cl_2)_2]_n$ (**13**)

Chemical formula	$C_{62}H_{48}Cl_4KNdO_8$
Crystal system	monoclinic
Space group	*C*2/*c*
a [Å]	27.736(6)
b [Å]	7.911(2)
c [Å]	26.035(5)
β [°]	108.93(3)
Volume of unit cell [Å^3]	5403(2)
Temperature [K]	153(2)
Z (no. of formula units per unit cell)	4
Type of absorption correction	none
μ [mm^{-1}] (absorption coefficient)	1.293
No. of reflections measured	6431
No. of independent reflections	4904
R_{int}	0.1296
R_1 ($I > 2\sigma(I)$)	0.0834
wR_2 (all data)	0.2195
Goof (Goodness of fit)	1.222

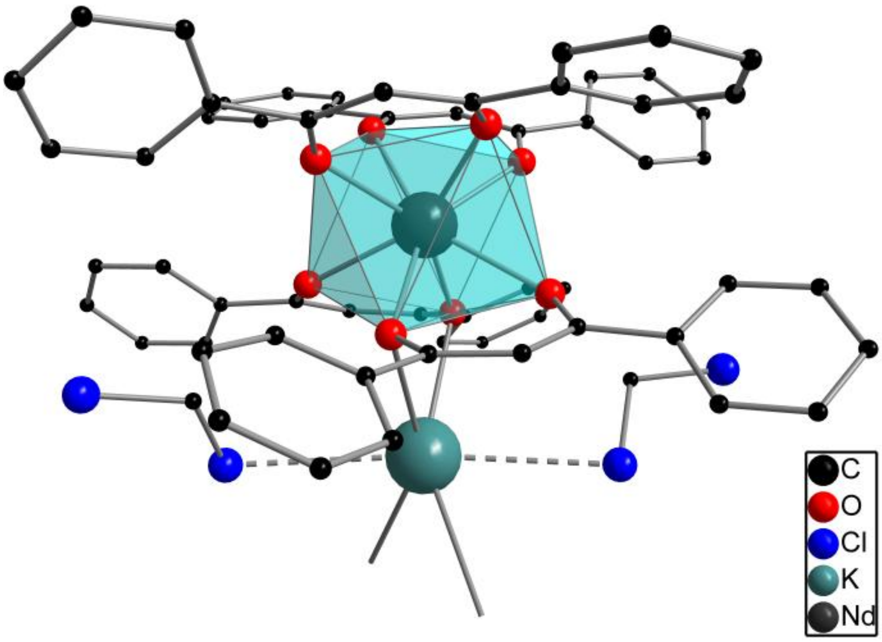

4.3.2.14 $[Cs\{Pr(Ph_2acac)_4\}\cdot 2(C_3H_7NO)]_n$ (**14**)

Chemical formula	$C_{66}H_{58}CsN_2O_{10}Pr$
Crystal system	monoclinic
Space group	*C*2/*c*
a [Å]	30.013(6)
b [Å]	7.927(2)
c [Å]	26.201(5)
β [°]	114.24(3)
Volume of unit cell [Å^3]	5683(2)
Temperature [K]	150(2)
Z (no. of formula units per unit cell)	4
Type of absorption correction	integration
μ [mm^{-1}] (absorption coefficient)	1.551
No. of reflections measured	7662
No. of independent reflections	4264
R_{int}	0.2083
R_1 ($I > 2\sigma(I)$)	0.1153
wR_2 (all data)	0.3242
Goof (Goodness of fit)	0.999

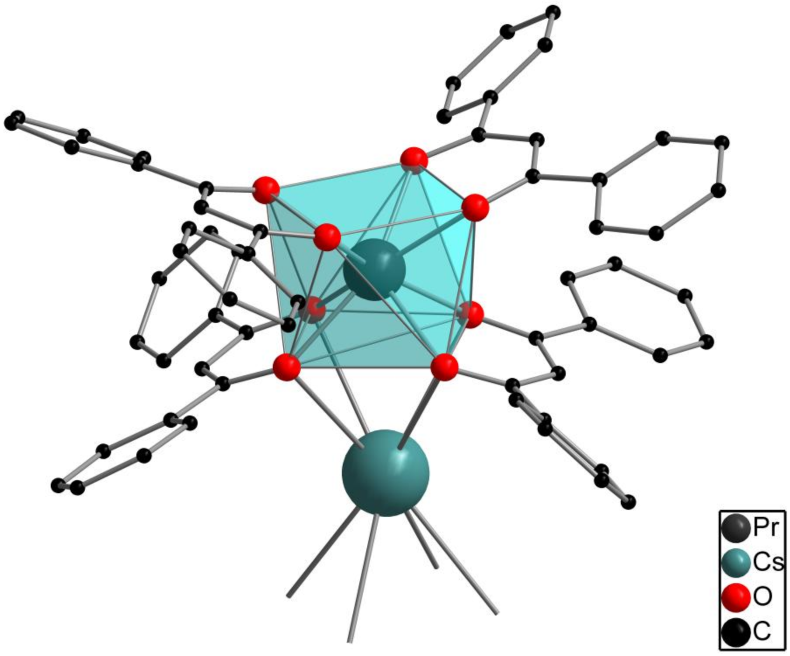

4.3.2.15 $[\mathrm{Cs}\{\mathrm{Nd}(\mathrm{Ph_2acac})_4\}\cdot 2(\mathrm{C_3H_7NO})]_n$ (**15**)

Chemical formula	$C_{66}H_{58}CsN_2NdO_{10}$
Crystal system	monoclinic
Space group	$C2/c$
a [Å]	30.002(7)
b [Å]	7.913(2)
c [Å]	26.166(9)
β [°]	114.08(3)
Volume of unit cell [$Å^3$]	5671(3)
Temperature [K]	293(2)
Z (no. of formula units per unit cell)	4
Type of absorption correction	integration
μ [mm^{-1}] (absorption coefficient)	1.611
No. of reflections measured	7643
No. of independent reflections	5085
R_{int}	0.1960
R_1 ($I > 2\sigma(I)$)	0.0423
wR_2 (all data)	0.0982
Goof (Goodness of fit)	0.897

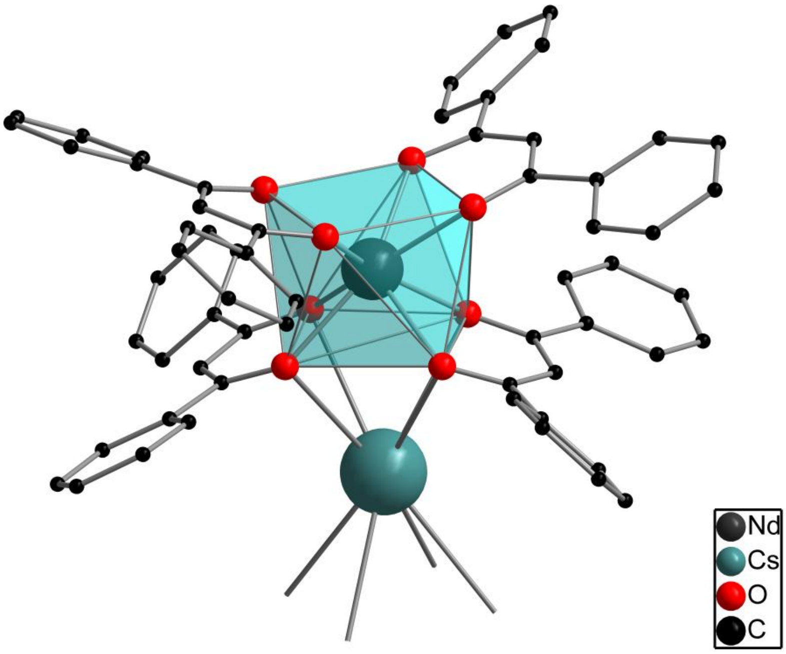

4.3.2.16 $[Cs\{Sm(Ph_2acac)_4\}\cdot 2(C_3H_7NO)]_n$ (**16**)

Chemical formula	$C_{66}H_{58}CsN_2O_{10}Sm$
Crystal system	monoclinic
Space group	$C2/c$
a [Å]	30.220(6)
b [Å]	8.002(2)
c [Å]	26.115(5)
β [°]	114.15(3)
Volume of unit cell [Å^3]	5762(2)
Temperature [K]	206(2)
Z (no. of formula units per unit cell)	4
Type of absorption correction	integration
μ [mm^{-1}] (absorption coefficient)	1.704
No. of reflections measured	7768
No. of independent reflections	7012
R_{int}	0.1065
R_1 ($I > 2\sigma(I)$)	0.1106
wR_2 (all data)	0.3035
Goof (Goodness of fit)	1.104

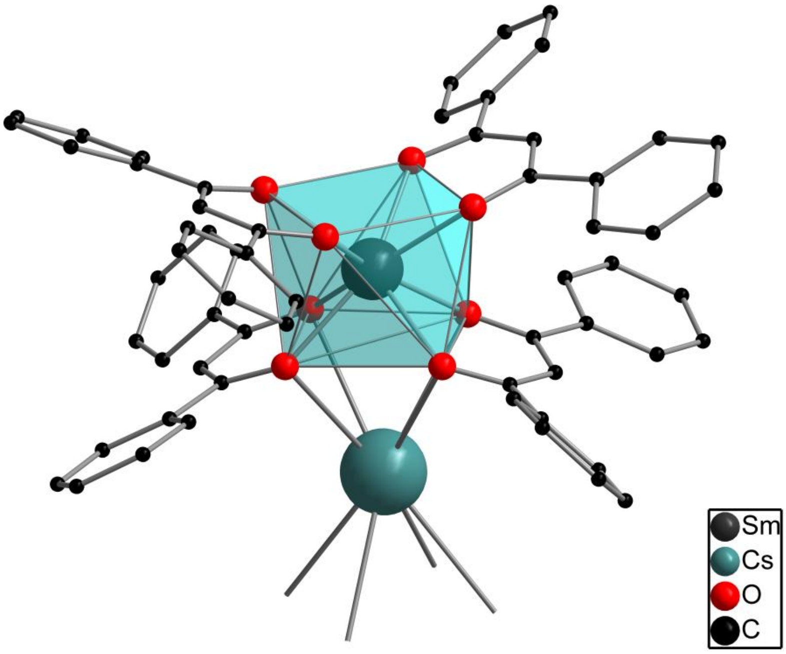

4.3.2.17 $[Cs\{Dy(Ph_2acac)_4\}\cdot 2(C_3H_7NO)]_n$ (**17**)

Chemical formula	$C_{66}H_{58}CsDyN_2O_4$
Crystal system	monoclinic
Space group	$C2/c$
a [Å]	30.068(6)
b [Å]	7.913(2)
c [Å]	25.811(5)
β [°]	113.84(3)
Volume of unit cell [Å^3]	5617(2)
Temperature [K]	150(2)
Z (no. of formula units per unit cell)	4
Type of absorption correction	integration
μ [mm^{-1}] (absorption coefficient)	2.033
No. of reflections measured	6451
No. of independent reflections	5154
R_{int}	0.1747
R_1 ($I > 2\sigma(I)$)	0.1064
wR_2 (all data)	0.2884
Goof (Goodness of fit)	1.097

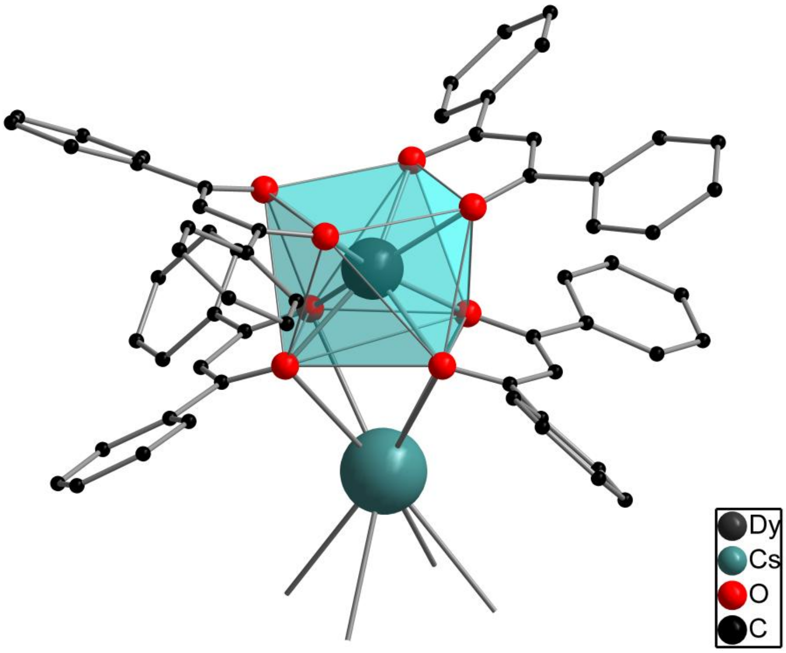

5 SUMMARY / ZUSAMMENFASSUNG

5.1 Summary

Novel functionalized rare earth metal clusters and polymers have been prepared, characterized and investigated with respect to various potential applications.

The literature known tetra- and pentanuclear rare earth metal hydroxy clusters $[Ln_4(\mu_3\text{-}OH)_2(Ph_2acac)_{10}]$ (Ln = Pr, Nd, Sm) and $[Ln_5(\mu_4\text{-}OH)(\mu_3\text{-}OH)_4(Ph_2acac)_{10}]$ (Ln = Y, Eu) were embedded into different polymer matrices applying the miniemulsion polymerization technique to give cluster-polymer hybrid nanocompounds with narrow size distributions. The polymer matrices involved were composed of polystyrene (PS), poly(methyl methacrylate) (PMMA), poly(lauryl methacrylate) (PLMA) and poly(butyl acrylate-*co*-methyl methacrylate) (PBA-*co*-MMA). As a consequence of encapsulation, aqueous dispersions containing the hydrophobic clusters with more than 1000 $mg\cdot L^{-1}$ could be prepared. Subsequent optical investigations revealed the retention of the encapsulated clusters' photophysical properties in aqueous dispersions. Additionally, a very efficient energy transfer from the ligand and polymeric unit to the Eu^{3+}-ions was observed.

Envisioning a functionalization of these pure Ph_2acac clusters, the pentanuclear mixed ligated rare earth metal hydroxy clusters $[Ln_5(\mu_4\text{-}OH)(\mu_3\text{-}OH)_4(\alpha\text{–}AA)_4(Ph_2acac)_6]$ (**1-6**) (Ln = Y: α–AA = *D*-PhGly (**1**), *L*-Pro (**2**), *L*-Val (**3**), *L*-Trp (**4**), Ph_2Gly (**5**); Ln = Dy: α–AA = *D*-PhGly (**6**)) were reproducibly prepared in gram scale and the corresponding solid state structures were established *via* single crystal X-ray analysis (Scheme 5.1). Clusters **1-6** display a square pyramidal $\{Ln_5(\mu_4\text{-}OH)(\mu_3\text{-}OH)_4\}^{10+}$ scaffold, which is coordinatively and electronically saturated by six chelating Ph_2acac ligands and four amino acid ligands acting as bridging chelates. The hydrodynamic radius r_H of valine cluster **3** was determined *via* NMR-based PGSE diffusion experiments, revealing the retention of the cluster's scaffold upon dissolution. Furthermore, 2D NMR experiments with **3** showed a heteronuclear cross coupling between ^{89}Y and ^{1}H nuclei.

Applying similar reaction conditions as for **1-6**, mixed ligated pentadecanuclear clusters accommodating the bifunctionalized peptoid ligand $PepCO_2$ of formula $[Ln_{15}(\mu_3\text{-}OH)_{20}(PepCO_2)_{10}(Ph_2acac)_{10}Cl]Cl_4$ (Ln = Y (**7**), Tb (**8**), Dy (**9**)) were obtained in gram scale (Scheme 5.1). ESI-MS experiments in methanol have shown that the hydroxy bridges in clusters **7-9** undergo a methanolysis. The hydrodynamic radius r_H of the diamagnetic cluster **7** determined *via* PGSE NMR diffusion experiments agrees very well with the value deduced from the X-ray data. The $^{1}H,^{89}Y$ gHMQC spectrum of **7** has confirmed the presence of two chemically distinguishable yttrium atoms. Magnetism and susceptibility measurements of dysprosium cluster **9** have revealed a behaviour which is typical for single-molecule-magnets (SMM). Terbium cluster **8** shows emission of orange luminescence at a wavelength of 613 nm. *In vitro* investigations were performed by incubating HeLa tumor cells with **7**-**9**, showing an internalization of the clusters and subsequent enrichment in either the endoplasmatic reticulum (**7** and **9**) or the cytosol and the nucleus (**8**).

Reaction of $[LnCl_3\cdot(H_2O)_6]$ (Ln = Y, Nd, Dy) with β-ketoester ethyl acetylacetate (acacOEtH) under basic conditions yielded the nonanuclear rare earth metal hydroxy clusters $[Ln_9(\mu_4\text{-}O)(\mu_4\text{-}OH)(\mu_3\text{-}OH)_8(acacOEt)_{16}]$ (Ln = Y (**10**), Nd (**11**), Dy (**12**)) (Scheme 5.1).

The conversion of $[NdCl_3\cdot(H_2O)_6]$ with four equivalents of Ph_2acacH and KO*t*Bu each gave a onedimensional coordination polymer of formula $[K(CH_2Cl_2)_2\{Nd(Ph_2acac)_4\}]_n$ (**13**) (Scheme 5.1), whereas analogous reactions using $[PrCl_3\cdot(H_2O)_7]$ and $[SmCl_3\cdot(H_2O)_6]$ afforded the literature known tetranuclear clusters $[Ln_4(\mu_3\text{-}OH)_2(Ph_2acac)_{10}]$ (Ln = Pr, Sm).

Analogous onedimensional coordination polymers $[Cs\{Ln(Ph_2acac)_4(C_3H_7NO)_2\}]_n$ (Ln = Pr (**14**), Nd (**15**), Sm (**16**), Dy (**17**)) were obtained using Cs_2CO_3 as base. The Ph_2acac ligands of the isostructural compounds **14**-**17** serve to link the metal atoms by chelating and bridging in μ:η^2:η^2-mode (Scheme 5.1). Since the ESI-MS spectra of **13**-**17** in DMF contain signal sets of several ionic species, complex equilibria in solution are suggested. Additionally, ultra-short-time dynamics in solution were investigated *via* femtosecond laser spectroscopy. The results allow an assignment of rare earth metal atom specific relaxation processes which arise from the lifetimes of their individual excited states.

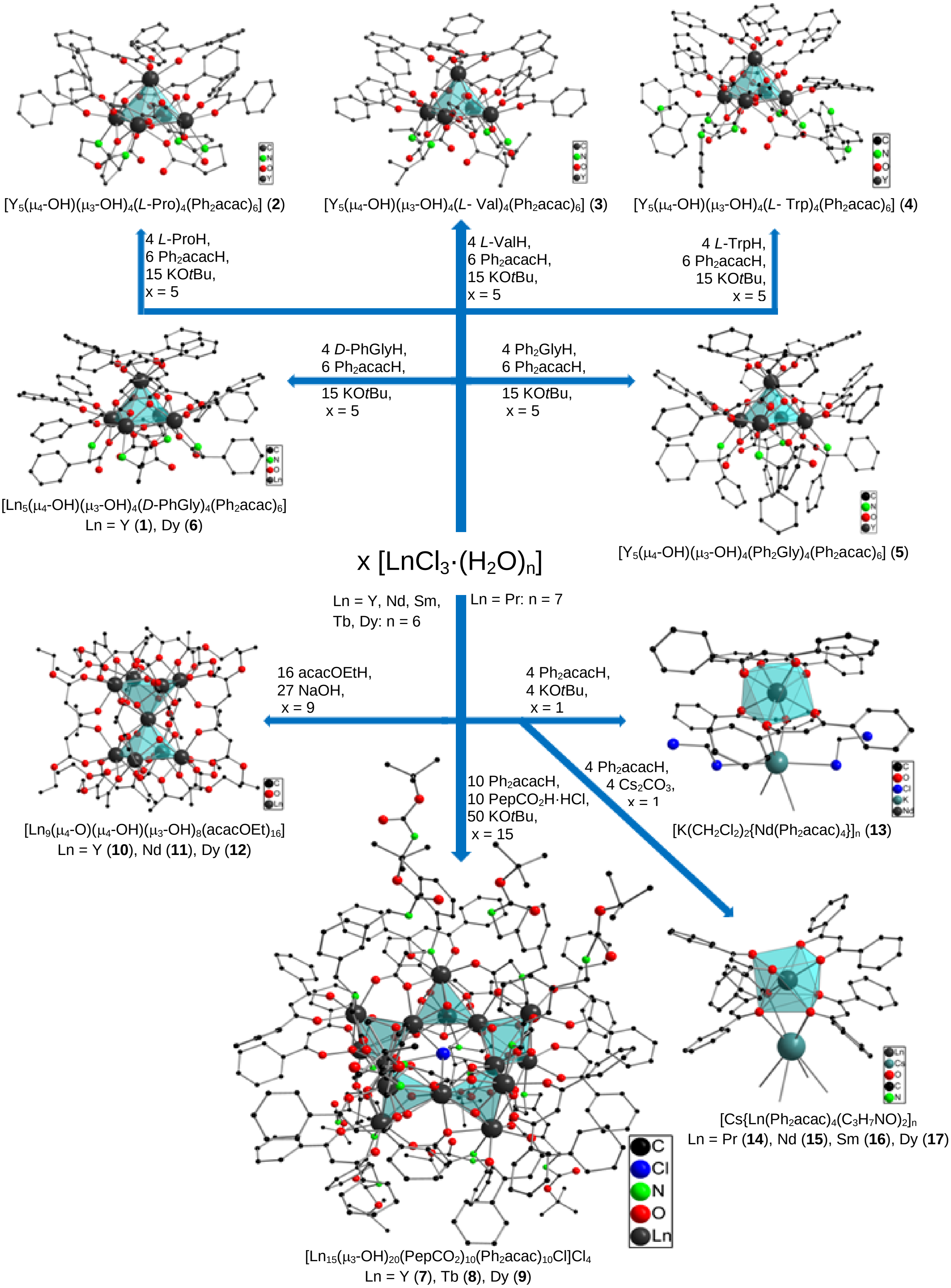

Scheme 5.1. General scheme of all compounds reported in this thesis: amino acid ligated clusters **1-6**, peptoid containing pentadecanuclear clusters **7-9**, nonanuclear clusters **10-12** and 1D-polymers **13-17**.

5.2 Zusammenfassung

Neuartige funktionalisierte Seltenerdmetallcluster und –polymere wurden synthetisiert, charakterisiert und mit Hinblick auf diverse Anwendungen untersucht.

Die literaturbekannten vier- und fünfkernigen Seltenerdmetallhydroxycluster $[Ln_4(\mu_3\text{-}OH)_2(Ph_2acac)_{10}]$ (Ln = Pr, Nd, Sm) und $[Ln_5(\mu_4\text{-}OH)(\mu_3\text{-}OH)_4(Ph_2acac)_{10}]$ (Ln = Y, Eu) wurden unter Anwendung der Miniemulsionspolymerisationstechnik in verschiedene polymere Matrices eingebettet um Cluster/Polymer Hybridnanopartikel mit schmalen Größenverteilungen zu erhalten. Die verwendeten polymeren Matrices bestanden aus Polystyrol (PS), Poly(methylmethacrylat) (PMMA), Poly(laurylmethacrylat) (PLMA) oder Poly(butylacrylat-*co*-methylmethacrylat) (PBA-*co*-MMA). Als Folge der Einkapselung konnten wässrige Dispersionen der hydrophoben Cluster mit mehr als 1000 $mg\cdot L^{-1}$ hergestellt werden. Anschließende optische Untersuchungen deckten die Beibehaltung der fotophysikalischen Eigenschaften in wässrigen Dispersionen auf. Neben diesen Erkenntnissen konnte ein sehr effizienter Energietransfer von den Liganden und den polymeren Fragmenten auf die Eu^{3+}-Ionen beobachtet werden.

Mit der Vision einer Funktionalisierung dieser reinen Ph_2acac-Cluster konnten die pentanuklearen gemischt ligierten Seltenerdmetallhydroxycluster $[Ln_5(\mu_4\text{-}OH)(\mu_3\text{-}OH)_4(\alpha\text{–}AS)_4(Ph_2acac)_6]$ (**1**-**6**) (Ln = Y: α–AS = *D*-PhGly (**1**), *L*-Pro (**2**), *L*-Val (**3**), *L*-Trp (**4**), Ph_2Gly (**5**); Ln = Dy: α–AS = *D*-PhGly (**6**)) reproduzierbar im Grammmaßstab dargestellt werden, und die zugehörigen Festkörperstrukturen wurden durch Einkristallröntgenstrukturanalysen ermittelt (Schema 5.1). Die Cluster **1**-**6** zeichnen sich durch ein quadratisch pyramidales $\{Ln_5(\mu_4\text{-}OH)(\mu_3\text{-}OH)_4\}^{10+}$-Gerüst aus, das koordinativ und elektronisch von sechs chelatisierenden Ph_2acac- und vier verbrückend chelatisierenden Aminosäureliganden gesättigt wird. Der hydrodynamische Radius r_H von **3** wurde experimentell über NMR-basierte PGSE-Messungen ermittelt, und er belegte die Beibehaltung der Clusterstruktur in Lösung. Zudem zeigten 2D NMR-Experimente mit **3** eine heteronukleare Kreuzkopplung zwischen ^{89}Y- und ^{1}H-Kernen.

Unter Anwendung ähnlicher Reaktionsbedingungen wie für **1**-**6** konnten die gemischt ligierten pentadecanuklearen Cluster mit dem Peptoidliganden $PepCO_2$ der Formel $[Ln_{15}(\mu_3\text{-}OH)_{20}(PepCO_2)_{10}(Ph_2acac)_{10}\,Cl]Cl_4$ (Ln = Y (**7**), Tb (**8**), Dy (**9**)) im Grammmaßstab erhalten werden (Schema 5.1). ESI-MS-Experimente zeigten, dass die Hydroxybrücken der Cluster **7**-**9** in Methanol einer Methanolyse unterzogen werden. Der über PGSE NMR-Diffusionsexperimente bestimmte hydrodynamische Radius r_H von **7** stimmt sehr gut mit dem aus den Röntgenstrukturdaten abgeleiteten Wert überein. Ein $^{1}H,^{89}Y$-gHMQC-Spektrum von **7** konnte die Präsenz von zwei chemisch unterscheidbaren Yttriumatomen bestätigen. Magnetismus- und Suszeptibilitätsmessungen an Dysprosiumcluster **9** deckten ein für Einzelmolekülmagneten (*engl.:* single-molecule-magnet (SMM)) typisches Verhalten auf. Die Terbiumverbindung **8** zeigte eine Emission in Form von oranger Lumineszenz bei einer Wellenlänge von 613 nm. *In vitro*-Untersuchungen wurden mit den Clustern **7**-**9** durch Inkubation an HeLa-Tumorzellen durchgeführt, die eine Internalisierung der Cluster und anschließende Anreicherungen in entweder dem endoplasmatischen Retikulum (**7** und **9**) oder dem Zytosol und dem Zellkern aufwiesen.

Eine Umsetzung von $[LnCl_3{\cdot}(H_2O)_6]$ (Ln = Y, Nd, Dy) mit dem β-Ketoester Acetylessigsäureethylacetat (acacOEtH) im basischen Milieu brachte die neunkernigen Seltenerdmetallhydroxycluster $[Ln_9(\mu_4\text{-}O)(\mu_4\text{-}OH)(\mu_3\text{-}OH)_8(acacOEt)_{16}]$ (Ln = Y (**10**), Nd (**11**), Dy (**12**)) hervor (Schema 5.1).

Die Reaktion von $[NdCl_3{\cdot}(H_2O)_6]$ mit jeweils vier Äquivalenten Ph_2acacH und KO*t*Bu ergab ein eindimensionales Koordinationspolymer der Formel $[K(CH_2Cl_2)_2\{Nd(Ph_2acac)_4]_n$ (**13**) (Schema 5.1), wohingegen aus analogen Umsetzungen unter Verwendung von $[PrCl_3{\cdot}(H_2O)_7]$ und $[SmCl_3{\cdot}(H_2O)_6]$ die literaturbekannten vierkernigen Cluster $[Ln_4(\mu_3\text{-}OH)_2(Ph_2acac)_{10}]$ (Ln = Pr, Sm) hervorgingen.

Analoge eindimensionale Koordinationspolymere $[Cs\{Ln(Ph_2acac)_4(C_3H_7NO)_2]_n$ (Ln = Pr (**14**), Nd (**15**), Sm (**16**), Dy (**17**)) wurden erhalten, wenn Cs_2CO_3 anstelle von KO*t*Bu als Base verwendet wurde. Die Ph_2acac-Liganden der isostrukturellen Verbindungen **14**-**17** koordinieren im $\mu{:}\eta^2{:}\eta^2$-Modus an die Metallatome, wodurch sie diese gleichzeitig chelatisieren und miteinander verbrücken (Schema 5.1). Da in den ESI-MS-Spektren von **13**-**17** in DMF Signalsätze von diversen ionischen Spezies beobachtet wurden, kann von komplexen Gleichgewichten in Lösung ausgegangen werden. Zusätzlich wurden Ultrakurzzeitdynamiken von **13**-**15** anhand von Femtosekundenlaserspektroskopie untersucht. Diese erlaubten eine seltenerdmetallatomspezifische Zuordnung jener Relaxationskonstanten, die von den individuellen Lebensdauern der jeweils angeregten Zustände herrühren.

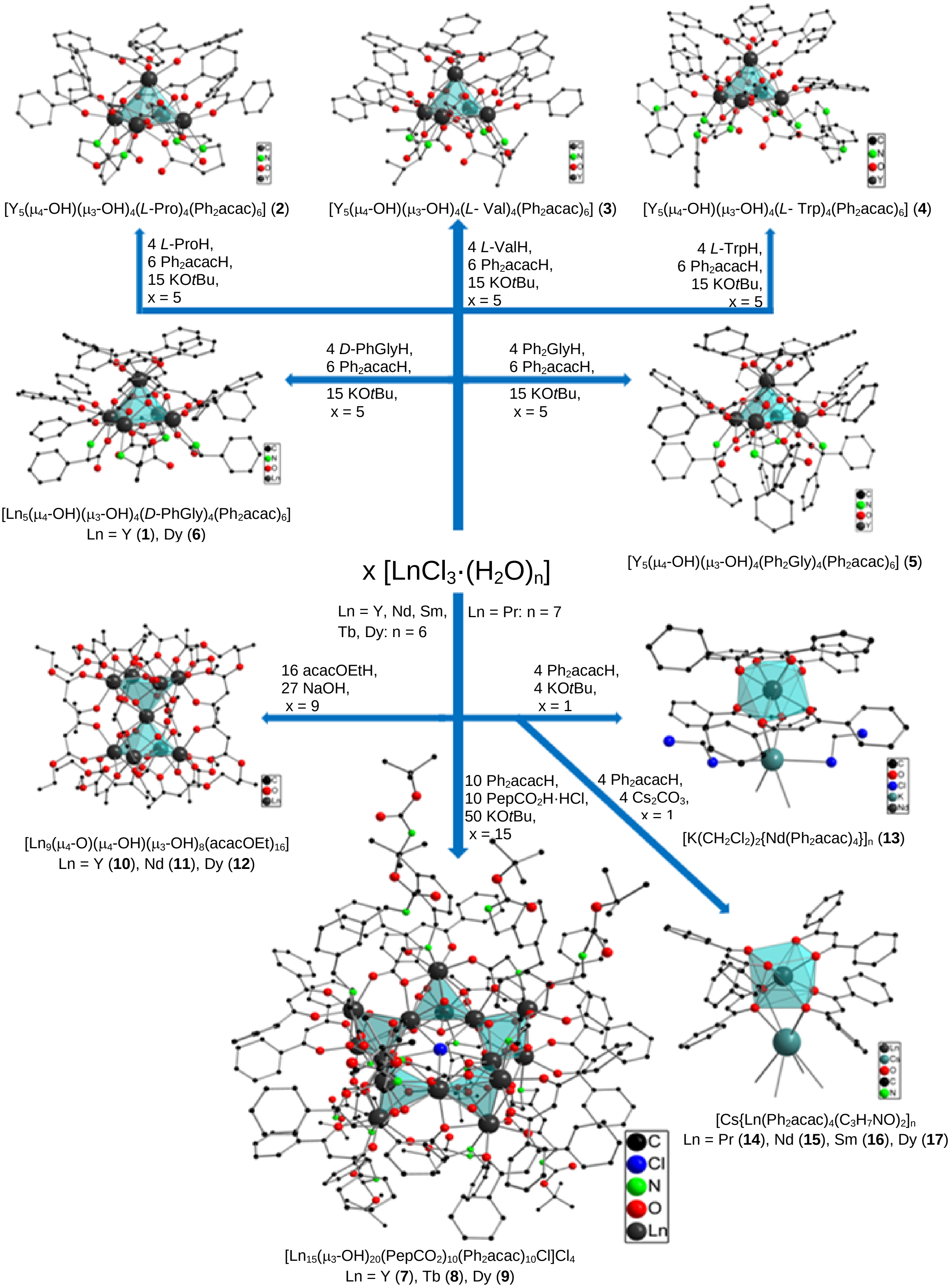

Scheme 5.1. Allgemeines Schema der in dieser Arbeit diskutierten Verbindungen: pentanukleare Aminosäurecluster **1-6**, pentadecanukleare Peptoidcluster **7-9**, nonanukleare Cluster **10-12** und 1D-Polymere **13-17**.

6 APPENDIX

6.1 Abbreviations and Acronyms

6.1.1 General

α-AAH	α-amino acid
acacOEtH	ethyl acetylacetate
acacOMeH	methyl acetylacetate
AFM	atomic force microscopy
Bu	butyl
*n*Bu	*n*-butyl
*t*Bu	*tert*-butyl
calcd.	calculated
CH_2Cl_2	dichloromethane
Cs_2CO_3	caesium carbonate
DMF	*N*,*N*-dimethylformamide
D-PhGlyH	*D*-phenyl glycine
Et	ethyl
EtOH	ethanol
h	hour(s)
ICP-MS	inductively coupled plasma mass spectrometry
ICP-OES	inductively coupled plasma optical emission spectrometry
KO*t*Bu	potassium *tert*-butoxide
Ln	rare earth metal atom or ion
L-ProH	*L*-proline
L-ValH	*L*-valine
L-TrpH	*L*-tryptophan
Me	methyl
MeOH	methanol
min	minute(s)
MMA	methyl methacrylate
n.d.	not determined
NEt_3	triethylamine
PBA-*co*-MMA	poly(butyl acrylate-*co*-methyl methacrylate)

PCCS	photon cross correlation spectroscopy
$PepCO_2 \cdot HCl$	2-[{3-(((*tert*-butoxycarbonyl)amino)methyl)-benzyl}amino]-acetic acid hydrochloride
Ph	phenyl
Ph_2acacH	dibenzoylmethane
Ph_2GlyH	2,2-diphenyl glycine
*i*Pr	*iso*-propyl
*n*Pr	*n*-propyl
PLMA	poly(lauryl methacrylate)
PS	polystyrene
R	organic group
r.t.	room temperature
SEM	scanning electron microscopy
t	time
T	temperature
TBAF	tetrabutylammonium fluoride
TEM	transmission electron microscopy
TFA	trifluoroacetic acid
THF	tetrahydrofuran
T_g	glass transition point
TOF	turnover frequency

6.1.2 Spectroscopy and Spectrometry

NMR	nuclear magnetic resonance
br	broad
d	doublet
dd	doublet of doublet
m	multiplet
qt	quintet
s	singlet
sept	septet
t	triplet

J	coupling constant
i	*ipso*
m	*meta*
o	*ortho*
p	*para*
ESI-MS	electronspray ionization mass spectrometry
IR	Infrared

6.2 Curriculum Vitae

Private

Name	Dominique Tobias Thielemann
Date of Birth	17.05.1982
Place of Birth	Berlin
Parents	Monika Tschümperlin and Jürgen Thielemann
Nationality	German
Family Status	not married

Occupation

since 02/2011	Postdoc studies in the group of Prof. Dr. Peter W. Roesky at the Institute of Inorganic Chemistry at the Karlsruhe Institute of Technology (KIT)
since 03/2008	Teaching assistant in undergraduate laboratory courses (Grundpraktikum Anorganische Chemie: “Quantitative Analyse”) at the Institute of Inorganic Chemistry at the Karlsruhe Institute of Technology (KIT)

Tertiary Education

02/2011	Winner of the *“Award for Best Session Chairperson”* prize at the 7. Koordinationschemie-Treffen at the Universität Stuttgart, **2011**, submitted by *European Journal of Inorganic Chemistry*
02/2011	Award of PhD degree in chemistry in the group of Prof. Dr. Peter W. Roesky at the Institute of Inorganic Chemistry at the Karlsruhe Institute of Technology (KIT) for a doctoral thesis entitled *Novel Functionalized Rare Earth Metal Clusters and Polymers*, predicate: *magna cum laude*
10/2010-02/2011	Fellowship in the Helmholtz-Kolleg featuring “Energy Related Catalysis”

09/2010	Winner of a poster prize award of the “Wöhler-Tagung 2010 - 15. Vortragstagung für Anorganische Chemie” in Freiburg featuring the title *New Amino Acid Ligated Yttrium Hydroxy Clusters*
03/2010-05/2010	Interdoc studies at the School of Chemistry at Monash University in the groups of Prof. Dr. Peter C. Junk, Prof. Dr. Glen B. Deacon and Prof. Dr. Phil Andrews in Melbourne (Victoria, Australia), studying on *New Chiral Rare Earth Metal Hydroxy Clusters*, funded by a scholarship of the Karlsruhe House of Young Scientists (KHYS)
since 03/2008	Continuation of the doctoral thesis at the Institute of Inorganic Chemistry at the Universität Karlsruhe (TH) (since 10/2009: Karlsruhe Institute of Technology KIT)) in the group of Prof. Dr. Peter W. Roesky
10/2007 – 02/2008	Doctoral thesis at the Institute of Inorganic Chemistry at the Freie Universität Berlin in the group of Prof. Dr. Peter W. Roesky
09/2007	Award of Master of Science degree in chemistryat the Freie Universität Berlin, predicate: *1,4*
03/2007 – 09/2007	Master thesis at the Institute of Inorganic Chemistry at the Freie Universität Berlin i the group of Prof. Dr. Peter W. Roesky entitled *Zur Darstellung und Untersuchung von Lanthanoidhydroxoclustern mit α-Aminosäure- und/oder Dibenzoyl-methanidliganden*
11/2006 – 01/2007	Research lab course at the Institute of Inorganic Chemistry at the Freie Universität Berlin in the group of Prof. Dr. Peter W. Roesky orking on the project *Bis(N-isopropyl-iminodiphenylphosphin)methan und Bis[N-(S)-α-methylbenzylimino-diphenylphosphin]methan*
08/2006 – 10/2006	Research lab course at the Institute of Organic Chemistry at the Freie Universiät Berlin in the group of Prof. Dr. Christian B. W. entitled *Vorstudien zur Aufklärung der Relativen Konfiguration von Kuhistanol C*
11/2005 – 01/2006	Research lab course at the Institute of Inorganic Chemistry at the Freie Universität Berlin in the group of Prof. Dr. Jens Beckmann issuing *Synthese von (S)-Bis(silyl)-binaphthylethern*

10/2005 – 09/2007	Master of Science studies, chemistry, Freie Universität Berlin
09/2005	Award of Bachelor of Science Degree in chemistry at the Freie Universität Berlin, predicate: *2,2*
07/2005 – 09/2005	Bachelor thesis at the Institute of Organic Chemistry at the Freie Universität Berlin in the group of Prof. Dr. Hans-Ulrich Reissig entitled *Samarium Diiodide Induced 8-endo-trig Cyclisations to Benzannulated Cyclooctanol Derivatives*
08/2004 – 09/2004	Practical Course in the company *Rapid Particle Systems GmbH* targeting the establishment of new redox systems capable of mediating fluorescence erasure in a mild fashion
10/2002 – 09/2005	Bachelor of Science studies in chemistry at the Freie Universität Berlin
12/2001 – 09/2002	Civil Service at the Wilmersdorfer Seniorenstiftung as a bureau assistant (Berlin)

School Education

06/2001	General university entrance qualification (allgemeine Hochschulreife), Leonardo-da-Vinci-Gymnasium, Berlin, predicate: *3,1*
08/1994-06/2001	Leonardo-da-Vinci-Gymnasium (high school), Berlin
08/1988-06/1994	Oskar-Heinroth-Grundschule (elementary school), Berlin

6.3 Publications

6.3.1 Articles

D. T. Thielemann, I. Fernández, P. W. Roesky
New Amino Acid Ligated Yttrium Hydroxy Clusters
Dalton Trans. **2010**, *39*, 6661-6666, *hot paper*.

C. P. Hauser, D. T. Thielemann, M. Adlung, C. Wickleder, P. W. Roesky, C. K. Weiss, K. Landfester
Luminescent Polymeric Dispersions and Films Based on Oligonuclear Lanthanide Clusters
Macromol. Chem. Phys. **2010**, *212*, 3, 286-296.

6.3.2 Conference Talks

Dominique T. Thielemann
Zur Darstellung und Untersuchung von Lanthanoidhydroxoclustern mit α-Aminosäure- und/ oder Dibenzoylmethanidliganden
Wissenschaftliches Colloquium von Arbeitsgruppen für Anorganische Chemie der Universitäten Berlin, Hannover, Karlsruhe, Marburg, Münster, Oxford, Regensburg und Tübingen, Hirschegg (Austria), **2007**.

Dominique T. Thielemann
Neue Koordinationspolymere und Cluster der Seltenerdmetalle
SPP conference of the DFG „Hochaggregierte Systeme und Magnetismus“ at the Ludwig-Maximilians-Universität Munich, **2007**.

Dominique T. Thielemann
Koordinationsoligomere der Lanthanoide: Synthese, Eigenschaften und Katalyse
SPP conference of the DFG „Cluster-Lumineszenz-Treffen“ at the Universität Siegen, **2008**.

Dominique T. Thielemann

The Structural Versatility of Lanthanide-based Coordination Oligomers

XXI. Tage der Seltenen Erden at the Ruhr-Universität Bochum, **2008**.

Dominique T. Thielemann

The Stepwise Functionalization of Lanthanide-based Coordination Oligomers

5. Koordinationschemie-Treffen at the Friedrich-Alexander-Universität Erlangen-Nuremberg, **2009**.

Dominique T. Thielemann

Neue Seltenerdmetallaminosäure-Verbindungen

Wissenschaftliches Colloquium von Arbeitsgruppen für Anorganische Chemie der Universitäten Berlin, Hannover, Karlsruhe, Leipzig, Marburg, Münster, Oxford, Regensburg und Tübingen, Hirschegg (Austria), **2009**.

Dominique T. Thielemann

15-Kernige Seltenerdmetallhydroxocluster mit Peptoidliganden

7. Koordinationschemie-Treffen at the Universität Stuttgart, **2011**, *winner of the "award for best session chairperson" prize*.

6.3.3 Poster Presentations

Dominique T. Thielemann, Simmi Datta, Peter W. Roesky

Chiral and Achiral Clusters of Hydroxo-bridged lanthanides

XX. Tage der Seltenen Erden at the Andreas Hermes Akademie GmbH in Bonn, **2007**.

Dominique T. Thielemann, Peter W. Roesky

Strukturchemie und Eigenschaften von Lanthanoid-Koordinationsoligomeren

14. Votragstagung der Wöhler-Vereinigung (GDCh) at the Technischen Universität Munich, Garching, **2008**.

Dominique T. Thielemann, Igancio Fernández, Peter W. Roesky

New Amino Acid Ligated Yttrium Hydroxy Clusters

6. Koordinationschemie-Treffen at the Johannes Gutenberg Universität Mainz, **2010**.

15. Votragstagung der Wöhler-Vereinigung (GDCh) at the Albert-Ludwigs-Universität Freiburg (Breisgau), **2010**, *winner of a poster prize award.*

7. REFERENCES

[1] S. Cotton, *Lanthanide and Actinide Chemistry*, John Wiley & Sons Ltd., Chichester, **2007**.

[2] K. Hans Wedepohl, *Geochim. Cosmochim. Acta* **1995**, *59*, 1217.

[3] R. Shannon, *Acta Crystallogr. Sect. A* **1976**, *32*, 751.

[4] N. Kaltsoyannis, P. Scott, *The f elements*, Oxford Chemistry Primers, Oxford, **1999**.

[5] E. Riedel, *Anorganische Chemie, Vol. 6*, de Gruyter Verlag, **2004**.

[6] K. S. Pitzer, *Acc. Chem. Res.* **1979**, *12*, 271.

[7] A. F. Hollemann, E. Wiberg, *Lehruch der Anorganischen Chemie, Vol. 101*, de Gruyter Verlag, Berlin, **1995**.

[8] J. Falbe, M. Regitz, *Römpp Lexikon Chemie, Vol. 10*, Thieme Verlag, Stuttgart/New York, **1996-1999**.

[9] K. Reinhardt, *Chemie in unserer Zeit* **1984**, *18*, 24.

[10] F. A. Cotton, G. Wilkinson, *Advanced Inorganic Chemistry, Vol. 5*, John Wiley & Sons, USA, **1988**.

[11] a)J. Shen, L.-D. Sun, C.-H. Yan, *Dalton Trans.* **2008**, 5687; b)G. Muller, *Dalton Trans.* **2009**, 9692; c)S. Petit, F. Baril-Robert, G. Pilet, C. Reber, D. Luneau, *Dalton Trans.* **2009**, 6809; d)S. V. Eliseeva, J.-C. G. Bunzli, *Chem. Soc. Rev.* **2010**, *39*, 189; e)J.-C. G. Bünzli, S. V. Eliseeva, in *Springer Series on Fluorescence* (Eds.: P. Hänninen, H. Härma), Springer Verlag, Berlin, **2010**.

[12] J. E. Geusic, H. M. Marcos, L. G. Uitert, *Applied Physical Letters* **1964**, *4*, 182.

[13] R. J. Mears, L. Reekie, I. M. Jauncey, D. N. Payne, *Electron. Lett.* **1987**, *23*, 1026.

[14] M. G. Lentschig, P. Reimer, U. L. Rausch-Lentschig, T. Allkemper, M. Oelerich, G. Laub, *Radiology* **1998**, *208*, 353.

[15] J. Kocher, F. Gumy, A.-S. Chauvin, J.-C. G. Bünzli, *J. Mater. Chem.* **2007**, *17*, 654.

[16] G. Urbain, *C. R. Acad. Sci. Paris* **1906**, *142*, 205.

[17] S. Shenoya, W. M. Yen, *Phosphor Handbook*, CRC Press Inc., Boca Raton (USA), **1999**.

[18] S. Cotton, in *Lanthanide and Actinide Chemistry*, John Wiley & Sons, Ltd, Chichester, **2006**.

[19] A. P. Ramirez, A. Hayashi, R. J. Cava, R. Siddharthan, B. S. Shastry, *Nature* **1999**, *399*, 333.

[20] M. T. Gamer, Y. Lan, P. W. Roesky, A. K. Powell, R. Clérac, *Inorg. Chem.* **2008**, *47*, 6581.

[21] a)J. Tang, I. Hewitt, N. T. Madhu, G. Chastanet, W. Wernsdorfer, C. E. Anson, C. Benelli, R. Sessoli, A. K. Powell, *Angew. Chem.* **2006**, *118*, 1761; b)V. Mereacre, A. M. Ako, R. Clérac, W. Wernsdorfer, I. J. Hewitt, C. E. Anson, A. K. Powell, *Chemistry – A European Journal* **2008**, *14*, 3577.

[22] D. Gatteschi, R. Sessoli, A. Cornia, *Chem. Commun.* **2000**, 725.

[23] C. J. Milios, S. Piligkos, E. K. Brechin, *Dalton Trans.* **2008**, 1809.

[24] a)L. J. d. Jongh, Kluwer Dordrecht, **1994**; b)G. Schmid, VCH Weinheim, **1994**.

[25] A. Müller, E. Krickemeyer, H. Bögge, M. Schmidtmann, F. Peters, *Angew. Chem. Int. Ed.* **1998**, *37*, 3359.

[26] H. Krautscheid, D. Fenske, G. Baum, M. Semmelmann, *Angewandte Chemie International Edition in English* **1993**, *32*, 1303.

[27] D. Fenske, N. Zhu, T. Langetepe, *Angew. Chem. Int. Ed.* **1998**, *37*, 2639.

[28] P. Sevillano, O. Fuhr, M. Kattannek, P. Nava, O. Hampe, S. Lebedkin, R. Ahlrichs, D. Fenske, M. M. Kappes, *Angew. Chem. Int. Ed.* **2006**, *45*, 3702.

[29] a)Z. Zheng, *Chem. Commun.* **2001**, 2521; b)R. Anwander, *Angew. Chem. Int. Ed.* **1998**, *37*, 599.

[30] M. R. Bürgstein, H. Berberich, P. W. Roesky, *Chemistry – A European Journal* **2001**, *7*, 3078.

[31] J. Gromada, A. Mortreux, T. Chenal, J. W. Ziller, F. Leising, J.-F. Carpentier, *Chemistry – A European Journal* **2002**, *8*, 3773.

[32] F. A. Cotton, *Quarterly Reviews, Chemical Society* **1966**, *20*, 389.

[33] M. Romanelli, G. A. Kumar, T. J. Emge, R. E. Riman, J. G. Brennan, *Angew. Chem. Int. Ed.* **2008**, *47*, 6049.

[34] a)Y. Guyot, A. Collombet, T. Somatri, A. Tkachuk, M. F. Joubert, *J. Alloys Compd.* **2002**, *341*, 174; b)X. Zhang, F. Lahoz, C. Serrano, G. Lacoste, E. Daran, *Quantum Electronics, IEEE Journal of* **2000**, *36*, 243; c)S. A. Payne, C. Bibeau, *J. Lumin.* **1998**, *79*, 143; d)L. C. Courrol, I. M. Ranieri, R. E. Samad, S. L. Baldochi, L. Gomes, A. Z. de Freitas, N. D. Vieira, in *Proc. SPIE-Int. Soc. Opt. Eng., Vol. 6100*, **2006**; e)R. Balda, I. Iparraguirre, J. Azkargota, J. R. Fernandez, in *Proc. SPIE-Int. Soc. Opt. Eng., Vol. 5131*, **2003**, p. 19.

[35] M. Fitzgerald, T. J. Emge, J. G. Brennan, *Inorg. Chem.* **2002**, *41*, 3528.

[36] a)B. Moulton, M. J. Zaworotko, *Chem. Rev.* **2001**, *101*, 1629; b)M. Eddaoudi, D. B. Moler, H. Li, B. Chen, T. M. Reineke, M. O'Keeffe, O. M. Yaghi, *Acc. Chem. Res.* **2001**, *34*, 319; c)A. Müller, P. Kögerler, *Coord. Chem. Rev.* **1999**, *182*, 3; d)R. E. P. Winpenny, *Chem. Soc. Rev.* **1998**, *27*, 447; e)C. Benelli, D. Gatteschi, *Chem. Rev.* **2002**, *102*, 2369; f)M. R. Bürgstein, P. W. Roesky, *Angew. Chem. Int. Ed.* **2000**, *39*, 549; g)M. R. Bürgstein, M. T. Gamer, P. W. Roesky, *J. Am. Chem. Soc.* **2004**, *126*, 5213; h)M.-B. Zhang, J. Zhang, S.-T. Zheng, G.-Y. Yang, *Angew. Chem. Int. Ed.* **2005**, *44*, 1385; i)X. Fang, T. M. Anderson, C. Benelli, C. L. Hill, *Chemistry – A European Journal* **2005**, *11*, 712; j)H. Schumann, G. Kociok-Köhn, J. Loebel, *Z. Anorg. Allg. Chem.* **1990**, *581*, 69.

[37] P. W. Roesky, G. Canseco-Melchor, A. Zulys, *Chem. Commun.* **2004**, 738.

[38] a)N. Sträter, W. N. Lipscomb, T. Klabunde, B. Krebs, *Angewandte Chemie International Edition in English* **1996**, *35*, 2024; b)J. Chin, *Curr. Opin. Chem. Biol.* **1997**, *1*, 514; c)J. Rammo, R. Hettich, A. Roigk, H.-J. Schneider, *Chem. Commun.* **1996**, 105.

[39] R. Anwander, F. C. Munck, T. Priermeier, W. Scherer, O. Runte, W. A. Herrmann, *Inorg. Chem.* **1997**, *36*, 3545.

[40] a)L. G. Hubert-Pfalzgraf, *Coord. Chem. Rev.* **1998**, *178-180*, 967; b)R. C. Mehrotra, A. Singh, U. M. Tripathi, *Chem. Rev.* **1991**, *91*, 1287.

[41] a)L. G. Hubert-Pfalzgraf, N. Miele-Pajot, R. Papiernik, J. Vaissermann, *Journal of the Chemical Society, Dalton Transactions* **1999**, 4127; b)R.-G. Xiong, J.-L. Zuo, Z. Yu, X.-Z. You, W. Chen, *Inorg. Chem. Commun.* **1999**, *2*, 490; c)V. Baskar, P. W. Roesky, *Z. Anorg. Allg. Chem.* **2005**, *631*, 2782; d)V. Baskar, P. W. Roesky, *Dalton Trans.* **2006**, 676; e)P. C. Andrews, T. Beck, C. M. Forsyth, B. H. Fraser, P. C. Junk, M. Massi, P. W. Roesky, *Dalton Trans.* **2007**, 5651; f)S. Datta, V. Baskar, H. Li, P. W. Roesky, *Eur. J. Inorg. Chem.* **2007**, *2007*, 4216; g)P. C. Andrews, T. Beck, B. H. Fraser, P. C. Junk, M. Massi, B. Moubaraki, K. S. Murray, M. Silberstein, *Polyhedron* **2009**, *28*, 2123; h)D. T. Thielemann, I. Fernandez, P. W. Roesky, *Dalton Trans.* **2010**, *39*, 6661.

[42] a)R. Wang, D. Song, S. Wang, *Chem. Commun.* **2002**, 368; b)D. N. L. Messerle, L. Bolinger, A. H. Stolpen, B. F. Mullan, D. Swenson, M. Madsen, *Acad. Radiol* **2005**, *12*, S46; c)X.-J. Kong, Y.-P. Ren, L.-S. Long, Z. Zheng, R.-B. Huang, L.-S. Zheng, *J. Am. Chem. Soc.* **2007**, *129*, 7016; d)X.-J. Kong, Y. Wu, L.-S. Long, L.-S. Zheng, Z. Zheng, *J. Am. Chem. Soc.* **2009**, *131*, 6918; e)Z. Zheng, *Handbook on the Physics and Chemistry of Rare Earths Elements, Vol. 40*, Elsevier, Amsterdam, **2010**.

[43] a)X. Gu, D. Xue, *Inorg. Chem.* **2007**, *46*, 3212; b)J.-W. Cheng, J. Zhang, S.-T. Zheng, M.-B. Zhang, G.-Y. Yang, *Angew. Chem. Int. Ed.* **2006**, *45*, 73; c)X.-J. Zheng, L.-P. Jin, S. Gao, *Inorg. Chem.* **2004**, *43*, 1600.

[44] X.-Y. Chen, X. Yang, B. J. Holliday, *Inorg. Chem.* **2010**, *49*, 2583.

[45] C. Kremer, J. Torres, S. Domínguez, A. Mederos, *Coord. Chem. Rev.* **2005**, *249*, 567.

[46] H.-y. Zhang, H.-j. Yu, H.-x. Xu, J.-s. Ren, X.-g. Qu, *Polyhedron* **2007**, *26*, 5250.

[47] R. Wang, H. Liu, M. D. Carducci, T. Jin, C. Zheng, Z. Zheng, *Inorg. Chem.* **2001**, *40*, 2743.

[48] Ruiyao Wang, Hugh D. Selby, Hui Liu, Michael D. Carducci, Tianzhu Jin, Zhiping Zheng, J. W. Anthis, R. J. Staples, *Inorg. Chem.* **2002**, *41*, 278.

[49] Ruiyao Wang, Zhiping Zheng, Tianzhu Jin, R. J. Staples, *Angew. Chem. Int. Ed.* **1999**, *38*, 1813.

[50] a)D. Casanova, Domitille Giaume, Thierry Gacoin, Jean-Pierre Boilot, A. Alexandrou, *J. Phys. Chem. B* **2006**, *110*, 19264; b)Emmanuel Beaurepaire, Vale´rie Buissette, Martin-Pierre Sauviat, Domitille Giaume, Khalid Lahlil, Antoine Mercuri, Didier Casanova, Arnaud Huignard, Jean-Louis Martin, Thierry Gacoin, Jean-Pierre Boilot, A. Alexandrou, *Nano Lett.* **2004**, *4*, 2079.

[51] K. Ando, H. Kawaguchi, *J. Colloid Interface Sci.* **2005**, *285*, 619.

[52] a)L. P. Ramírez, M. Antonietti, K. Landfester, *Macromol. Chem. Phys.* **2006**, *207*, 160; b)A. Manzke, C. Pfahler, O. Dubbers, A. Plettl, P. Ziemann, D. Crespy, E. Schreiber, U. Ziener, K. Landfester, *Advanced Materials* **2007**, *19*, 1337; c)C. Vancaeyzeele, O. Ornatsky, V. Baranov, L. Shen, A. Abdelrahman, M. A. Winnik, *J. Am. Chem. Soc.* **2007**, *129*, 13653.

[53] a)K. Landfester, C. K. Weiss, *Adv. Polym. Sci.* **2010**, *229*, 1; b)C. K. Weiss, K. Landfester, *Adv. Polym. Sci.*, 10.1007/12_2010_61.

[54] K. Tamaki, M. Shimomura, *Int. J. Nanosci.* **2002**, *5*, 533.

[55] K. Tamaki, H. Yabu, T. Isoshima, M. Hara, M. Shimomura, *Colloids and Surfaces A: Physicochemical and Engineering Aspects* **2006**, *284-285*, 355.

[56] a)C. K. Weiss, M. R. Lorenz, K. Landfester, V. Mailänder, *Macromol. Biosci.* **2007**, *7*, 883; b)S. Lorenz, C. P. Hauser, B. Autenrieth, C. K. Weiss, K. Landfester, V. Mailänder, *Macromol. Biosci.* **2010**, *10*, 1034.

[57] M. Bradley, M. Ashokkumar, F. Grieser, *J. Am. Chem. Soc.* **2003**, *125*, 525.

[58] N. Vogel, C. P. Hauser, K. Schuller, K. Landfester, C. K. Weiss, *Macromol. Chem. Phys.* **2010**, *211*, 1355.

[59] C. P. Hauser, D. T. Thielemann, M. Adlung, C. Wickleder, P. W. Roesky, C. K. Weiss, K. Landfester, *Macromol. Chem. & Phys.* **2011**, *accepted*.

[60] K. Landfester, J. Eisenblätter, R. Rothe, *J. Coat. Technol. Res.* **2004**, *1*, 65.

[61] R. M. Supkowski, W. D. Horrocks, *Inorg. Chim. Acta* **2002**, *340*, 44.

[62] A. Beeby, S. Faulkner, *Chem. Phys. Lett.* **1997**, *266*, 116.

[63] J.-C. G. Bunzli, C. Piguet, *Chem. Soc. Rev.* **2005**, *34*, 1048.

[64] a)L. J. Basile, *J. Chem. Phys.* **1962**, *36*, 2204; b)T. Li, C. Zhou, M. Jiang, *Polym. Bull.* **1991**, *25*, 211.

[65] R. D. Shannon, C. T. Prewitt, *Acta Crystallogr. Sect. A* **1969**, *B25*, 925.

[66] a)Y. Cohen, L. Avram, L. Frish, *Angew. Chem. Int. Ed.* **2005**, *44*, 520; b)T. Brand, E. J. Cabrita, S. Berger, *Prog. Nucl. Magn. Reson. Spectrosc.* **2005**, *46*, 159; c)P. S. Pregosin, P. G. A. Kumar, I. Fernández, *Chem. Rev.* **2005**, *105*, 2977.

[67] a)F. G. R. J. B. Lambert, *Reidel* **1983**; b)J. Mason, *Plenum Press* **1987**; c)P. S. Pregosin, *Elsevier* **1991**; d)B. E. M. R. K. Harris, *Academic Press* **2007**.

[68] a)D. Rehder, *Elsevier* **1991**, 1; b)R. E. White, T. P. Hanusa, *Organometallics* **2006**, *25*, 5621.

[69] a)A. S. J. Kronenbitter, *J. Magn. Reson* **1977**, *25*, 147; b)G. V. F. R. M. Adam, D. G. Reid, *J. Magn. Reson* **1979**, *33*, 655; c)P. L. R. G. C. Levy, J. T. Bailey, **1980**, 167; d)J. Eppinger, M. Spiegler, W. Hieringer, W. A. Herrmann, R. Anwander, *J. Am. Chem. Soc.* **2000**, *122*, 3080.

[70] a)W. J. Evans, J. H. Meadows, A. G. Kostka, G. L. Closs, *Organometallics* **1985**, *4*, 324; b)K. H. den Haan, J. H. Teuben, *J. Chem. Soc., Chem. Commun.* **1986**, 682; c)W. J. Evans, M. S. Sollberger, S. I. Khan, R. Bau, *J. Am. Chem. Soc.* **1988**, *110*, 439; d)D. Stern, M. Sabat, T. J. Marks, *J. Am. Chem. Soc.* **1990**, *112*, 9558; e)C. J. Schaverien, *Organometallics* **1994**, *13*, 69; f)T. I. Gountchev, T. D. Tilley, *Organometallics* **1999**, *18*, 2896.

[71] S.-G. Lee, *Bull. Korean Chem. Soc.* **1996**, *17*, 589.

[72] P. S. Coan, L. G. Hubert-Pfalzgraf, K. G. Caulton, *Inorg. Chem.* **1992**, *31*, 1262.

[73] a)T. G. Wetzel, S. Dehnen, P. W. Roesky, *Angew. Chem. Int. Ed.* **1999**, *38*, 1086; b)N. J. Hill, W. Levason, M. C. Popham, G. Reid, M. Webster, *Polyhedron* **2002**, *21*, 445; c)P. W. Roesky, M. T. Gamer, N. Marinos, *Chemistry – A European Journal* **2004**, *10*, 3537.

[74] a)C. G. Pernin, J. A. Ibers, *Inorg. Chem.* **1999**, *38*, 5478; b)C. G. Pernin, J. A. Ibers, *Inorg. Chem.* **2000**, *39*, 1222.

[75] a)K. Eggenberger, E. Birtalan, T. Schröder, S. Bräse, P. Nick, *ChemBioChem* **2009**, *10*, 2504; b)B. Rudat, E. Birtalan, I. Thomé, D. K. Kölmel, V. L. Horhoiu, M. D.

Wissert, U. Lemmer, H.-J. r. Eisler, T. S. Balaban, S. Bräse, *The Journal of Physical Chemistry B* **2010**, *114*, 13473.

[76] J. Tang, I. Hewitt, N. T. Madhu, G. Chastanet, W. Wernsdorfer, C. E. Anson, C. Benelli, R. Sessoli, A. K. Powell, *Angew. Chem. Int. Ed.* **2006**, *45*, 1729.

[77] a)A. Mishra, W. Wernsdorfer, K. A. Abboud, G. Christou, *J. Am. Chem. Soc.* **2004**, *126*, 15648; b)C. M. Zaleski, J. W. Kampf, T. Mallah, M. L. Kirk, V. L. Pecoraro, *Inorg. Chem.* **2007**, *46*, 1954; c)C. Aronica, G. Pilet, G. Chastanet, W. Wernsdorfer, J.-F. Jacquot, D. Luneau, *Angew. Chem. Int. Ed.* **2006**, *45*, 4659; d)G. Poneti, K. Bernot, L. Bogani, A. Caneschi, R. Sessoli, W. Wernsdorfer, D. Gatteschi, *Chem. Commun.* **2007**, 1807.

[78] O. Deutschbein, R. Tomaschek, *Annalen der Physik* **1937**, *5*, 311.

[79] Z. Zheng, in *Handbook on the Physics and Chemistry of Rare Earths Elements, Vol. 40* (Eds.: K. A. Gschneidner Jr., J.-C. G. Bünzli, V. K. Pecharsky), Elsevier, Amsterdam, **2010**, pp. 109.

[80] R. Rahbari, T. Sheahan, V. Modes, *BioTechniques* **2009**, *46*, 277.

[81] K. Nassau, *The Physics and Chemistry of Colour: The Fifteen Causes of Colour, Vol. 2*, Wiley & Sons, New York, **2001**.

[82] R. Brückner, *Reaktionsmechanismen, Vol. 2*, Spectrum Akademischer Verlag GmbH, Heidelberg-Berlin, **2003**.

[83] S. Routier, L. Saugé, N. Ayerbe, G. Coudert, J.-Y. Mérour, *Tetrahedron Lett.* **2002**, *43*, 589.

[84] B. Yin, Y. Zhang, *Chin. J. Chem.* **2009**, *27*, 1645.

[85] A. Kuttan, S. Nowshudin, M. N. A. Rao, *Tetrahedron Lett.* **2004**, *45*, 2663.

[86] E. Marcantoni, M. Massaccesi, E. Torregiani, G. Bartoli, M. Bosco, L. Sambri, *J. Org. Chem.* **2001**, *66*, 4430.

[87] N. J. Tom, W. M. Simon, H. N. Frost, M. Ewing, *Tetrahedron Lett.* **2004**, *45*, 905.

[88] H. H. Wasserman, G. D. Berger, K. R. Cho, *Tetrahedron Lett.* **1982**, *23*, 465.

[89] D. S. Bose, K. K. Kumar, A. V. N. Reddy, *Synthetic Communications: An International Journal for Rapid Communication of Synthetic Organic Chemistry* **2003**, *33*, 445

[90] H. Sun, S. G. DiMagno, *J. Am. Chem. Soc.* **2005**, *127*, 2050.

[91] G. Xu, Z.-M. Wang, Z. He, Z. Lü, C.-S. Liao, C.-H. Yan, *Inorg. Chem.* **2002**, *41*, 6802.

[92] M. Addamo, G. Bombieri, E. Foresti, M. D. Grillone, M. Volpe, *Inorg. Chem.* **2004**, *43*, 1603.

[93] I. Shinkai, Y. Ohta, *Bioorg. Med. Chem.* **1996**, *4*, 3.

[94] a)R. Rizzoli, B. Buchs, J. P. Bonjour, *Int. J. Cancer* **1992**, *50*, 706; b)S. Nussbaum, R. Warrell, R. Rude, J. Glusman, J. Bilezikian, A. Stewart, M. Stepanavage, J. Sacco, S. Averbuch, B. Gertz, *Journal of Clinical Oncology* **1993**, *11*, 1618.

[95] P. Filipponi, M. Pedetti, F. Beghe, B. Giovagnini, M. Miam, S. Cristallini, *Bone* **1994**, *15*, 261.

[96] a)S. D. Averbuch, *Cancer* **1993**, *72*, 3443; b)S. E. Papapoulos, *Am. J. Med.* **1993**, *95*, 485; c)H. Fleisch, *Seminars in Arthritis and Rheumatism* **1994**, *23*, 261.

[97] T. D. Newbound, M. R. Colsman, M. M. Miller, G. P. Wulfsberg, O. P. Anderson, S. H. Strauss, *J. Am. Chem. Soc.* **1989**, *111*, 3762.

[98] G. M. Sheldrick, *Acta Crystallogr., Sect. A* **2008**, *64*, 112.

Cooperations

National:

Dr. Matthias Adlung: optical investigations on cluster-polymer hybrid compounds
Institute of Inorganic Chemistry, University of Siegen

Dr. Esther Birtalan: peptoid synthesis
Institute of Organic Chemistry, Karlsruhe Institute of Technology

Prof. Dr. Stefan Bräse: support for peptoid synthesis and *in vitro* investigations
Institute of Organic Chemistry, Karlsruhe Institute of Technology

Christoph Hauser: preparation and characterization of cluster-polymer hybrid compounds
Max-Planck-Institute for Polymer Research (Mainz)

Dr. Melanie Klinger: femtosecond laser spectroscopy with polymeric chains
Institute of Physical Chemistry, Karlsruhe Institute of Technology

Dominik Kölmel: peptoid synthesis
Institute of Organic Chemistry, Karlsruhe Institute of Technology

Dr. Yanhua Lan: Magnetic measurements with pentadecanuclear clusters and polymer chains
Institute of Inorganic Chemistry, Karlsruhe Institute of Technology

Prof. Dr. Katharina Landfester: support for cluster-polymer hybrid compounds
Max-Planck-Institute for Polymer Research (Mainz)

Dr. Marco Neumaier: ESI-MS investigations on pentadecanuclear clusters
Institute of Meteorolgy and Climate Research, Karlsruhe Institute of Technology

Prof. Fr. Annie K.Powell: support for magnetic measurements
Institute of Inorganic Chemistry, Karlsruhe Institute of Technology

Dr. Birgit Rudat: optical investigations on pentadecanuclear clusters
Light Technology Institute, Karlsruhe Institute of Technology

Dr. Ute Schepers: *in vitro* investigations on pentadecanuclear clusters
Institute for Toxicology and Genetics, Karlsruhe Institute of Technology

Priv.-Doz. Dr. habil. Andreas-Neil Unterreiner: support for femtosecond laser spectroscopy
Institute of Physical Chemistry, Karlsruhe Institute of Technology

Dr. Clemens Weiss: support for cluster-polymer hybrid compounds
Max-Planck-Institute for Polymer Research (Mainz)

Prof. Dr. Claudia Wickleder: support for optical investigations on cluster-polymer compounds
Institute of Inorganic Chemistry, University of Siegen

International:

Prof. Dr. Phil Andrews: support for the preparation of polymeric chains and stay in Australia
School of Chemistry, Monash University (Melbourne, Australia)

Prof. Dr. Glen Deacon: support for the preparation of polymeric chains and stay in Australia
School of Chemistry, Monash University (Melbourne, Australia)

Dr. Ignacio Fernándo: multidimensional NMR measurements of penta- and pentadecanuclear cluster compounds
Institute of Organic Chemistry, University of Almeria (Spain)

Prof. Dr. Peter C. Junk: support for the preparation of polymeric chains and stay in Australia
School of Chemistry, Monash University (Melbourne, Australia)

Danksagung

Herrn Prof. Dr. Peter W. Roesky möchte ich ausdrücklich für die Möglichkeit danken, meine Doktorarbeit und die damit verbundene äußerst interessante Aufgabenstellung in seinem Arbeitskreis bearbeiten zu dürfen. Seine Zugänglichkeit für verschiedenste Problemstellungen zu jeder Zeit, seine Ideen sowie sein Vertrauen ermöglichten letztlich mein Erreichtes. Des weiteren möchte ich mich bei ihm für seine uneingeschränkt zuverlässige Mentorentätigkeit in den Jahren 2005-2007 bedanken, innerhalb welcher er mich beständig ermutigte meine eigenen Grenzen nicht nur zu erreichen, sondern auch zu erweitern um letztlich den sich anschließenden Weg zu ebnen.

Herrn Priv.-Doz. Dr. Thorsten Stumpf möchte ich für die freundliche und vor allem spontane Übernahme des Zweitgutachtens meiner Dissertation danken.

Ich möchte mich auch ausdrücklich beim Karlsruhe House of Young Scientists (KHYS) für die Finanzierung meines Interdocstudiums in Australien bedanken.

Bei Dr. Jelena Jenter und Dr. Michal Wiecko möchte ich mich für die äußerst gewissenhaften und gründlichen Korrekturen meiner Dissertation bedanken. Zudem möchte ich den beiden ganz herzlich für Ihre Freundschaft in all den Jahren sowie für Ihre Unterstützung in Australien danken.

Ich möchte allen zuvor genannten Kooperationspartner/innen ganz herzlich für die sukzessive Aufwertung meiner bzw. unserer Ergebnisse danken, woraus sich der eigentliche Wert der zugrundeliegenden Arbeit überhaupt erst ergab.

An dieser Stelle möchte ich allen voran Prof. Dr. Stefan Bräse, Dr. Esther Birtalan und Dominik Kölmel für die zuverlässige und unbegrenzte Verfügbarkeit der Peptoidliganden danken, die mein Thema erst so richtig in Fahrt gebracht haben.

Dr. Ute Schepers möchte ich für die umfangreichen *in vitro*-Untersuchungen meiner Cluster danken.

Dr. Birgit Rudat sei ausdrücklich für die engagierten Lumineszenzmessungen gedankt.

Prof. Dr. Annie K. Powell und Dr. Yanhua Lan möchte ich für die Untersuchung der magnetischen Eigenschaften meiner Cluster und Polymere danken.

Dr. Ignacio Fernández möchte ich für die umfassenden NMR-Untersuchungen an meinen Verbindungen danken.

Dr. Marco Neumaier möchte ich für die ESI-MS-Studien danken.

Prof. Dr. Katharina Landfester, Dr. Clemens Weiss und Christoph Hauser möchte ich für die zuverlässige Zusammenarbeit mit Hinblick auf die Cluster-Polymer Hybridnanopartikel und allen zugehörigen Untersuchungen danken.

Prof. Dr. Claudia Wickleder und Dr. Matthias Adlung möchte ich für die Untersuchung der Lumineszenzeigenschaften der Cluster-Polymer Hybridnanopartikel danken.

Priv.-Doz. Dr. Andreas-Neil Unterreiner und Dr. Melanie Klinger danke ich für die fruchtbare Zusammenarbeit im Rahmen der Ultrakurzeitdynamiken meiner Verbindungen.

Prof. Dr. Peter C. Junk, Prof. Dr Glen B. Deacon und Prof. Dr. Phil Andrews möchte ich für die Möglichkeit danken in Ihren Arbeitskreisen arbeiten zu dürfen und gleichzeitig in „down under“ die wohl beste Zeit meines bisherigen Lebens verbringen zu dürfen. Auch an dieser Stelle sei noch einmal Herrn Prof. Dr. Peter W. Roesky gedankt, ohne dessen Zuspruch dieser Aufenthalt in Australien nicht möglich gewesen wäre. Ihren Arbeitskreisen möchte ich für die uneingeschränkte Integration danken, durch die ich mich wie ein vollwertiges Mitglied trotz meiner doch kuzen Verweildauer fühlen konnte.

Meinem ehemaligen Forschungspraktikanten Nicholas Arleth möchte ich für seinen Fleiß und seinen wissenschaftlichen Beitrag im Rahmen seines Praktikums bei mir danken.

Dr. Michael Gamer, Sibylle Schneider und Petra Smie möchte ich für das Messen meiner Kristallstrukturen danken.

Es sei allen Servicemitarbeitern im Hause herzlich für Ihre zuverlässige Arbeit gedankt, wobei allen voran Frank Rieß und Werner Kastner als äußerst beispielhaft genannt werden sollen, mit deren Zuverdienst ich/wir viele unmöglich erscheinende Projekt verwirklichen konnten.

Dr. Karolin Löhnwitz, Dr. Nils Meyer und Dr. Michal Wiecko möchte ich für all die fruchtbaren wissenschaftlichen Gespräche danken, aus denen ich viel lernen konnte. Den Dreien sowie Benjamin Rohrer und Carsten Strzalka möchte ich aber auch für die privaten lustigen Stunden sowie für die akkustischen Inspirationen, die wir im Rahmen der Proben unserer Heavy Metal-Band „Chemical Warfare“ erlangen konnten, danken.

Dr. Sebastian Marks möchte ich für die gute Atmosphäre in unserem stets metallisch beschallten Labor danken, sowie für zahlreiche spaßige Konzert- und Festivalbesuche.

Dr. Paul Benndorf möchte ich für seine unzählbaren fachlichen Hilfen bzgl. etwaiger IT-Probleme meinerseits danken, ohne die mein Laptop wahrscheinlich schon viel früher den Geist aufgegeben hätte.

Anja Lühl möchte ich für Ihre Freundschaft und für die vielen amüsanten Kaffee-, Tratsch- und Kekspausen danken.

Allen weiteren aktuellen sowie ehemaligen Mitarbeitern, Diplomanden und Praktikanten des AK Roesky möchte ich für die angenehme Arbeitsatmosphäre danken.

Im Speziellen möchte ich nochmals bei Dr. Karolin Löhnwitz für die uneingeschränkte selische Unterstützung in allen Lebenslagen während meines Forschungspraktikums, meiner Masterarbeit und meiner Promotion danken. Insbesondere während meiner Promotion konnte diese Form der Unterstützung deutlichst intensiviert werden, was sowohl zu einer gesunden Ablenkung von der Arbeit als auch zu einem unbändigen Zuspruch zu dieser Arbeit beitrug.

Für seine uneingeschränkte Freundschaft und Loyalität möchte ich Sven Seifert danken, die seit nunmehr ca. Oktober 1982 anhält, sprich seitdem wir auf dem Boden rumgekrochen sind und simultan Windeln gefüllt haben. Im Besonderen möchte ich ihm auch für all die gemeinsamen extremsportlichen Aktivitäten auf Ski und Rad danken, während denen ich mich stets von der Laborkocherei erholen konnte um gleichzeitig neue Motivation und Ideen schöpfen zu können.

Raphael Speth und Markus Hund möchte ich ebenfalls im Speziellen für die langjährigen Freundschaften danken, aber vor allem dafür, dass sie mir in schwersten Zeiten stets beistanden und immer an mich geglaubt haben.

Gleichwohl möchte ich auch meinen Freund/innen Ellen Beck, Darjan Salimi, David Patzer, Marco Grunwald, Heiko Lamm, Stefan Förster, Nico Mam, Marcel „Siegbert“ Hoffmann, Oliver „Captain Blood“ Blatt, André Gabriel, Carsten „Qualle“ Strzalka, Benjamin Rohrer, Maciek Jodkiewicz, Rouven Steffenhagen, und allen anderen, die sich als solche verstehen, danken…und zwar dafür, dass man sich über so viele Jahre hinweg immer wieder bereitwillig dazu erklärt hat, wirklich jeden Blödsinn mit mir hemmungslos durchzuziehen und durchzustehen…

In diesem Sinne möchte ich nochmal Marcel Hoffmann nunmehr für die gemeinsame, glorreiche Erstellung mannigfaltiger PC-Protokolle inklusive argen Debatten über Fehlerrechnung danken, welche wir ohne seinen Megadrive und „Street Fighter“ niemals hinbekommen hätten…hehehe…

Auch Oliver Blatt sei hier nochmal separat gedankt, mit dem ich gemeinsame Kristallographieprotokolle stets mit todesmetallischen Moschpausen erfolgreich durchstehen konnte…

Aus meinen Karlsruher Zeiten möchte ich allen voran meinem Freund und Trainer Christian Ratzky für ziemlich coole Zeiten hier in der Baden-Metropole danken, und zwar sowohl auf als auch neben dem Platz. Und allen anderen Kollegen des TC Grün Weiß Karlsruhe für geile Matches und auch derbe Abreibungen…;)

Am herausragendsten seien jedoch meine lieben Eltern genannt, ohne deren grenzenlose seelische sowie finanzielle Unterstützung das Lebensprojekt „Studium und Promotion“ nicht im Ansatz möglich gewesen wäre, und zwar schon gar nicht innerhalb der Zeit, die ich dafür schlussendlich benötigt habe. Auch meinen Stiefeltern und –familien sei an dieser Stelle für Ihr Verständnis und Ihre selbstlose Unterstützung gedankt. Zuguterletzt möchte ich mich auch noch bei meinen Großeltern, meiner Tante, meinem Onkel, meiner Cousine und allen weiteren Verwandten dafür bedanken, dass sie mich in meinem Tun stets bestärkt und bestätigt haben.